Universitat Politècnica de València
Departamento de Máquinas y Motores Térmicos

UNIVERSITAT
POLITÈCNICA
DE VALÈNCIA

Doctoral Thesis

Development of Integrated Models for Thermal Management in Hybrid Vehicles

Presented by:

Mr. Amin Dreif Bennany

Supervised by:

Dr. Pablo César Olmeda González

In fulfillment of the requisites for the degree of
Doctor of Philosophy

València, April 2023

Ph.D. Thesis

Development of Integrated Models for Thermal Management in Hybrid Vehicles

Presented by: Mr. Amin Dreif Bennany
Supervised by: Dr. Pablo César Olmeda González

Defense Committee:

Chairman: Dr. José Manuel Luján Martínez
Secretary: Dr. Octavio Armas Vergel
Member: Dr. Richard Burke

Reviewing board:

Dr. Noureddine Guerrassi
Dr. Richard Burke
Dr. Pablo Fernández-Yáñez Luján

València, April 2023

Abstract

In recent years, the automotive industry has made a great effort to produce more efficient and less polluting propulsion systems without diminishing their performance. The new regulations imposed by the authorities have pushed the industry towards the electrification of powertrains while, technologies developed for the conventional propulsion system based on alternative internal combustion engines (ICEs), are no longer sufficient.

Numerical modeling has proven to be an indispensable tool for the design, development and optimization of thermal management systems in electrified powertrains, saving costs and reducing development time. Thermal management in ICEs has always been important for improving consumption, emissions and safety. However, it is even more important in hybrid powertrains, due to the complexity of the system and the intermittent operation of the ICE. In addition, electrified powertrains have various heat sources (i.e., ICE, battery, Electric machine) with different thermal operating requirements.

The main objective of this work was to develop thermal models to study the improvement of thermal management systems in electrified powertrains (i.e., hybrid electric vehicle), shedding light and quantifying the influence of different strategies on performance, safety and efficiency of the vehicles.

The methodology developed in this paper consisted both in carrying out experiments and in developing numerical models. In fact, an extensive experimental campaign was carried out to validate the various models of the electrified powertrain. The data obtained from the experimental campaigns served to calibrate and validate the models as well as to corroborate the results obtained by the numerical studies.

Firstly, the different thermal management strategies were studied independently for each component of the powertrain. For the ICE, the use of nanofluids, insulation of exhaust manifold and ports as well as the volume change of its hydraulic circuits were studied. Similarly, the impact of different strategies for the thermal improvement of batteries was evaluated. Furthermore, the electric machine model was used for developing experimental tests which emulated the thermal damage produced in real driving cycles. Secondly, the powertrain models were integrated using a

co-simulation standard to assess the impact of an integrated thermal management system. Finally, a new control energy management system was implemented to assess the impact of considering the ICE thermal state when deciding the power split of the hybrid vehicle.

The results have shown that the use of nanofluids has a very limited impact on both the ICE and the battery's thermal behaviour. In addition, they also showed that by reducing the volume of coolant by 45 %, the reduction in ICE warm up time and fuel consumption compared to the base case were 7 % and 0.4 %, respectively. In addition, for cold conditions (-7°C), the impact was even greater, obtaining a reduction in warm up time and fuel consumption of 13 % and 0.5 % respectively. On the other hand, the results concluded that during the warming of ICE, the integrated thermal management system improved energy consumption by 1.74 % and 3 % for warm (20°C) and cold (-20°C) conditions, respectively. This is because the integrated TMS makes it possible to prevent the ICE temperature drop when the powertrain is in pure electric mode. Finally, significant gains during Worldwide harmonized Light vehicles Test Cycles (WLTC) and Real Driving Emissions (RDE) cycles were observed when the ICE thermal state was chosen when deciding the power distribution.

Resum

En els últims anys, la indústria de l'automoció ha fet un gran esforç per a produir sistemes de propulsió més eficients i menys contaminants sense minvar el seu rendiment. Les noves regulacions imposades per les autoritats han espentat a la indústria cap a l'electrificació dels sistemes de propulsió mentre que les tecnologies desenvolupades per al sistema de propulsió convencional, basat en motors de combustió interna alternatius (MCIA), ja no són suficients.

El modelatge numèric ha demostrat ser una eina indispensable per al disseny, desenvolupament i optimització de sistemes de gestió tèrmica en trens motrius electrificats, estalviant costos i reduint el temps de desenvolupament. La gestió tèrmica en els MCIA sempre ha sigut important per a millorar el consum, les emissions i la seguretat. No obstant això, és encara més important en els sistemes de propulsió híbrids, a causa de la complexitat del sistema i al funcionament intermitent del MCIA. A més, els trens motrius electrificats tenen diverses fonts de calor (és a dir, MCIA, bateria, màquina elèctrica) amb diferents requisits de funcionament tèrmic.

L'objectiu principal d'aquest treball va ser desenvolupar models tèrmics per a estudiar la millora dels sistemes de gestió tèrmica en sistemes de propulsió electrificats (és a dir, vehicle híbrid), estudiant i quantificant la influència de diferents estratègies en el rendiment, la seguretat i l'eficiència dels vehicles.

La metodologia desenvolupada en aquest treball va consistir tant en la realització d'experiments com en el desenvolupament de models numèrics. De fet, es va dur a terme una extensa campanya experimental per a validar els diferents models del tren motriu electrificat. Les dades obtingudes de les campanyes experimentals van servir per a calibrar i validar els models així com per a corroborar els resultats obtinguts pels estudis numèrics.

En primer lloc, es van estudiar les diferents estratègies de gestió tèrmica de manera independent per a cada component del tren motriu. Per al MCIA es va estudiar l'ús de nanofluids, l'aïllament del col·lector i ports d'eixida així com el canvi de volum dels seus circuits hidràulics. D'igual forma, es va avaluar l'impacte de diferents estratègies per a la millora tèrmica de les bateries. A més, el model de màquina elèctrica es va utilitzar per a desenvolupar proves experimentals que emulaven el mal tèrmic

produït en cicles reals de conducció. En segon lloc, els models de tren motriu es van integrar utilitzant un estàndard de co-simulació per a avaluar l'impacte d'un sistema de gestió tèrmica integrat. Finalment, es va implementar un nou control del sistema de gestió d'energia per a avaluar l'impacte de considerar l'estat tèrmic del MCIA al moment de decidir la distribució de potència del vehicle híbrid.

Els resultats han demostrat que l'ús de nanofluids té un impacte molt limitat tant en el MCIA com en el comportament tèrmic de la bateria. A més, també van mostrar que en reduir el volum de refrigerant en un 45 %, la reducció en el temps de calfament del MCIA i el consum de combustible en comparació amb el cas base va ser del 7 % i del 0.4 %, respectivament. A més, per a condicions de fred (-7°C), l'impacte va ser encara major, obtenint una reducció del temps de calfament i del consum de combustible del 13 % i del 0.5 % respectivament. D'altra banda, els resultats van concloure que durant el calfament del MCIA, el sistema integrat de gestió tèrmica va millorar el consum d'energia en un 1.74 % i un 3 % per a condicions de calor (20°C) i fred (-20°C), respectivament. Això es deu a que el sistema de gestió tèrmica integrat permet evitar la caiguda de temperatura del MCIA quan el sistema de propulsió està en manera elèctrica pura. Finalment, es van observar guanys significatius durant els cicles de prova de vehicles lleugers harmonitzats a tot el món (WLTC) i els cicles d'emissions de conducció real (RDE) quan es va considerar l'estat tèrmic del MCIA en decidir la distribució de potencia.

Resumen

En los últimos años, la industria de la automoción ha hecho un gran esfuerzo para producir sistemas de propulsión más eficientes y menos contaminantes sin menguar su rendimiento. Las nuevas regulaciones impuestas por las autoridades han empujado a la industria hacia la electrificación de los sistemas de propulsión mientras que las tecnologías desarrolladas para el sistema de propulsión convencional, basado en motores de combustión interna alternativos (MCIA), ya no son suficientes.

El modelado numérico ha demostrado ser una herramienta indispensable para el diseño, desarrollo y optimización de sistemas de gestión térmica en trenes motrices electrificados, ahorrando costes y reduciendo el tiempo de desarrollo. La gestión térmica en los MCIA siempre ha sido importante para mejorar el consumo, las emisiones y la seguridad. Sin embargo, es todavía más importante en los sistemas de propulsión híbridos, a causa de la complejidad del sistema y al funcionamiento intermitente del MCIA. Además, los trenes motrices electrificados tienen varias fuentes de calor (es decir, MCIA, batería, máquina eléctrica) con diferentes requisitos de funcionamiento térmico.

El objetivo principal de este trabajo ha sido desarrollar modelos térmicos para estudiar la mejora de los sistemas de gestión térmica en sistemas de propulsión electrificados (es decir, vehículo híbrido), estudiando y cuantificando la influencia de diferentes estrategias en el rendimiento, la seguridad y la eficiencia de los vehículos.

La metodología desarrollada en este trabajo consistió tanto en la realización de experimentos como en el desarrollo de modelos numéricos. De hecho, se llevó a cabo una extensa campaña experimental para validar los diferentes modelos del tren motriz electrificado. Los datos obtenidos de las campañas experimentales sirvieron para calibrar y validar los modelos así como para corroborar los resultados obtenidos por los estudios numéricos.

En primer lugar, se estudiaron las diferentes estrategias de gestión térmica de manera independiente para cada componente del tren motriz. Para el MCIA se estudió el uso de nanofluidos, el aislamiento del colector y puertos de escape, así como el cambio de volumen de sus circuitos hidráulicos. De igual forma, se evaluó el impacto de diferentes estrategias para la mejora térmica de las baterías. Además, el modelo de máquina eléctrica se utilizó para desarrollar pruebas experimentales que emulaban

el daño térmico producido en ciclos reales de conducción. En segundo lugar, los modelos de tren motriz se integraron utilizando un estándar de co-simulación para evaluar el impacto de un sistema de gestión térmica integrado. Finalmente, se implementó un nuevo control del sistema de gestión de energía para evaluar el impacto de considerar el estado térmico del MCIA al momento de decidir la distribución de potencia del vehículo híbrido.

Los resultados han demostrado que el uso de nanofluidos tiene un impacto muy limitado tanto en el MCIA como en el comportamiento térmico de la batería. Además, también mostraron que al reducir el volumen de refrigerante en un 45 %, la reducción en el tiempo de calentamiento del MCIA y el consumo de combustible en comparación con el caso baso fue del 7 % y del 0.4 %, respectivamente. Además, para condiciones de frío (-7°C), el impacto fue todavía mayor, obteniendo una reducción del tiempo de calentamiento y del consumo de combustible del 13 % y del 0.5 % respectivamente. Por otro lado, los resultados concluyeron que durante el calentamiento del MCIA, el sistema integrado de gestión térmica mejoró el consumo de energía en un 1.74 % y un 3 % para condiciones de calor (20°C) y frío (-20°C), respectivamente. Esto se debe al hecho que el sistema de gestión térmica integrado permite evitar la caída de temperatura del MCIA cuando el sistema de propulsión está en manera eléctrica pura. Finalmente, se observaron ganancias significativas en los ciclos de prueba de vehículos ligeros armonizados en todo el mundo (WLTC) y los ciclos de emisiones de conducción real (RDE) cuando se consideró el estado térmico del MCIA al decidir la distribución de potencia.

Acknowledgments

First and foremost, I would like to praise and thank Allah (God), The Almighty, for giving me my life, guiding me into goodness, and surrounding me with great, caring, and knowledgeable people during the elaboration of my Ph.D. Thesis.

Special gratitude to my beloved family; my parents Khalid and Zohra, my dear brothers Achraf and Miloud, and my beloved wife Hind.

Special mention deserves my supervisor and friend Dr. Pablo César Olmeda González for his mentoring, support, guidance, and patience during the last years.

My gratitude also to the professors who were directly or indirectly involved in this research: Dr. Alberto Broatch, Dr. Benjamín Plá, Dr. Jaime Martín, Dr. Antonio Torregrosa, Dra. Xandra Margot and Dr. Francisco José Arnau.

I want to extend my sincere gratitude to Bernardo Planells for carrying on the experimental tests and all the members of CMT-Motores Térmicos, including researchers I worked with, professors, technicians, and administration staff. Especially, Amparo Cutillas, for her dedication, responsibility, and clear guidance through all the administrative procedures.

Of course, I wish to thank my friends and work colleagues at the office in order of seniority: Alejandro Gómez, Álvaro Redondo, Sebastian Aceros, and Luca Agizza. Thank you for turning the office into a small family.

Funding

The author would like to sincerely acknowledge the founding support provided by Conselleria de Innovación, Universidades, Ciencia y Sociedad Digital in the framework of the Ayuda Predoctoral GVA. (ACIF/2020/234).

Additionally the author would also acknowledge the support provided by Renault S.A.S.

Contents

List of figures

List of tables

Nomenclature

Acronyms

0D/1D/3D	0/1/3 Dimensional
BEVs	Battery Electric Vehicles
BMEP	Break Mean Effective Pressure
BSFC	Brake Specific Fuel Consumption
BTMS	Battery Thermal Management System
CG-TVD	Corberán-Gascón Total Variation Diminishing
CFL	Courant-Friedrichs-Lewy
CPU	Central Processing Unit
CFD	Computational Fluid Dynamic
CAC	Charge Air Cooling
DP	Dynamic Programming
ECEM	Equivalent Circuit Electric Model
EDS	Electric Drive System
EDTMS	Electric Drive Thermal Management System
EMS	Energy Management System
ECU	Electronic Control Unit
EGR	Exhaust Gas Recirculation
EV	Electric Vehicles
EVO	Exhaust Valve Opening
ECMS	Equivalent Consumption Management Strategy
EM	Electric Machine
FEM	Finite Element Analysis

FMI	Functional Mock-up Interface
FMU	Functional Mock Up Unit
FSM	Fast Simulation Method
GDI	Gasoline Direct Injection
GHG	Green House Gas
GPF	Gasoline Particulate Filter
HEVs	Hybrid Electric Vehicles
HVAC	Heating, Ventilating and Air Conditioning
HX	heat Exchanger
HSG	High-voltage Starter Generator
ICE	Internal Combustion Engines
ICEVs	Internal Combustion Engine Vehicles
ITMS	Integrated Thermal Management Systems
IVC	Intake Valve Closing
LTM	Lumped Thermal Model
MPC	Model Predictive Control
NTU	Number Transferred Units
ODE	Ordinary Differential Equation
OEMs	Original Equipment Manufacturers
PHEV	Plug-in Hybrid Electric Vehicles
PID	Proportional Integral Derivative
PMP	Pontryagin´s Minimum Principle
PMSM	Permanent Magnet Synchronous Motor
RCCI	Reactivity Controlled Compression Ignition
RDE	Real Driving Emission
TM	Thermal Management
TMS	Thermal Management System
TWC	Three-Way Catalyst
SI	Spark Ignition
SOC	State of Charge
VEMOD	Virtual Engine Model
WLTC	Worldwide harmonised Light vehicle Test Cycle
xEVs	Electrified Vehicles
Latin characters	
A	area
c_p	heat capacity at constant pressure
c	heat capacity
$[C]$	capacitances matrix
d	distance

h	convection heat transfer coefficient
I	current
k	thermal conductivity
$[K]$	thermal conductances matrix
K	hydraulic resistance coefficient
K_{fa}	equivalent heat conductance between fluid and ambient
m	mass
$\dot{m}$	mass flow
OCV	open circuit voltage
$\dot{m}$	mass flow rate
N	speed
P	power
$\dot{Q}$	heat exchanged or generated
R_0	independent coefficient of the hydraulic resistance
R_1	linear coefficient of the hydraulic resistance
R_2	quadratic coefficient of the hydraulic resistance
T	temperature
$[T]$	array of nodes temperature
U	gas velocity
V	voltage
$\dot{V}$	volumetric flow mass
Greek symbols	
Δt	time step
Δx	local mesh size
ΔP	total pressure drop
ε	emissivity coefficient
σ	Stefan-Boltzmann Constant
η	efficiency
υ	speed of sound
ρ	density
ϕ	nanoparticle concentration
γ	ratio of nanolayer and nanoparticle conductivities
β	ratio of nanolayer thickness and nanaparticle radio
μ	dynamic viscosity
Subscript	
amb	ambient
b	base fluid
$cell$	battery cell
g	gas node

i, j	solid nodes
l	liquid node
n	nodes number
nf	nanofluid
p	nanoparticle
r	refrigerant
req	required
t	current time
$t + \Delta t$	next time step
Superscript	
bc	boundary conditions
i	solid node

List of publications

Amin Dreif Bennany is co-author of the publications detailed in this section, with the supervision of other members of the I.U. CMT-Motores Térmicos (CMT), and specially by Prof. Pablo César Olmeda González. The publications in this section are merely the publications resulting from the researching activities performed during the candidate's doctorate. The respondent carried out several experimental activities, which were analysed and processed in order to back up the studies and assumptions pretended, as well as the development of models presented in the publications. The analysis and discussion of results and procedures were done in collaboration with the thesis director (Prof. Pablo César Olmeda González) and with the co-authors of each publication. Each author's contribution to each study is specified in the "contributions description section" in the different studies. Any requirement to guarantee the fulfilment of the Ph.D. works, such as materials, software licenses and test benches were provided by the UPV and CMT. The results of the works cited in this section have been improved, ordered, linked, completed, and further discussed in the present thesis manuscript. The aforementioned or whatever other publications, have been appropriately referred to, in the document itself. However, for the sake of readiness and avoidance of reiterative structure at each chapters' beginning, the publications of this list may not have been specifically cited every time, as part of the contents, figures and discussions have been partially taken from the PhD candidate publications. This section compensates and justifies that the basis of the inno-

vative component has already been presented in the publications specified in this section, therefore constituting Mr. Dreif's thesis document. The signature of PhD candidate follows the CMT members seniority signing order protocol. Hence, in most publications, the PhD candidate becomes the last signer according to this protocol.

[1] Broatch, A.; Olmeda, P.; Pla, B; **Dreif, A.**; Onorati; A. ; Marinoni, A. (2023) Numerical assessment of integrated thermal management systems in electrified powertrains. Applied Thermal Engineering (221).

[2] Broatch, A.; Olmeda, P.; Martín, J.; **Dreif, A.** (2022) Improvement in engine thermal management by changing coolant and oil mass. Applied Thermal Engineering (212).

[3] Torregrosa, A. J.; Broatch, A.; Olmeda, P.; **Dreif, A.** (2021) Assessment of the improvement of internal combustion engines cooling system using nanofluids and nanoencapsulated phase change materials. International Journal of Engine Research, 6 (22), 1939 - 1957.

[4] Broatch, A.; Olmeda, P.; Pla, B.; **Dreif, A**. (2023) Novel Energy Management Control Strategy for Improving Efficiency in Hybrid Powertrains. Energies, 17 (16), 1 - 21.

[5] Marinoni, A.; Onorati, A.; Montenegro, G.; Sforza, L.; Cerri, T.; Olmeda, P.; **Dreif, A**. (2023) RDE cycle simulation by 0D/1D models to investigate IC engine performance and cylinder-out emissions. International Journal of Engine Research.

[6] Broatch, A.; Olmeda, P.; Martín, J.; **Dreif, A**. (2020). Numerical Study of the Maximum Impact on Engine Efficiency When Insulating the Engine Exhaust Manifold and Ports during Steady and Transient Conditions. EN 3rd CO2 Reduction for Transportation Systems Conference Digital. (1 - 11). Torino, Italy: SAE International.

[7] Olmeda, P.; Pla, B.; **Dreif, A**; Planells, B. (2022). Integrated thermal management in hybrid vehicles by means of numerical simulation. EN XII Congreso Nacional y III Internacional de Ingeniería Termodinámica (12 CNIT). (680 - 689). Madrid, Spain.

1 Introduction

1.1 Background

Concerns about the efficient use of the available energetic resources have been a major issue for a long time, acquiring a central role after the energetic crisis of the seventies. Along with this motivation which led to big instability in the energetic supply and a high increase in fuel prices, in recent years it has appeared a new one. Nowadays environmental concerns are widespread mainly due to two types of environmental problems arising from intensive use of fossil fuels (See Figure 1.1): global scale effects (i.e. climate change) and local scale effects (i.e. poor air quality in cities).

The automotive industry has traditionally been one of the main consumers of fossil energy sources. Additionally, the continuous development of the economical powers together with the growth of the world population, has contributed enormously to the increase of greenhouse gases (GHG) emissions as it can be seen in Figure 1.2. For instance, carbon dioxide emissions are the primary driver of global climate change and a great increment (40 % in the last 2 decades) has been produced in last years. In 2016, the transportation sector was responsible for the 16.2 % of the global GHG emissions according to the data provided in Our World in Data [1].

Additionally, the road transport is the largest source of air pollution in cities being responsible for more than 39 % of NO_x emissions in EU

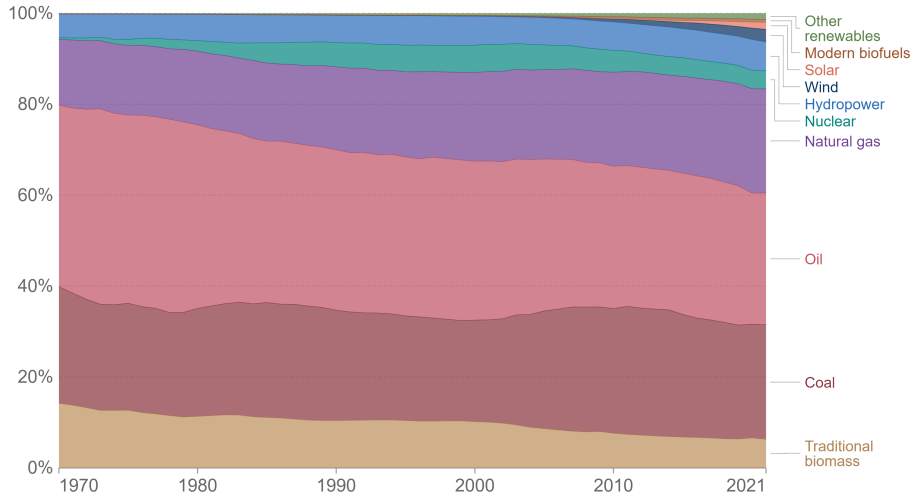

Figure 1.1: Global primary energy consumption [1].

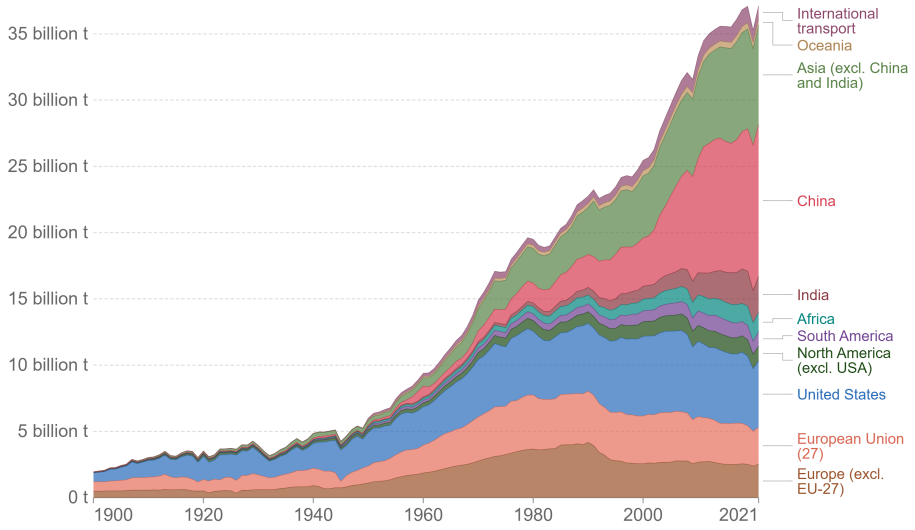

Figure 1.2: Global CO2 emissions from fossil fuels increase in the last years. [1]

during 2018. Aiming to solve this problem, several governments of the world leading countries have been continuously dictating regulations to promote the development of more efficient propulsive systems. All this, while keeping vehicles affordable for consumers and promoting competitiveness. For instance, the Euro 7 standard regulation proposed by the European Commission targets a reduction of 35 % of total NO_x emissions from cars and vans in 2035. In regard to CO_2 emissions, EU commission aims to reach a 55 % GHG emissions reduction by 2030 and to achieve climate neutral by 2050.

Moreover, the new regulations also dictated the modification of the homologation driving cycle: from the New European Driving Cycle (NEDC) to the Worldwide Harmonized Light Vehicles Test Procedure (WLTP) and the implementation of emissions in real driving conditions (Real Driving Emissions, RDE). Hence, adding further challenges for the European automotive industry. The introduction of the previous regulations implies an increase in development costs and disrupted the current fuel saving strategies.

In view of the current socio-political restrictions and market demands, automotive manufacturers are investing a large amount of resources in research and development (R&D) to further develop innovative powertrains in order to improve their efficiency and reduce their environmental impact [2]. Vehicle electrification has proven to be a promising solution for achieving that aim [3]. Investigations have demonstrated that the hybrid propulsive systems can reduce exhaust emissions and improve fuel economy compared to the traditional propulsive systems based on the internal combustion engine (ICE) [4]. Nevertheless, increasing the rate of vehicle electrification traduces in more expensive vehicles because of the battery and power electronics cost [5]. Overall, electrified vehicles (xEVs) are considered as an important part of the future transportation as a substitute for internal combustion engine vehicles (ICEVs). Although the battery electric vehicles (BEVs) have higher price, they have shown to be competitive and can be expected to be more prevalent in the market due to several attractive features, such as higher energy efficiency, lower maintenance frequency, faster acceleration, and noiseless and emission-free operation [6]. However, BEVs suffer from some obstacles, such as weight, higher cost, limited driving range, extra recharging time and overloaded batteries. Thus, hybrid electric vehicles (HEVs) or plug-in hybrid electric vehicles (PHEV), combining an internal combustion engine (ICE) with an electric motor, have been widely developed because they combine the

merits of BEVs and ICEVs. Compared with ICEVs, HEVs can consume less fossil fuel and generate lower GHG emissions; while compared with BEVs, HEVs avoid range anxiety due to the power support from ICEs and self-charging batteries. Furthermore, PHEVs can be directly charged from the grid increasing their electric mobility and diminishing the ICE dependence [7].

Also, in recent decades, a large number of virtual tools have been developed to assist in the design of propulsion plant development. From detailed modeling of the combustion processes of the internal combustion engine to transmission analysis and fuel consumption of the complete vehicle. However, these tools have been, for the most part, standalone tools and have not been particularly well connected to each other. On the other hand, future powertrain solutions for hybrid vehicles will encompass an increasing number of complex subsystems. The optimal choice of these subsystems of the propulsion plant must be made from a global scope, that is, the models of the subsystems must communicate and interact with each other [8].

From an energy point of view, the availability of different energy sources in a hybrid vehicle implies the possibility that the propulsion plant works in many different ways, with possible substantial advantages of one way of operating over another, both in fuel consumption and emissions at the expense of architectural complexity and also more complex control [9]. In hybrid vehicles, the control system has several challenges: on the one hand, the ICE, the battery and the electric motor are controlled to adjust to the required operating points according to a set of individual operating conditions (temperatures, safety , etc.). On the other hand, managing the interaction among the devices. It is generally accepted that a substantial part of the performance in a hybrid vehicle is based on the use of appropriate control strategies for the individual elements of the propulsion plant, but strategies for energy management at the system level are also required [10].

One of the main challenges in hybrid engines is related to the question: how to split energy to minimize fuel consumption and, eventually, pollutant emissions?, in addition to simultaneously meeting other performance criteria and maintaining a set of constraints. On the other hand, the size and selection of the appropriate elements of the propulsion plant may also depend on the control strategies to be used [11]. Therefore, it seems necessary to include, in the simulation tool, a control framework to allow, on the one hand, the integration of the propulsion plant elements

and, on the other, provide a fair basis for the evaluation and comparison of different alternatives.

Thermal management (TM) of internal combustion engines is essential to cool the engine's construction elements, but it is also essential to reduce fuel consumption and pollutant emissions during engine warm-up. In hybrid electric vehicles (HEV), in addition to the ICE, thermal management must include all subsystems in which heat exchanges occur, such as the air conditioning system (AC) and the Electric Drive System (EDS) [12]. Currently, to optimize TM strategies in ICE, one-dimensional (1D), three-dimensional (3D) or 1D/3D co-simulation computational tools are applied. 3D numerical simulation allows the details of complex thermodynamic and flow characteristics of engines to be evaluated. 1D modeling approaches are applicable and convenient for rapid definition and modification of flexible TM strategies. 1D modeling is less computationally expensive and provides good accuracy for engineering design calculations [8].

The main challenges related to thermal management of hybrid vehicles are:

- Impact quantification of the ICE discontinuous operation in terms of thermal behavior of the engine, fuel consumption and the operation of the after-treatment devices.

- The achievement of adequate and reliable thermal management strategies to reduce the warm-up time and increase the cool-down time of the ICE during its start-up and shutdown, respectively.

- The establishment of synergies between the thermohydraulic flows of the ICE and the EDS to propose and evaluate the possible interactions between the cooling systems of both systems.

- Study of the thermal behavior of the new elements (for example, batteries, power electronics, electric motor) of hybrid vehicles that require a controlled management of the thermal state.

- The application of new cooling strategies to meet the different needs of the elements in terms of operating temperatures, interaction of thermal flows between different systems, intelligent energy management and control strategy for optimal operation of the complete system, etc.

The implementation of a flexible and reliable 1D model to evaluate the cooling of the components of the propulsion plant of hybrid vehicles will allow the definition of active and innovative cooling strategies to reduce the warm up time. The optimal solution will lead to an improvement in the vehicle's fuel consumption and an increase in the exhaust gas temperature, which will contribute to reduce polluting emissions due to the early activation of the ICE aftertreatment systems.

These activities will also contribute to determining the synergies between the thermal flows of different elements: ICE, battery, EDS and AC, a fact that will allow the integration of solutions to optimize thermal management. Likewise, global management will allow the elimination of redundant equipment in the vehicle. In order to obtain an intelligent flow of thermal energy, a control strategy will be elaborated for the complete thermal management at the vehicle level. Under these conditions, this research project is proposed.

1.2 Scope and objectives

The main objective of this PhD thesis is to contribute to the thermal management of electrified vehicles, specially, those with hybrid powertrains which strongly depend on the ICE performance and efficiency (i.e., HEV or PHEV). To this end, the aim is to identify the mechanisms that lead to the improvement of thermal management systems while shedding light and quantifying the influence of different strategies on vehicle performance, safety and efficiency.

To achieve this main objective it is necessary to meet several specific sub-objectives:

- To develop a modelling and experimentally based methodology to accurately evaluate thermal management systems from both component and integrated level. Additionally, the developed modelling tools should be validated with either experimental data carried out in the present work or from literature. The experimental measurements will consider not only steady-state test but also very dynamic transient cycle which represent real driving conditions.

- To develop numerical models for each component of the electrified vehicle. Each component submodel has been constructed in a specialized software and interconnected. Implementing a modelling tool capable of reproducing all the thermohydraulic phenomena of a ICE

through a physics-based approach considering the interrelation of the phenomena within the ICE and its different subsystems. Additionally, in-house models need to be developed for the main electric components for calculating their thermal state and the heat rejected to TMS.

- To study independent thermal strategies for the ICE, battery and EDS using the developed models. To evaluate both the designing of the cooling system and oil circuit layout on the engine performance. To assess the use of nanofluids as a coolant medium seems to be an interesting alternative.

- To couple the ICE, battery, EDS and thermohydraulic models by means of standardized co-simulation interface.

- To assess the degree of interaction of the heat flows of an hybrid powertrain system in order to evaluate the viability of integrated concepts of thermal management systems (ITMS). To evaluate the impact of this ITMS on fuel consumption and temperature operation under transient cycles.

- To implement an energy management system to optimize the power-split for a series-parallel hybrid vehicle architecture. The developed control will take consideration the thermal state of the engine and its impact on the overall efficiency.

- To experimentally evaluate the fuel gains obtained with the energy management system. In order to assess the engine fuel consumption variation with the temperature, an extensive experimental campaign was carried out at different engine coolant temperatures. The validation of the control strategy was carried out in the testbench and further simulations were performed to evaluate fuel gain in transient cycles.

1.3 Outline

The present work is divided as follows:

Aiming to fulfil the objectives of the present work, the research activities started with a thorough literature review about different components of the electrified vehicles as it will be detailed in Chapter 2. Special

attention was given to the thermal management of the powertrain components: ICE, battery, electric motors and generators and inverter. Furthermore, investigation regarding the methodologies and tools used for studying these components was also carried out. Finally, relevant studies on thermal strategies at a component level and from an integrated approach were also investigated.

Later, the descriptions of test facilities that were used for collecting the experimental data for both ICEs and batteries are detailed in Chapter 3. The experimental measurements were a fundamental reference for several studies of the thesis' research as well as for calibrating the models.

The modelling tools employed for developing the thesis' studies are detailed in Chapter 4. The engine model is constructed using different submodels which are physically based. Different modeling tools are implemented according to the suitability and requirements of the studies. Regarding the electric components, the development of the battery and electric drive system models are also described. Among the different submodels, special attention is given to the heat transfer. The validation of the models is also presented in Chapter 4.

After that, the results obtained in different studies are presented in Chapter 5. The thermal management strategies studied for the ICE, battery along with the development of thermal durability test using the models developed and validated in Chapter 4. For the ICE, the impact of changing the hydraulic circuits volume, partial insulation of the exhaust gas line and the suitability of nanofluids as coolant are assessed. Furthermore, different thermal strategies for the battery are evaluated. Finally, holistic studies results are detailed considering an integrated thermal management system and a novel energy management system which account for the ICE thermal state.

In Chapter 6 a final overview of the work done and a summary of the most relevant contributions is made. To conclude, proposals to continue the research in the future are suggested.

2

Previous work and literature review

2.1 Thermal management in ICEs

As the internal combustion engines dominate the automotive market, the efforts to raise their efficiency have been continuous. The emissions legislation for the automotive industry has been targeting the reduction of the air pollutants released into the atmosphere in order to protect the environment. Special attention requires the air quality in the cities, which has drastically decreased until being harmful for the urban population [13][14]. Additionally, the legislation has set new testing cycles which cover a wide range of transient conditions as well as different ambient temperatures in order to quantify the real vehicle emissions and reduce the difference claimed between the previous homologation procedures and the real driving emissions tests [15]. In order to comply with those limitations while reducing fuel consumption and maintaining the performance of the engine, the automotive industry has developed and implemented several advanced technologies inside the fields of engine thermal management (e.g., split

cooling, active thermal cooling), air management (e.g., flexible valve actuation, EGR), combustion (e.g., RCCI, low temperature combustion) and aftertreatment systems (e.g., implementing different combinations among TWC, GPF, HCT, SCR, EHC)[16][17]. Furthermore, there is also research on new fuels (e.g., hydrogen, ammonia) [18], improvements on engine subsystems as: new injection strategies (e.g., direct co-injection), improvements in turbochargers technology (e.g., variable geometry turbines, waste-gate) [19] or reducing heat losses improving the internal heat transfer (e.g., swirl, coating) [20].

Furthermore, several investigations related to increasing engine thermal efficiency focusing on the engine thermal management were performed over the last years. This system is responsible for avoiding the failure of the engine material while maintaining the coolant temperature within optimum range. Special attention should be given at their warming process. During this stage the engines work below the design temperature which produces an increase in both fuel consumption and pollutant emissions [21]. Because of this, the minimization of warm up duration is one of the main objectives of the new thermal management systems. The importance of the warming process has even increased after hybrid automotive emergence in the market; since, in this kind of vehicles, intermittent operation of the combustion engine multiplies the number of these processes. According to [22] more than 20 % of the fuel energy is rejected to the coolant and then evacuated to the ambient through the radiator in steady state conditions. Moreover, this energy is much higher (around 50 % for some engine operating points) during engine warm up since the coolant temperature is much lower and part of the energy is invested in heating the coolant [23]. Thus, better use of that energy, specially during warm up of the engine, would lead to an improvement of engine performance. It is important to identify how the engine thermal management system (ETMS) impacts on the engine fuel efficiency and emissions. The ETMS has a great influence on frictional losses, auxiliary power requirements and combustion boundary conditions such as combustion chamber temperature, charge temperature and density.

In addition, the common engine thermal management system (e.g., pumps, pipes, valves, radiator) is usually designed for the wide open throttle condition which corresponds with the maximum heat rejected to the coolant [24]. This oversized system is far from being efficient when the engine is working with part load conditions. Specially, during transient cycles starting from cold conditions.

During steady state conditions, the ETMS main focus is to maintain the temperature within optimum operative range. Consequently, reducing mechanical losses and increasing the system efficiency. However, in transient conditions, the aim is to reduce the warm up time to achieve optimum operation conditions.

Several investigations regarding different engine cooling strategies are found in literature. One that has been studied in recent years has been splitting of the cooling system. Thus, dividing the engine coolant circuit into at least two different circuits. One, cooler, running through the cylinder head aiming for an increase of volumetric efficiency and decrease in charge temperature. The other, for the engine block, runs warmer in order to decrease frictional losses and, indirectly, in cylinder peak pressure. For instance, Osman A. et al. [25] proposed a new cooling circuit in which the majority of the coolant flow rate was directed into the cylinder head. This was achieved by modifying the cylinder block, cylinder head and gasket. Experimental results showed that the coolant pressure loss was decreased along with the required coolant flow rate for maximum heat rejection conditions. This opened the possibility for reducing the thermal inertia of the system since lower coolant volume was needed to fill the circuit compared to the baseline engine.

In order to investigate the effect of split cooling in the thermal management of the engine, different tools and approaches have been used [26][27]. Kang H et al.[28] developed an integrated 1D thermal model for studying the advantages of using different coolant circuits for cylinder block and head alongside active thermal management using electric devices. Results showed that the engine efficiency increased by 3 % while the warm up time was reduced by more than 35 %. Soujanya C et al.[29] used a 1D model to evaluate the advantages of splitting the cooling by means of two thermostats which had the function of blocking the flow through the engine block till warm conditions were reached while letting the flow through the cylinder head. The coolant flows validation of the model showed less than 10 % relative error. Similarly, split cooling of the cylinder head and liner has been studied by means of a mathematical model in [30]. Results showed that the split cooling configuration can reduce warm-up time of 10 % during a NEDC (New European Driving Cycle) cycle.

Another thermal management technologies consisted in implementing heat exchangers into the engine gas circuit. Sakuma T. et al. [31] developed a novel exhaust recovery systems (EHRS) and evaluated its impact on engine fuel consumption by means of experimental vehicle testing. Ac-

cording to the results, around 2 % of fuel saving could be achieved with the EHRS during engine warm up time. Another approach for enhancing heat transfer is the nucleate boiling. Pi S et al. [32] studied the impact of nucleate boiling in the engine cooling system by means of CFD simulation. A significant heat transfer increment was observed in the cylinder head when compared with pure convection due to the increase of heat transfer coefficient between the engine material and the coolant. Nevertheless, this strategy requires a quick and precise control of the temperature due to the fact what the system is working close to the critic conditions which, surpassed, would rapidly increase the material temperature ending with catastrophic consequences.

In the same research framework, active cooling has showed interesting results in terms of fuel economy in internal combustion engines. Haghighat A.K. et al [33] developed a electronically controlled cooling system to evaluate the impact on fuel consumption and emissions. For this, they performed an experimental campaign for validating the model during transient conditions. Additionally, they obtained the optimum coolant temperature and the heat rejected by the engine for different operating points which served as an input for the novel controlled coolant model. Although simulation results showed a potential fuel consumption savings of 1.1 %, the implementation cost of electric actuated pumps in the cooling system and the corresponding electronic control need to be considered. Additionally, oil temperature plays a critical role on engine performance during warming up time. Higher operating temperature of the engine would rise the oil temperature reducing frictional losses because of the decrease of oil viscosity. A differentiation between coolant and oil temperature effect was not evaluated in the study. For instance, D. Di Battista et al. [34] focused on evaluating the fuel savings and emission reduction produced by engine oil thermal management. They modified the oil sump of a 3 L engine in order to temporary reduce the aspirated oil volume during the warm up time. When the engine reached thermal stability, the confined oil volume is liberated restoring the original volume. They also implemented an EHR system in the oil circuit aiming to further reduce the engine warming process. Results showed that the oil volume modification lead to fuel savings around 1 % during NEDC cycle. D. Di Battista and R. Cipollone [35] developed a mathematical model for studying the advantages of speeding oil warm up. For this, they evaluated three different technologies: by passing the oil cooler, heating the oil using the exhaust gases and partially reducing oil mass inside the oil circuit. Results showed

a 65-70 % of oil warm up time reduction when all three technologies were implemented. According to the conclusions of the study, a maximum gain of 2.1 % could be achieved inn terms of fuel savings. Torregrosa A. et al [21] assessed the influence of different cooling system configuration on engine fuel consumption and emissions. They implemented two valves in the cooling circuit, one in the by-pass branch and the other, in the expansion tank path. Thus, the cooling fluid was temporarily blocked during engine warm up. Different valve states were simulated with a calibrated thermohydraulic model, and the best configuration was experimentally tested. For the best cooling configuration, fuel consumption and warm up time were reduced in 1.6 % and 22.3 %, respectively. In this work, both coolant and oil systems were modeled and implemented in a integrated virtual engine model. Consequently, the engine model is capable of predicting the fuel consumption produced by any modification of its subsystems.

In the conventional configuration of the engine hydraulic circuits, the coolant and oil pumps are driven by the engine crankshaft with a constant transmission ratio. In order to optimize the system and reduce the power consumed by the pumps and fan, an advanced ETMS was proposed in which the transmission ratios of the oil and coolant pumps as well as the fun were electrically controlled [36]. Di Bartolomeo et al. [37] studied the benefits of using a controlled electric coolant pump during WLTC (Worldwide harmonized Light vehicles Test) cycles. Experimental results showed that a design optimization focused on real operating points along with an optimum control strategy would decrease the pump power consumption around 10 %. Although, the results were promising the impact on the overall engine fuel consumption was not evaluated. R. Cipollone et al. [38] implemented a sliding vane rotary pump in a validated vehicle model. The new pump was experimentally characterized for validating the model. Simulations for transient homologation cycles showed improvements between 0.2-0.5 % of the propulsive energy. G. Di Giovine et al. [39] performed a similar study in which they evaluated the impact on engine performance when the conventional centrifugal pump was changed by a triple-screw pump. An improvement was observed using this volumetric pump during the simulation of a homologation cycle since the positive displacement pump energy consumption was 18.5 % lower.

Modeling tools have been essential for assessing the performance of different advanced ETMS configurations due to the cost and time to marked reduction. 1D models have been useful to simulate complex and large systems with a acceptable calculation time. A ETMS is composed by

different types of elements which shall be modeled taking into account the trade-off between precision and calculation time [40]. Kumar A. et al. [41] studied different cooling circuits by means of 1D virtual modelling using FlowMASTER tool. They validated the base engine by means of experimental measurements in cold conditions (-23 °C) and then performed several simulations with modified coolant circuits. For this, they implemented a simplified (based on three nodes) lumped thermal model in order to calculate the heat rejected to the coolant circuit and oil circuits. Additionally, with the experimental data, they obtained look up tables for heat rejected by the combustion process and the friction which feed the thermal model. Results showed a warm up time reduction of 19.8 % for the engine cooling circuit implementing a regulating valve located downstream the engine.

The improvement of the engine cooling system is one of the solutions considered to face the increasingly strong requirements to the engines [42]. New cooling systems, more efficient and smaller, could get reductions in both fuel consumption and pollutant emissions. Possible improvements include the use of more complex systems of thermal management [43], which are able to adapt the refrigeration to the engine operating conditions and focus its efforts on critical areas of the engine, not wasting energy on those not as critical.

One of the studied options to reduce the warming duration is by using innovative refrigerant fluids, with better thermal properties. Choi [44] in 1995 at the Argonne National Laboratory (ANL) started the study of one of the most promising new kind of refrigerant which were coined nanofluids. The nanofluids consist in conventional refrigerants such as water, oil or mixtures of water and glycols where tiny solid particles (particles with a size smaller than 100 nm) are dispersed [45]. This addition is an attempt to improve fluid thermal properties by taking advantage of the generally higher thermal conductivity of the solids.

Most studies performed about nanofluids have pointed out a noticeable increase of their thermal conductivity compared to conventional fluids [46]. This feature results in higher heat transfer coefficients [47] enabling the use of less coolant flows [48]. On the contrary, wall shear stress values for nanofluids is greater than that of the base liquid [49]. Additionally, nanofluids have a smaller specific heat due to the lower nanoparticles material specific heat; which together with the use of less coolant flows would, in principle, shorten engine heating times. Nevertheless, they will also reduce the engine cooling time which is negative in hybrid powertrains

because of the intermittent operating conditions. Furthermore it could be mentioned other potential benefits of use nanofluids as, for instance, reducing the size and weight of the cooling system. That, in turn, would bring reductions in fuel consumption and free up space to address new more aerodynamic designs.

The study of the use of nanofluids on internal combustion engines is very limited: a numerical study on the effect of nanofluids on the warm-up time of an engine has been studied in [50] where a reduction of this time is observed. Kulkarni et al. [51] used nanofluids in a cogeneration system and the results showed an increase on heat exchanger efficient due to higher heat transfer coefficient but a decrease on the cogeneration efficient due to the lower heat capacity of the mixture with nanofluids.

Simultaneously, several research literature has been published regarding the improvement of engine efficiency and emissions production through thermal insulation. Broatch et al. evaluated the impact of different insulation coatings in the cylinder walls [52]. H. Kosaka et al. investigated the effects of insulating the combustion chamber walls with materials characterized by low thermal conductivity and volumetric heat capacity in order to increase engine efficiency by reducing temperature difference between the combustion wall chamber and the gas [16]. All these researches were focused on reducing heat losses during the combustion process inside the combustion chamber and were evaluated by means of computational fluid dynamic software (CFD). Moreover, work related to implement thermal barriers on the engine exhaust manifold can be found. M. Ekström et al. studied different coatings in order to improve the life and fatigue of the exhaust pipe materials and results showed that temperature could be reduced 50 ºC with 0.2 mm of coating [53]. Following the same line of work, J. Luján et al. realized a numerical study of the potential of thermal insulation of the engine exhaust ports and the turbocharger in steady state operating conditions. Results showed a positive impact, reducing basic fuel consumption and increasing the exhaust inlet turbine temperature [54]. Additionally, in order to reduce the heat rejected to the coolant and increase engine efficiency while reducing emissions, the insulation of engine exhaust ports and manifold was investigated through experimental measurements and numerical tools in different conditions [55]. Results showed that fuel consumption could be decreased up to 0.6 %. Furthermore, turbine outlet gas enthalpy increased by 12 % while pollutant emissions diminished by 30 %.

The aftertreatment devices require to be at a minimum temperature

range for optimal behavior. For instance, the colder the surrounding conditions the higher time is needed for catalytic converter to light off (temperature at which conversion reaches 50%) increasing the production of pollutant emissions (i.e. NOx) during that period. Thus, reducing the heat losses between the engine outlet and turbine intake seems to have a great potential for reducing emissions during the heating of the aftertreatment devices in transient conditions, especially in cold starts [56]. J.R. Serrano et al. studied combined active (valve timing) and passive strategies (different valve diameters and manifold designs) by means of a 0D/1D engine model aiming to evaluate the impact on exhaust temperature and basic fuel consumption [57].

Although several studies have been published about the improvement of the different subsystems of the ETMS, an absence of literature is observed when it comes to the study of the thermal management system from a holistic approach [6].

2.2 Thermal management in battery systems

The battery is responsible for storing energy in electrified vehicles. This energy is hoarded in chemical form. The basic components of the batteries are the positive and negative electrodes, electrolyte, separator, current collector and a case. Although different battery technologies are available, Li-ion batteries have better characteristics for their use in xEV compared to their competitors. These characteristics are: high specific energy and power, long cycling life, and low self-discharge rates [58]. Figure 2.1 shows a Ragone plot representing the comparison among different battery technologies in terms of energy and power density. It can be seen that Lead acid battery suffers from low specific energy which normally ranges between 20 - 40 Wh/kg. Nickel Metal Hydride battery (Ni-MH) has recently been used in HEVs for having higher specific energy, calendar cycle and life compared to the Lead acid. However, their cost per kWh is higher. Furthermore, Figure 2.1 also shows that Lithium-ion batteries (Li-Ion) present the highest energy density. Additionally, they also have high efficiency and life span. All these features explain their extended use by the automotive industry. However, there are some drawbacks to take into consideration. They are expensive, present safety issues (i.e. thermal runaway) and their production raw materials are limited [59]. A great effort has been invested into implementing new materials (i.e. for the cathodes) to improve the Li-Ion cell battery characteristics. Table 2.1 shows the

principal advantages and disadvantages of Li-Ion technologies.

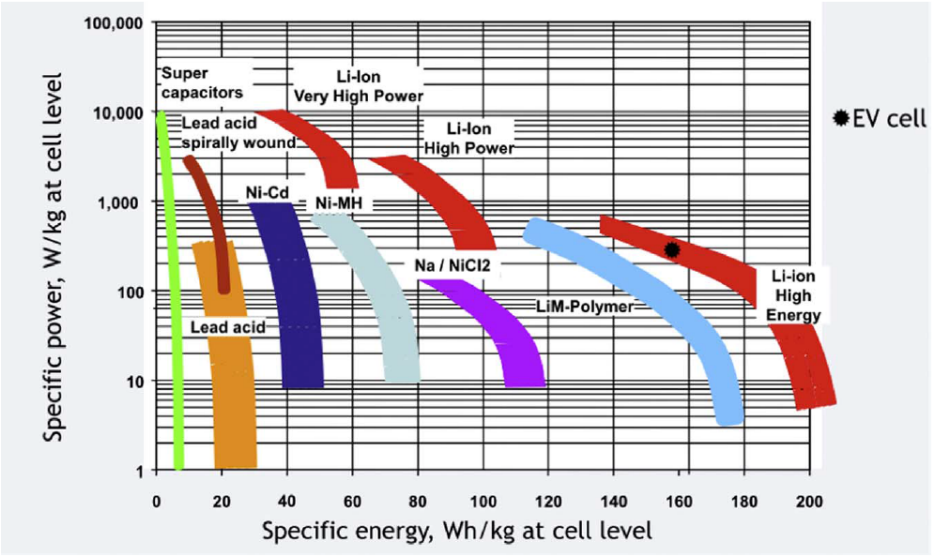

Figure 2.1: Specific energy and power of the main battery technologies. [59].

Battery cell geometry is a very important feature since it will directly impact on the packaging of the battery pack of the vehicle. Given the space limitation in the vehicle, a optimum distribution of the cells is critical to maximize the use of the space available. There are three basic geometric types of battery cells used in electrified vehicles: cylindrical, prismatic and pouch. Cylindrical cells are cheaper and the most mature ones and relatively easy to manufacture (e.g. Tesla, BMW mini). However, they have limitations in terms of power and normally support lower C-rates (unit to measure the speed at which a battery is fully charged or discharged) given their difficulty to evacuate heat. Prismatic cells are normally larger delivering more energy and power since their shape allows a better heat dissipation. Finally, pouch cells can deliver more power and they are efficient when it comes to space usage. However, battery packs made of pouch cells require an additional structure since the pouch cell casing has low mechanical resistance. For instance, Erb et al. examined the effect of cell geometry size on thermal management for air cooled packs by means of numerical simulation. Results showed that prismatic cells required less air flow rate, while cylindrical cell minimized pressure drop [60]. Figure

Table 2.1: Comparison of different Lithium-ion battery technologies [59].

Technology	Advantages	Disadvantages
Lithium Cobalt Oxide (LiCoO2)	Power and energy density	Safety, cost
Nickel Cobalt and Aluminium (NCA)	Power and energy density, calendar and cycle life	Safety
Nickel Manganese Cobalt (NMC)	Power and energy density, Cycle and calendar life	Safety
Lithium Polymer (LiMnO4)	Power density	Calendar life
Lithium ion phosphate (LiFePO4)	Safety	Energy density, calendar life

2.2 shows the main cell geometries used in xEV. In xEV the cells are connected together in different configurations and packaged with control and safety circuitry to form a battery module. Similarly, modules are then combined and connected to additional control circuitry, a battery thermal management system (BTMS), power electronics to form a battery pack [61]. The electrical connection between cells and modules is performed in series and parallel according to capacity and power requirements. On one hand, connecting individual cells in series increases voltage (power) of the array while the total amperage remains the same. On the other hand, connecting individual cells in parallel increases the array intensity while maintaining the voltage [62]. Figure 2.3 shows a generic battery packaging for cylindrical and prismatic cells.

A battery pack has two main subsystems: the battery management system (BMS) and the battery thermal management system (BTMS). Both systems need to predict the temperature of the cells for control and temperature management purposes.

In regard to the battery performance and safety, the BTMS plays a critical role. In fact, the operating temperature of Li-ion battery directly impacts its total capacity, maximum power and durability. Additionally, overheated cells of the battery pack could led to a thermal runaway and failure [63]. On the contrary, operating the cells at cold temperatures (i.e., sub-zero) will drop battery efficiency and critically limiting the discharge capacity. Consequently, the xEV range would be directly reduced [61]. According to literature, optimum temperature range of the battery is approximately between 15°C and 35°C depending on cell chemistry and type. Furthermore, the internal temperature gradient within cells is also important to be minimized for improving performance [64]. Table 2.2

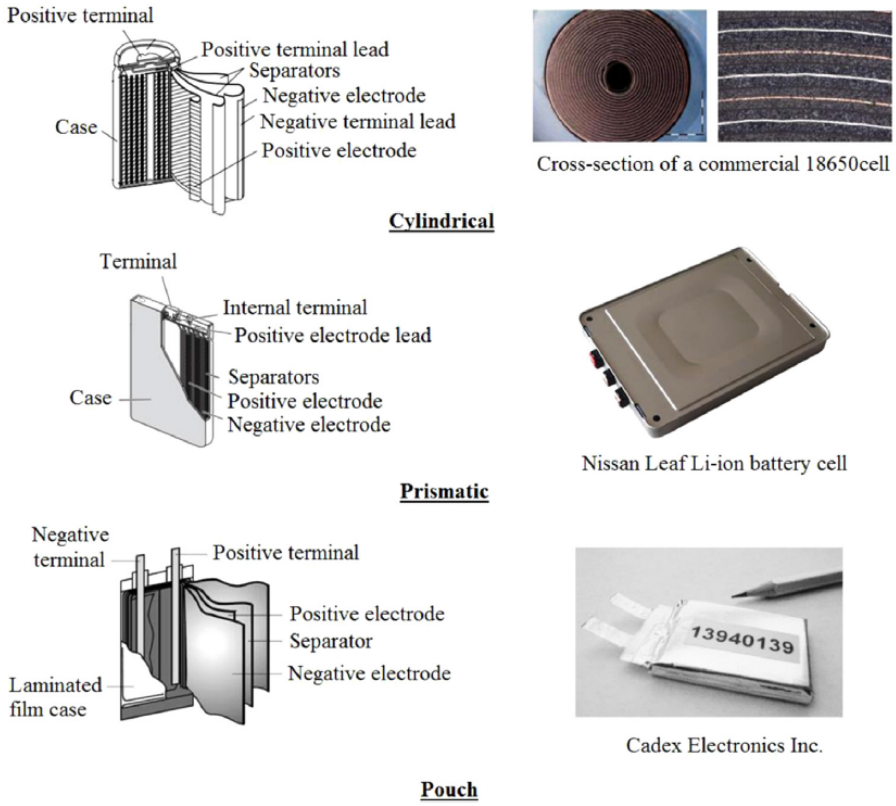

Figure 2.2: Battery cell geometries [61].

summarizes the main causes and effects on the battery cell according to their temperature [65].

In real time operation of the vehicle, both battery systems need to predict the temperature of the cells for control and thermal management purposes. During the designing phase or optimization of the system, it is fundamental to predict the heat rejected by the cells of the battery and calculate their temperature for designing the proper TMS. Along with experimentation, the modelling approach has been extensively applied in the last years to thermally study the batteries at different physical levels. Heat generation inside the battery is a complex process which required electrochemical reaction knowledge which are affected by time, temperature, space and current distribution. Normally, battery thermal models

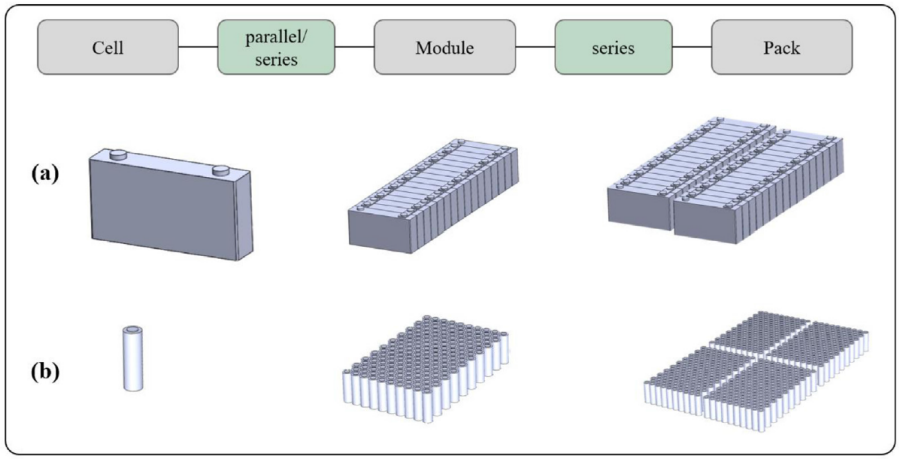

Figure 2.3: Overview of battery packs indicating two constructions with (a) cylindrical and (b) prismatic cells [62].

consist of different sub-models; electrochemical, mechanical, thermal or electrical. Depending on the simulation requirements, these models could work independently or coupled. Depending on the level of detail and precision required, models could be 0D/1D to 3D models which require much more computational effort.

The electrochemical and equivalent electric circuit (EEC) models are the most common methods for calculating the cell heat generation. The former (electrochemical) is physically based and normally one-dimensional which consists on a set of equations (see Figure 2.4) describing kinetics, transport phenomena and energy dissipation of a cell. Doyle validated and demonstrated the applicability of such model to almost any of the existing Lithium-Ion systems [66]. He et al. developed an electrochemical model of Li-Ion and implemented a novel solver for reducing computational effort while maintaining accuracy [67]. Physically the model describes two composite electrodes and a separator, along with 1D transport of lithium-ions from the negative electrodes to the positive electrode though the separator. Miranda et al. coupled a thermal model with an electrochemical model to study the impact of the temperature and the active materials in Li-Ion battery cell performance [68].

The equivalent electric circuit model is much simpler compared to the electrochemical and does not consider the physical fundamentals of the

Table 2.2: Causes and effects of battery cell temperature on safety and performance [65].

Cell Temp.	**Cause**	**Lead to**	**Effect**
⇑⇑ Higher ⇑⇑	Electrolyte decomposition	Irreversible lithium loss	Capacity fade
	Continuous side reactions at low rate	Impedance Rise	Power fade
	Decrease of accessible anode surface for Li-ion intercalation		Capacity fade
	Decomposition of binder	Loss of mechanical stability	Capacity fade
25°C to 40°C	Maximum cycle life		
15°C to 24°C	Superior energy storage capacity		
⇓⇓ Lower ⇓⇓	Lithium plating	Irreversible loss of lithium	Capacity or/and power fade
	Electrolyte decomposition	Electrolyte loss	

battery. However, it requires much less computational effort and several research has demonstrated their usefulness and accuracy, specially in cases where the internal reactions of the cell are not needed and the input/output variables of the battery take preference. This kind of models use electric components such as resistors, capacitors and voltage sources to implement an electric circuit of the cell. The typical EEC model used for xEV are: Internal Resistance Model (Rint), Resistance Capacitance (RC) model, Thevenin model (1^{st} order) or PNGV (Partnership for New Generation of Vehicles) model [69][70][71]. Figure 2.5 shows the schematic representation of the different EECMs.

The heat generation in the battery cell is due to reversible and irreversible processes (ohmic losses). Different equations have been proposed to model battery heat generation [61]. Although more complex and accurate equations can be found in literature, Bernardi et al. [72] formulated the thermodynamic energy balance on a single cell, and a simplified form (Equation 2.1) was derived from it:

$$q = I(OCV - V) - I(T\frac{dOCV}{dT}) \tag{2.1}$$

where the first term on the right side of Equation 2.1 is the joule heating,

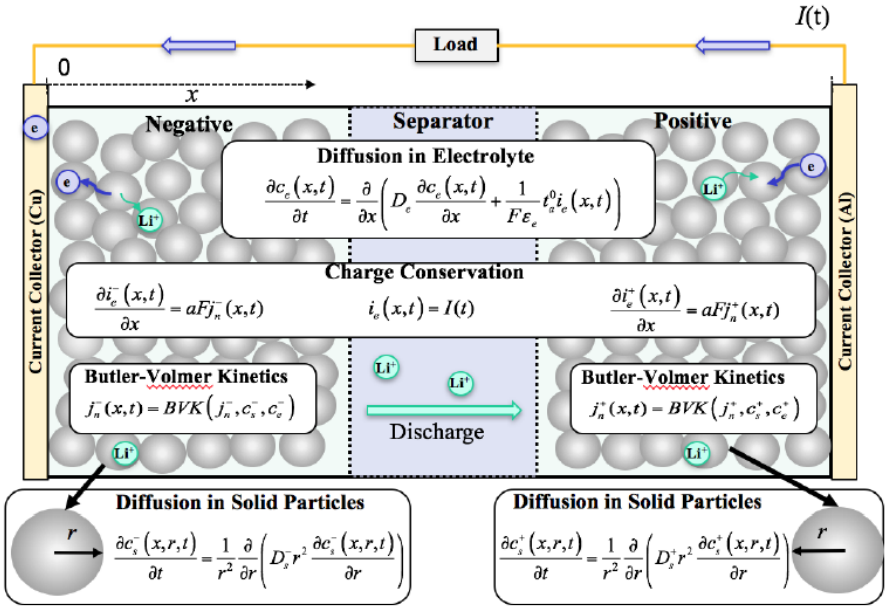

Figure 2.4: Electrochemical physics-based for Li-Ion batteries [67].

the second represent the entropy change, I the discharge current density, OCV the open circuit potential and V the cell voltage. This equation has been widely accepted in small lithium-ion batteries if assuming no heat from mixing or phase change, uniform temperature or SOC, and only one electrochemical reaction takes place.

Several investigations have been performed in order to develop efficient BTMS that maintain the cells temperature of the battery within the optimum range while decreasing the gradient temperature in the battery pack. The BTMS can be classified into different categories (see Figure 2.6) depending on type of cooling contact (direct or indirect), phase state of coolant (gas, liquid or phase change material) or its integration with the heating, ventilating and air conditioning (HVAC) system. Additionally, there are novel BTMS based on the use of heat pipes or thermoelectric technology [73]. Another emerging technologies are spray cooling, immersion cooling, and flow boiling cooling [74][75][76].

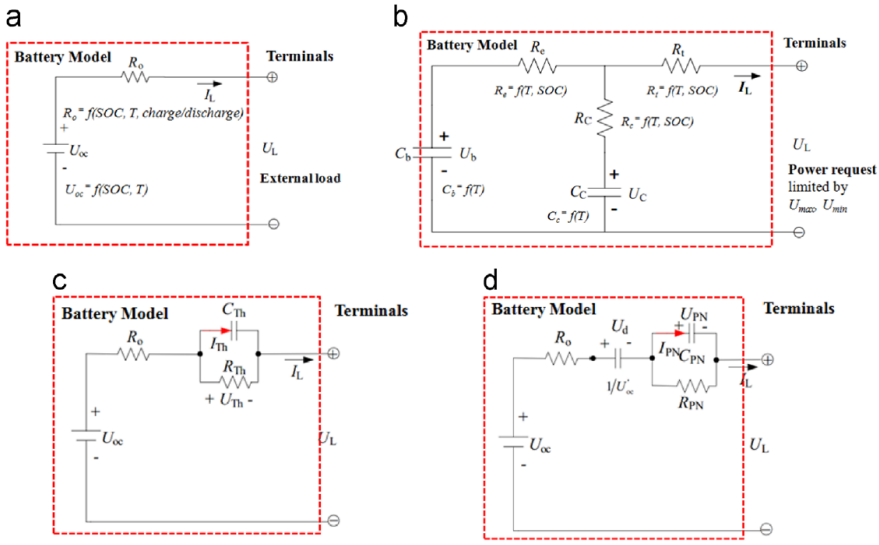

Figure 2.5: Equivalent electric circuit models; a) Rint model; b) RC model; c) Thevenin model and d) PNGV model [61].

2.3 Thermal management in electric drives

The electric drive system (EDS) of an HEV is responsible for the energy conversion between electrical and mechanical power and it consists in an inverter and a electric machine. Figure 2.7 shows an example of the integration disclosed by BMW. On one hand, this system works as a motor when consuming energy from the battery in order to drive the wheels. On the other hand, as a generator when charging the battery using the energy provided by the ICE or the regenerative braking. In xEVs, there is increasing tendency toward the improvement of power density and efficiency of traction machines. They are expected be high efficiency, have high rated torque, high starting torque, wide speed range, high overload capacity, high power at cruising speeds, high constant power speed range (CPSR), high specific power and power density, fast dynamic response, good flux weakening capability at high speeds, high reliability and good fault tolerance characteristics [77].

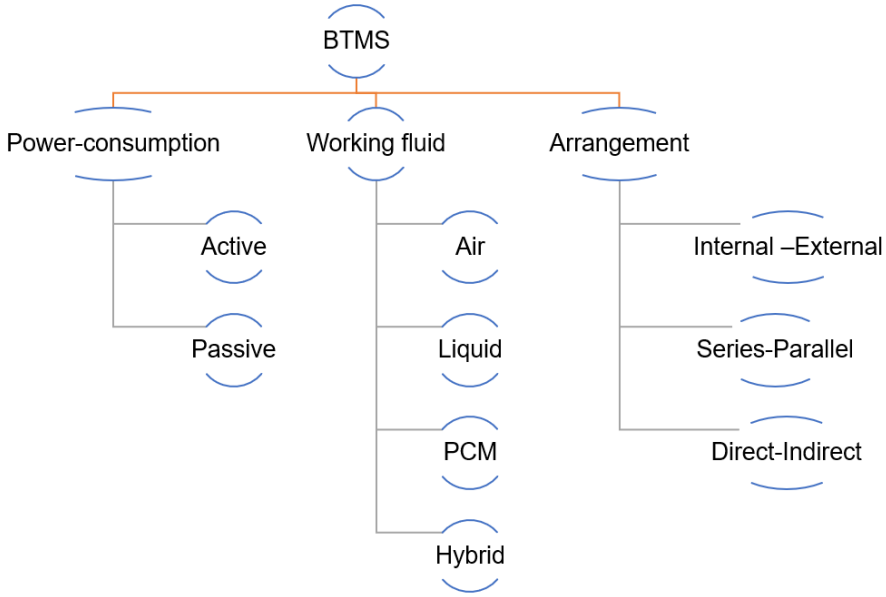

Figure 2.6: Battery thermal management classification.

2.3.1 Electric machine

Depending on power requirements of the vehicle and the design of the propulsive system, some xEVs use more than one electric machine (i.e. in the front and rear axle or one per wheel for high performance vehicles). Although there are other types, the most used electric machines are: DC machines, induction machines (IM), permanent magnet synchronous machines (PMSM), switched reluctance machines and synchronous reluctance machines. Each group have its own advantages and drawback for their application in the electrified powertrain. For instance, the Tesla Model 3 (2017) used a PMSM while the Tesla S60 is driven by an IM. Figure 2.8 shows some examples of rotor and stator components for IM and PMSM.

The energy consumed by the electric machine is divided into brake power and power losses which are divided mainly into winding Joule losses, iron losses and mechanical losses. This produces an increment in the temperature of the machine components and, if the material limits are reached, lead to the machine's failure. In the case of PMSM, the magnet performance is affected by its temperature. Hence, the machine magnetic field, magnetic flux density in the air gap and core are influenced. Consequently, iron losses and permanent magnet eddy current losses would vary. Fur-

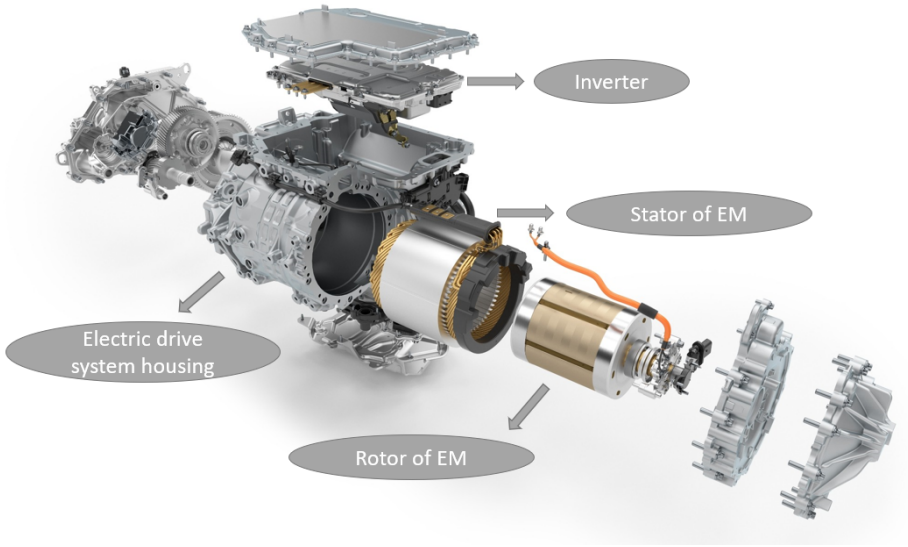

Figure 2.7: EDS components (BMW).

thermore, the properties of the materials are also temperature dependent (i.e. thermal conductivity of the copper, magnet properties). Normally, the highest temperatures in these machines are observed in the windings due to the joule effect and the low conductivity of the winding insulating material. The temperature in the winding is normally measured in the middle and the ends (in the axial direction). The coolest temperature is find in the housing of the machine. Increasing the demanded power directly and non-linearly increases the stator and rotor losses of the machine and a more heat needs to be evacuated. Thus, efficient TMS in the electric drives are essential for minimizing the temperature of their hotspots. The TMS for the EDS cooling depends on the structural scheme of the electric machine and the performance of the cooling jacket. Several cooling techniques have been studied and implemented in the electric drive thermal management system (EDTMS). Liquid cooling using water and glicol through the jacket, oil spraying for cooling the magnets, forced air cooling, direct water cooling, alternative cooling fluids, immersion cooling, heat pipes, phase change materials, vapour compression refrigeration, thermoelectric cooling and Stirling cycle cooling [78].

Extensive research can be found in literature regarding thermal modeling of electric machines. In general, the simulation methods used can

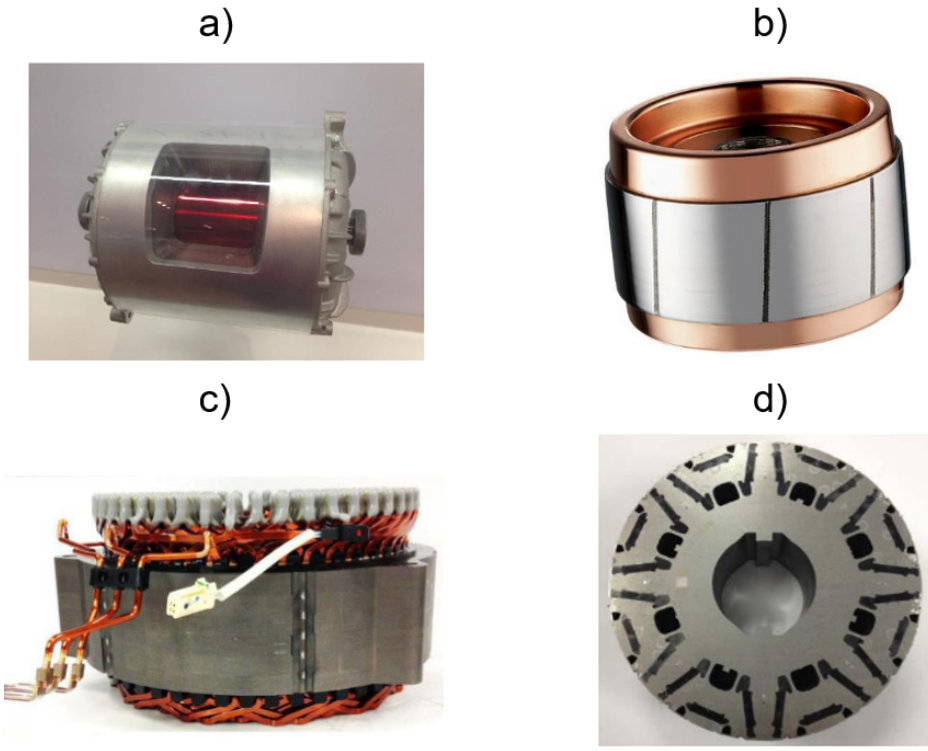

Figure 2.8: EM components. a) Tesla IM cut-out, b) die-cast copper rotor for IM, c) Stator distributed winding design in Prius 2017 and d) Rotor design of the interior permanent magnet (IPM) machine in Prius 2017 [77].

be divided into: lumped thermal model (LTM), finite element analysis (FEA), computational fluid dynamics (CFD) or conjugate heat transfer (CHT). The selection of the methodology taken depended on the level of detail required from the simulation, the computational resources, simulation speed, accuracy or application. Demetriades et al. developed a real-time thermal model of a air cooled PMSM using a LTM. For this, they discretized the geometry of the machine into different nodes can calibrated the thermal resistances among them [79]. Figure 2.9 shows a schematic representation of the heat flows inside the machine (left image) and the layout of the equivalent LTM of the machine. For implementing the heat losses they used look up tables of the machine losses which were function of the machine operating point. Results of the experimental validation of

the mode showed a good agreement with experimental temperatures.

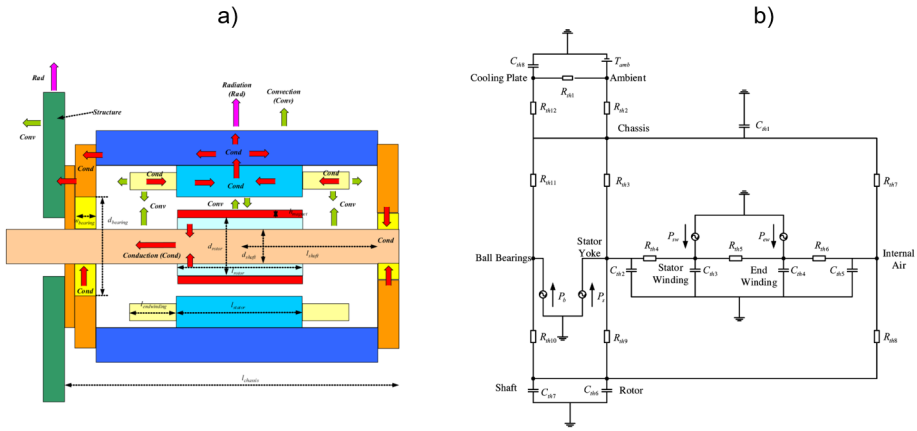

Figure 2.9: Lumped thermal model of PMSM with air cooling. a) Heat flow diagram and b) Thermal equivalent network presented by Demetriades et al. [79].

In a more recent study, LeGuyadec et al. (See Figure 2.10) constructed a LTM of an electric machine derived from a more complex model developed with FEA simulation software. As use case, they took a PMSM cooled by water/glycol through de housing cooling channels and oil splattered on the end-windings area of the stator. They considered as main heat losses, the heat generated in the windings and the stator iron while neglected the rest. Furthermore, they performed a sensitivity analysis to determine which thermal parameters influenced the temperature distribution of the machine. The heat transfer convective coefficient between the oil fluid and the end windings proved to be the most relevant when it comes to maximum temperatures. The thermal conductance between the stator and the casing showed more impact on rotor, oil tooth and slot temperatures. Results showed that the LTM fit the temperatures found by the FEA with less than 3 % of error [80].

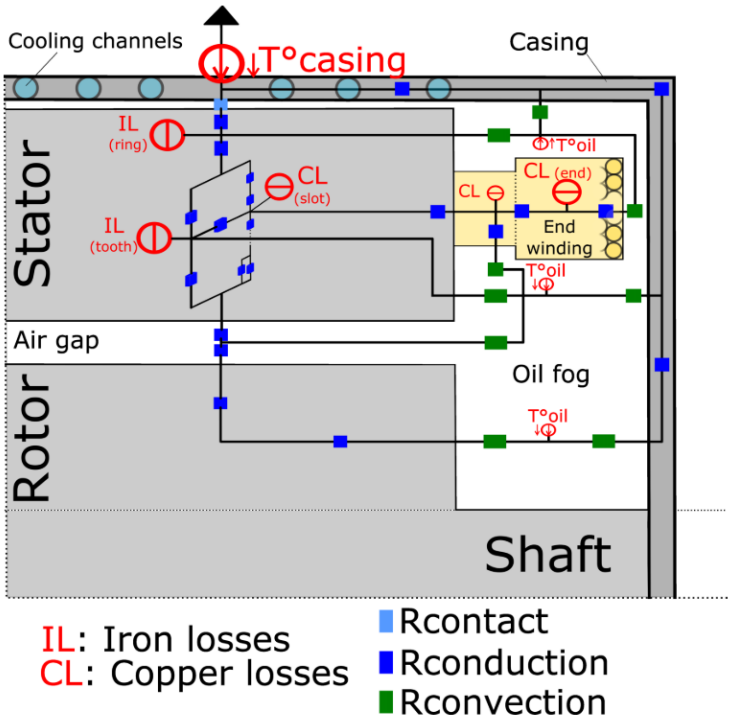

Figure 2.10: Lumped thermal model of PMSM with water/glycol and oil cooling presented by LeGuyadec et al. [80].

Fang et al. studied two novel TMS for PMSMs based on heat pipes. They analysed the impact of different ambient temperatures for different operating conditions. For this, they used experimental measurements and numerical simulation. Results demonstrated that the peak temperature of the PMSM under rated conditions can be significantly reduced by 22.3%, which helps increasing the power density of PMSMs [81]. Grachev et al. used FEA simulations to study the heat transfer in IMs used for HEV. Results have shown that increasing the air gap between overhang parts and stator reduced temperature gradients of the machine [82]. Rehman et al. performed a 3D numerical thermal analysis of an IM with different configurations of the cooling jacket and cooling flows [83].

For correctly developing the TMS of an electric machine, it is very important to correctly compute the heat losses. So, different approaches were followed in literature. Normally, the more accuracy required the more complex are the equations necessary for precisely calculating the

heat losses needed to describe mechanical, thermal and electromagnetic physics phenomena. Kong et al. carried out a thermal analysis comparing Surface Permanent Magnet (SPM) and Interior Permanent Magnet (IPM) machines by means of high fidelity (HF) analytical model and FEA simulation. Results showed that the analytical model presented great accuracy compared to both FEA and experimental measurements [84]. A typical approach when limited data is available is to use efficiency maps of the machine. However, with this approach, only the total heat loss is calculated and the heat loss distribution is not considered. Another approach is to use specialised commercial software (i.e., Motor-CAD, Flux...). Zeaiter et al. implemented an inverse heat trasfer methodology to calculate the heat losses by means of experimental temperature measurements in PMSM [85]. Other authors have used the equations proposed by Bousbaine et al. for performing the thermal analysis of the EM [86]. Another established methodology is to construct an Equivalent Electric Circuit which is normally calibrated with specific experimental tests for calibrating each parameter of the ECM [87].

2.3.2 Inverter

The inverter is a power electronics device integrated with the EM in the electric drive system of the xEVs. Depending on the vehicle architecture different electric converters can be needed (DC-DC, AC-DC or DC-AC). Similarly to the EM, manufacturers have invested a great effort developing and implementing inverters with high specific and power density, high reliability and low cost. Nowadays, the propulsive systems technology continues to push performance and efficiency boundaries for xEV applications. The trend of the EDS is to operate at higher speeds in order to increase power density and overall efficiency. In [88] a benchmark of the different inverter technology used in the automotive industry is presented.

The inverter is responsible for converting the direct current (DC) coming from the battery into alternative current (AC) going to the EM or viceversa (i.e., converting the AC coming from the EM to DC going to the battery to charge it). The inverters are divided into power modules which at the same time consists of switching devices or chips (See Figure 2.11). These are the transistors and diodes. IGBTs and MOSFET switching devices are the most common used in traction application. Since IGBTs exhibit slower switching frequency and longer turn-off time at higher temperatures, they cause higher switching losses and are less efficient than the

MOSFETs. However, IGBTs support higher operating voltages and have relatively low on-state voltage. Silicon (Si) is the conventional semiconductor material used to manufacture the power module chips. However, new wide bandgap semiconductor materials (Silicon carbide (SiC) and Gallium nitride (GaN)) are being used to improve their performance [89].

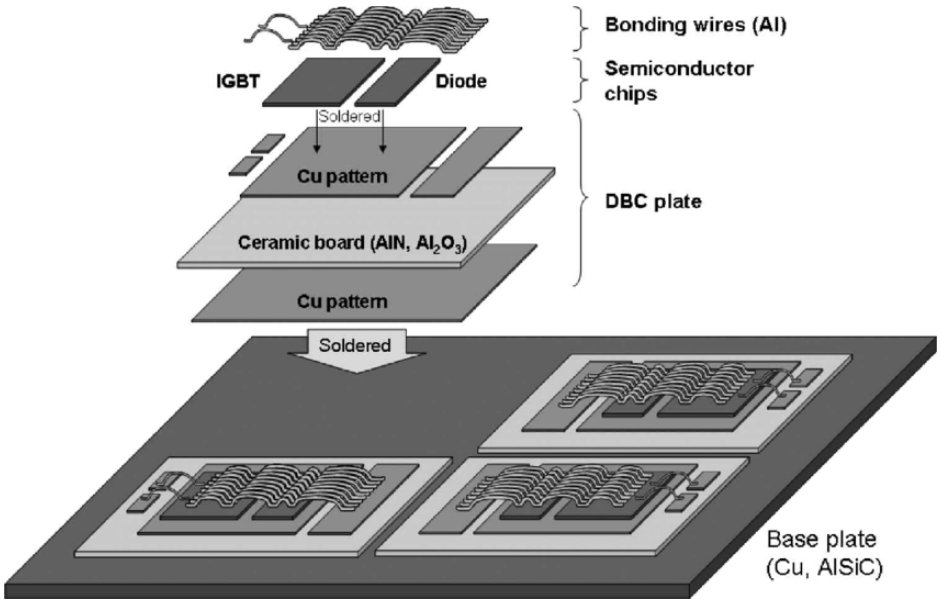

Figure 2.11: Conventional IGBT power module structure by Shen et al. [90].

Although inverts are one of the most efficient components of the HEV propulsive system, temperature also impacts their performance, efficiency, durability and safety. Their operation generates heat which is divided into conduction and switching power losses [90]. Hence, thermal management in inverters has been extensively studied and several technologies have been researched. Abramushkina et at. performed an extensive review for thermal managements in inverters used for xEVs [91].

Numerical models have been presented in literature to study the inverter thermal behaviour. For instance, the junction temperature of the inverter chips is a critical variable which limits the inverter power demand. According to literature, a typical maximum temperature ranges from 130°C to 170°C for MOSFET and IGBT, respectively [88]. Fan et al. developed an electro-thermal model for optimizing the inverter design

in high power applications [92]. Ning et al. experimentally studied three novel IGBT power modules for HEV with different methods for bonding with the cooling system [93]. Lie et al. studied different packaging technologies of IGBT power modules by means of FEA numerical simulation. Thermal, mechanical and electrical characteristics were simulated to design IGBT power module presented in the study [94].

2.4 Thermal management in HEV

Hybrid Electric Vehicles (HEV) use an internal combustion engine and, at least, one electric machine to propel the wheels. The fuel tank and the battery act as an energy reservoirs for the vehicle propulsive system. The battery converts its chemical energy into DC electrical power which is converted into AC electric power by the power electronics system (inverter/converter). This power is then used by the electric machine to produce mechanical power and move the wheels of the vehicle. In some electrified powertrain architectures, the reversibility (i.e., it works as motor and generator) is exploited. For example, the battery is charged recovering braking energy (i.e., regenerative breaking). Hybrid vehicles benefit both from the advantages of the ICE (i.e. range, energy and power density...) and the electrification (i.e. lower tailpipe emissions and noise reduction). Hence, they provide an optimum solution for the transition from the ICEV to BEV [95]. The propulsive system of the hybrid vehicle presents a high complexity and requires an advanced control of its different subsystems.

Depending on the level of hybridization, the HEV are divided into micro, mild, full and plug-in hybrids. The micro hybrids are usually equipped with a conventional ICE, start/stop system and braking energy recovery system. Similarly, the mild have an additional electric motor and higher battery power. The electric power is only used for starting or greater power delivery. The first category which can propel the vehicle only in electric mode are the full hybrids which have even higher battery power and electric machine. In this case, the battery is charged with the energy coming from the fuel. Finally, the plug-in hybrids include battery charging from the grid.

In regard to the power transmission, three different architectures are possible for HEVs. Series, parallel or series-parallel. This one is the most wide-spread powertrain among the HEV. It could deliver power to the wheels simultaneously from the ICE shaft and the electric motor shaft. On the contrary, the series architecture only uses the ICE to charge the

battery by means of a generator and the power electronics system [96]. Finally, in the parallel-series design the vehicle has the flexibility to run in both modes.

Independently of the level of hybridization or the architecture type, the thermal management (TM) is critical for maintaining the HEV subsystems temperature within optimum range avoiding their failure while increasing durability, efficiency and performance.

The TMS in the conventional internal combustion engine vehicles is composed by the cylinders block and head of the ICE, the turbocharger cooling system, the EGR heat exchanger, oil cooler, radiator, main turbopump and aerotherm. In Figure 2.12 a generic cooling circuit for a ICEV is presented. This basic cooling circuit has been in continuous development since early in the 20th century and several research have been published [8]. Studies extend from experimental designing process till the electrification of the system actuators (i.e.,pumps, valves, etc) in order to improve fuel efficiency and reduce emissions. This circuit is normally coupled to the cabin of the vehicle through the aerotherm heat exchanger and to the oil circuit by means of the oil cooler. In addition to the engine block, the exhaust gas recirculation (EGR) system also exchanges heat between the engine gas and the cooling circuit.

For the HEV case, the system is even more complex since additional subsystems are needed. Specially, for the full hybrids in which higher power demand is demanded from the electric drive and battery. Hence, a battery thermal management system (BTMS) and a electric drive thermal management systems (EDTMS) are implemented in the TMS of the HEV. Furthermore, each component of the propulsive system of the vehicle has different temperature requirements. Wang et al. designed a cooling system with high and low temperature cooling loops to separate the high temperature components from the low temperature ones [97].

Park developed a vehicle thermal management system (VTMS) for a heavy duty military vehicle. This vehicle was a HEV with series power transmission architecture. Given the weigh and high torques demanded by these vehicles a reliable TMS is critical for the correct operation of the different components of the vehicle. Furthermore, this VTMS also contributes to protect high tech on-board electric equipment, battery pack and military personal from thermal damage [98]. Numerical simulation was fundamental for predicting the components heat generation which depended on their operating conditions. The author co-simulated both the vehicle power system and its TMS. This allowed to predict the effect of

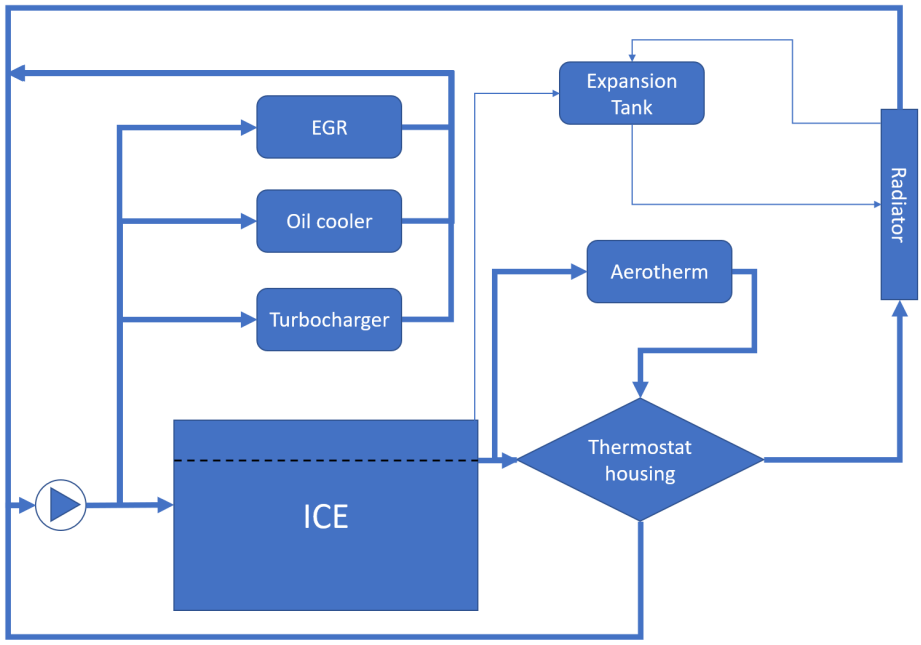

Figure 2.12: Generic cooling circuit layout for an ICEVs

the temperature on the powertrain components and increased accuracy of the simulations and contributed to improve the VTMS design. Figure 2.13 shows the layout of the integrated VTMS. It can be observed that three different loops are present; one for the engine cooling, other for the electric drive (i.e., electric machine, power electronics) and, the last for battery TMS which uses oil as coolant. Additionally, a refrigerant loop for the AC system of the cabin. The refrigeration loop and the battery cooling system are connected by the evaporator heat exchanger. This is necessary since ambient temperature could be higher than battery operating conditions, specially, for warm climate locations.

The TMS of the HEV has to be able to evacuate the heat generated by the components for the vehicle for the most demanding conditions. For the sizing of the system, a typical approach is to use the peak generation of each component to obtain a first size estimation of the system.

The use case used by Park consisted in a vehicle with a weight of 20 T, an engine maximum power of 300 kW, a generator fo 300 kW, two motors of 150 kW of maximum power each and a battery capacity of 28.5 kWh.

Figure 2.14 shows the heat rejected distribution for three driving con-

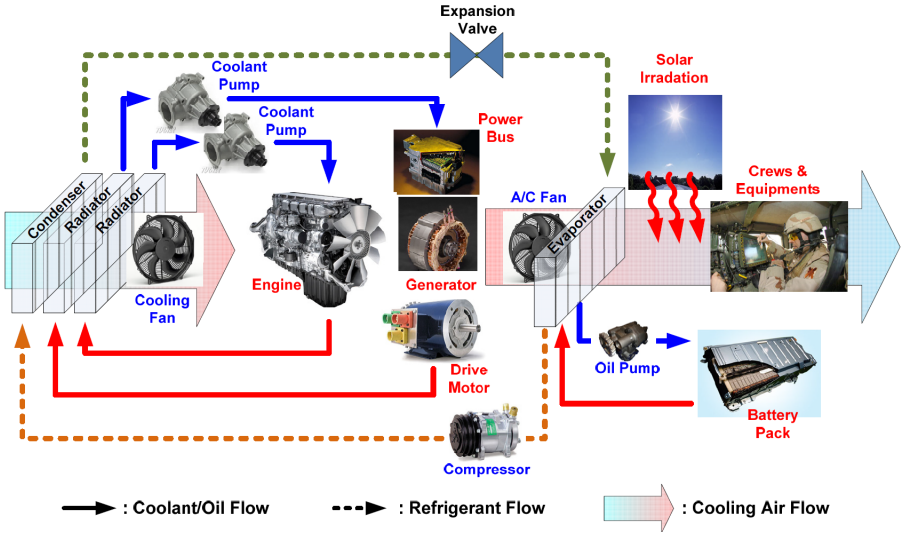

Figure 2.13: VTMS developed by Park [98]

ditions. It can be observed that, for this vehicle features, the engine is the component with more heat rejected independently of the driving cycle. In second place, the electric components and, in third, the AC system.

Okamoto et al. [99] presented a thermal management of a hybrid vehicle using a heat pump in order to increase the overall efficiency in cold weather. During these conditions, thermal energy is delivered to the engine aiming to reduce tail pipe emissions and improve efficiency. Additionally, energy is also invested in heating the cabin for passengers thermal comfort. A key technology in HEV is the engine stop capability, which allows the engine turning off when coolant temperature reaches a certain value. This value is increased in cold weather to heat up the cabin. Hence, the weather significantly affects fuel consumption for the HEV, specially in cold conditions. Increasing the efficiency of the engine would directly improve the fuel economy in cold weathers for HEV.

Normally, in conventional HEV, the engine is turned on (idling) in order to warm up the cabin as long as neither brake power nor battery charge are needed. In these conditions, the engine works in low efficiency operating points. However, implementing a heat pump increases the efficiency of the system since the engine idling time is decreased. Furthermore, the inherent heat pump efficiency is higher than using the engine waste heat or using a electric heater. Commercial vehicle such as the Nissan Leaf,

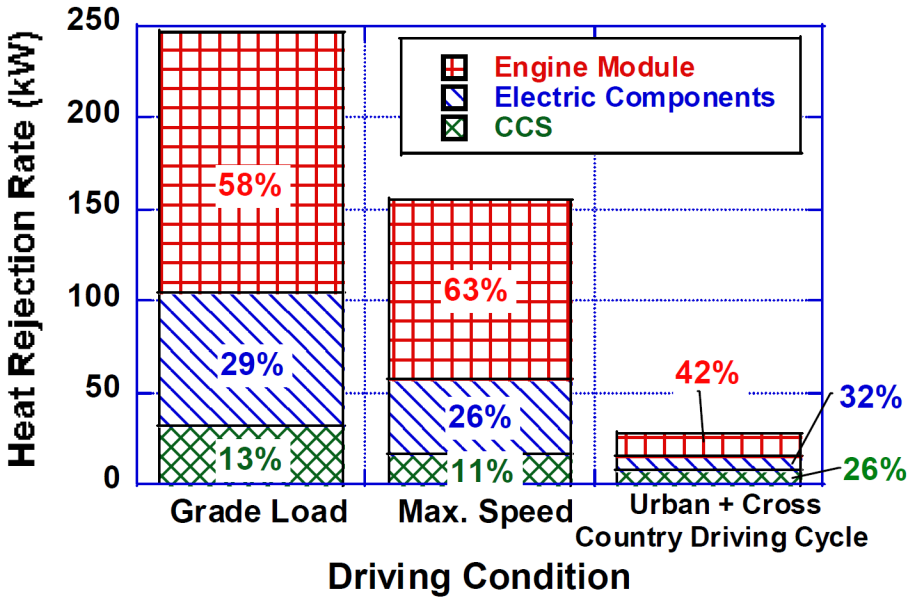

Figure 2.14: Averaged heat rejected distribution (engine module, electric components and cabin control system) by a heavy duty SHEV [98]

BMW I3 and Toyota Plug-in Prius include heat pumps. Figure 2.15 shows both a conventional cooling circuit layout and a HEV cooling circuit with a heat pump developed by Okamoto. This cooling circuit consisted in a water cooled condenser to which the heat generated by the heat pump was delivered through a refrigerant. A shut off valve was implemented between the engine and heap pump to allow independent operation when required. Authors used a 1-D thermal model implemented in a commercial software to optimize the system and develop an optimum control strategy to minimize fuel consumption vehicle while fulfilling thermal requirements and limiting engine tail pipe emissions. Results demonstrated fuel savings around 10% for a ambient temperature of 5 °C.

With the integration of mechanical and electrical components, the integration of the AC with other subsystems of the HEV became a critical issue. Several research has been published in order to improve operating performance and reduce energy consumption [100][101][102]. Bennion et al. [103] presented techniques for quantifying the integration of different systems of an electrified drive system during transient duty cycles. For this, different vehicles going from ICEV to PHEV were selected for the

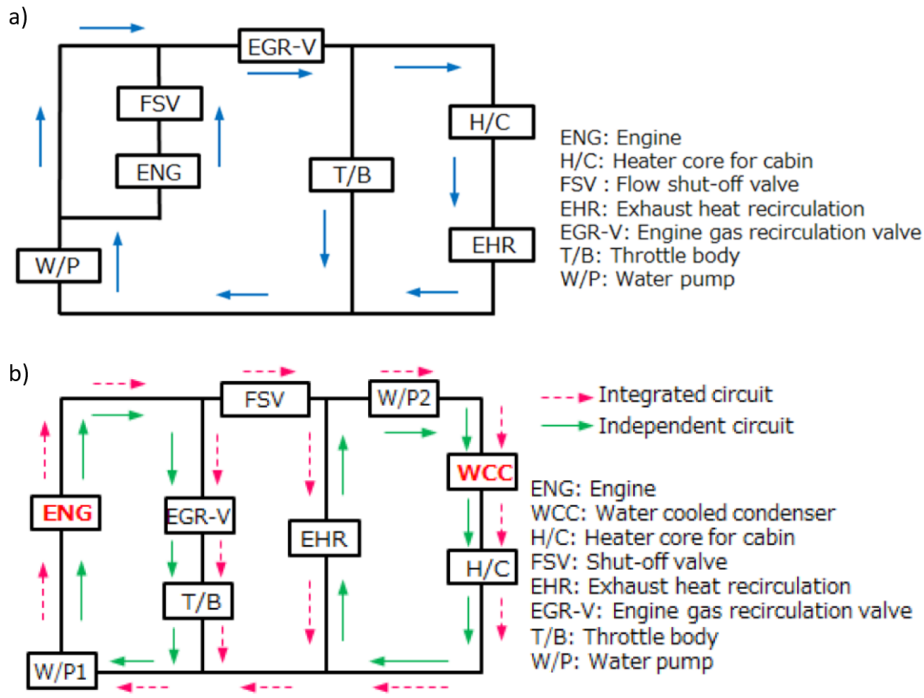

Figure 2.15: a) Layout of coolant circuit for a conventional HV. b) Layout of coolant circuit for a system with a heat pump. [99]

study. The heat load of each subsystem of the powertrain was calculated taking into account the results obtained from transient cycles simulation. On average, the heat rejected as percentage of input energy by the ICE, power electronics and electric machine were 30%, 10% and 10%, respectively. Taking as baseline the VTMS showed in Figure 2.16, the authors aimed to integrate the electric drive cooling loop into the VTMS while reducing the number of cooling loops. This would reduce production cost of the vehicle. Two possible option were evaluated by the authors. Either integrating the EDS with the ICE coolant system or with the AC one. In the first case, considering a single cooling loop, the power electronics inverter would have to tolerate inlet coolant temperatures up to 105 °C. More advantages were obtained with the second case, in which the EDS worked at lower temperatures avoiding possible thermal damage. In this approach, the integration of the AC and electric drive systems is performed by utilizing a low temperature liquid coolant as showed in

plot b) of Figure 2.16. This technology improved front end packaging, reduced refrigerant lines, and increased AC condenser package flexibility. Additionally, locating the AC condenser close to eh HVAC system would reduce pipe lengths, leading to a reduction of pressure drop.

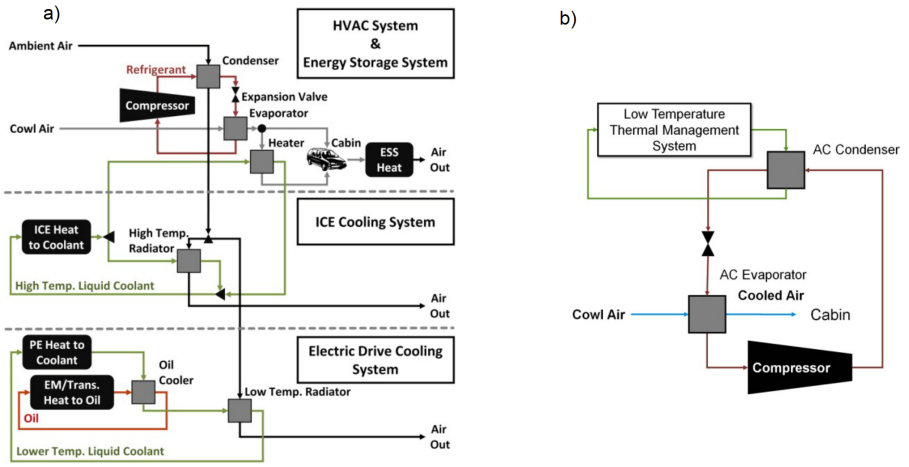

Figure 2.16: a) General schematic of the thermal management systems for HVAC, ESS (Energy Storage System), ICE, and electric drive systems (assumes the ESS is cooled with cabin air). b) General schematic of electric drive and AC integrated thermal management system [103].

Similarly, Ap et al. [104] proposed a low temperature liquid coolant loop for the air conditioning (AC) condenser, charge air cooler, and fuel cooler, and stated that supplying 60 °C coolant to the liquid-to-refrigerant condenser ensures adequate AC performance. The 60°C coolant temperature for the AC condenser is similar to the peak coolant temperatures for current production hybrid electric vehicles.

Cao et al. [105] implemented an integrated control strategy in an ITMS which consisted in a three loop cooling system. The VTMS had two different radiators, one for the electric machine and power electronics/MCU (Motor Control Unit) and other for the ICE. A heat exchanger connecting the EM and the power electronics, was implemented. Furthermore, the battery system (or ESS) was liked with the AC with the chiller heat exchanger. It can be observed in Figure 2.17 that the cooling loops of battery, EDS and ICE were independent from each other.

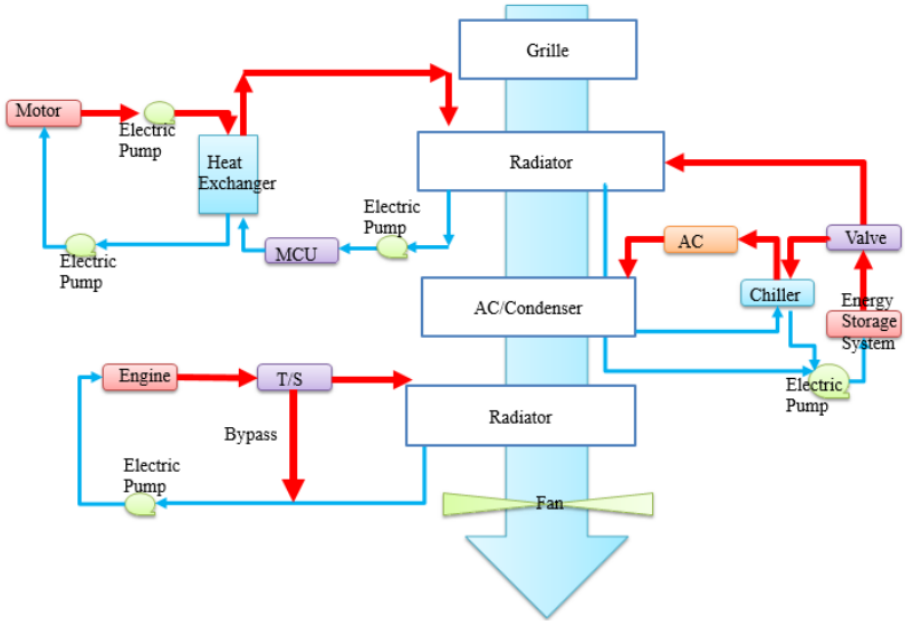

Figure 2.17: Vehicle cooling system architecture (EP: Electric Pump, MP: Mechanical Pump, T/S: Thermostat, HX: Heat Exchanger) [105].

Dong [106] proposed a design methodology of an ITMS for an PHEV. The ITMS included high, medium an low temperature circuits. A refrigerant and battery coolant circuit were also implemented as it can be seen in Figure 2.18. Additionally, a logic threshold method was used for the control strategy using component temperature as control parameter. The proposed ITMS demonstrated that could fulfill temperature requirements for each component of the vehicle.

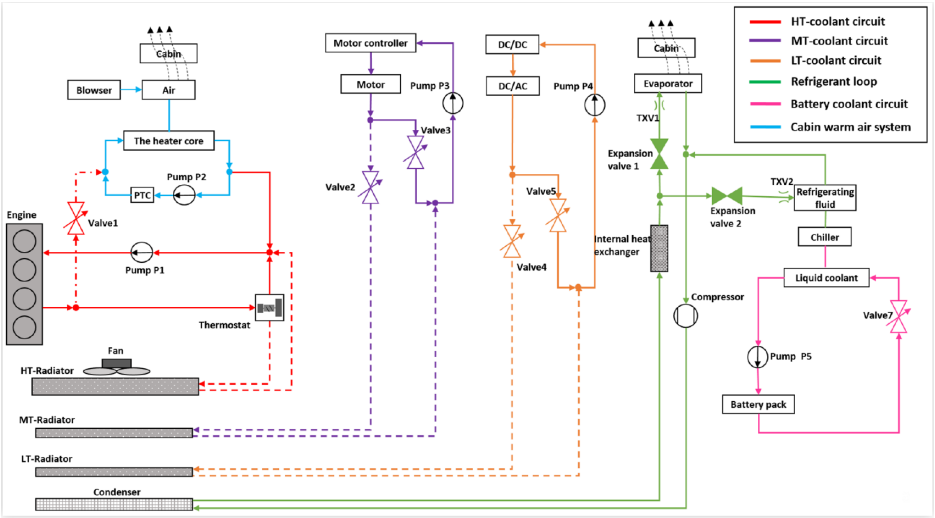

Figure 2.18: Schematic of the integrated TMS of a PHEV vehicle proposed by Dong [106].

2.5 Modeling and integration of thermal management systems

Taking into account the diversity of the integrated thermal management systems (ITMS) used by the automotive original equipment manufacturers (OEMs) in their vehicles, it is very clear that an optimum solution is still far from being achieved. Additionally, the different available architectures in xEVs along with their multitude subcomponents make very difficult to find a perfect solution for the vehicle TMS. Each component of HEVs have different thermal requirements. Normally, after the refrigerant loop of the air conditioning system, the cooling loop of the battery has the lowest temperature among the cooling circuits of the vehicle (between 20°C and 35°C). Some degrees higher, the operative temperature range of the power electronics ranges between 50°C and 70°C. Finally, for the ICE, optimum operative temperature is considered to be around 90°C [3]. Consequently, the ITMS has to be able work in different temperature levels. Thus, the automotive industry presents a diverse level on thermal integration. For the case of BEV, BMW has combined the cooling and heating of the battery with the air conditioning in their BMW i3 (2014) model. Additionally, it has another TMS for cooling the powertrain. The model Tesla S 60 (2013) holds one of the most holistic TMS of the market

coupling the cooling of the power electronics, electric machine and battery. Similarly to the BMW i3, the Nissan LEAF (2017) integrates a holistic TMS for the powertrain through active liquid cooling. For its battery, passive air cooling was selected [77].

Numerical tools have become essential for improving the design, developing and testing processes of electrified vehicles. Reducing time to market and obtaining a more optimized solution. However, in most of the cases, specific software or applications are used for modelling each component or subsystem being unable to evaluate the impact of the solution from a holistic perspective [3]. Two different approaches can be taken to avoid this issue. On one hand, benefiting from the extended libraries of some commercial software, modelling every component of the system with the same platform is a possible solution [107][108][109]. However, this option presents two main drawbacks. Firstly, modelling accuracy is forfeited given the fact that some applications were constructed from the begging aiming to the improvement of a specific subsystem or component. Additionally, several improvements have been implemented in those applications during the last years. Secondly, in larger projects (as it is the case of EVs development), different departments are involved in the process. Each one being specialised in a certain modelling software. On the other hand, a more sophisticated solution, it is to integrate a standardized co-simulation interface. This approach benefits from the accuracy of each specific tool and enables to perform a holistic system simulation. The Functional Mock-Up Interface (FMI) has became commonly used in several simulation tools [110] during the last years.

In this framework, several investigations have been carried out. P. Lu et al. [111] implemented an integrated thermal management system by means of 1D/3D coupling. They modelled the engine cooling circuit, air conditioning and the vehicle under-hood. However, the engine gas circuit was not considered and possible fuel saving were not evaluated. Casoli et al. presented the coupling of ICE, hydraulic circuits in order to develop control models using both Simulink and AMESim simulation platforms [112]. Although the study proved the integration tools potential, only steady-state conditions were evaluated for a conventional engine. R. Yuan et al. published a detailed review on the sate of the art of numerical approaches for the virtual holistic thermal and energy management of hybrid vehicles. The investigations showed that great effort had been invested in studying the thermal management of the hybrid vehicle mainly focusing on the battery [3] [113]. M. Cao et al. reported a design of

an integrated cooling system using Matlab/Simulink along with in-house tools for thermal control development [105]. Although the proposed TMS considered different temperature levels for the HEV subcomponents, the components efficiency was not evaluated. G. Lang et al. presented a study of a cooling circuit layout based on three different circuits and simulated the system for different ambient and load conditions [114]. However, the thermal integration between different cooling circuits and their impact on fuel savings was not evaluated.

Several ITMS have been studied for BEVS [115][116]. However, the integrated thermal modeling with co-simulation approach still needs further exploration and development for hybrid powertrains [117]. J. Ma developed a novel vehicle integrated thermal management system for pure electric vehicles and validated the system through simulation and experimental measurements [118]. S. Hemmati et al. [119] developed a novel model-based optimization platform for the optimal cabin heating operation of a PHEV with engine-assisted heating for cold climate and explored an integrated operation of cabin heating, engine, and aftertreatment for connected PHEVs during real-world drive cycles. However, they used a simplified control oriented ICE thermal model for the ICE and a few effort was invested in developing a model capable of capturing the ICE dynamics, thermal behaviour and fuel consumption during transient operation. M. Shams-Zahraei [120] implemented a new EMS incorporating an engine thermal management based on dynamic programming-based algorithm. Although the control strategy contributed the fuel consumption savings, the implemented TMS only considered the interaction between the thermal flows of the ICE, Cabin and Battery while EDS worked independently.

2.6 Energy Management System

In view of the current socio-political restrictions and market demands the automotive industry has invested a great amount of effort into electrified vehicles [121]. Furthermore, the worldwide electric vehicles (EV) market share is expected to grow a 26.8 % each year till 2030 while the production and selling of conventional internal combustion engine vehicles (ICEV) will be strongly reduced [122]. Although the cost of battery electric vehicles (BEV) has decreased it is still higher than its competitors (i.e. hybrid electric vehicle (HEV), ICE vehicle...). Additionally, the absence of sufficient recharging infrastructure, limited travel range or charge time are still critical drawbacks for the full electric vehicles [123].

In fact, the energy management system (EMS) of the HEV is fundamental for efficiently operating the propulsive system while complying with the required power and safety requirements [124]. To achieve this goal, several research has been published using different methodologies and requirements [125][126].

On one hand, dynamic programming (DP) and Pontryagin´s minimum principle (PMP) are numerical methods widely used in vehicle optimization [127][128]. These control strategies are non casual and require a pre-known velocity profile of the vehicle. On the other hand, model predictive control (MPC) and equivalent consumption minimization strategy (ECMS) have been implemented for online optimization [129][130]. Hwang [131] applied the ECMS to optimize the performance of fuel consumption in an advanced hybrid system. Results showed benefits around 8 % when compared to a ruled based control strategy. Zhang et al. [132] proposed a short-term optimal control based on MPC that considers powertrains transient motion significantly improving engine fuel consumption.

However, few research have been published considering the thermal state of the engine [133]. Chu et al. [134] implemented an energy management strategy considering the warming up of the engine using the DP algorithm to optimize the fuel consumption. Results showed gains up to 2 %. Lescot et al. [135] combined both a thermal management system and an energy management strategy based on ECMS by implementing the engine thermal state in the cost function. Gains on fuel consumption varied between 0.64 % and 2.8 % depending on the transient cycle.

Therefore, model-based methods allowing to predict what is the impact of a set of possible control actions, to choose the one minimizing the associated cost has shown large potential to exploit the advantages of xEVs. The method proposed in this work follows this second path because of two main reasons; better potential to optimize energy consumption than heuristic methods and provides the best possible powertrain performance in each scenario. Then, it is a very powerful tool to compare different design decisions in a fair way since the control strategy will be optimized for every particular design.

2.7 Powertrain heat transfer

Multiple heat transfer processes take place in the hybrid powertrain components. The fundamental heat transfer mechanisms are: conduction, convection and radiation. These are described by Equations 2.2 to 2.9.

Equation 2.2 represents the Fourier's law of heat conduction. It applies to heat conduction under the assumptions of unidirectionality, steady state, absence of heat generation and isotropic. Fourier's law implies that heat flux density is proportional to the temperature gradient. The constant of proportionality k is the thermal conductivity of the material, which is a measure of the ability of a material to conduct heat. Heat is conducted in the direction of decreasing temperature, and the temperature gradient becomes negative when temperature decreases with increasing x. The negative sign ensures that heat transfer in the positive x direction is a positive quantity.

Alternatively, the equation can be expressed in terms of heat flux as Equation 2.3, because $q = \frac{Q}{A}$. A is cross-sectional area normal to the direction of heat flux. The temperature distribution $q = \frac{dT}{dx}$ has to be determined for each geometry through integration of the unidirectional heat equation, Eq. 2.5.

$$\frac{dq}{dt} = \dot{q} = -k\,\nabla T = -k\,\frac{dT}{dx} \tag{2.2}$$

$$\frac{dQ}{dt} = \dot{Q} = -k\,A\,\frac{dT}{dx} \tag{2.3}$$

$$\frac{d}{dx}\left(k\,\frac{dT}{dx}\right) = 0 \tag{2.4}$$

If k is constant:

$$k\,\frac{d^2T}{dx^2} = 0 \tag{2.5}$$

Convection is heat transfer between a fluid and a solid surface. Fundamentally, that is the combination of heat conduction (energy transfer) and advection (mass transfer). Convection is modeled by Newton's law of cooling, Equation 2.6. Newton's law of cooling states that heat flux density is proportional to the temperature difference between the fluid and the surface. In convection, h is the transport property. It is called convective heat transfer coefficient. Alternatively, the equation can be formulated in terms of heat flux as Equation 2.7, taking into account surface area A.

$$\dot{q} = h\,(T_{fluid} - T_{wall}) \tag{2.6}$$

$$\dot{Q} = h\,A\,(T_{fluid} - T_{wall}) \tag{2.7}$$

The third kind of heat transfer is radiation. Radiation is determined by Equation 2.8. In the equation, ε is emissivity, σ is the Stefan-Boltzmann

constant and F is a view factor between the two bodies. Equation 2.9 shows the expression considering heat flux. Radiative heat transfer does not need a physical medium to exist.

$$\dot{q} = \varepsilon \, \sigma \, F \, (T_1^4 - T_2^4) \tag{2.8}$$

$$\dot{Q} = \varepsilon \, \sigma \, F \, A \, (T_1^4 - T_2^4) \tag{2.9}$$

Among the three mechanisms, convection is the one that concentrates more engine research. Though thermal conduction has a relevant role in engines, the most critical processes are dominated by convection. Among those convective processes, the most important one is heat transfer between in-cylinder gas and cylinder walls. Radiation has lower significance in the engine heat transfer processes. Similarly, extensive research effort has been invested in improving the convection heat transfer between the battery cells surface and the coolant fluid. Internally, both conduction and convection process are relevant given the solid (i.e., cathode, anode) and liquid (i.e., electrolyte) parts of the cells. Radiation is normally neglected if the temperatures are within normal operating ranges. However, for extreme cases, (e.g., thermal runway studies), radiation is also considered since high temperatures are achieved.

Thermal management systems in electric machines normally focuses in improving the heat transfer convection process between the solid parts (i.e., casing, windings, shaft) and the coolant (i.e., water/glycol, oil). Conduction is also considered when designing the machine and selecting the materials, specially in locations difficult to cool (i.e., magnets, active windings).

Better conduction heat transfer between the different inverter layers is critical for evacuation the heat generated in the chips and not exceeding junction temperature limits. Convection is also studied between the cold plate and the coolant.

3 Experimental test facilities

3.1 Introduction

The methodology followed during the elaboration of the present work consisted in both experimental measurements and the implementation of different modelling tools. As it was demonstrated in Chapter 2, most of the studies rely on simulation for exploring the application of different architectures, strategies, systems or designs when assessing the powertrain thermal management. Similarly, the same approach was followed in the present work. However, the results can only be considered valid once the tools used for performing the studies are validated in similar conditions. For this, either experimental testing or literature data was used. Two testbenches were used to perform the actives regarding the ICE. One additional testbench was used for battery cell characterisation. These experimental facilities had two main functions. On one hand, they served as a fundamental source for constructing, developing, calibrating and validating the numerical models. On the other hand, they were used to validate the results obtained from the numerical studies.

3.2 ICE Diesel - Testbench 1

The production engine modeled and tested in the testbench 1 was a 1.6 L Diesel engine, four stroke and four cylinders (4 valves per cylinder). Figure 3.1 shows the engine already installed in the testbench. The main features of the engine are shown in Table 3.1.

The engine gas circuit has both high pressure exhaust gas recirculation (HPEGR) and low pressure exhaust gas recirculation (LPEGR) systems along with a turbocharger with variable geometry. Both EGR consist in gas-liquid heat exchangers (interconnected with the coolant circuit). This turbocharger is not cooled by water, but all the heat coming from the turbine and mechanical losses are dissipated by the lubricating oil and the surrounding ambient. Finally, the aftertreatment system consists of a close-coupled DOC and DPF brick.

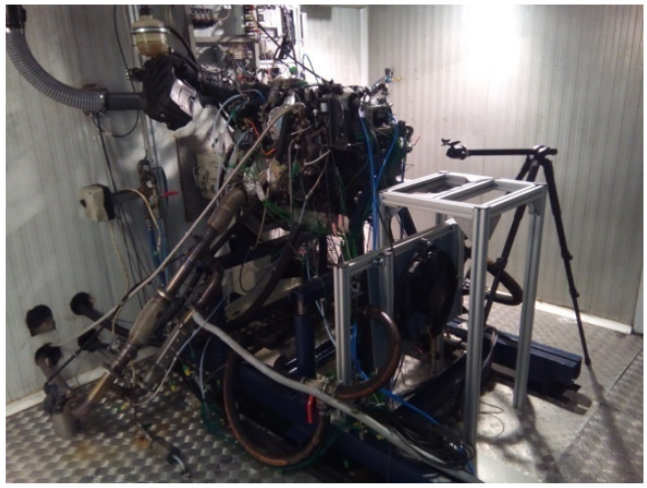

Figure 3.1: Testbench 1, Diesel ICE.

The test bed was equipped with different measurement tools that were thoroughly calibrated before the measurement campaign. Several temperature, mass flow and pressure sensors were installed in the gas circuit and the hydraulic circuits of the engine. All of them calibrated and connected to a data acquisition system.

To have detailed information of the intake and exhaust gases thermodynamic conditions, several pressure and temperature sensors were located along all gases paths. Figure 3.2 shows the temperature and pressure sen-

Table 3.1: Engine features of testbench 1

Parameter	Value
Displacement	1600 cm^3
Number of cylinders	4
Bore	80 mm
Stroke	79.5 mm
Number of cyliders	4 in line
Number of valves	4 per cylinder
Max torque @ speed	320 Nm @ 1750 rpm
Max power @ speed	96 kW @ 4000 rpm
Compression ratio	15.4 : 1

sors location as well as the engine air path.

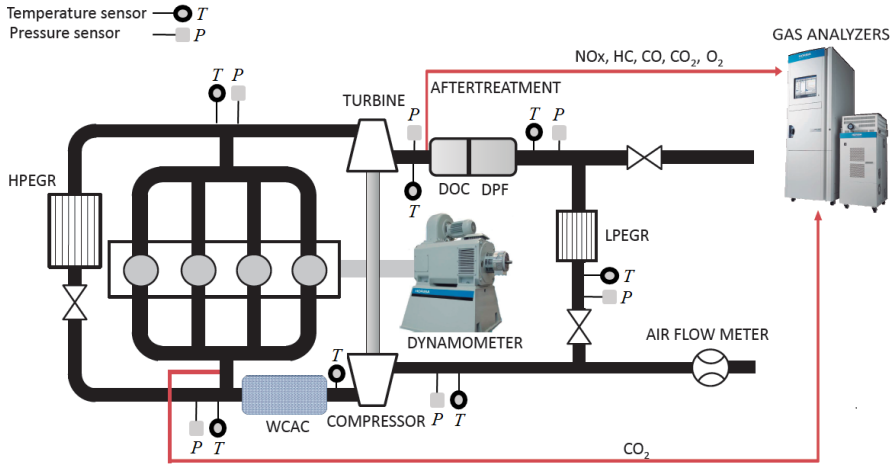

Figure 3.2: Schematic of the 1.6 L Diesel engine coolant circuit. Instrumentation location.

Additionally, the original coolant and oil circuits were adapted and instrumented to measure the mass flows and temperatures necessary to determine the heat rejection to the coolant, oil and intercooler independently. The coolant temperature sensor was installed upstream and downstream the engine while the oil temperature sensor was situated downstream the oil pump and before the oil cooler (as it can be seen in Figure 3.4). Similarly, the coolant flow downstream the radiator was also measured. Figure 3.3 shows the coolant circuit layout of the engine and the sensors location.

Starting from the coolant pump outlet, the fluid path is divided into three different paths: to the engine inlet, the LP-EGR and the HPEGR. After leaving the engine, the coolant goes into the by pass valve or/and the radiator depending on the coolant temperature (the thermostat opens and closes this path depending on the engine outlet temperature). Finally, the coolant fluid coming from the radiator, by-pass valve, oil cooler and expansion bottle flows into the the coolant pump. The by-pass valve was set always opened during the experimental tests.

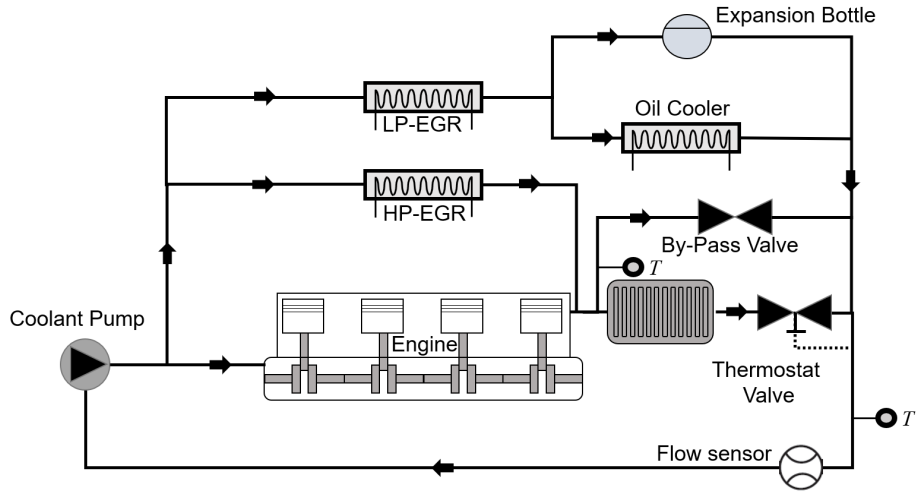

Figure 3.3: Schematic of the 1.6 L Diesel coolant circuit. Temperatures and flow sensors location.

An independent coolant circuit was implemented in the test bench for cooling the engine water charge air cooling (WCAC).

The engine speed was measured with an encoder while a dynamometer was used for measuring the engine torque. The dynamometer is regulated based on the eddy current principle and was selected for testing light-duty engines with a maximum torque of 400 Nm. The encoder consisted in a Kistler crank-angle type 2613A capable to measure engine speeds raging from 0 to 20000 rpm.

In particular, temperatures of gases were measured with K-type thermocouples (with a 0.75 % accuracy) while the ducts pressure is measured with PME P40 transmitters. Temperatures of liquids were measured with PT100 resistance temperature detectors (with a linear uncertainty 0.3 %).

The fuel measurement systems consisted in a AVL 7333S fuel balance.

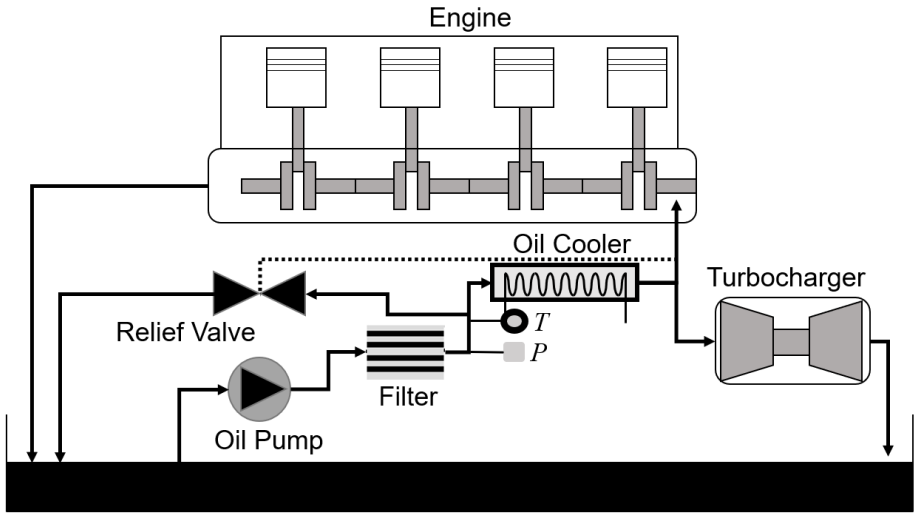

Figure 3.4: Schematic of the 1.6 L Diesel oil circuit. Temperatures and pressure sensors location.

The functioning of this device is based on the gravimetric measurement principle (i.e., the fuel consumed is calculated directly by measuring the rate at which the fuel measuring vessel weigh decreases). This device could measure from 0 to 150 kg/h with an uncertainity of 0.12 % within fuel temperatures of -10°C and 70°C. For measuring the air mass flow, a Sensy flow meter FMT700-P was installed. This could measure maximum flows up to 900 kg/h with 0.8 % accuracy.

Table 3.2 summarizes the main instrumentation equipment.

The engine control was performed by using a commercial controller system (STARS). This communicates the dynamometer with the engine pedal and actuator. A PID controller in closed loop was implemented for controlling the dynamometer speed and torque. Using the data of the vehicle (gear ratio), the vehicle's speed is converter to target engine speed. Furthermore, the engine torque is set by means of the electrical dynamometer load that takes into account transmission losses, road friction, dynamic drag and vehicle mass. The pedal position actuator is modified to reach target speed as a response to torque variations.

Additionally, the engine control unit (ECU) provided data regarding different instantaneous signals from the engine (e.g., in-cylinder pressure,

Table 3.2: Laboratory instrumentation of testbench 1

Variable	Instrument	Range	Accuracy
Crank angle	Encoder	0-360°	±0.02°
Torque	Dynamometer	0-400 Nm	±0.5 Nm
Fuel mass flow	AVL 733S fuel balance	0-150 kg/h	±0.12 %
Gas/wall temperature	k-type thermocouple	70-1520 K	±0.75 %
Air mass flow	ABB flow meter FMT700-P	0-1700 kg/h	±0.8 %
Duct pressure	PMA Transmitter P40	0-400 bar	Linearity 0.3%
Coolant flow	Khrohne 400 Optiflux	4.5-90 L/min	±0.5 %
Oil pressure	Piezoresistive transducer	0-10 bar	±25 mbar
Coolant/Oil temperature	Thermal Resistance PT100	-200 °C - 800 °C	±0.1 °C
Emissions	Horiba MEXA @ AVL Opacimeter		

intake and exhaust pressures, rail pressure and the current clamp signal corresponding to the injection command) as well as real-time control of different combustion parameters such as combustion phasing or duration. Also served to control the engine settings by modifying the required parameters such as the EGR valve position, VGT position, injection quantity and timing.

The test cell allowed testing in different environmental conditions. Going from ambient conditions to -15 °C in the test cell. Temperature sensitive devices (i.e., gas analysers, fuel measurements system) where located outside the test cell.

This testbench allowed the engine operation in both steady state and transient conditions. The measurements were also repeated in order to study their repeatability given the present uncertainties (sensors error, engine performance and boundary test conditions variability).

The engine operation was carried out by the calibration included in the ECU. In stationary tests, the engine was warmed up till the engine coolant temperature stabilized (thermostat opened) and the variation was less than half a degree C per minute.

The complete engine model has been calibrated and validated in steady state and transient operating conditions. In first place, the stationary measurements served to set up the testbench and calibrate the initial models. Secondly, the dynamic simulations served to performed the last fitting of the model for transient validations at different environmental conditions.

The testing campaign consisted in 26 steady state points varying from low to high engine speed and from low to high load with the aim of covering a wide range of the engine map (as seen in Table 3.3) distributed along the engine map and three Worldwide harmonized Light vehicles Test

procedure (WLTP) transient cycles. Figure 3.5 shows the measurement points together with the engine map and the trace of operating points of the WLTC cycle. Among the steady state tests, three of them were in cold conditions and the rest at ambient conditions.

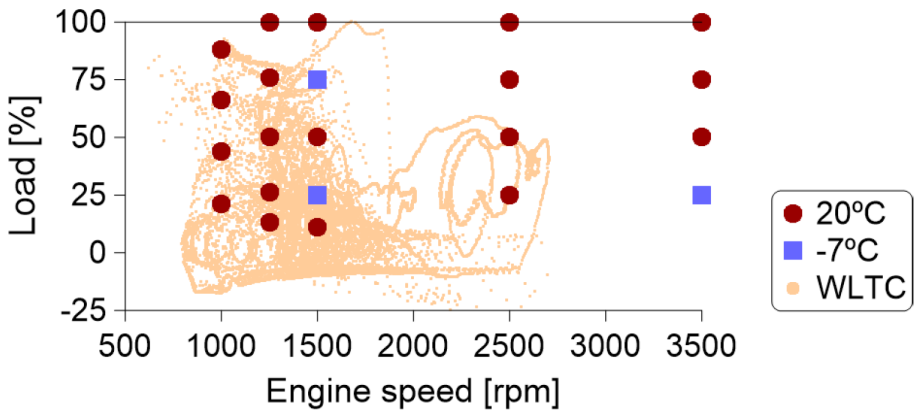

Figure 3.5: Steady state operating points for validation and WLTC cycle.

For the case of WLTP transient cycles, they were tested in ambient (setting the temperature of test cell to 20 °C during the cycle), cold (setting the temperature of test cell at -7 °C during all the cycle) and warm (starting the cycle with the engine already warmed up and setting the test cell temperature to 20 °C during all the cycle) as it is shows in Table 3.4.

Table 3.3: Steady state testing campaign in testbench 1

Steady state	
Speed (rpm)	**Load (%)**
850	idle
1000	21, 44, 66, 88
1250	13, 26, 50, 76, 100
1500	11, 25*, 50, 75*, 100
2500	25, 50, 75, 100
3500	25*, 50, 75, 100

* Performed in ambient, warm and cold conditions.

Table 3.4: Transient testing campaign in Testbench 1

	Transient	
Cycle	**Engine temp.**	**Test cell temp.**
WLTC warm	80°C	20°C
WLTC ambient	20°C	20°C
WLTC cold	- 7°C	- 7°C

3.3 ICE Gasoline - Testbench 2

In this section a description of the experimental campaign performed with the Gasoline ICE is presented. This engine has a displacement of 999 cm^3 with straight-3 cylinders. It also includes direct injection and wast gate turbocharger. Additionally, it implements the variable valve timing (VVT) technology. The engine produces 83 kW of power at 5250 rpm. The characteristics of this engine allow its implementation in hybrid powertrains for light-duty vehicles. Figure 3.6 shows the Gasoline engine installation in Testbench 2. The engine features are summarized in Table 3.5.

Figure 3.6: Testbench 2, Gasoline ICE.

The measurements were performed in a highly instrumented testbench. This was equipped with different measurement tools that were thoroughly calibrated before the measurement campaign. Several temperature, mass

Table 3.5: Engine specifications of testbench 2

Parameter	Value
Displacement	999 cm^3
Diameter	81.3 mm
Stroke	72.2 mm
Number of cylinders	3 in line
Number of valves	4 per cylinder
Max torque @ speed	182.3 Nm @ 2250 rpm
Max power @ speed	83.0 kW @ 5250 rpm

flow and pressure sensors were installed in the gas circuit and the hydraulic circuits of the engine. All of them calibrated and connected to a data acquisition system.

For the gas circuit, temperatures and pressures were measured at the compressor inlet and outlet, at the intake manifold, at the turbine inlet and outlet, at the exhaust manifold and at the inlet and outlet of the exhaust gas after-treatment system as it can be seen in Figure 3.7. The in-cylinder pressure was measured in one cylinder.

Similarly, for the coolant circuit, temperatures upstream and downstream of the different elements were measured (i.e., engine block, radiator, turbocharger, oil cooler...) as it is observed in Figure 3.8. Three flow sensors were installed in the main branches. Although the original circuit considered an aerotherm, this was not installed in the testbench (upper branch in parallel with the turbocharger) and basically this brand redirected the engine outlet flow to the main pump inlet. Additionally, it can be seen that the turbocharger is also cooled by this circuit. The coolant fluid consisted in a mix of water/glycol (50 %). This coolant was propelled by a mechanical turbopump with a 1.5 speed ratio (between the pump and the engine). An additional electric pump was installed in the circuit which was activated by the ECU when the turbocharger had high temperatures and the engine was turned off. Hence, protecting the turbocharger from overheating. A double effect thermostat served to maintain the radiator path closed till the engine warm up was achieved. During this period, the coolant was redirected to the main pump.

Given the limited space in the oil circuit, less sensors were installed. One temperature sensor was added before the oil pump (i.e., oil sump) and another pressure sensor after the oil cooler. The circuit was very similar to the one presented in Figure 3.4.

The testbench was equipped with state-of-art components that allowed

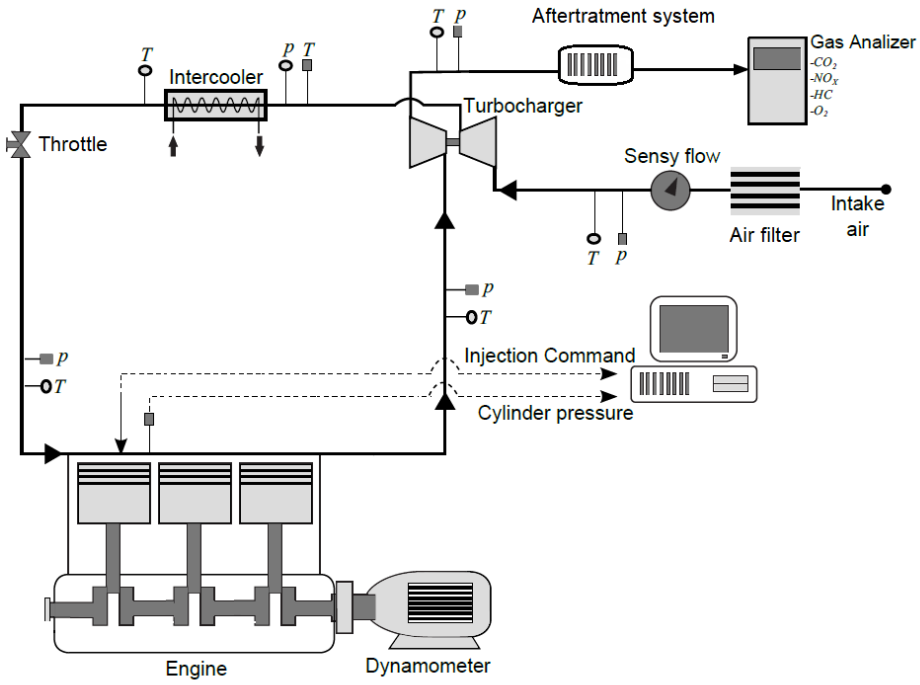

Figure 3.7: Schematic of Gasoline ICE gas circuit instrumented in Test-bench 2.

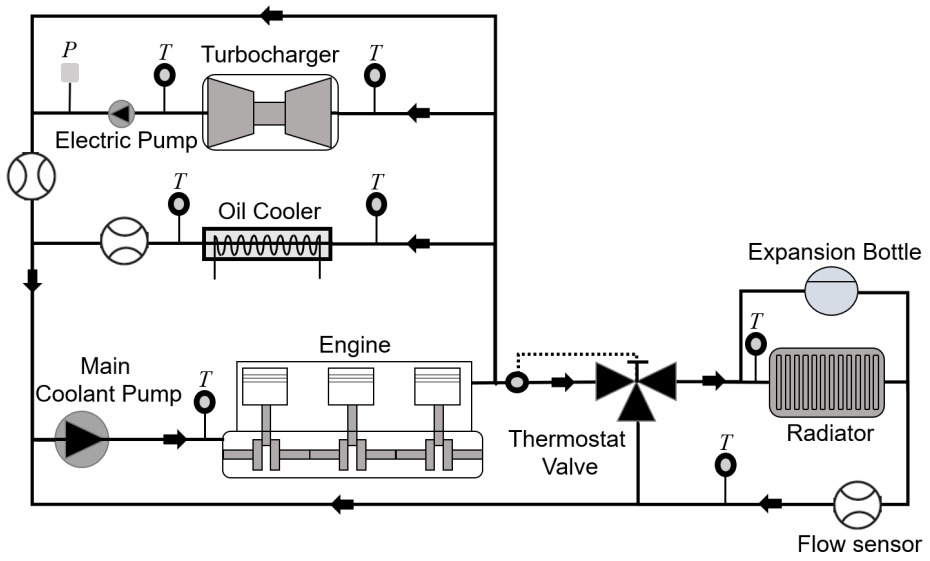

Figure 3.8: Schematic of Gasoline ICE coolant circuit instrumented in Testbench 2.

the operation of the engine in both steady state and transient conditions. The instrumentation and engine operation control of this engine was similar to the one detailed for the Diesel engine. For instance, fuel and air mass flows were measured with the same sensors.

Table 3.6 summarizes the main instrumentation equipment.

Table 3.6: Laboratory instrumentation of testbench 2

Variable	Instrument	Range	Accuracy
Engine speed	Encoder	0-7500 rpm	±1 rpm
Torque	Dynamometer	0-400 Nm	±0.5 %
Fluid temperatures	k-type thermocouple	70-1520 K	±2 K
Fuel mass flow	AVL 733S fuel balance	0-150 kg/h	±0.12 %
Air mass flow	ABB flow meter FMT700-P	0-1700 kg/h	±0.8 %
In-cylinder pressure	AVL GH13P	0-200 bar	±0.3 %
Coolant flow	OPTIFLUX 4000	4.5-90 lpm	±0.5 %
Oil pressure	Piezoresistive transducer	0-10 bar	±25 mbar
Emissions	Horiba MEXA @ AVL Smoke meter		

Additionally, the experimental campaign performed for this work considered several steady state running conditions within the engine perfor-

mance map. The tested conditions have been the following:

- Ten points ranging from 1000 rpm to 5250 rpm at full load: they were used, first to validate engine measurements and secondly to adjust hydraulic parameters.
- Ten points going from 1000 rpm to 5250 rpm in motoring conditions. They have been used to obtain the main uncertainties of the engine: compression ratio, heat transfer coefficients, thermodynamic delay and deformations coefficient. These are parameters for the combustion analysis tool (CALMEC) in which the main experimental input is the in-cylinder pressure signal. The first law of thermodynamics is applied between IVC (intake valve closing) and EVO (exhaust valve opening) to calculate the rate of heat release as the main result [136][20]. Among the results, the heat rejected to the coolant and oil is also calculated, which served to calibrate the heat rejected to the hydraulic circuits.
- Sixty-three points from low load (3 BMEP) to high load (around 22 BMEP) covering a wide range of the engine map.
- Repetition of the engine map measurements at different coolant temperatures for evaluating the impact of the engine temperature on its performance and efficiency.
- Different RDE and WLTC cycles for models validation and evaluation of new energy management strategies.

In order to validate the experimental measurements of the engine provided by the manufacturer a total of 73 operating points were evaluated in steady state conditions (including 10 full loads). Each test point corresponds to a given load/speed operating condition shown in the engine map of Figure 3.9. These are the engine torque, engine speed, air and fuel consumption, pressures and temperatures throughout the engine, flow rates, pressures and temperatures of the hydraulic circuit and gas emissions. Measurements were made during 30 consecutive seconds. In this way, both the mean values and the standard deviation of each parameter have been calculated. The last variable allows to evaluate the dispersion of the measurements. Additionally, the instantaneous pressure signals for the in-cylinder and the intake/exhaust manifolds were measured with a resolution of 0.2 crank angle degrees. 69 engine cycles were considered for each operating point. The maximum engine speed tested was 5250 rpm.

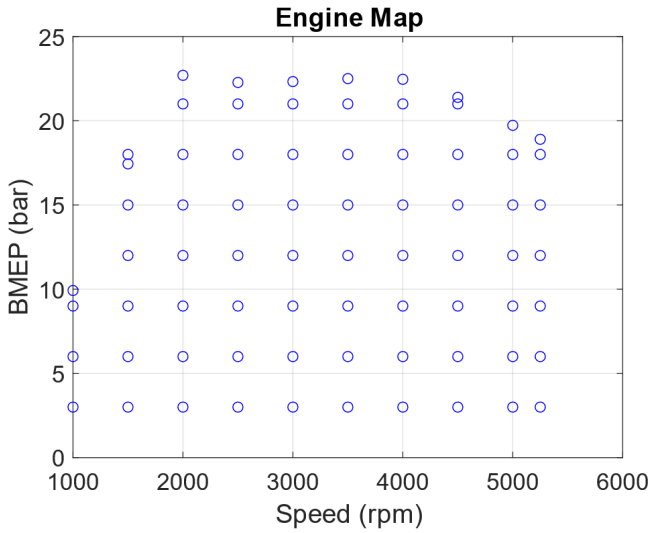

Figure 3.9: Gasoline ICE steady state campaign.

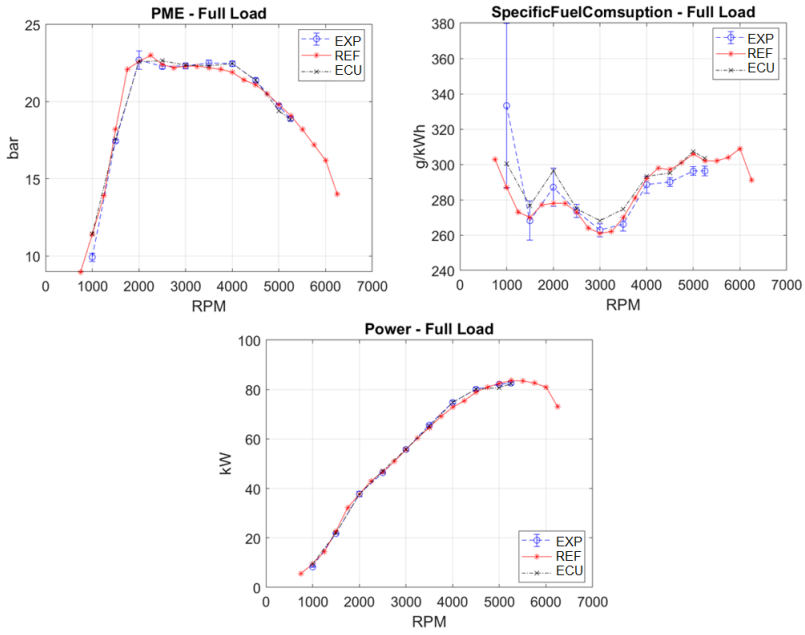

Figure 3.10: Gasoline ICE steady state campaign.

The validation was performed by comparing measurements at full load with the respective measurements delivered by the engine manufacturer. The experimental data were classified into three groups: global parameters, mean pressures, and mean temperatures. Some parameters recorded by the ECU have been also included in the comparison when available and it is important to point out that some of these parameters are estimated values. For the sake of brevity, only the global parameters are presented in this work. Figure 3.10 shows the comparison between the reference (REF) and measured (EXP) most relevant operating parameters of the engine. It is observed that except for some small differences in the specific fuel consumption at low speed, all the curves obtained from the experimental campaign collapse very well with the reference. These results lead to conclude that the performance measurement of the engine is within the dispersion limits established by the manufacturer.

3.4 Battery testbench

The main purpose of this installation was to produce experimental data for developing the battery model which is described the battery section of Chapter 4. Figure 3.11 presents the overall methodology followed in this work. First, the tasks consisted in the pre-conditioning of the testbench and the sensor calibration. Then, the characterization tests were carried out at different current demands and temperatures. Afterwards, an optimization algorithm was used for generating the fitting parameters of the model using the generated experimental data. Finally, dynamic cycles were launched in the testbench to validate the model in real operating conditions.

The installation for testing the battery cell was mainly formed by a battery tester, thermal chamber, temperature sensors, infrared camera and a data acquisition device. Figure 3.12 shows the general scheme of the testbench used for characterize the cells used in this work. The battery was characterized at a cell level as it can be seen in Figure 3.13. The cells were installed inside the test chamber in order to characterize them at different environmental temperatures. The cells were connected to a bidirectional current source (battery tester emulator) with 4 channels which controlled input current and voltage. Simultaneously, the battery tester was electrically connected to the electric grid. Temperature of the cell was measured on the surface by means of thermocouples.

Table 3.7 presents a list of the main calibrated instruments used in the

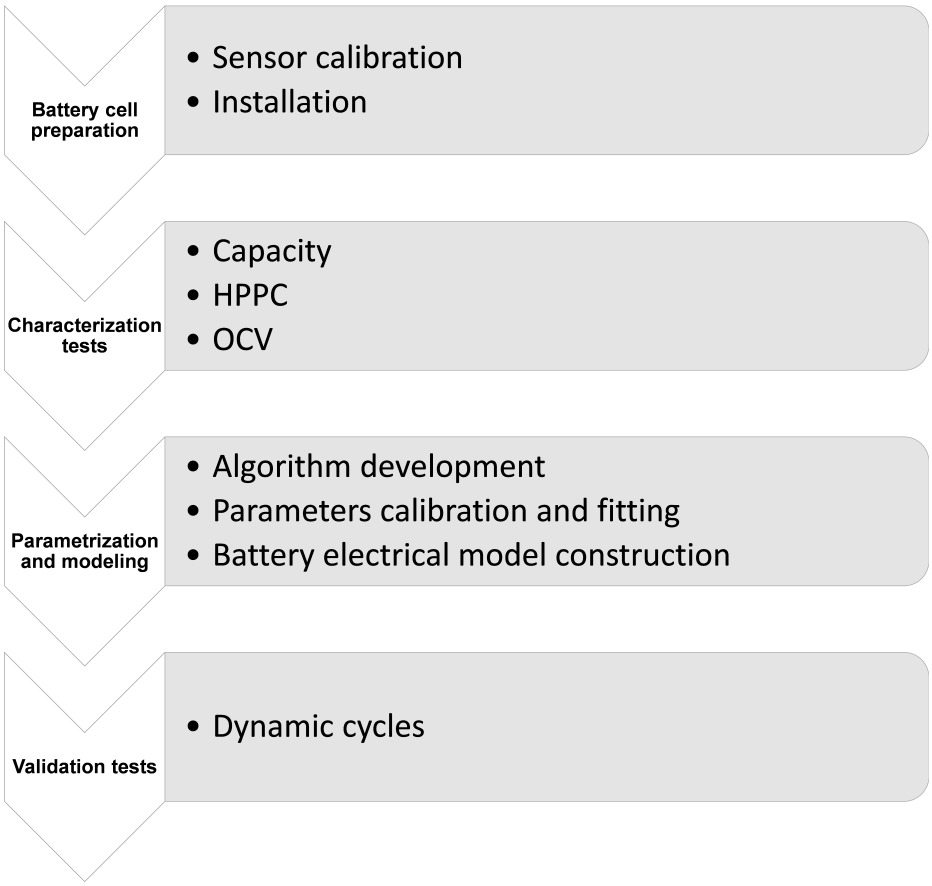

Figure 3.11: Methodology for battery cell characterization and validation

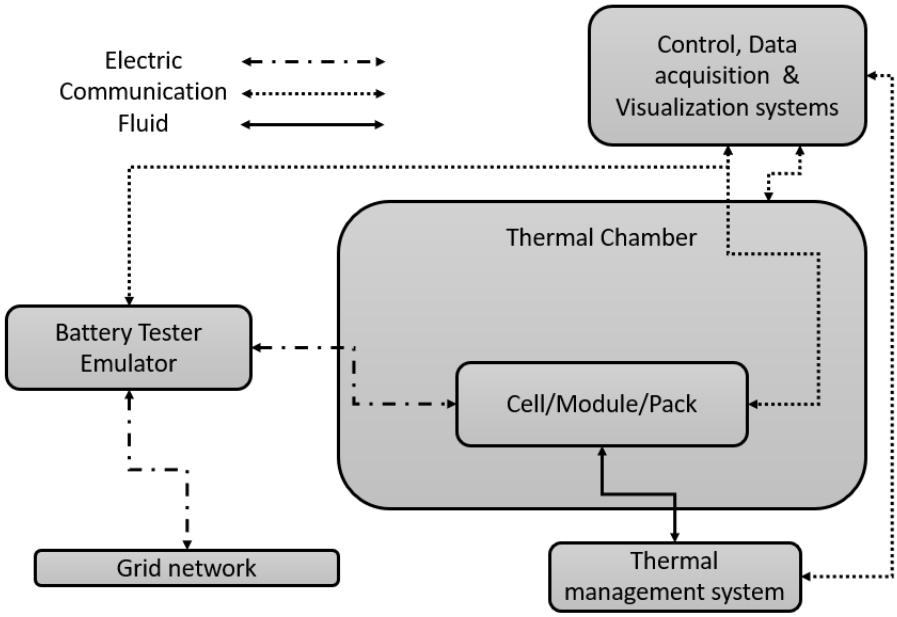

Figure 3.12: Schematic of battery laboratory.

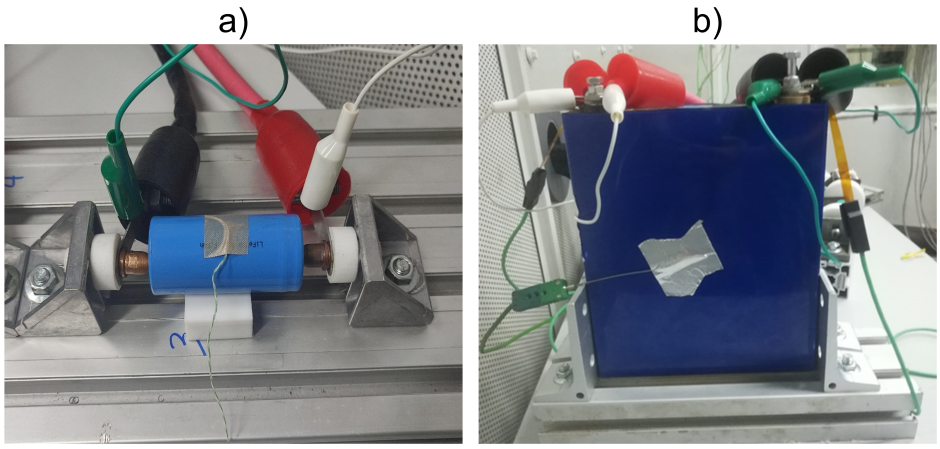

Figure 3.13: Battery cells. Cylindrical (a) and Prismatic (b).

battery laboratory.

Table 3.7: Battery laboratory instrumentation

Variable	Instrument	Range	Accuracy
Voltage & Current	Battery tester	10 V - 100 A	0.015%
Ambient temperature	Thermal chamber	-70 - 180 °C	±0.3 K
Temperature	k-type thermocouple	70 - 1520 K	±2 K
Temperature distribution	Infrared camera FLIR X6801	-20 - 2000 °C	±2 °C
Temperature	Data Loggers Agilent 34972A	-	-

Two different cells were tested in order to validate the models implemented in this work. On one hand a cylindrical cell with LFP chemistry with 3.8 Ah of nominal capacity. On the other hand, a prismatic cell with LTO chemistry and 23 Ah of capacity. Table 3.8 shows the features of the cells used in the present work.

Table 3.8: Features of the battery cells

Battery cell name	N1	N2
Chemistry	LFP	LTO
Shape	Cylindrical	Prismatic
Nominal Voltage (V)	3.2	2.3
Nominal Capacity (Ah)	6	23
Weight (kg)	0.087	0.55
Volume (L)	0.035	0.26

In order to characterize the cells a series of specific experimental test were performed. These tests were critical to determine the parameters for the developed submodels of the battery which depended on cell temperature, current direction (i.e., charge or discharge), c-rate (i.e., the measurement of current in which a battery is charged and discharged at) and state of charge (SOC).

The cell characterisation tests were as follows:

- A capacity test aiming to determine the real electrical capacity of the cell. In other words, the usable electrical energy available in the cell. Obviously, the higher the battery SOC, the higher the remaining capacity. Hence, this variable mainly depended on the SOC of the battery. Additionally, temperature and current power also impacted the cell capacity. In order to capture this effects, a precise mapping was obtained by performing capacity tests at different temperatures

and discharge rates. Figure 3.14 shows an example of the capacity test of cell N1 at 0 °C.

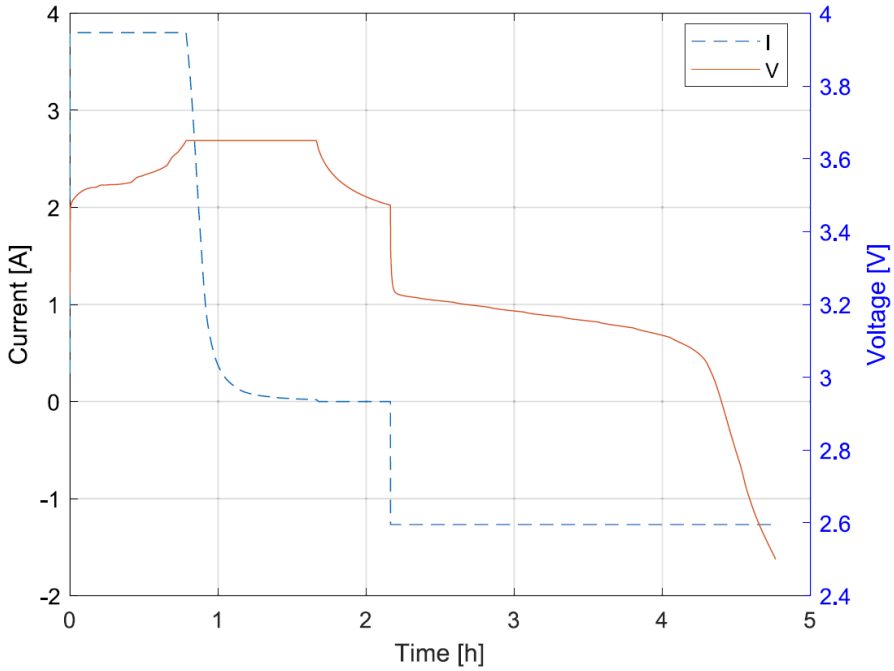

Figure 3.14: N1 cell capacity test [137]

- Figure 3.15 shows the Hybrid Pulse Power Characterization (HPPC) test which served to determine the ohmic resistance R_0, the polarization resistance R_1 and the polarization capacitance C_1.
- The open circuit voltage (OCV) test (See Figure 3.16) served to determine the terminal voltage of the cells. This variable was function of the cells SOC.

The processed data of the different experimental tests for the battery cells N1 and N2 were already presented in [137] and [138], respectively.

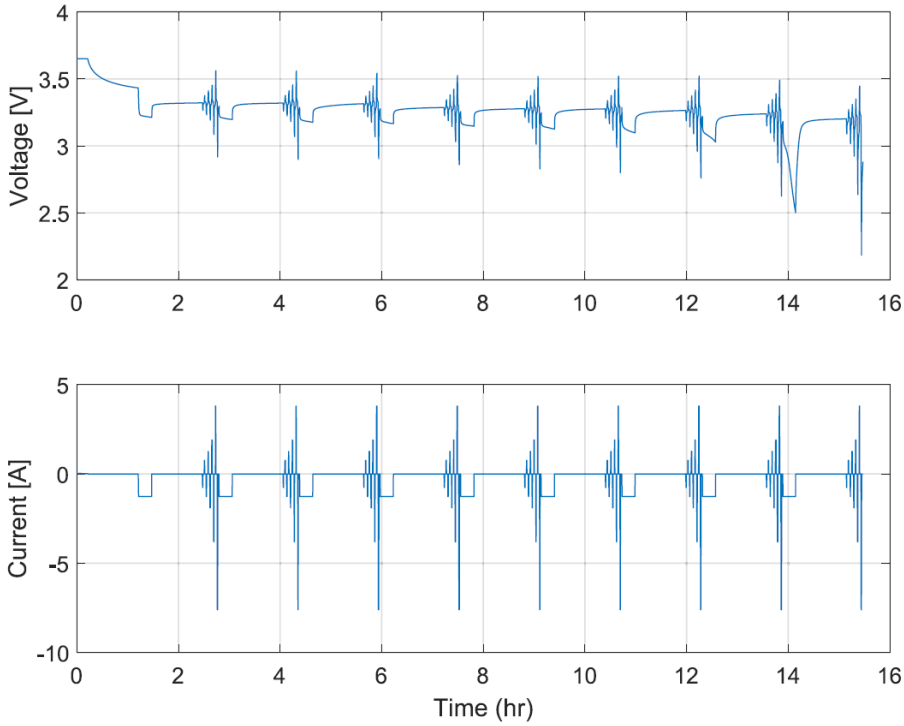

Figure 3.15: N1 cell HPPC test [137]

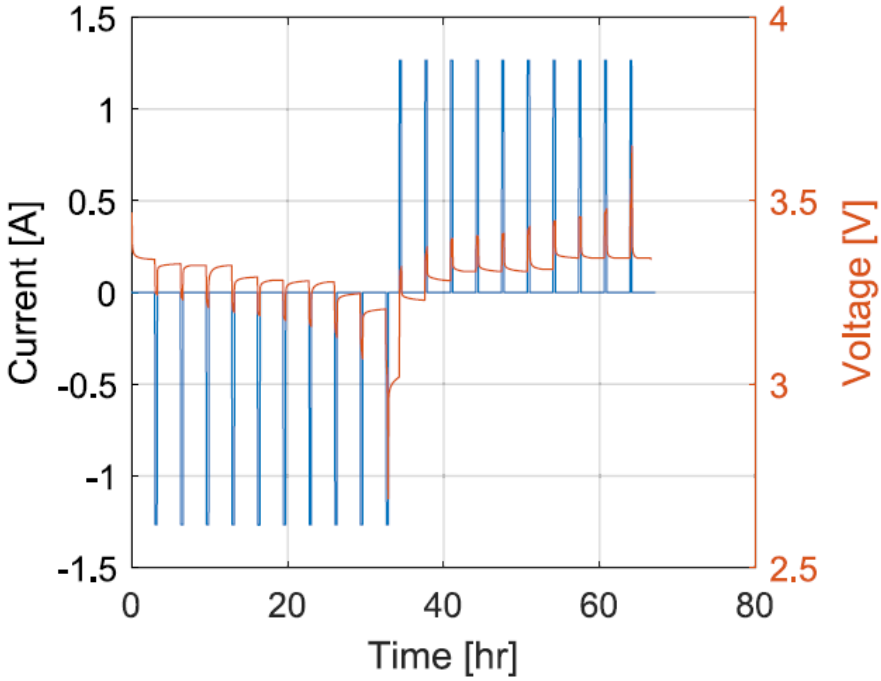

Figure 3.16: N1 cell OCV test [137]

4 Modeling tools

4.1 Introduction

The numerical models implemented in this work have been developed in different software platforms. In fact, the engine gas circuit of the Diesel and Gasoline engines have been modelled with Virtual Engine Model (VEMOD) and GASDYN software, respectively [139] [140]. Furthermore, the thermal management and lubricant systems (i.e., oil, coolant circuits) were constructed using the VEMOD (Virtual Engine Model) software. For the case of the Gasoline engine, a standarized co-simulation framework named Functional Mock up Interface (FMI) was implemented in order to couple the gas model code of GASDIN with VEMOD's thermal submodels (i.e., ICE Thermal model and Thermohydraulic model). Hence, benefiting from the strengths of both simulation tools. Significant modifications were implemented in the interface code for enabling their correct communication.

Additionally, the electric and thermal submodels of the battery were modeled in C++ language using Microsoft Visual Studio. Similarly, the electric drive (i.e., electric machine and inverter) was implemented by means of in-house software, power losses and efficiency maps provided by the manufacturer. The thermal model and the simplified AC cabin models were implemented using MATLAB code and python library. Finally, MATLAB/Simulink software was used to develop and simulate the energy management system of hybrid powertrains.

It is important to state the capacities and precision expected from the surrogate models. It is well known that increasing the detail and precision of the models usually translates in more simulation time. The developed models of this research aim to simulation times close to real time. Thus, although 3D simulations are used for validation, each one of the numerical submodels are based on 0D/1D modelling approach in order to reduce computational effort.

Table 4.1: Submodels integration in VEMOD [141]

		FLUID CIRCUITS		
		Gas circuit	Coolant circuit	Oil circuit
ENGINE SYSTEMS	Engine block	• Combustion and emissions submodel. • Gas dynamics model. • ICE Thermal submodel.	• ICE Thermal submodel. • Thermohydraulic submodel.	• ICE Thermal submodel. • Thermohydraulic submodel. • Mechanical losses submodel.
	Turbocharger	• Gas dynamics model. • ICE Thermal submodel.	• ICE Thermal submodel. • Thermohydraulic submodel.	• ICE Thermal submodel. • Thermohydraulic submodel. • Mechanical losses submodel.
	Coolers	• Gas dynamics model. • ICE Thermal submodel.	• ICE Thermal submodel. • Thermohydraulic submodel.	• ICE Thermal submodel. • Thermohydraulic submodel.
	Pumps		• ICE Thermal submodel. • Thermohydraulic submodel. • Mechanical losses submodel.	• ICE Thermal submodel. • Thermohydraulic submodel. • Mechanical losses submodel.
	Exhaust line	• Gas dynamics model. • Heat transfer submodel. • DOC and DPF submodels.		
	Ducts	• Gas dynamics model. • Heat transfer submodel.	• Thermohydraulic submodel.	• Thermohydraulic submodel.

4.2 Virtual Engine Model (VEMOD)

The software in which several of the ICE submodels were implemented was developed and tested at CMT-Motores Térmicos named as VEMOD [141]. This program allows to model the complete ICE in 0D/1D simulation framework. In order to perform accurate simulations, all the main engine components and systems were modeled.(e.g. 1D gas circuit, high and low pressure EGR, turbocharger, aftertreatment, hydraulic circuits, control system , etc.).

Figure 4.1 shows the information flow between systems during the simulation in steady and transient conditions. The engine control unit (ECU) modelled using Matlab/Simulink is connected through sensors and actuators to the different physical submodels of the engine model. The ECU model actuates over the throttle position, EGR valves, VGT, etc., according to the engine sensors information [141].

Table 4.1 represents the submodels integration inside the main engine model. The studies performed in this work involved the development, modification and calibration of the gas, coolant and oil circuits. Special attention was given to engine block, cylinder liner and head, piston, intake and exhaust pipes, intake and exhaust manifolds since evaluating and improving the heat transfer in these areas presented great potential for improving engine performance, efficiency and emissions. Only the relevant submodels developed and implemented in the scope of this work will be explained in the following sections. An extensive description is found in reference [142] for the rest of the submodels.

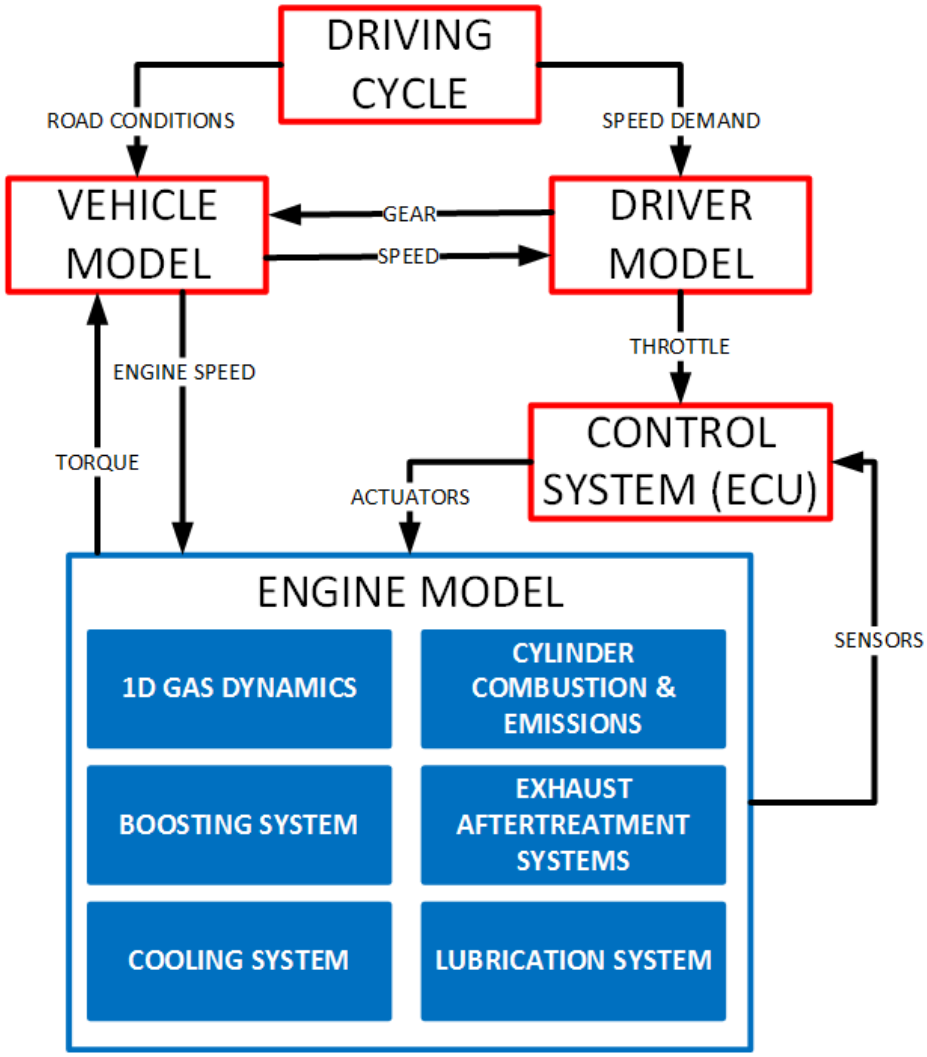

Figure 4.1: Flowchart of Virtual Engine Model (VEMOD) [141]

4.2.1 Diesel ICE Gas dynamic submodel

For the present work it is important that the model accurately calculates the temperature and pressure in different parts of the gas circuit. For instance, intake and exhaust ports temperatures will be critical due to the fact that both the gas intake and exhaust temperatures are directly affected by coolant temperature which is given as input by the hydraulic circuit submodel. The model has proven to be effective on calculating the different thermo-fluid dynamic processes taking place in the cylinder, manifolds, pipes, ports, turbocharger, heat exchangers and aftertreatment system.

The pipes are considered 1D ducts while the cylinders and coolers are considered 0D elements. In these, mass and energy conservation laws are solved, while for 1D ducts all physical phenomena are took into account in the calculation such as; wave interactions, the gas composition, heat transfer and friction. The 1D ducts are meshed in cells and the mass, momentum and energy equations are solved in each cell.

The heat transfer between the fluid and the solid in the different pipes is calculated according to the Equation 4.1.

$$q_i = A_i \, h_{i,in} \, (T_g - T_{w,in}) \, \Delta t \tag{4.1}$$

Where q_i represents the heat transferred between the gas and pipe walls, A_i is the surface in which the heat transfer takes place while the T_g and $T_{w,in}$ stand for the temperature of the gas and the temperature of the inner wall surface, respectively. $h_{i,in}$ is the heat transfer coefficient between gas and wall which is calculated depending on where the pipe is situated in the engine structure. For the case of the intake and exhaust port pipes, the gas temperature is calculated for each time step while the inner wall temperature is provided by the engine lumped thermal model for each cycle. This is justified since the gas temperature varies several degrees while the temperature of the engine block walls vary much less (6°C at most) during each cycle.

The turbocharger submodel used is based on a 0D compressor and turbine submodel. In [57] a detailed explanation of the design and validation of the turbine model can be found. The compressor submodel used is the one developed in [143].

Additionally, the injection is based on four injectors empirically characterized by their opening and closing times according to the injection pressure. Moreover, this submodel is responsible for calculating the injec-

tion rate which is the main input for the combustion process.

Figure 4.2 shows the schematic layout of the gas circuit implemented in VEMOD. All basic elements of the Diesel engine were modelled. Following the air path, the gas circuit can be divided into intake line, compressor (i.e., charger), WCAC, intake manifold, engine block (consisting in four cylinders), exhaust manifold, HPEGR line, turbine (i.e., turbo), LPEGR, AFS and exhaust line.

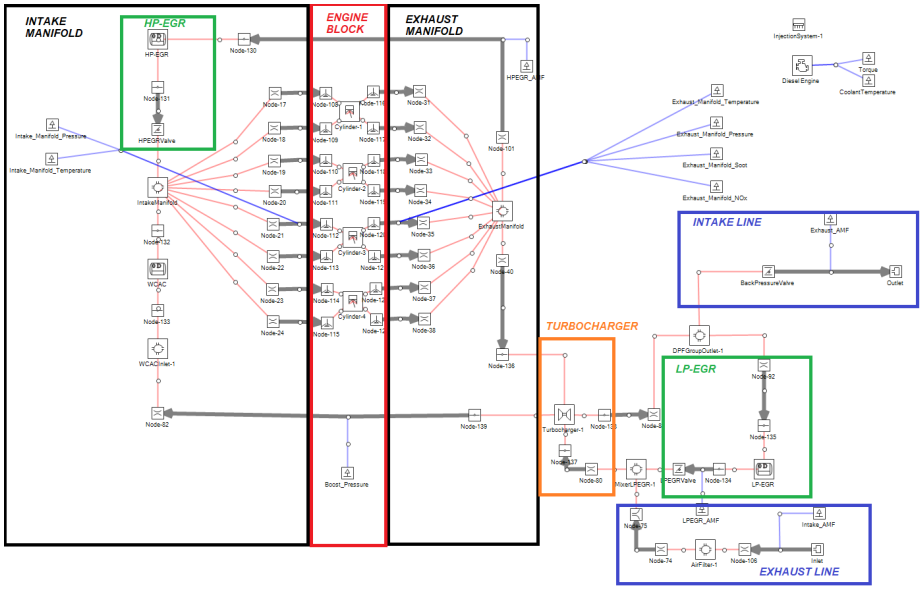

Figure 4.2: Scheme of ICE Diesel gas circuit implemented in VEMOD

4.2.2 Diesel ICE Thermal submodel

The engine heat transfer phenomena in the Diesel engine was calculated using ICE Thermal submodel. It is based in a lumped thermal model which discretizes the engine materials and fluids into several nodes. This submodel was flexible and capable to adapt to different engine geometries. The features of the engines presented in Chapter 3 were used to set up this submodel. This model calculates the heat rejected from combustion chamber and cylinder ports. It also calculates the heat transfer between the different solid parts of the engine block. This lumped model discretizes the engine into multiple nodes strategically situated in the cylinder-head, liner and piston aiming to accurately predict the temperature in the main

parts of the engine. Additionally, the coolant jacket is also divided into several nodes. The nodes are considered isothermal (i.e. without inside thermal gradients) and isotropic (i.e. homogeneous physical properties in all directions). Each node has its own volume, thermal conductivity, specific density and thermal capacitance which are introduced in the lumped model. This model is based on Equation 4.2 and Equation 4.3 which are the result of applying an energy balance for the material (structural parts of the engine) and the fluid nodes respectively. Figure 4.3 shows a scheme of the heat transfer processes considered in the solid node i.

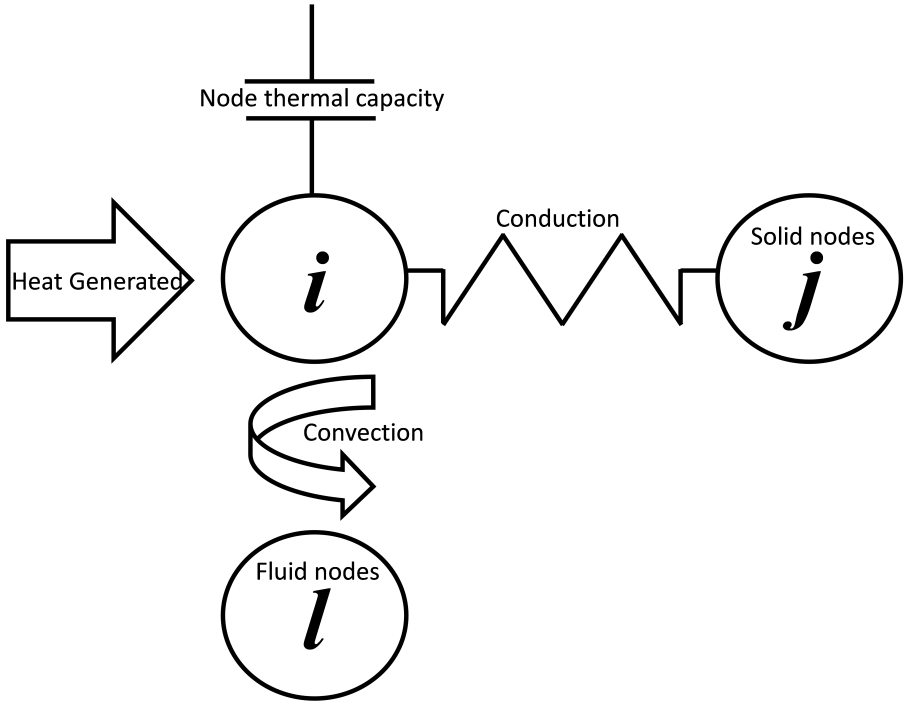

Figure 4.3: Heat transfer in engine solid nodes.

$$m_i\, c \left(\frac{T^i_{t+\Delta t} - T^i_t}{\Delta t} \right) = \sum_j \frac{k_{ij}\, A_{ij}}{d_{ij}} \left(T^j_{t+\Delta t} - T^i_{t+\Delta t} \right) + \sum_k \dot{Q}_{k \to i} + \sum_l h_{li}\, A_{li} \left(T^l_{t+\Delta t} - T^i_{t+\Delta t} \right) \tag{4.2}$$

In Equation 4.2, the temperature increase of node i is equal to the ex-

changed heat flux (by conduction with node j and convection mechanisms with node l) and the heat generated in the node (i.e. friction power).

Where m_i, c and T_t^i are the mass, heat capacity and current temperature of the solid node i, respectively. Additionally, k_{ij} stand for the thermal conductivity between solid nodes i and j. Furthermore, A_{ij} and d_{ij} are the area and width between solid nodes. $T_{t+\Delta t}^j$ is the temperature of node j for the next time step (Δt). $\dot{Q}_{k\to i}$ represents the heat generated in the node. h_{li} is the convection heat transfer coefficient between a solid node i and fluid node l, A_{li} is the area between them while $T_{t+\Delta t}^l$ represents the temperature of the fluid node for the next time step. The temperatures from the right hand side of the Equation 4.2 are evaluated at the instant $t+\Delta t$ (implicit method) in order to ensure the model stability when transient processes are simulated. Contrary to the explicit method, higher computational time is required.

In addition, the energy balance of the coolant nodes is shown in Equation 4.3 where the temperature of each node is computed as the arithmetic mean between the inlet and outlet. In this equation, the sum of the thermal energy stored in the fluid node, the enthalpy drop, the heat generated and the exchanged heat through convection is taken into consideration as it can be seen in Figure 4.4.

$$\begin{aligned}\frac{m_l\, c_p}{\Delta t}\left(\frac{T_{t+\Delta t}^{l,ou}+T_{t+\Delta t}^{l,in}}{2}-\frac{T_t^{l,ou}+T_t^{l,in}}{2}\right)+\dot{m}_l\, c_p\left(T_{t+\Delta t}^{l,ou}-T_{t+\Delta t}^{l,in}\right)\\ =\sum_k \dot{Q}_{k\to l}+\sum_i h_{ij}\, A_{ij}\left(T_{t+\Delta t}^{j}-\frac{T_{t+\Delta t}^{l,ou}+T_{t+\Delta t}^{l,in}}{2}\right)\end{aligned} \tag{4.3}$$

Where m_l, c_p and $\dot{m}_l$ represent the mass, heat capacity and mass flow of fluid nodes, respectively.

In order to use the lumped capacitance model in different engines and to reduce the calculation times a simplified geometry of an engine has been used. This simplification takes into account the most usual geometries for the piston, cylinder-head and liner and they are related to the main geometrical characteristics of an engine as piston diameter, stroke or compression ratio, valves diameters. Then, the simplified geometry was divided into different nodes according to the localization of the biggest thermal gradients and the location of the thermocouples used in the experimental validation [26]. The nodes in each of the elements has been chosen as follows:

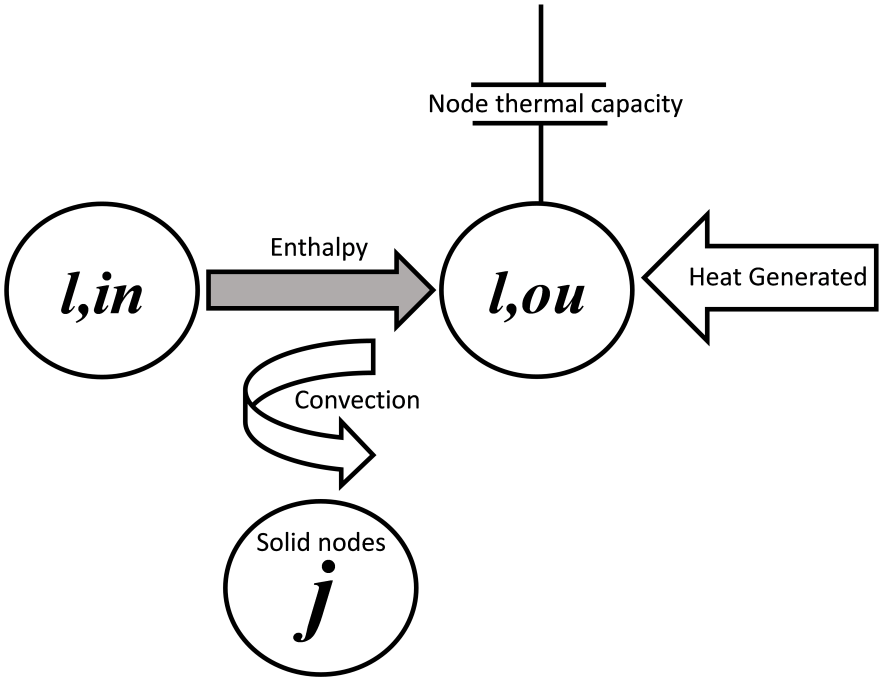

Figure 4.4: Heat transfer in engine liquid nodes.

- The cylinder is divided into five axial nodes, two radial and six circumferential, adding another line of nodes outside of the top of the cylinder, in such a way that the first axial level has three radial levels. Consequently, the cylinder has 66 nodes as shown in Figure 4.5.

- The piston is divided into ten nodes with azimuthal symmetry as shown in Figure 4.5.

- Undoubtedly the division of the head-cylinder is the hardest one due to its complicated geometry and its large amount of components. Because of this the head-cylinder is simplified taking into account only the main components with plain shapes. The number of used nodes in this case is 35, a scheme of their distribution is shown in Figure 4.5.

- Finally, the coolant has been divided in several nodes in order to improve the accuracy of its thermal balance. First, the coolant is split in two main paths: one passing through the liner and the other flowing through the cylinder-head. The coolant path is shown in Figure 4.6. Besides, each of these two main paths, the coolant is divided in different nodes:

  - The coolant which crosses the head-cylinder is divided in two nodes, one in contact with the intake area and another with the exhaust area.
  - The coolant which crosses the cylinder is divided in four axial levels and five circumferential. The coolant has one circumferential node less than the cylinder because one of the circumferential columns of nodes in the cylinder is considered insulated because it has no contact with the coolant and it is in contact with an analogous node of the next cylinder, this one corresponds with the first circumferential nodes of Figure 4.5.

Consequently, the total number of metalic nodes is 111 while there are 22 different coolant nodes. The rest of the boundary conditions are: lubricating oil, in-cylinder gases, inlet air and exhaust gases. These boundary conditions are characterized by their average temperatures and film coefficients. These are the only boundary conditions considered in the model, i.e. other possible boundary conditions as external surfaces are neglected.

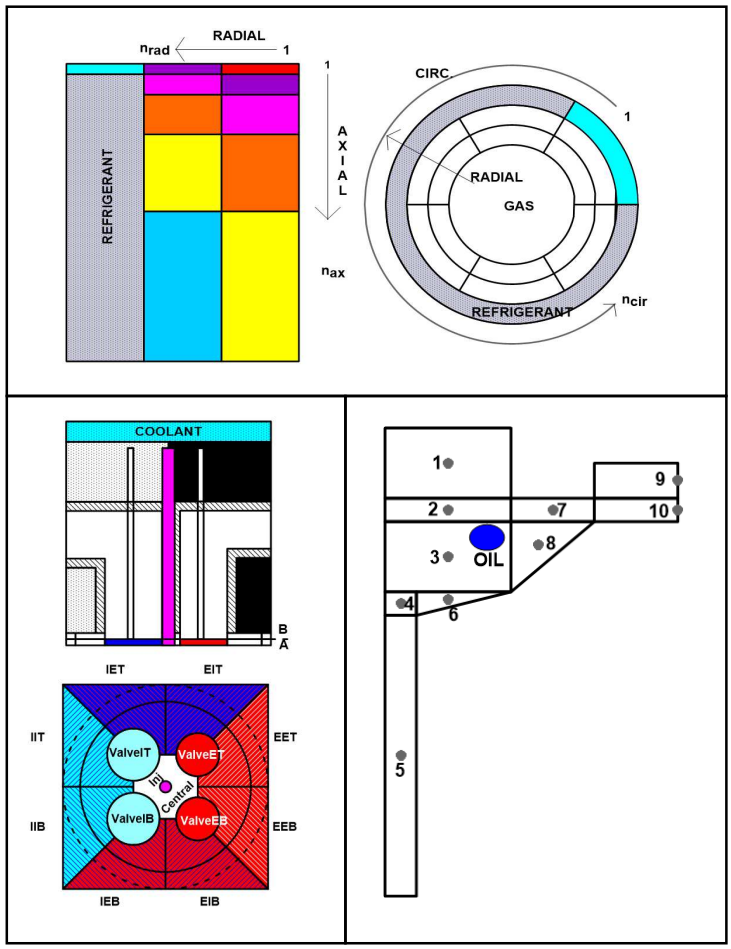

Figure 4.5: General node mesh for the ICE Thermal model of Diesel engine

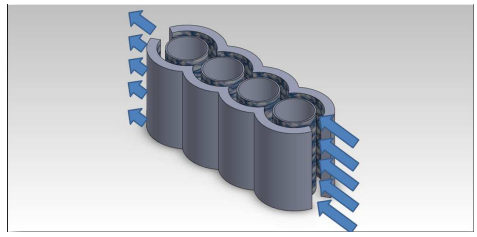

Figure 4.6: Coolant flow in the liner and head-cylinder.

As mentioned, the coolant flow is split in two paths, one enveloping the cylinder liner and the other flowing through the cylinder head. In order to calculate the convective heat transfer coefficient in the coolant, two correlations have been used due to the speed difference in the two paths. For the liner, a modification of the Grimson correlation (Equation 4.4) [144] was used and, for the cylinder-head, a variation of Dittus-Boelter correlation (Equation 4.5) was implemented [145].

$$Nu = 1.13\, b_1\, b_3\, Re_{D,max}^{b_2}\, Pr^{\frac{1}{3}} \tag{4.4}$$

$$Nu = 0.023\, Re^{0.8}\, Pr^{0.4} \tag{4.5}$$

Where b_1 and b_2 are constants depending on the distance between the cylinders, and b_3 is a constant which corrects the correlation for the case of banks with less than ten rows of tubes. Nu, $Re_{D,max}$ and Pr stand for the Nusselt, Reynolds and Prandtl numbers, respectively.

The cylinder lumped thermal model will be responsible of providing the combustion model of two main inputs; the wall temperatures and the injector temperature. This variable is needed in order to determine the fuel temperature which directly impacts on the fuel density, and, consequently, in the fuel consumption.

Regarding the rest of boundary conditions; the temperature and convective heat transfer coefficients of the oil, in-cylinder gases, inlet air and exhaust gases. They are averaged for each cycle and introduced to the lumped thermal model.

For calculating the convective heat transfer coefficient of the gas inside the combustion chamber a modified Woschni‘s correlation (Equation 4.6) was implemented in the thermal lumped model [146][147]. More detailed information regarding the correlation can be found in [148].

$$h_w = C_1 \cdot D^{-0.2} \cdot p^{0.8} \cdot T_g^{-0.53} \cdot \left(C_{w1} \cdot c_m + C_{W2} \cdot c_u + C_2 \left(\frac{V \cdot T_{IVC}}{P_{IVC} \cdot V_{IVC}} \right) (p - p_o) \right)^{0.8} \tag{4.6}$$

Where the parameters C_1, C_{w1}, C_{W2} and C_2 are tuned according to the experimental data obtained from motored and firing tests. Additionally, c_m is the mean piston speed, c_u is the instantaneous tangential velocity of the gas in the chamber, p_o is the pressure in the chamber in motored conditions assuming polytropic evolution, p and T are the pressure and

temperature inside the combustion chamber while T_{IVC}, P_{IVC} and V_{IVC} are the temperature, the pressure and the volume at intake valve closing (IVC) respectively [149].

Steady state validation

In order to validate the ICE lumped model a set of experimental measurements were used. These measurements were carried out over an engine whose features were summarized in Chapter 3. Several thermocouples were placed in the engine, each of these correspond with a structural node of the lumped model. The thermocouple logged the temperature evolution in several operation conditions. The data from the thermocouples were compared with the model predictions; some of the results are presented in Figure 4.7. In the plots of the Figure 4.7 it can be seen how the model predictions correspond fairly well to the experimental data obtained.

Transient validation

In order to validate the model in transient simulations it was checked the correspondence between the experimental data and the predicted results when the engine underwent a sudden change. To carry out these comparisons the engine was set in a constant speed and load conditions and then it was applied a sudden change in one of the parameters, keeping the other constant. For instance, Figure 4.8 show the results for the changes occurred when, with the engine running at 2000 rpm and 6.54 bar of bmep, the load is raised until 18.77 bar keeping the speed constant.

Figure 4.8 shows a good agreement between the predicted results by the model and the experimental data obtained in the engine. This model served as a fundamental tool for assessing the use of nanofluids as coolant fluids in the engine as it will be shown in Chapter 5.

4.2.3 Diesel ICE Thermohydraulic submodel

Both coolant and oil circuits were constructed with the thermohydraulic model. The principal components of the hydraulic circuits were characterized as follows:

- Pumps: The main inputs for the pumps are the internal volume, the speed ratio between the pump and the engine, the flow head curve and the efficiency curve.

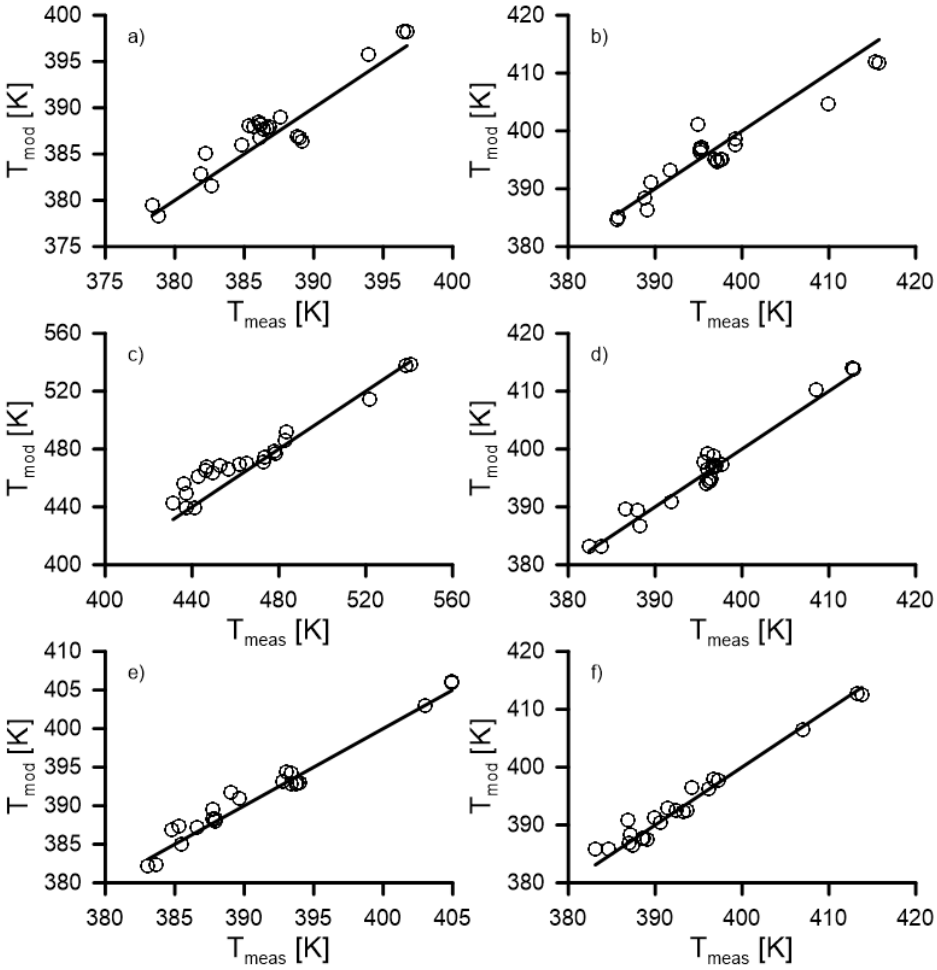

Figure 4.7: Predicted versus measured temperatures in cylinder 1: a) Exhaust side at 8 mm, b) Injector hole exhaust side at 8.7 mm, c) Cylinder 1 bowl rim , d) Exhaust valve seat at 3.5 mm, e) Intake valve seat at 3.5 mm f) Admission side at 3.5 mm

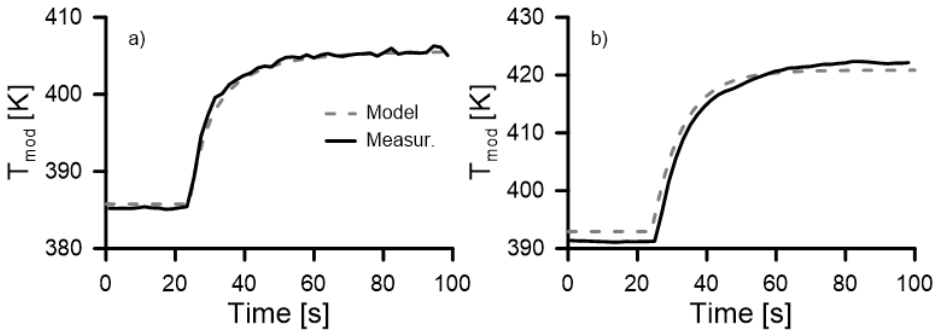

Figure 4.8: Predicted versus measured temperatures in cylinder 1: a) Exhaust side at 8 mm, b) Intake valve seat at 3.5 mm

- Pipes: The pipes were defined by their diameter, length and friction coefficient.
- Thermostat: The thermostat was modeled as a valve which creates a localized hydraulic resistance depending on the thermostat opening lift. Likewise, this opening lift is function of the coolant temperature as it was detailed in the [140].
- Heat exchangers: The heat exchangers of the are also implemented in the model by their volume, type and hydraulic resistance coefficients.

Consequently, the total volume of the circuits will be equal to the sum of the different component volumes.

The thermo-hydraulic model calculates the pressure and the flows by applying the continuity and energy conservation laws according to Equations 4.7 and 4.8 for each node and mesh, respectively. Where $\dot{V}$ is the volumetric flow mass. In Equation 4.8, R_2, R_1 and R_0 represent the quadratic, linear and independent coefficients of the hydraulic resistance respectively. The network is formed by several hydraulic components (i.e. pumps, valves, thermostat, heat exchangers, volumes...). As it can be seen in Figure 4.9, the network is composed by branches (a series of joined hydraulic components between node and node), meshes (joined branches forming closed loops) and nodes (joins of more than two branches).

$$\sum \dot{V} = 0 \tag{4.7}$$

$$\sum R_2 \dot{V}^2 + \sum R_1 \dot{V} + \sum R_0 = 0 \tag{4.8}$$

For the calculation of the temperature distribution, the branches are divided into several fluid volumes which move according to the flow. Simultaneously, depending on the heat exchanger type, the heat exchanger submodel calculates the heat and updates the temperatures of the fluid cells or volumes following the Equation 4.9. Where T_i^t is the new temperature of fluid volume, T_i^{t-1} is the temperature of the fluid volume in the previous time step, Q is the heat exchanged, m is the fluid mass of the fluid volume and Cp is the fluid heat capacity, which is calculated for the mean temperature between the inlet and outlet. The heat sources such as; cylinders, high pressure EGR, low pressure EGR, oil cooler, radiator and turbocharger are modeled by the heat exchanger submodel. Finally, the main outputs of the model are pumps power, pressure, flows and temperatures in each position of the circuit.

$$T_i^t = T_i^{t-1} + \frac{Q}{mC_p} \tag{4.9}$$

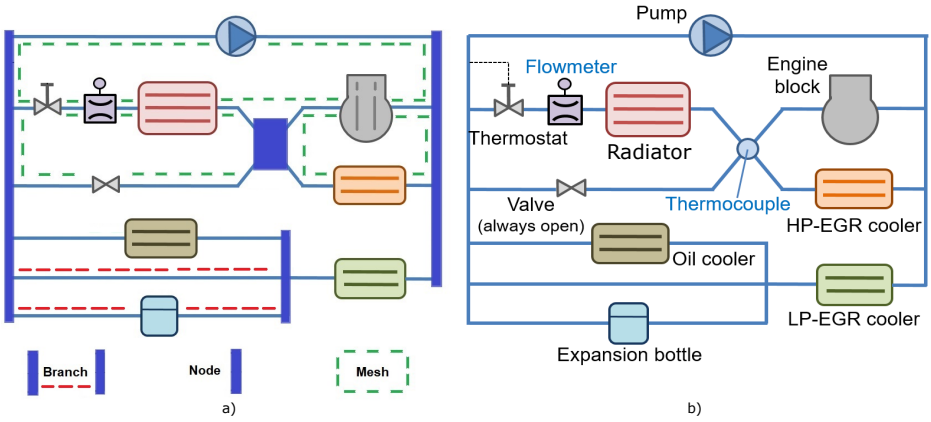

Figure 4.9: Diesel ICE Coolant circuit modeling: a) Nodes, branches and meshes of the circuit, b) Layout of the circuit

The thermo-hydraulic model is integrated within the engine model. For instance, the engine speed is an input required for calculating the pumps speed of both the coolant and oil circuits as it can be seen in Figure 4.10. It can also be observed that the flow rates are output of the model and used to calculate the heat rejected by the other engine submodels.

For the case of the engine and the turbocharger, the heat exchanger

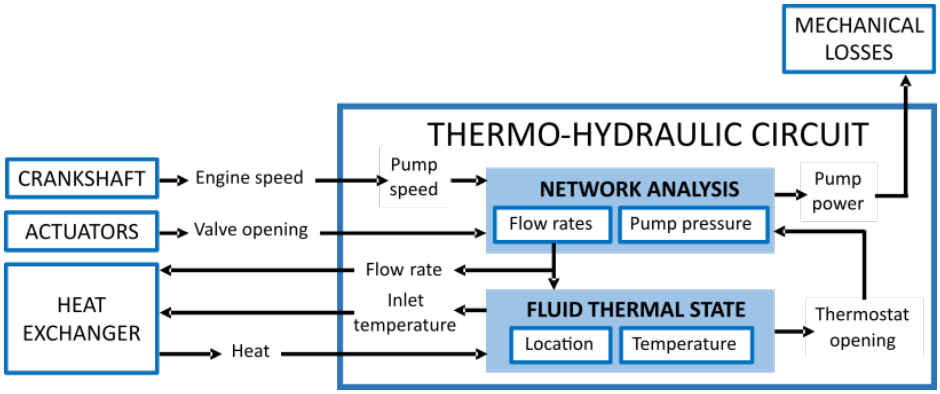

Figure 4.10: Integration scheme for the thermo-hydraulic model [140]

submodel receives the heat which is calculated by lumped thermal model of the engine and turbocharger [150][151]. For the elements whose main purpose is to exchange heat between two fluids the calculation is made by means of Number of Transfer Units (NTU) method. The main inputs for these heat exchangers are; the overall heat transfer coefficient, area, heat transfer surface and the heat exchanger type (e.g. simple parallel flow, simple counterflow, shell and tube, cross flow with both fluids unmixed, effectiveness table...).

In Figure 4.9 and Figure 4.11 the schemes of coolant and oil circuit of the modeled engine are presented.

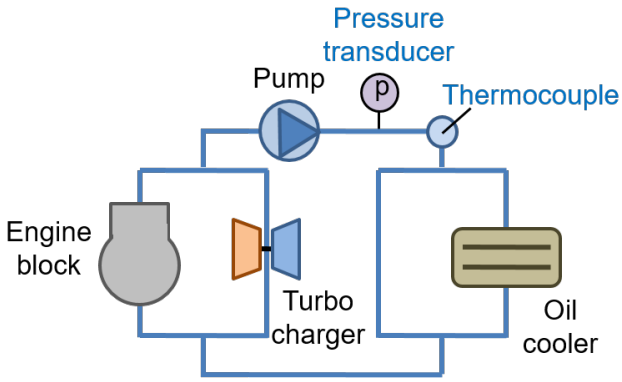

Figure 4.11: Diesel ICE Oil circuit layout

For the present work, some of the parameters of the model (i.e. friction

losses coefficient in the pipes, hydraulic resistance...), as it was stated in previous sections, were adjusted with the experimental measurements.

4.2.4 Holistic validation of Diesel ICE model

Steady state

In order to validate the engine model all the working points mentioned in the experimental campaign section were used. For the sake of brevity, only some plots of those validations are presented and the most relevant variables: air mass flow, indicated mean effective pressure (IMEP), fuel mass consumption, engine torque (Figure 4.12), oil pressure and temperature, coolant volumetric flow and temperature (Figure 4.13), for the studied thermal management strategy presented in this work are shown.

In Figure 4.12 the relative errors of between the steady state simulations and experimental measurements are presented. The analysis of air mass flow, IMEP, fuel consumption and torque is presented in four different plots. The averaged relative error obtained for the engine torque was less than 0.2 % while for the air mass flow it was 1.2 %. Particularly, the mean relative error in fuel mass consumption was less than 1.3 %. Additionally, it can be observed a slight trend when the fuel consumption is increased. The relative error was diluted as the fuel rate increased. Regarding the indicated mean effective pressure, the errors were less than 0.8 %. Overall, the coefficient of determination (R^2) for each of the variables was around 0.99.

On one hand, plots a) and b) of Figure 4.13 show the comparison between model and experimental measurements of the oil pressure and temperature. The model displayed a great accuracy since the calculated R^2 for the oil pressure measurement was 0.98. Pressures showed a mean relative error below 4 %. Although the relative error was high, the coefficient of determination was better, and the model was considered capable of predicting the behaviour of the experiments. Regarding oil temperature, the mean relative error was lower than 0.4 % (0.2 °C) and the maximum error was 1.2 % for all the simulated points.

On the other hand, for the coolant circuit, the coolant temperature and flow rate were selected for the model validation. In Figure 4.13 it can be seen that the coolant flow was accurately predicted by the model obtaining a coefficient of determination (R^2) of 0.98 and a mean error less than 2 %. Regarding the prediction of the coolant temperature, the mean relative error was below 0.2 % with a R^2 of 0.97.

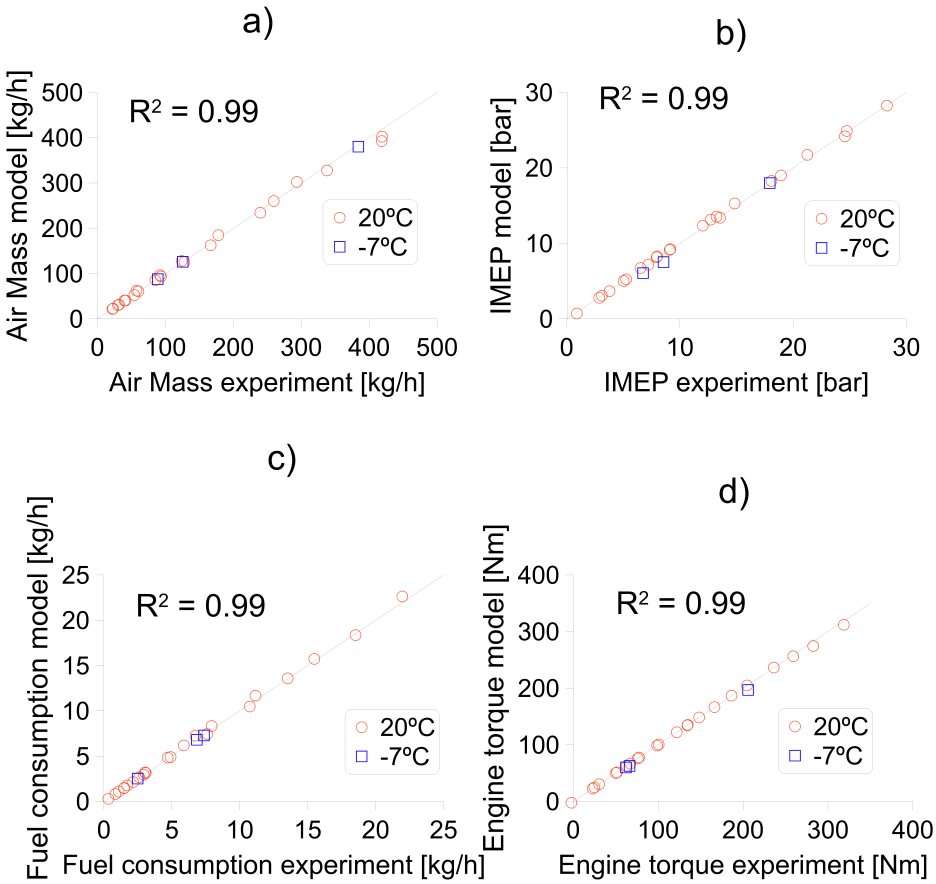

Figure 4.12: Engine performance validation in steady state conditions. a) Air mass flow error b) IMEP error c) Fuel consumption error d) Torque error

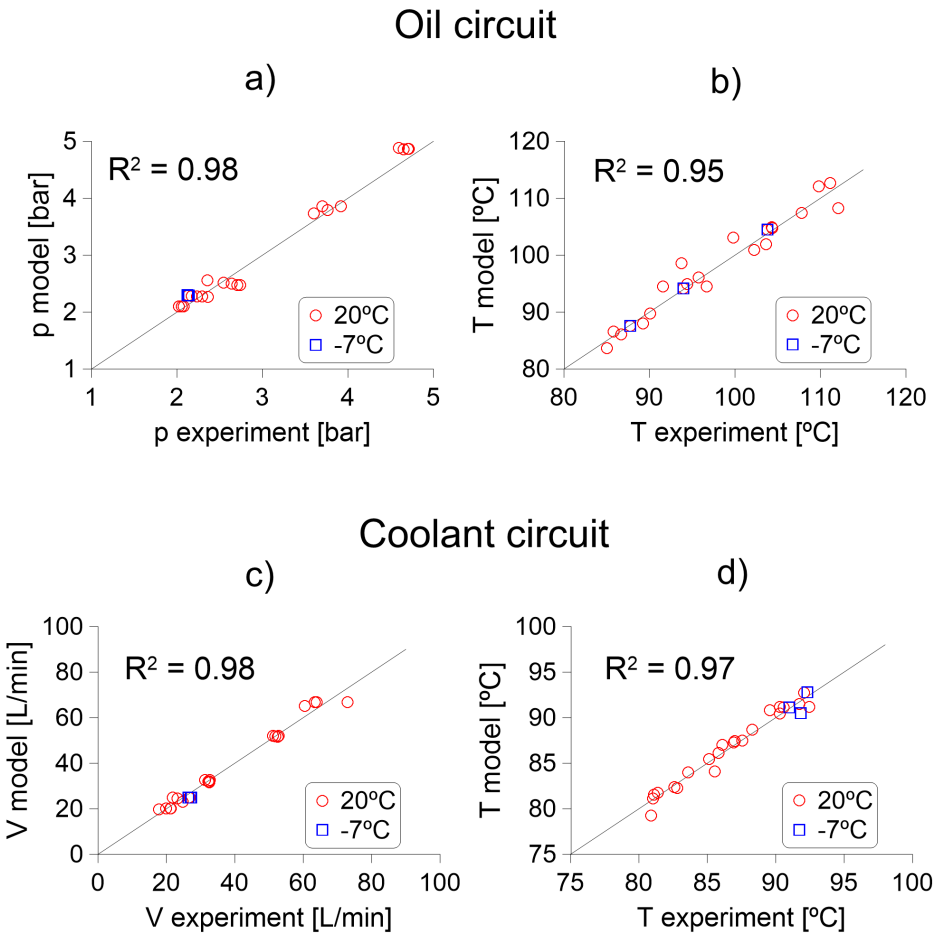

Figure 4.13: Hydraulic circuit validation. Experimental vs simulation. a) Oil pressure, b) Oil temperature, c) Coolant flow rate and d) Coolant temperature

Transient conditions

In order to validate the model in transient conditions, the WLTC cycle was simulated starting from three different conditions; cold, ambient and warm as it was previously explained. However, for this work, only simulations in ambient and cold conditions were validated because the main impact on changing the fluid mass of the hydraulic circuits it was only significant during the engine warming process.

Figure 4.14 shows the engine performance validation for ambient conditions. It can be seen that torque and fuel mass consumption are well captured by the model. The mean error in torque and fuel mass were 2.4 % and 1.5 % respectively.

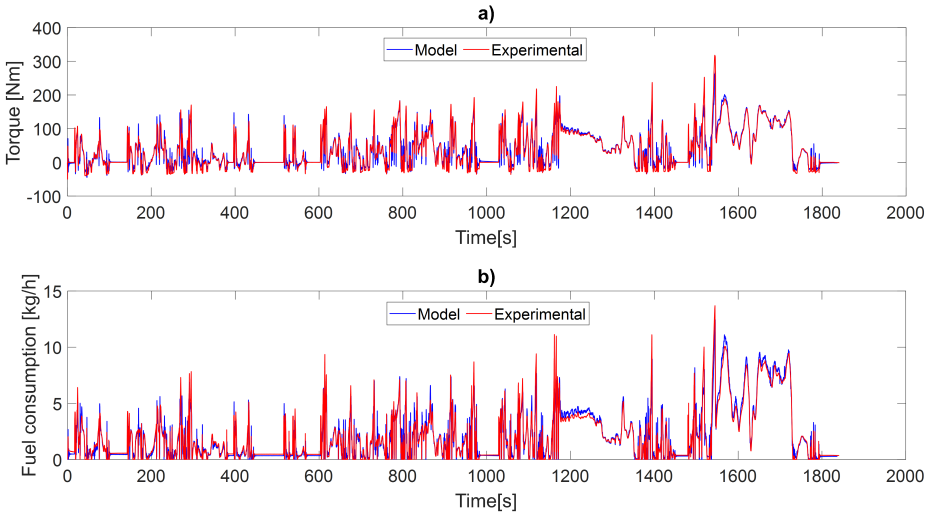

Figure 4.14: Engine performance validation in a WLTC cycle in ambient conditions. a) Torque b) Fuel consumption

Regarding the coolant and oil circuits, the temperature evolution during the cycle was predicted with a mean error of 0.8 % for the coolant and 1 % for the lubricant as it can be observed in Figure 4.15 and Figure 4.16. This was considered accurate taking into account the several heat sources in the model. Although the trend is completely captured in the coolant temperature evolution, during some part of the engine warming process (between 100 s and 700 s), the temperature increase of the model is slightly lower that the experimental one. This small deviation could be caused for two main reasons, either the engine heat rejected by the model

is lower than the real one or the thermal capacity of the cooling circuit is slightly higher. This is also seen in the last 300 s of the cycle. Regarding the oil temperature evolution, the model slightly overestimates the temperature after 750 s practically until the end of the cycle. Even though both models are connected by the oil cooler, there is not an apparent relationship between the small inaccuracies showed in the plots.

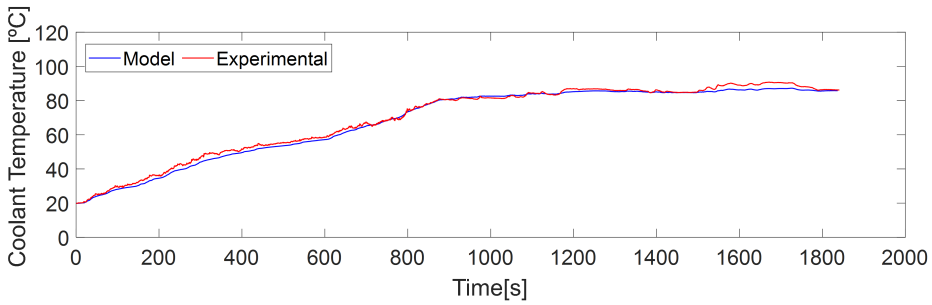

Figure 4.15: Coolant temperature validation during a WLTC cycle in ambient conditions

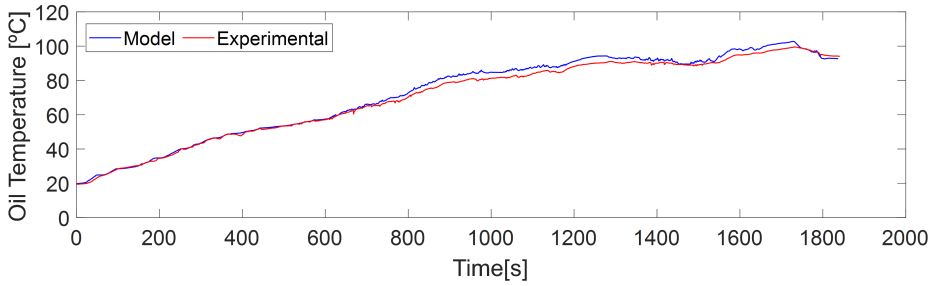

Figure 4.16: Oil temperature validation during a WLTC cycle in ambient conditions

For cold conditions, the model also showed a good accuracy and a capacity of reproducing the engine performance. Figure 4.17 demonstrates that the dynamism is captured by the model in these conditions. The mean error in the torque and the fuel mass were 2.5 % and 2 % respectively. Additionally, the model slightly overestimates both torque and injected fuel mass during the cycle periods with high speed and load.

In regard to the hydraulic circuits the model showed a relative mean error of 1.6 % and 2.3 % for the coolant and oil temperatures evolution

respectively. On one hand, in Figure 4.18 it can be seen that the coolant temperature evolution is perfectly captured during the first 550 s of the simulation. However, in the medium and high demanding conditions of the cycle (between 500 s and 1300 s), the increment of the coolant temperature is higher than the measurements. Despite this prediction difference, the model is able to capture the trend and the mean error was considered acceptable for the purpose of the study. On the other hand, Figure 4.19 shows that the oil temperature presents a similar behaviour. The model correctly simulates the trend during warm up time (1300 s) and slightly overestimates the temperature between 950 s and 1400 s. In the last 250 s of the cycle it is observed that the oil is cooled more than the experimental. As the coolant temperature (See Figure 4.18), which is used for cooling the oil, in the model is slightly overestimated between 1000 s and 1400 s, the oil temperature is also slightly overestimated in this period. In Figure 4.9 it can be seen that the oil cooler is immediately after the coolant pump and the radiator outlet (the LPEGR is no activated in cold conditions).

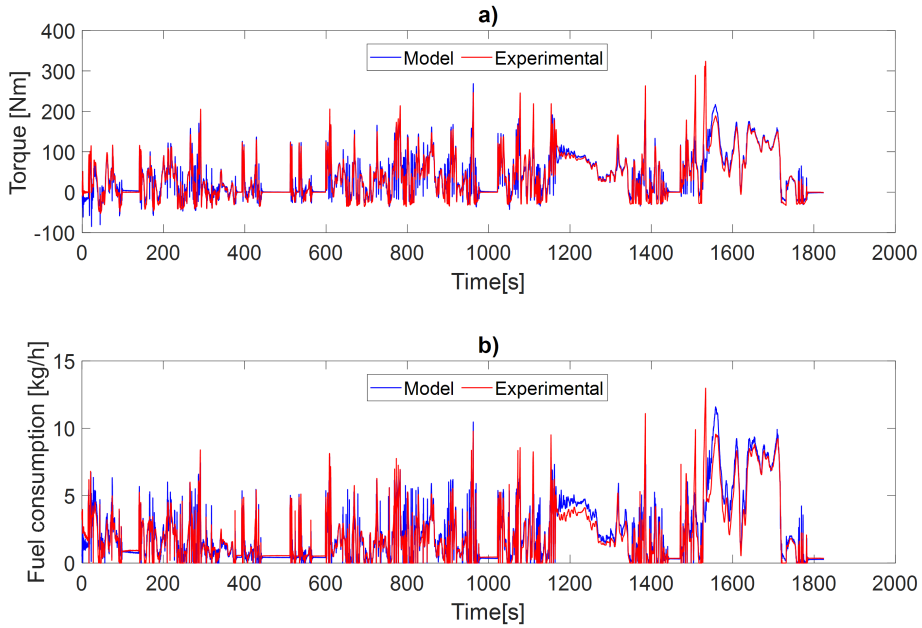

Figure 4.17: Engine performance validation in a WLTC cycle in cold conditions. a) Torque b) Fuel consumption

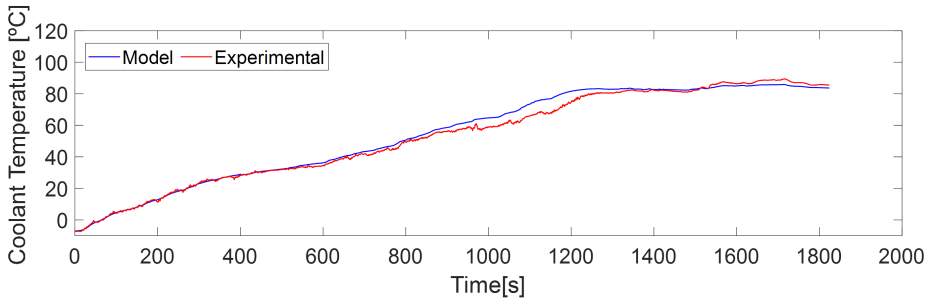

Figure 4.18: Coolant temperature validation during a WLTC cycle in cold conditions

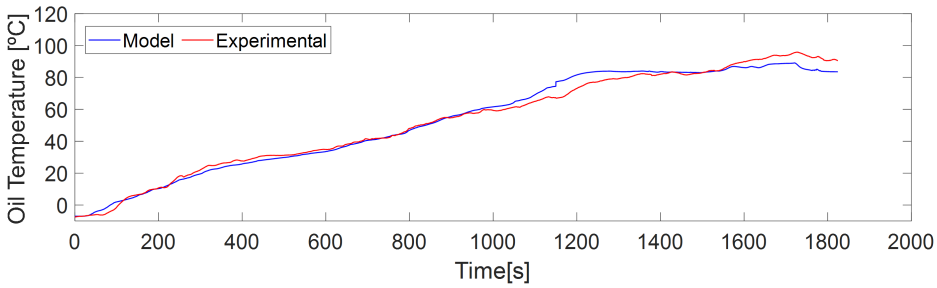

Figure 4.19: Oil temperature validation during a WLTC cycle in cold conditions

4.3 GASDYN and VEMOD submodels - FMI co-simulation

The Gasoline ICE engine was modelled in a virtual simulation platform used to simulate an hybrid powertrain used in a PHEV. For this, models constructed and calibrated in VEMOD and GASDYN simulation tools were co-simulated to develop the ICE digital twin. Therefore, the standarized FMI 2.0 was implemented to be able to exchange dynamic models between those modeling tools. With this method, the data is exchanged through discrete communication points (i.e., inputs/outputs) and are independently solved by their own solver. The synchronization between subsystems is carried out by the master simulation platform (MATLAB/Simulink).

The numerical code named GASDYN has been developed since 1996 at the Department of Energy of Politecnico di Milano. The model allows a 1D (one-dimensional) simulation of unsteady reacting flows in the intake and exhaust systems of internal combustion engines, both Otto and Diesel cycle, naturally aspirated or turbocharged, including the after-treatment systems and silencers. The GASDYN code has been continuously developed and integrated with innovative aspects by the IC Engine Research Group at the Department of Energy [152].

GASDYN software was reponsible for modeling and solving the thermfluid dynamics of the engine gas circuit while the VEMOD thermal sumbodels calculated the thermo-hydraulic phenomena taking place in the engine block, coolant and oil fluids. The inner surfaces of the in-cylinder walls were the interphase between both models.

4.3.1 Gasoline ICE Gas dynamic submodel

The internal combustion engine gas circuit is numerically described by the 1D thermo-fluid dynamic model of GASDYN code. The conservation equations of mass, energy, and momentum for an unsteady, ideal, compressible gas flow with friction and heat transfer at the pipe walls, are solved on a one-dimensional domain, representing the ducts, resorting to 0D submodels and boundary conditions to model pipe junctions, turbochargers, and cylinders. The CG-TVD, or Corberán-Gascón "total variation diminishing" formulation [153], numerical scheme is used for the solution of the conservation equations along the 1D pipe-system; this is an explicit, 2nd order numerical method, with a timestep determined

by the Courant-Friedrichs-Lewy (CFL) [154] condition which requires the timestep to be the minimum value of the Equation 4.10 applied to the whole domain considering the local mesh size Δx, speed of sound υ and gas velocity U.

$$\Delta t = \frac{\Delta x}{\upsilon + |U|} \tag{4.10}$$

The boundary conditions are instead assumed quasi-steady at each time step, solved by applying a characteristic-based approach. In particular, the compressor and turbine exploit a map-based approach. To decrease the computational effort required by the simulation of long RDE cycles, a 1D numerical solver called FSM (Fast Simulation Method) has been developed and applied, on the basis of the "1D Cell" numerical scheme [139]. This numerical method can provide a good mass conservation also on coarse meshes, allowing to increase the mesh size and the corresponding time step, hence significantly decreasing the simulation time, to reach a CPU/real time ratio around 2.0 – 2.5. The SI engine combustion process is modelled by a multi-zone approach, to evaluate the thermodynamic properties and chemical composition inside the combustion chamber. The in-cylinder mixture is first divided into two zones, unburnt and burned gas, separated by a flame front, which is assumed to be spherical and infinitesimally thin. The solution of mass and energy equations applied to the burned and unburned zones allows the computation of the pressure and temperature of the two zones. The burnt zone is then further divided into a certain number of zones of equal mass, created during the combustion process. Each zone is spherical, centred on the spark plug and exchanges heat with the cylinder walls, according to the respective surface area. Pressure in the combustion chamber is assumed constant and the chemical composition is computed in each zone. The solver exploits the Zimont's model to compute the turbulent flame velocity from the laminar velocity, taking account of the turbulence intensity generated in the combustion chamber [139].

The complete 1D model of the 1.0L, 3-cylinder GDI engine has been built, considering a detailed description of the whole intake and exhaust system layout. The maps of the turbocharger have been interpolated and extrapolated, to be suitable for use in the 1D model solver. The complete operating map of the GDI engine has been configured with information concerning for example the air-to-fuel ratio, spark advance timing, variable valve timing actuation, compressor boost pressure target and intercooler

efficiency. The corresponding 1D schematic is reported in Figure 4.20. The same model has been used to simulate steady state operating points of the engine map and transient RDE operation. In the 1D schematic the throttle body and the wastegate PID controllers are highlighted, used to control the target torque and boost pressure. The catalytic converter element is also present, to correctly predict the back pressure.

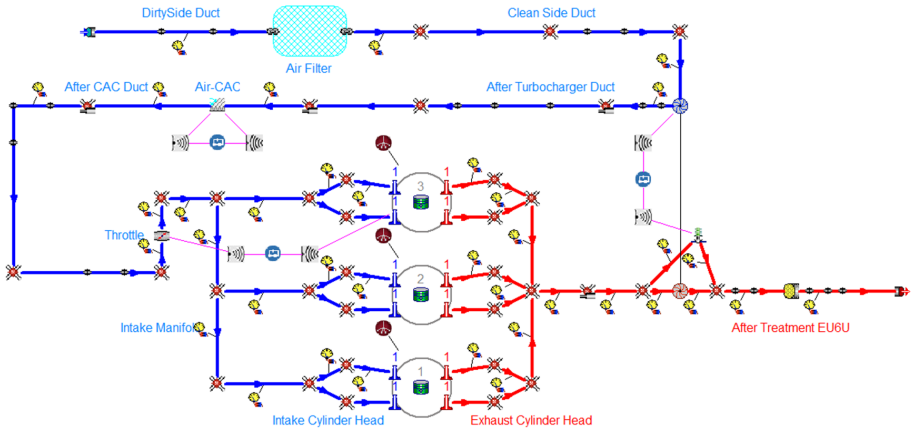

Figure 4.20: 1D ICE Thermo-Fluid Dynamic Model of the Gasoline ICE

4.3.2 Gasoline ICE Thermal submodel

This model was the responsible for calculating the temperature distribution in the cylinders of the Gasoline engine as well as the heat exchanged with the coolant and lubricant oil. Regarding its interaction with other submodels, it was interconnected with the thermo-fluid dyanamic model and the Thermohydraulic model. This model was developed so it could receive as an input the heat rejected from the in-cylinder gas to the material walls (liner, head and piston) which was calculated with the ICE Thermo-Fluid Dynamic Model (Section 4.3).

Although the discretization method and the number of nodes for the material were the same as for the Diesel engine, the geometry and the piston structure was modified according to the features of the Gasoline engine. This model is based on a 3D lumped thermal network approach and is composed by 111 material nodes strategically distributed. The cylinder liner, cylinder-head and piston were divided into 66, 35 and 10 nodes, respectively. Figure 4.21 shows the discretization of each part of

the engine cylinders. The multiple nodes were considered isothermal and isotropic. They were defined according to the geometry and characteristics of the engine given by the manufacturer. Each node had its volume, density, thermal capacity and conductivity. Additional to the material nodes, 6 fluid nodes were included in order to account for the heat rejected to the coolant and oil. Both inlet and outlet nodes of coolant thorough the liner (2 nodes) and cylinder-head (2 nodes) were implemented. Similarly, inlet and outlet nodes of oil were included. It is important to note that inlet nodes served as boundary conditions and were imposed by the values given by the thermohydraulic model (Section 4.3.3). In Figure 4.24, the integration of the ICE Lumped Thermal Model with the other submodels of the ICE is presented (where the main interaction among these models are shown).

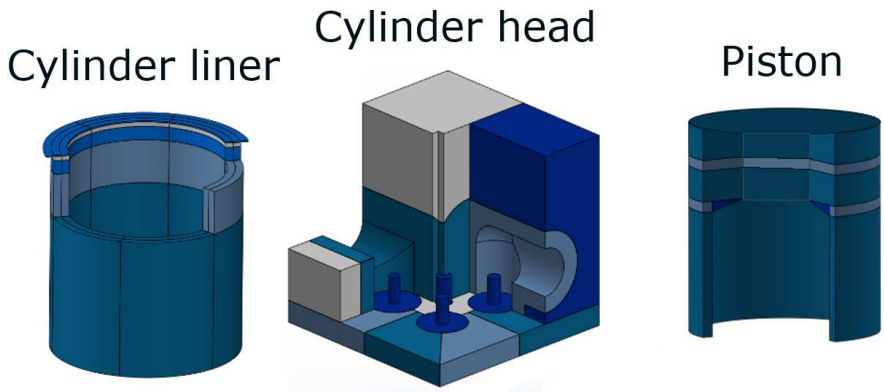

Figure 4.21: Gasoline ICE Lumped Thermal Model

The governing equations of the thermal model describing the Gasoline engine block were the same as those presented in the Section 4.2.2. The heat transfer mechanisms considered in the ICE thermal model were conduction (among the solid material nodes) and convection (between the material and the fluid) as it can be observed in the Equation 4.2 and Equation 4.3. These equations were obtained from performing and energy balance for each node. In order to increase the stability of the solver, an implicit numerical method for solving the equations was implemented. Furthermore, the equations were rearranged in a matrix array aiming to reduce the simulation time as it is seen in Equation 4.11.

$$[T_{t+\Delta t}]_{nx1} = ([K]_{nxn} - [C]_{nxn})^{-1} \left([T^{bc}]_{nx1} - [C]_{nxn}[T_t]_{nx1} \right) \quad (4.11)$$

Where n is the total number of nodes. $[T_{t+\Delta t}]_{nx1}$ is the array of nodes temperature for the next calculation step while $[T_t]_{nx1}$ is the vector of temperatures for the current time. $[K]_{nxn}$ and $[C]_{nxn}$ represent the thermal conductances and capacitances, respectively. $[T^{bc}]_{nx1}$ is the boundary condition array and consists of temperature or heat values of the nodes considered as boundary condition (i.e. coolant inlet temperature, oil inlet temperature or solid nodes in contact with the in-cylinder gas in which heat is generated). It is important to note that the boundary conditions are directly dependant on the integration of the submodel. In other words, the defined inputs of the submodel determined the number of nodes taken as a boundary condition.

4.3.3 Gasoline ICE Thermohydraulic submodel

The 0D/1D thermohydraulic model was responsible for calculating the temperatures, flows and pressures in the circuits of the different thermal management systems present in the propulsive system of an PHEV. The same source code was used for developing the different hydraulic circuits of the hybrid propulsive system. These include the TMS of the ICE, battery and EDS. Additionally, a thermohydraulic model was also developed for the lubricant circuit of the engine.

The thermo-hydraulic model is based on Equations 4.7, 4.8 and 4.12. Once the geometry and the layout of the circuits are interpreted by the model, its solver calculates the pressure and flows by applying the continuity and energy conservation laws for each closed loop of the circuit. Afterwards, in order to calculate the temperature distribution, the circuits is divided into several fluid volumes and the energy balance is performed according to the Equation 4.9 for each volume.

$$\frac{m_{fv}\, c_p}{\Delta t} \left(T_{t+\Delta t} - T_t\right) = K_{fa} \left(T_{amb} - T_{t+\Delta t}\right) + \dot{Q} \quad (4.12)$$

Where T_t is the current temperature of fluid volume, $T_{t+\Delta t}$ is the temperature of the fluid volume in the next time step, m_{fv} corresponds with the mass of the fluid volume and c_p is the fluid heat capacity. K_{fa} stands

for te equivalent heat conductance between fluid and ambient. This parameter accounts for the heat conductivity and convection processes. Finally, the T_{amb} is the ambient temperature while $\dot{Q}$ represents the heat exchanged with other submodels (i.e. heat rejected from the ICE to coolant).

The coolant and oil circuits of the engine were formed by several different elements. Figure 4.22 and Figure 4.23 show both the layout of the engine hydraulic circuits. For the coolant circuit, the geometry (i.e. length and diameter) was experimentally measured for the accessible pipes while for the oil, a simplification of the circuit was taken and only the main paths and components were implemented in the model according to the data provided from the manufacturer.

It is important to highlight that the coolant circuit used in the testbench was not exactly the same as the one implemented in the vehicle. For instance, the aerotherm was not installed in the testbench and was replaced by a pipe. The radiator was replaced by a controlled water/water heat exchanger of shell a and tubes in order to improve the control over coolant temperature. The lengths of some paths were slightly different because of the addition of the instrumentation (i.e. flow meters) in the circuit.

The main pump of the coolant circuit was characterised by its volume, speed ratio between pump and engine, head pressure and efficiency curves. The speed of this turbopump depended on the engine regime. According to the experimental data, the coefficients of the curve were calibrated. This component provides the necessary pressure and flow for the correct operation of the system. Additionally, the pipes were defined by their diameter, length and friction coefficient. The thermostat was modeled as a valve which creates a localized hydraulic resistance depending on the thermostat opening lift. Likewise, this opening lift is function of the coolant temperature as it was detailed in the [140]. The implementation ot the heat exchangers was performed for the engine cylinders, the turbocharger, radiator and the oil cooler. They were defined by their volume, type (i.e. shell and tubes) and hydraulic resistance coefficients. The heat flux calculated by the ICE Lumped Thermal Model is transferred to the coolant by means of this heat exchanger. For the case of the heat rejected by the turbocharger, the experimental heat luck up table (i.e. calculated using the flow and temperature difference) is used as input in the simulations. The oil cooler is a heat exchanger responsible of the thermal interaction between the coolant and the oil circuit. It also produces a pressure drop depending on the flow rate. The heat exchanged between both fluids (oil

and coolant) is calculated according to the NTU (Number Transferred Units) method. For the radiator, a heat exchanger with controlled outlet temperature was implemented as it was performed in the testbench.

According to Figure 4.22, five well-differentiated coolant branches are observed after the engine outlet. Through the thermostat to the radiator, across the bypass to the main pump, to the oil cooler, to the turbocharger or through the pipe replacing the aerotherm. These two last paths merge into the aerotherm branch as it can be seen in Figure 4.22. For the sake of clarity, two thermostats are shown in Figure 4.22. The one named thermostat represents the element in the path to the radiator while the bypass one, corresponds with the friction element situated in the coolant path when thermostat is closed.

The coolant flow in each branch is described as follows:

- Radiator and by-pass branch: This branch has two paths depending on the coolant temperature. The thermostat opening determines the amount of flow that circulates in each path according to the temperature of the coolant and ECU (Electronic Control Unit) signal. When the engine is cold, i.e. thermostat closed, the fluid will flow through the internal by-pass of the engine, a path that will take the fluid directly to the engine inlet. As the engine temperature increases and therefore thermostat starts to open, part of the flow will be derived to the radiator branch, where heat will be rejected to the environment. Finally, when thermostat is completely opened, coolant will not flow through the by-pass branch. Additionally, the radiator branch forms an additional loop with the expansion tank.

- Oil cooler branch: This branch contains the oil cooler, which is in charge of cooling the oil. The coolant is extracted from engine internal circuit and return to water pump inlet. This is the element connecting both coolant and oil circuit

- Aerotherm branch: The remaining branch of the circuit is the one that contains both the replaced aerotherm and the turbocharger. In this branch, the merging between the flow coming from the turbocharger and the one coming from the aerotherm (replaced by a pipe in the testbench as previously mentioned).

Similarly, the oil circuit is composed by the cylinder heat exchangers, turbocharger heat exchanger, and the oil cooler. Additionally, a positive

displacement pump was implemented as it can bee seen in Figure 4.23. The characterization process was similar to the one taken for the coolant circuit. The heat rejected by the cylinders (mainly by the piston) was calculated by the ICE Lumped Thermal Model.

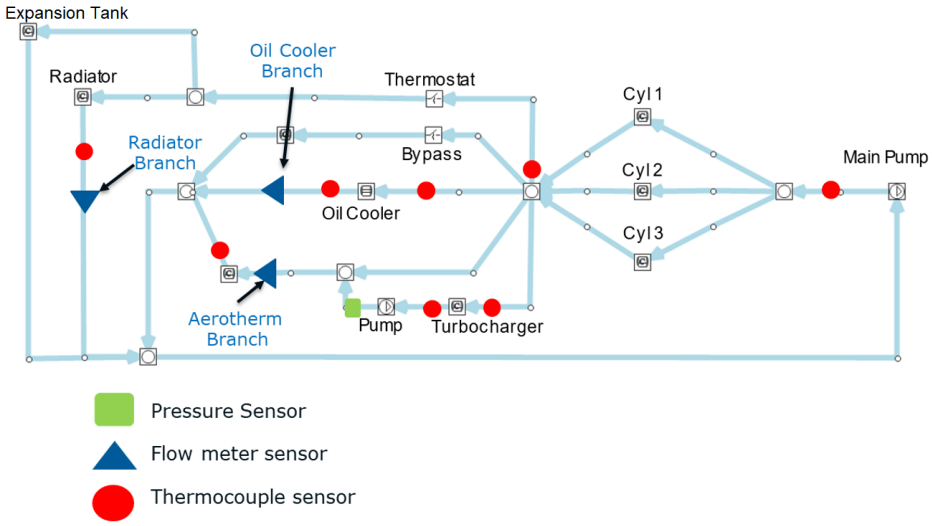

Figure 4.22: Gasoline ICE Coolant circuit layout

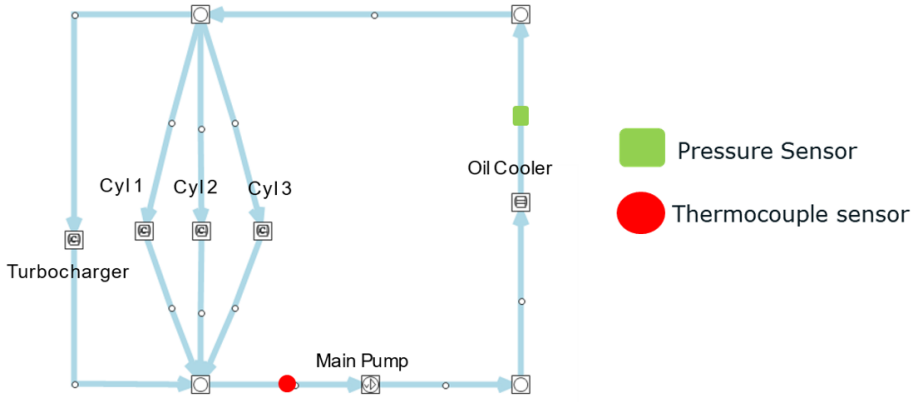

Figure 4.23: Gasoline ICE Oil circuit layout

The engine speed is a boundary condition of the ICE Thermohydraulic Model which will determine the speed of both coolant and oil pumps.

Additionally, the ambient temperature is needed as an input so the heat transfer with the ambient is taken into account. Finally, the heat rejected to coolant and oil are also a fundamental input to the model. Figure 4.24 presents the overall integration of the ICE models.

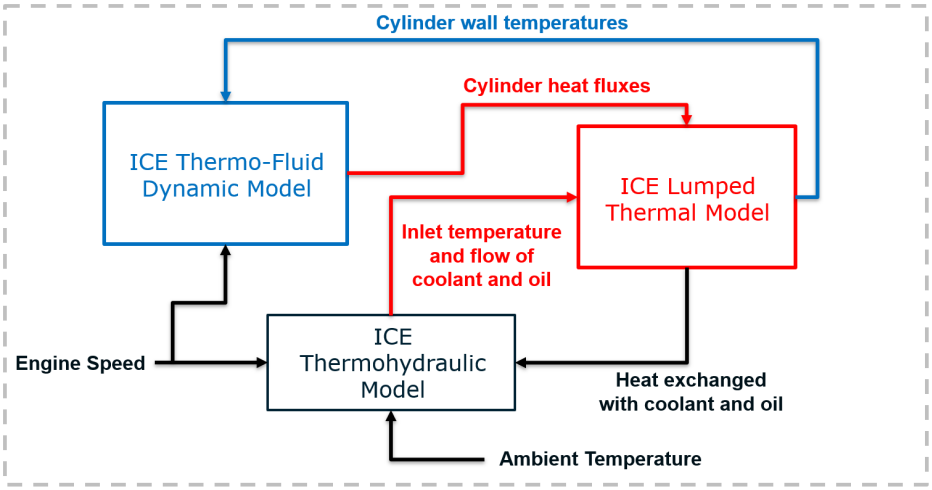

Figure 4.24: Integration of ICE Lumped Thermal Model, ICE Thermo-Fluid Dynamic Model and ICE Thermohydraulic Model.

4.3.4 Holistic validation of Gasoline ICE model

In this section, the validation of the Gasoline ICE submodels in both steady state and transient conditions is presented. For the transient validations, Real Driving Emission cycles were tested and simulated. These cycles considered engine starts and stops according to their real operation in a hybrid powertrain.

Steady state

In this section the validation of ICE submodels in steady state conditions are presented. For the thermohydraulic model, the validation process was performed in two steps. Firstly, the coolant flows were compared with the measurements followed by a fitting process in which the hydraulic resistances were adjusted. Secondly, the predicted temperatures were compared with the measurements performed in the testbench. In this case, both the thermo-hydraulic model and the engine model are needed to

accurately predict the heat rejected by different elements to the thermo-hydraulic model.

The Gasdyn 1D model has been validated on a steady state map of measured operating conditions. A general satisfactory agreement has been achieved. The measured brake mean effective pressure was well matched in all operating points, with a PID controller acting on the throttle opening, whereas the target boost pressure has always been reached by acting on the wastegate opening with a PID controller. Figure 4.25 shows the contour plots of the measured and computed brake specific fuel consumption for a direct comparison. The corresponding relative and absolute errors on the whole steady state engine map are presented as well. Overall, the agreement is good, with few regions characterized by a maximum error around 5%, showing a good quantitative and qualitative prediction level in general. This result is very important, allowing the use of the 1D engine model across non-mapped operating conditions during the simulation of RDE driving cycles, where the focus is on the evaluation of cumulative fuel consumption during transient operation.

In order to validate the coolant flows, additional measurements were required for modeling the behavior of the thermostat.

- First, measurements at different engine speeds with the thermostat closed were used to adjust the flows through the oil cooler and aerotherm branches. Figure 4.26 shows the predicted and measured volumetric flow rate versus engine speed of the coolant across the radiator, aerotherm and oil cooler branches for both open (Op. Th.) and closed thermostat (Cl.Th) positions.

- Afterwards, the measurements with thermostat completely open and closed were used to calibrate the coolant flow in radiator's branch and to determine the hydraulic resistance of the thermostat when thermostat is completely open.

- Finally, the full load operating points were used for calibrating partial openings of the thermostat. Figure 4.27 shows the results obtained for full load when only the opening degree was modified. The model seems to slightly over-predict the aerotherm flow at low speeds and slightly underestimate it for high speeds. For the case of the oil cooler, the model seems to slightly underestimate the flows for speeds higher than 3500 rpm.

The process followed for adjusting the thermostat allowed to capture both

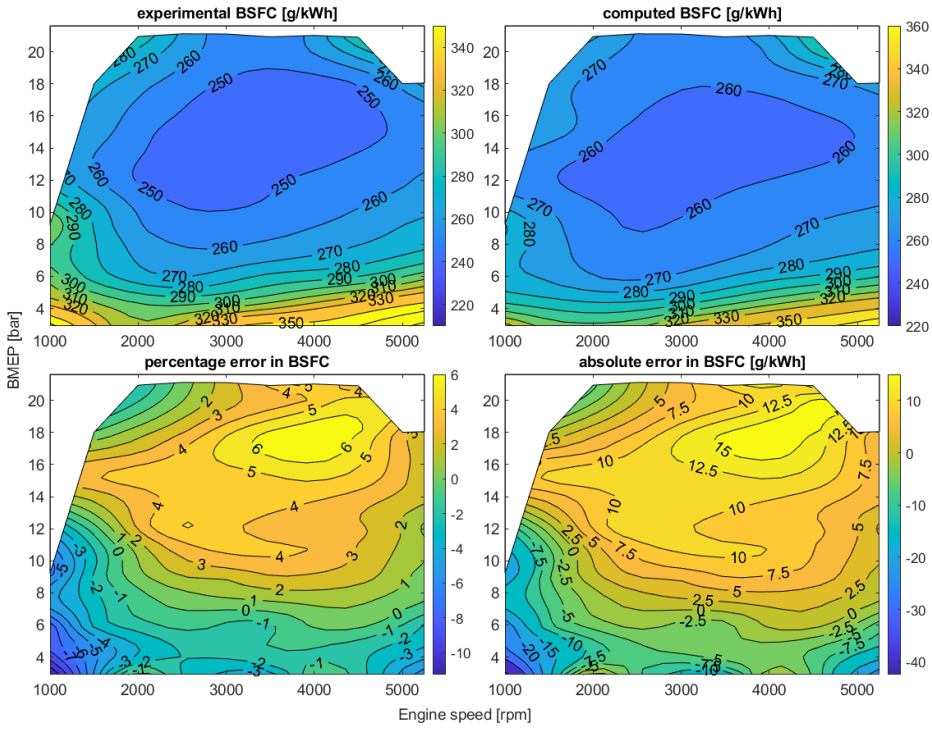

Figure 4.25: Experimental validation of ICE fuel consumption

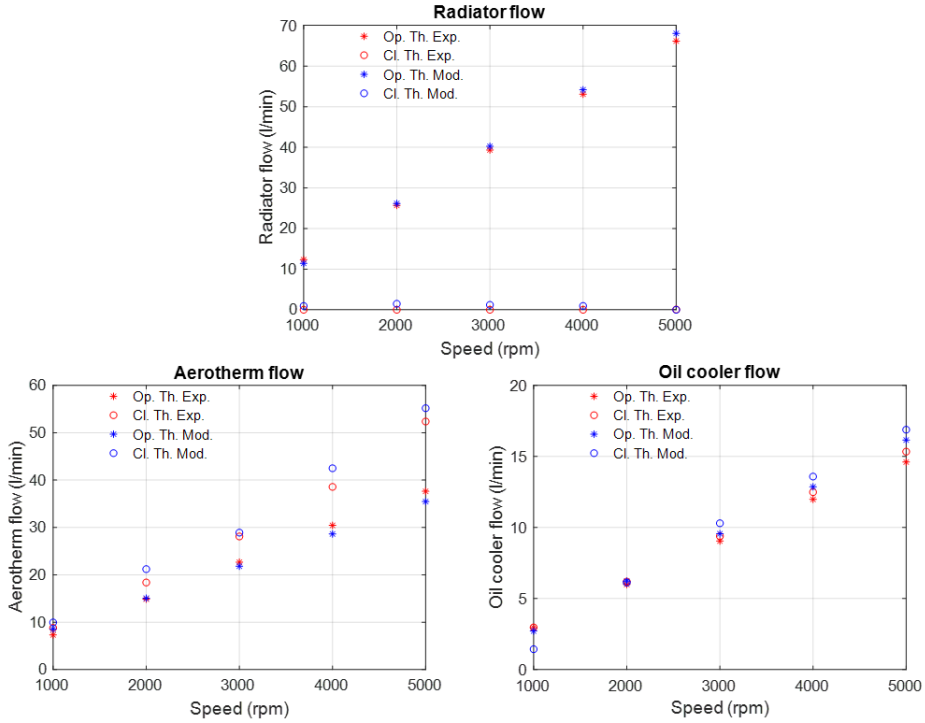

Figure 4.26: Validation of the additional coolant flow measurements with thermostat open (Op) and closed (Cl)

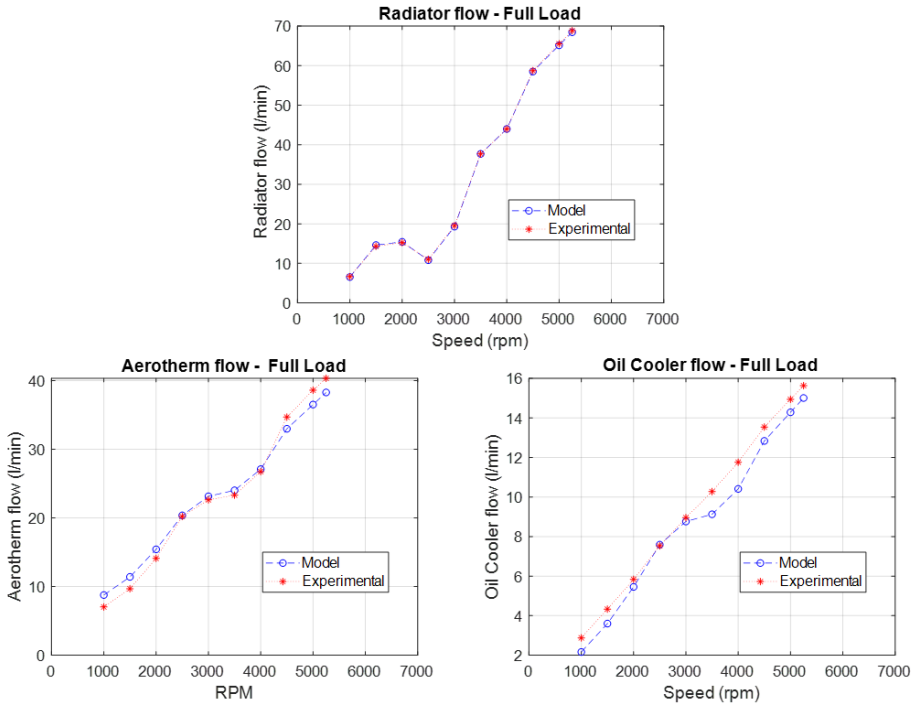

Figure 4.27: Validation of radiator, aerotherm and oil cooler flows for full load conditions

the maximum and the minimum values of the radiator flow (maximum and minimum opening degree).

The parameters modified for the fitting process were the friction of the pipes, the hydraulic resistance of the heat exchangers (radiator, oil cooler, cylinders, turbocharger) and the hydraulic resistance of the thermostat. Note that for the case of the thermostat, its hydraulic resistance depends on its opening degree, and this changes with the engine operating point according to the temperature of the coolant and the ECU signal. Once the adjustment process was finished, the validation of the three flows was performed for the rest of the engine map.

Figure 4.28 shows a comparison between model results and experimental measurements of radiator coolant flows, in all the map and with different thermostat openings. The contour plots show a good agreement between predictions and experimental data which indicates that hydraulic resistances in all the elements have been well estimated. The error in radiator flow prediction is less than ±3% except in one operating condition, at which reaches 6.5% at 2500 rpm and 12 BMEP.

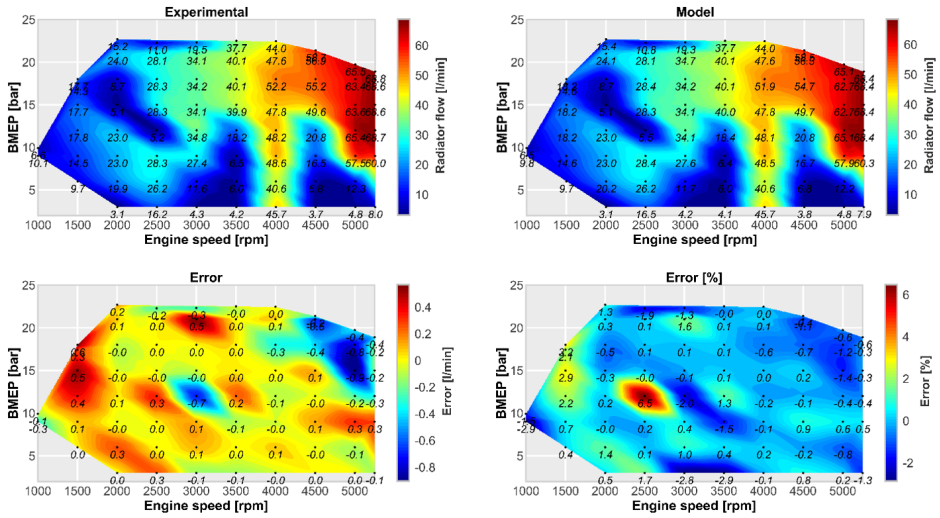

Figure 4.28: Radiator branch flow validation. Experimental (top left), Model (top right), Absolute error (bottom left) and Relative error (bottom right).

Overall, the model was considered to correctly predict the flows thorough the different branches in the coolant circuit for the whole engine map.

For the validation of the hydraulic circuits' temperatures the heat rejected by both the engine and the turbocharger are required. With this purpose, the heat rejected used as input for the model was estimated by using the experimental measurements.

Once the flows are validated, the thermal fitting mostly depend on the heat exchanged in the different heat exchangers implemented in the hydraulic circuits. In the coolant circuit, the radiator, the cylinders, the turbocharger and the oil cooler are the elements that dissipate heat to the coolant. In the oil circuit, the turbocharger, the oil cooler and the cylinders are the elements dissipate heat to the oil. Among all the heat exchangers, the radiator and the oil cooler efficiency were used for fitting the temperatures in the circuits. However, to adjust the temperature drop in the different components, the proper heat had to be supplied to the system.

The procedure followed for adjusting and validating the thermal state has the following steps:

- Validate the coolant temperature drop of the engine with the measured heat flow.
- Adjust the engine inlet coolant temperature by modifying the heat rejected by the radiator.
- Validate the oil temperature by adjusting the oil cooler efficiency.
- Refine the heat rejected by the radiator.
- Validate the temperatures of different locations of the coolant circuit.

The heat rejected by the cylinders for each operating point was estimated with the experimental data and used as input in the cylinders (emulated with heat exchangers) of the coolant circuit. The results obtained (see Figure 4.29) confirm that the model accurately predicts the coolant temperature drop in the engine.

Figures 4.30 and 4.31 show the comparison between the predicted and measured coolant temperatures at the inlet and outlet of the engine. The evaluation of the reliability of the model for predicting the oil temperature is presented in Figure 4.32. In both circuits, the observed errors were demonstrated the capability of the model.

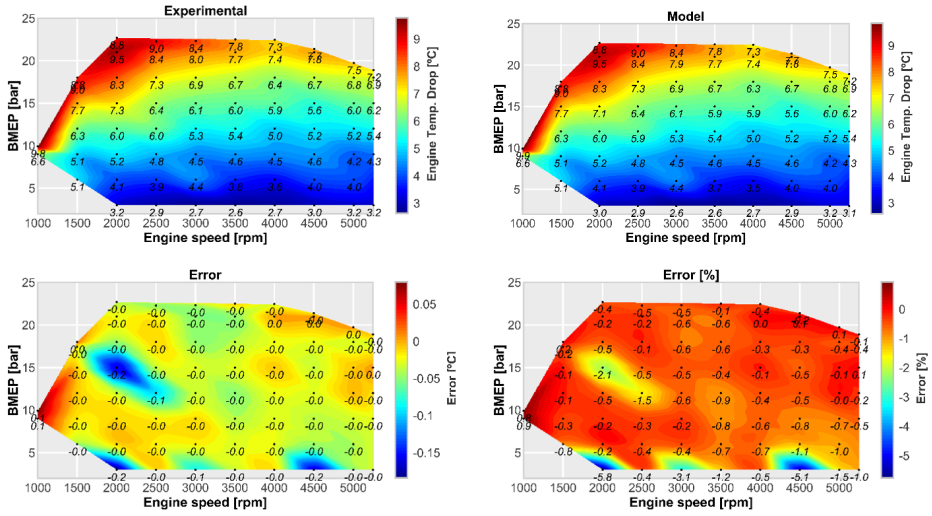

Figure 4.29: Engine temperature drop validation. Experimental (top left), Model (top right), Absolute error (bottom left) and Relative error (bottom right)

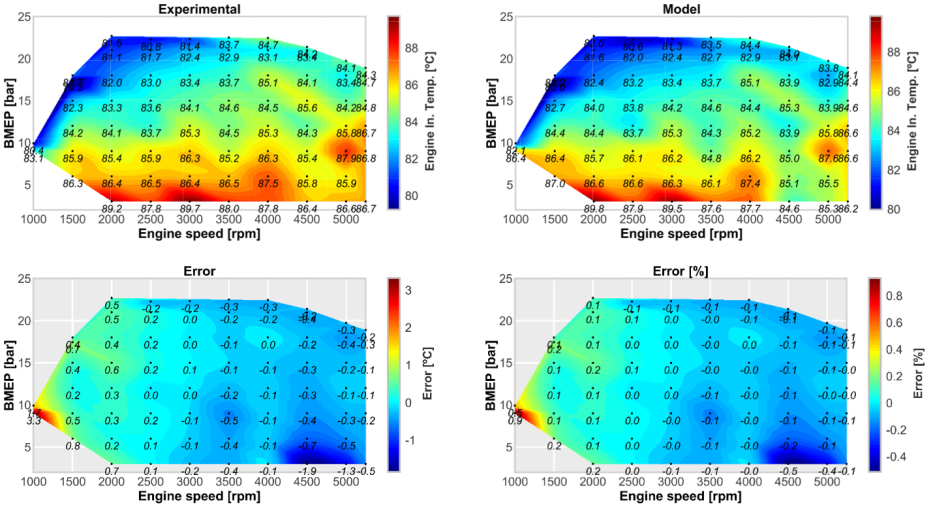

Figure 4.30: Engine inlet coolant temperature validation. Experimental (top left), Model (top right), Absolute error (bottom left) and Relative error (bottom right)

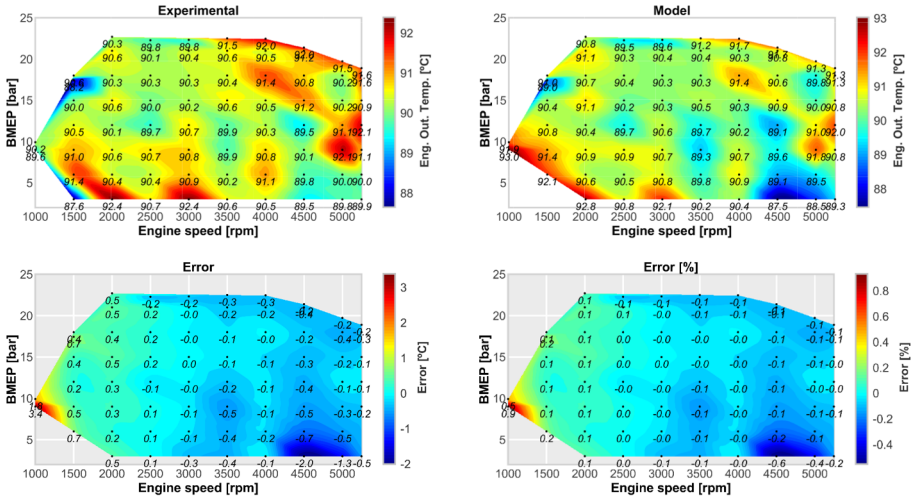

Figure 4.31: Engine outlet coolant temperature. Experimental (top left), Model (top right), Absolute error (bottom left) and Relative error (bottom right)

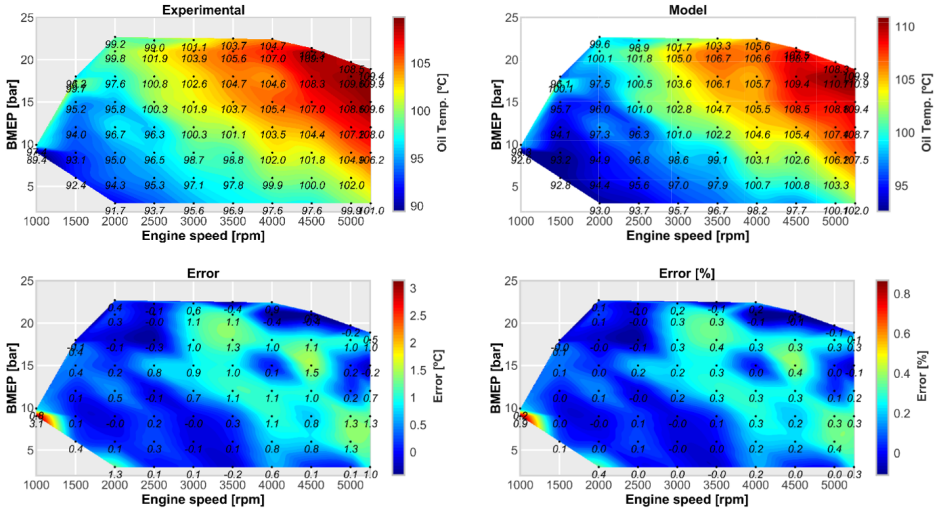

Figure 4.32: Oil temperature validation. Experimental (top left), Model (top right), Absolute error (bottom left) and Relative error (bottom right)

Transient conditions

To validate the coupling among the ICE main sub-models in transient conditions, three different RDE (Real Driving Emission) cycles were simulated [155]. These cycles were defined by the control model. The considered cycles are soft, medium, and high (aggressive) cycle depending on their acceleration aggressiveness as Figure 4.33 shows. The three cycles comply the limits established by the standards. The aggressive cycle is below the upper limit imposed by the 95 percentile of the product between velocity and positive acceleration while the soft cycle is above the lower limit of RPA (Relative Positive Acceleration) at urban, rural and motorway driving conditions. These cycles were defined using a drive cycle generator developed in the work presented in reference [155]. This generator has been developed to synthesize cycles complying all the regulatory requirements of the real drive emission testing.

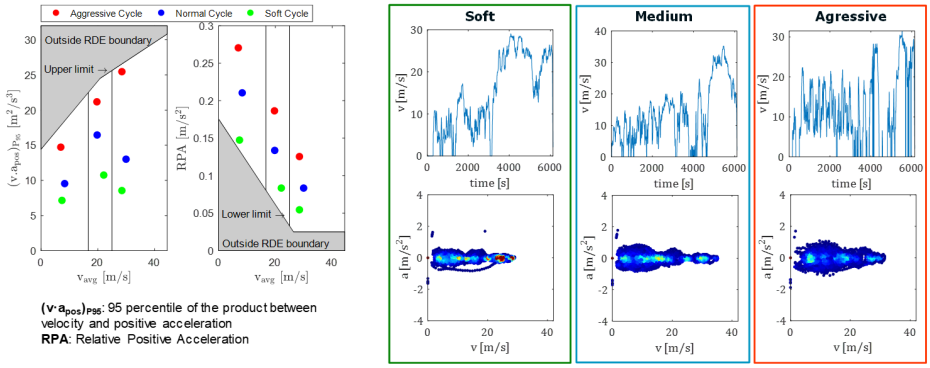

Figure 4.33: Soft, Medium, and High RDE cycles

During transient simulations, the same 1D engine model is run, changing the engine speed and torque requested cycle-by-cycle. The engine speed is imposed to the model, while the torque request is targeted with an internal PID controller. All the information regarding the engine operating parameters, such as spark advance, valve timing and target boost pressure are interpolated according to the engine speed/torque map introduced in the steady state model. This approach allows to include a fully physical transient model of the GDI engine in the vehicle simulation.

Figure 4.34 shows the comparison between predicted by the model (coupling of ICE Lumped Thermal Model, ICE Thermo-Fluid Dynamic Model and ICE Thermohydraulic Model) and measured engine speed and

torque evolution of ICE during the three different RDE cycles defined before. The very good concordance between these two engine parameters is remarkable for the three cycles.

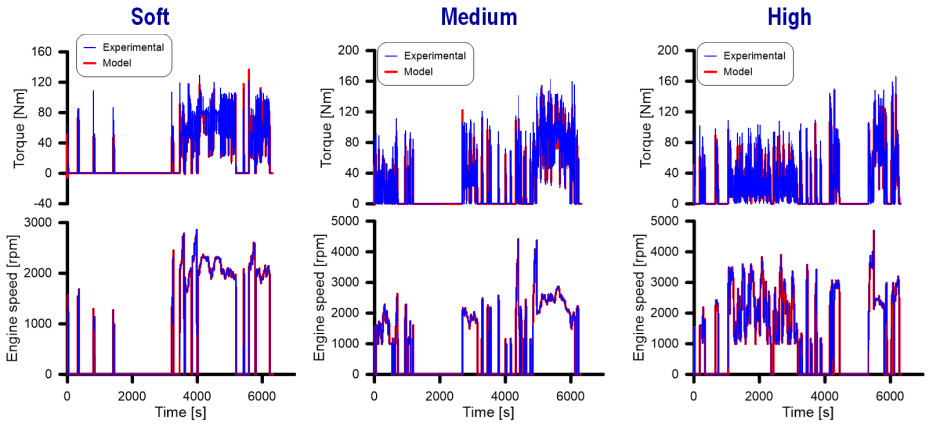

Figure 4.34: Validation results for engine performance for RDE cycles

Figure 4.35 shows the comparison between the measured and calculated coolant temperature at the inlet of the engine. In general, a good collapse of these results can be observed for the three cycles. Although the coolant temperature shows some discrepancy between 1000 s and 2800 s in the medium RDE cycle, the overall accuracy can be considered acceptable since the temperature rise and drop during starts and stops of the engine were correctly predicted by the model during all cycles. The comparison between the measured and predicted volumetric flow rate of the coolant through the oil cooler branch is presented in Figure 4.36. These results show the remarkable capacity of the co-simulation tool to predict the coolant flow evolution at RDE cycles operation.

In Figure 4.37 the oil temperature evolution is presented for the RDE cycles. In the soft cycle, it is observed that the model slightly overestimates the temperature during the first 1200s. Additionally, after 5750s the model underestimates the temperature because the coolant temperature is also underestimated by the model in that period. The same behaviour is observed for the last part of the medium cycle. Overall, the model was considered able to predict the trend of the oil temperature with good accuracy.

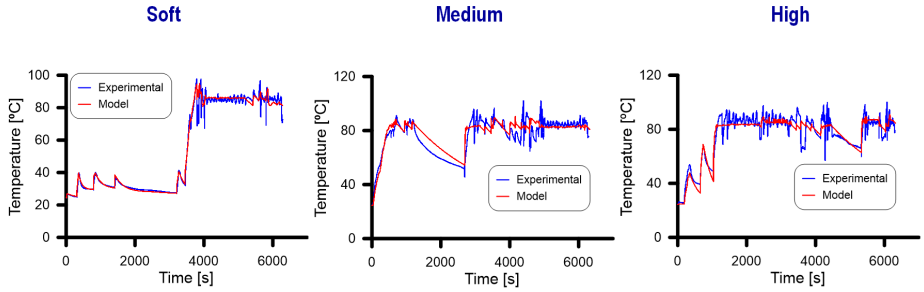

Figure 4.35: Validation of coolant engine inlet temperature in RDE cycles

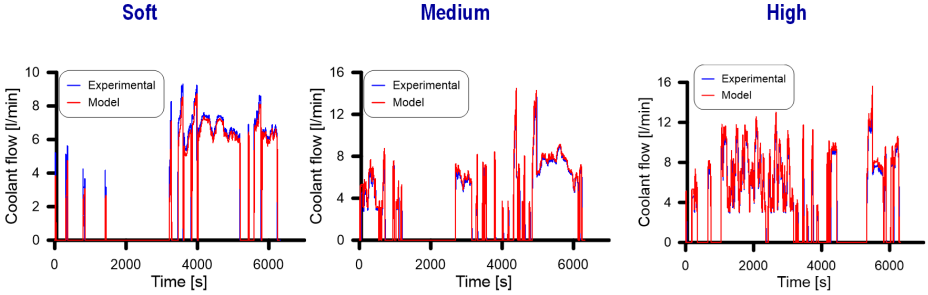

Figure 4.36: Validation of oil cooler coolant flow in RDE cycles

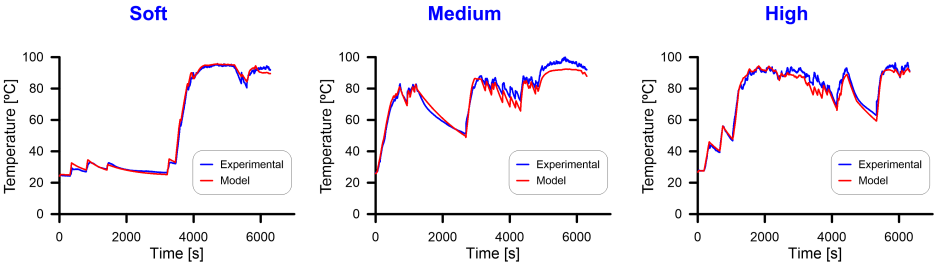

Figure 4.37: Validation of oil Temperature in the RDE cycles

4.4 Battery Model

The battery model was divided into three different submodels: the electric, thermal and thermo-hydraulic model. The power supplied and required by the battery is determined by the strategy established by the control model(i.e., energy management system) of the vehicle during the cycle. This power is the main input to the electric model of the battery which calculates the heat generated by the battery. Then, the thermal model used that heat power to solve the temperature distributions of the cells and predict the heat rejected to the coolant. For this, the coolant temperature and flow are required from the thermo-hydraulic model of the battery. Figure 4.38 shows a scheme of the main communication between battery submodels.

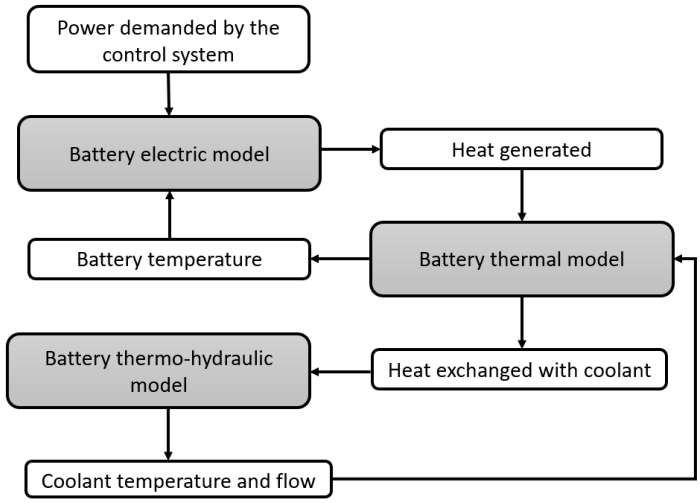

Figure 4.38: Main interaction between battery submodels

4.4.1 Battery electric model

The electrical power demanded from the battery could either be positive or negative depending on the current direction (i.e., current flowing from the inverter of the EDS to the battery or vice-versa). Positive in case of charge and negative otherwise was the criteria taken for the present work. In both cases, the cell current and voltage limits are considered in the model according to the indications provided by the cell data sheet.

The number of cells and their electrical connection among each other are taken as input parameters of the battery model. The model assumes that the battery pack is electrically equilibrated and has an ideal battery management systems capable of maintaining the same SOC in every cell. The power demanded or supplied to the battery ($P_{battdem}(t)$) is divided by the voltage of the battery ($V_{batt}(t - \Delta t)$) in the previous time step (Δt) and the number of cells connected in parallel ($I_{celldem}(t)$) in order to calculate the demanded cell current according to Equation 4.13.

$$I_{celldem}(t) = \frac{P_{battdem}(t)}{V_{batt(t-\Delta t)} N_{par}} \tag{4.13}$$

If the demanded cell current is higher than the limits given by the manufacturer, it is limited to the maximum value allowed. This limit is different for charging and discharging. This current is the main input to the battery cell equivalent circuit electric model (ECEM) of the battery. This first order RC circuit is responsible for calculating the voltage across the terminals of the cell. Figure 4.39 presents the scheme of the solved electric circuit.

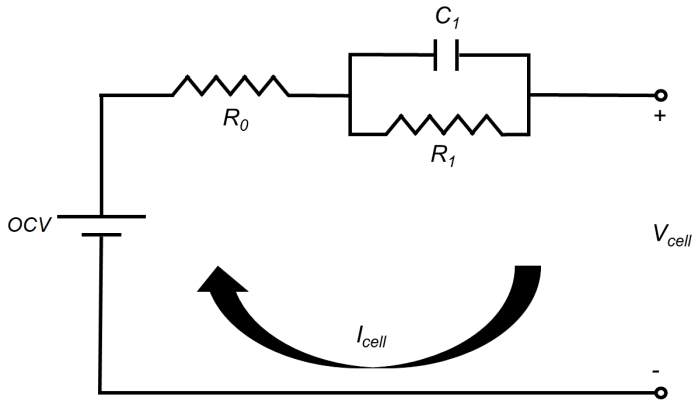

Figure 4.39: First order ECEM of the battery cells

Where I_{cell} is the cell electric current, OCV is the open circuit voltage and V_{cell} is the cell voltage. The parameters R_0, R_1 and C_1 are the internal ohmic resistance, the polarization resistance and the polarization capacitance, respectively. These parameters depend on SOC, C-rate and temperature of the cell and were obtained using the data from the experimental measurements detailed in Chapter 3. In order to solve the circuit,

Equations 4.14 and 4.15 were implemented.

$$\frac{dV_c}{dt} = \frac{1}{C_1(C-rate, SOC, T)}(I_{cell} - \frac{V_c}{R_1(C-rate, SOC, T)}) \tag{4.14}$$

$$V_{celldem}(t) = OCV(SOC)(t) - I_{cell}(t)R_0(C-rate, SOC, T)(t) - V_c(t) \tag{4.15}$$

Similarly, if the calculated $V_{celldem}$ is outside the upper and lower cell voltage limits, this variable is set to the limit and a new cell current is calculated with the Equations 4.16 and 4.17.

$$I_{cell}(t) = \frac{OCV(SOC(t)) - V_{cell}(t) - V_c(t)}{R_0} \tag{4.16}$$

$$V_c(t) = \int \frac{OCV(t) - V_{cell}(t) - (\frac{R_1+R_0}{R_1})V_c(t)}{C_1R_0})dt \tag{4.17}$$

To adequately estimate the open circuit voltage of the cell, the state of charge (SOC) is calculated for each time step according to Equation 4.18. This take as main input the previously calculated cell current. It is important to state that the SOC depends on the cell capacity ($Cap(T)$) which is affected by the cell temperature (T).

$$SOC(t) = SOC(t-\Delta t) - \frac{1}{Cap(T)}\int_{t-\Delta t}^{t} I_{cell}(t)dt \tag{4.18}$$

Finally, the heat generated in the cell ($\dot{Q}_{cell}$) is calculated according to the Equation 4.19. The first term of the right hand of the equation represents the irreversible heat generated due to Joule effect while the second term describes the reversible entropic processes. Afterwards, this heat power is multiplied by the total number of cells to calculate the total heat power rejected by the battery pack to the cooling system. Figure 4.40 presents the workflow of the battery electric submodel.

$$\dot{Q}_{cell} = I_{cell} \cdot (OCV - V_{cell}) + I \cdot T\frac{\partial OCV}{\partial T} \tag{4.19}$$

Custom algorithms were developed in order to extract the parameters from all pulses results automatically based on the Equation 4.14 and 4.15. Figure 4.41 present the open circuit voltage curves of both cylindrical (N1) and prismatic (N2) cells. Additionally, Figure 4.42 and Figure 4.43 present

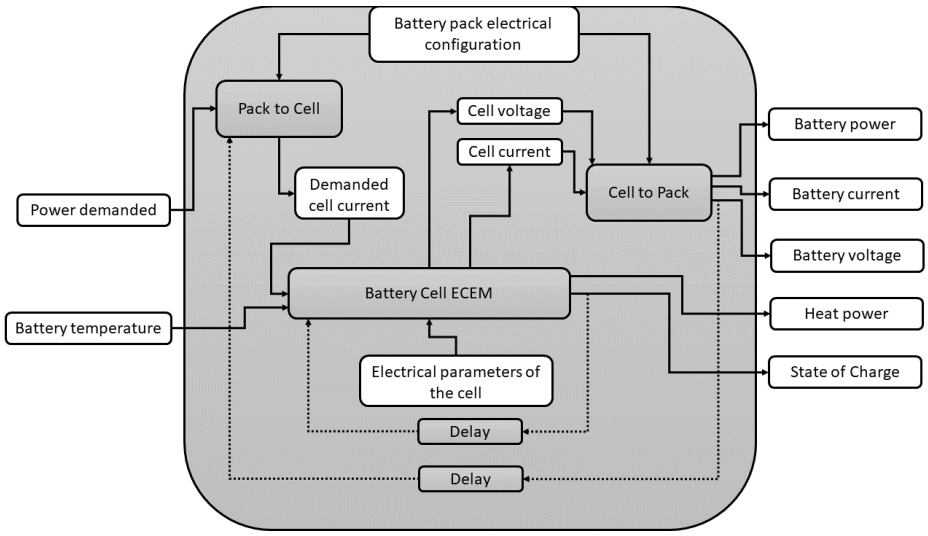

Figure 4.40: Algorithm for the electric submodel of the battery

the final parametrization results for the cylindrical and prismatic cells, respectively. All these parameters were extracted from the experimental characterization tests. The parameters showed in the plots correspond with the tests performed at 20°C.

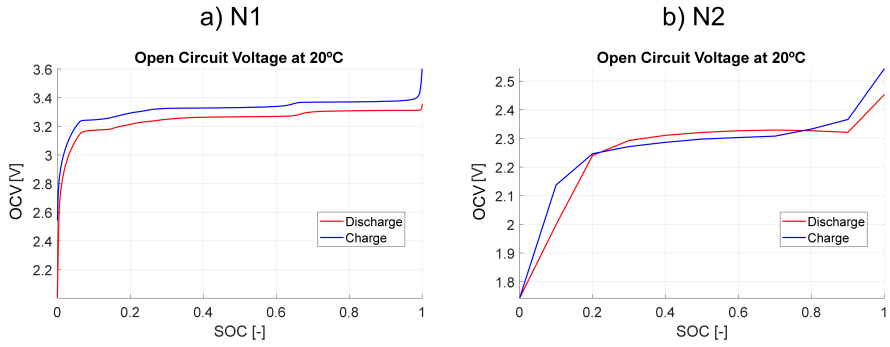

Figure 4.41: Open circuit voltage curve at 20°C

4.4.2 Battery thermal model

The thermal model of the battery used the heat generated in the cells to calculate the temperature distribution of the cells. This model consisted

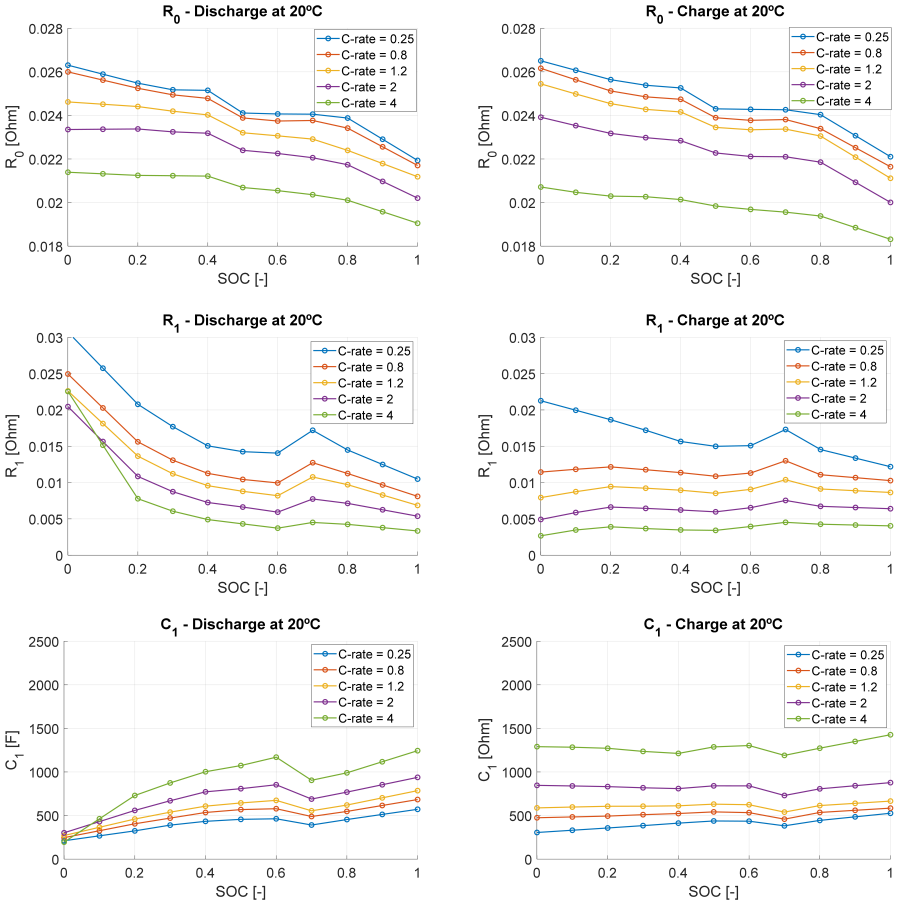

Figure 4.42: ECEM parameters identification for the cylindrical battery cell at 20°C

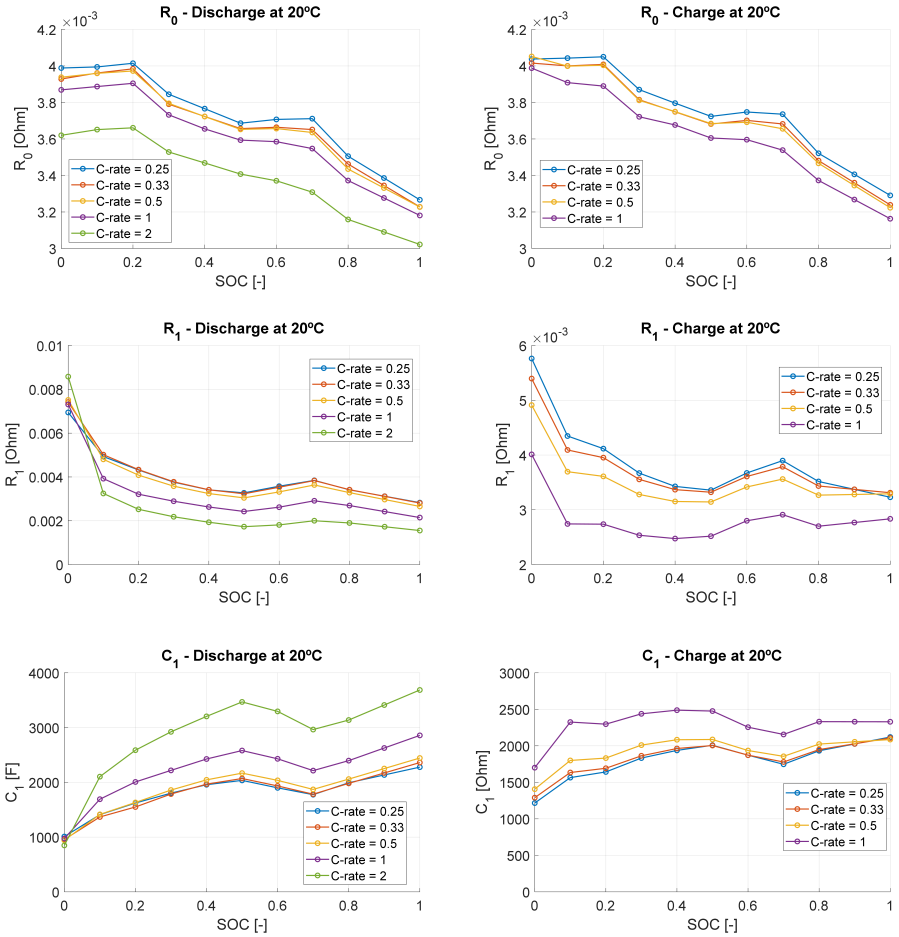

Figure 4.43: ECEM parameters identification for the prismatic battery cell at 20°C

in a lumped thermal and was based on the previously described Equation 4.11. The nodes were assumed isotropic and isothermal. Both cylindrical and prismatic cells were implemented in the model and was automatized to select one or the other to build the battery pack. The first was meshed into 5 nodes while the second was discretized into 11 nodes. Figure 4.44 shows a scheme of the heat flux path in both cylindrical and prismatic cells. On one hand, the cylindrical cell was divided into the superficial node, both terminals and core node. An additional fluid node for the surrounding fluid was also included. On the other hand, 6 superficial nodes, 2 nodes for the positive and negative terminals, and 1 core node were implemented for the prismatic cell. For the boundary conditions two additional nodes for the coolant and air were included.

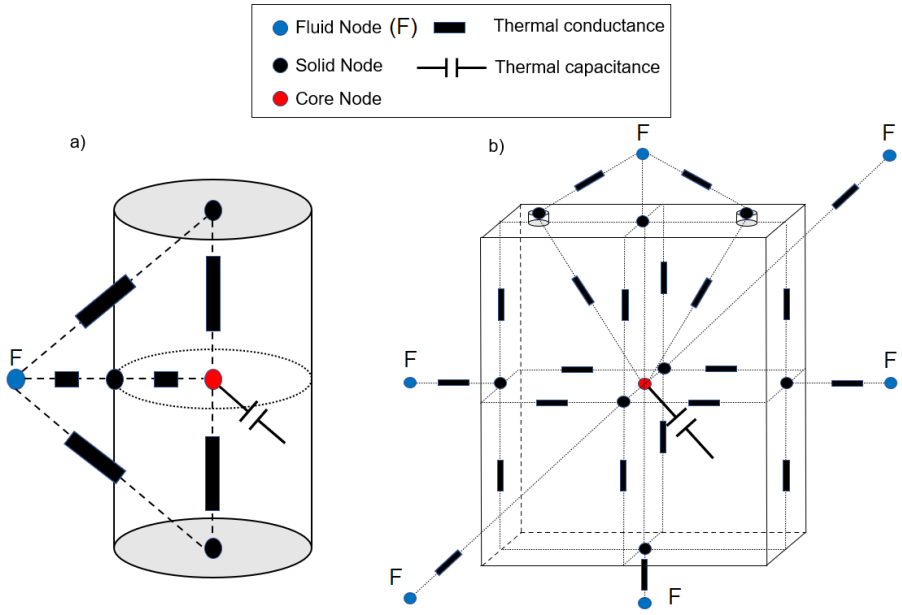

Figure 4.44: Lumped thermal model of cylindrical (a) and prismatic (b) cells

The manufacturing process has a great impact on the thermal conductance in the cells. Normally, the electrode stack of the battery cells follow a jelly rolls geometric arrangement. The core of a cell battery is constructed of several cell electrode assemblies. Hence, the cell is formed by different layers with different physical properties properties. Each electrode assembly includes a negative electrode, two separator sheets, and a

positive electrode. The electrodes include active materials coated on both sides of current collector foils. Various active materials can be applied on electrodes depending on the chemistry of the Li-ion cell. All layers, except current collectors, are porous and are soaked in a concentrated electrolyte liquid. The in-plane overall thermal conductivity exceeds the perpendicular thermal conductivity by about one magnitude due to the current collector's high thermal conductivity. The radial direction is limited by the low thermal conductivity of the electrolyte soaked separator. For instance, in the cylindrical cell the axial (or parallel) conductivity is two orders of magnitude higher than the thermal conductivity in radial direction (or series). In order to obtain the thermal conductance between solid nodes, the geometry of the cell and the thermal properties were considered. The thermal properties were obtained from literature according to the data given in [156] and [157]. The heat generated in the core of the cell is conducted through the solid until the surface and terminals. Then, convective heat transfer takes place between the terminals and the environment (i.e., air and coolant). Table 4.2 presents the thermal properties implemented in the model.

Table 4.2: Battery cell thermal properties

Cylindrical			
Zone	**Density** (kg/m^3)	**Thermal capacity** ($J/kg \cdot K$)	**Thermal conductivity**($W/m \cdot K$)**: Parallel @ Series**
Positive tab	2719	871	202
Negative tab	8978	381	387.6
Core	2047	825	32 @ 0.2
Prismatic			
Zone	**Density** (kg/m^3)	**Thermal capacity** ($J/kg \cdot K$)	**Thermal conductivity**($W/m \cdot K$)**: Parallel @ Series**
Positive tab	2719	871	202
Negative tab	8978	381	387.6
Core	2092	678	18.2 @ 0.735

For calculating the convection heat transefer phonomena a modified version of the Dittus Boelter equation for completly developed flux (See Equation 4.20) was implemented for surface-coolant thermal conductances. For the heat transfer with the ambient a constant natural convection coefficient of 5 W/m^2K was considered.

$$Nu = a \cdot 0.023 \cdot Re^{0.8} \cdot Pr^{0.3} \tag{4.20}$$

where Nu, Re, and Pr are the Nusselt, Reynolds and Prandlt numbers, respectively. a is a correction factor used for calibration.

4.4.3 Battery thermo-hydraulic model

The battery pack used for the studies of these work was constructed by 144 prismatic 23 Ah LTO battery cells (N2). The cell characteristics are summarized in Table 3.8.

The battery pack was divided into 12 modules of 12 cells each one. The thermal management system (TMS) defined for cooling the cells was based on an indirect cooling through the cell base using a cooling plate. This TMS was divided into 6 paths of coolant running under the battery modules (see Figure 8). Additionally, computational fluid dynamic (CFD) results obtained from previous work were used to calculate the pressure drop across the battery thermal management system [158]. Figure 4.45 shows the velocities and the coolant paths through the TMS. First, calculations at different coolant flows (from 0.5 kg/s to 2.5 kg/s) were performed. Then, the obtained pressure drop for each coolant flow was used to determine the hydraulic resistance coefficient according to Equation 4.21.

$$\Delta P = K\dot{m}^2 \tag{4.21}$$

Where ΔP is the total pressure drop, K is the hydraulic resistance coefficient and $dotm$ is the mass flow rate.

Figure 4.63 (left) shows the scheme of the battery thermal management system (BTMS). This BTMS was constructed using a main heat exchanger (named Battery in Figure 4.63) which will be responsible to dissipate the heat rejected by the battery pack to the coolant. The selected coolant was based on a mix of Glycol (50%) and water. This heat power is calculated by using the ECEM approach as it was previously stated. Additionally, the BTMS also includes a pump, a cooler/heater, a thermostat which starts opening when the coolant temperature at the outlet of the battery reaches 30°C and different pipes to connect the elements. The coolant flow propelled by the pump was set constant and calculated considering the maximum heat rejected by the battery pack in the complete cycle and a maximum temperature drop across the BTMS of 2°C. According to the literature, one of the objective of the BTMS is to decrease the temperature gradient through the battery pack. Hence, decreasing this temperature drop will directly impact the temperature gradients among the cells.

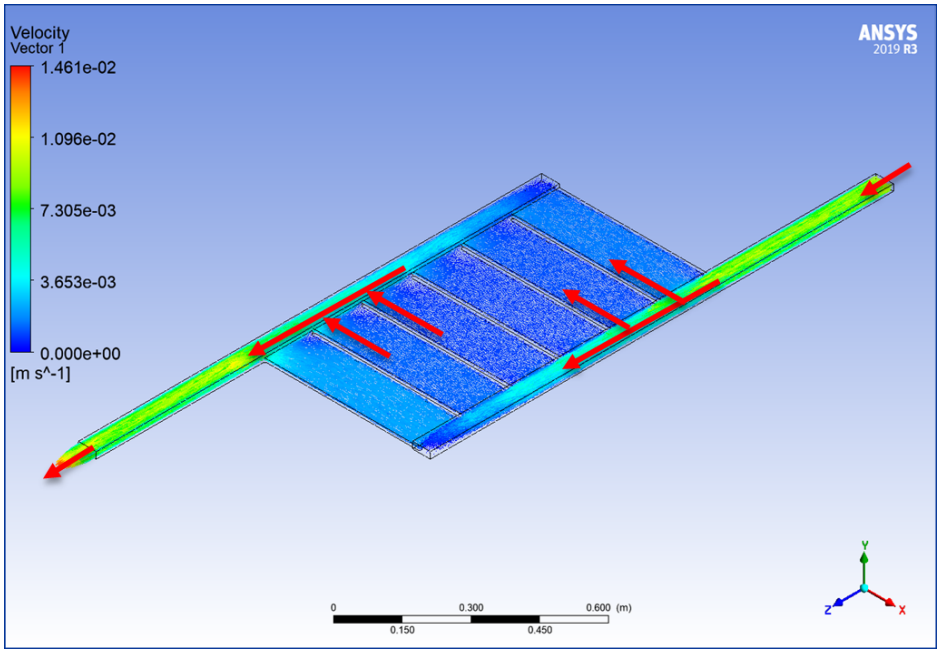

Figure 4.45: Coolant path of Battery TMS (CFD)

4.4.4 Validation of Battery model

In order to validate the battery model, transient cycles with dynamic behaviour were experimental tested in the testbench and simulated. A current demand profile was imposed as input and the terminal voltage of the cell was measured and compared to simulation. Similarly, with the surface temperature of the cells.

Figure 4.46 presents the terminal voltage of the cylindrical cell (N1) and its surface temperature during the cycle. It can be observed that the model accurately predicts the voltage and temperature of the cell. Overall, the relative mean errors obtained for the voltage and surface temperature were 1.05 % and 1.4 %, respectively.

Figure 4.47 presents the cell voltage evolution and the surface temperature evolution during a transient cycle for the prismatic cell (N2). It can be observed that the electric model of the battery is capable to follow the dynamic variations of the electric variables. When the battery is discharged the voltage of the cell decreases and increases when the battery is charged. As it was stated previously, the importance of estimating properly the electric parameters is fundamental to calculate the heat gen-

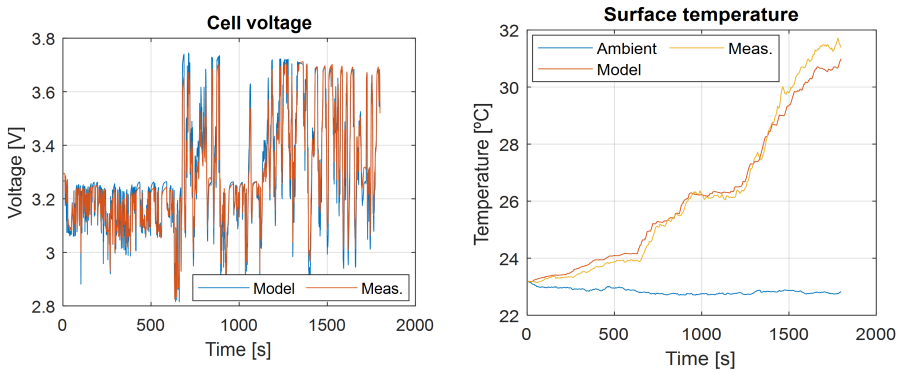

Figure 4.46: Electric (left plot) and thermal validation (right plot) of the cylindrical cell (N1) during dynamic cycle

erated in the cells of the battery. Consequently, the temperature of the cells increases as it is seen in the left plot of the 4.47. The model is also accurately predicting the temperature evolution of the cell. Overall, the mean relative error obtained the voltage and the temperature were 0.7 % and 0.3 % respectively.

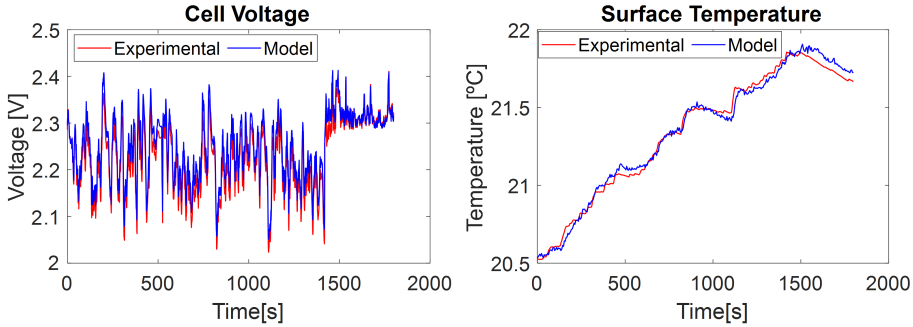

Figure 4.47: Electric (left plot) and thermal validation (right plot) of the prismatic cell (N2) during dynamic cycle

4.5 Electric Drive System

The electric drive system (EDS) consists in two main subcomponents: the electric machine (EM) and the inverter. The EM modelled in this work consisted in a permanent magnet synchronous machine with water

cooling through the stator and oil cooling through the rotor and stator. The inverter mainly consisted in power modules which were formed by electronic chips (i.e., transistors and diodes).

In order to predict the temperatures and calculate the heat rejected to the thermal management system (i.e., cooling circuits) of the electric drive, a thermal model was developed for each device. Both models were based on the Equation 4.11.

4.5.1 Heat losses of the EM

In order to account for the heat losses produced in the EM, an in-house software was implemented in MATLAB to calculate the losses in the windings by means of the phase voltage and current, speed, torque measured in the testbench. Similarly, the friction losses were obtained. For calculating the losses in the iron core and magnets, the machine was modelled with the commercial software ALTAIR FLUX and the corresponding iron losses maps were obtained for steady state operating conditions.

Figure 4.48 shows the power losses distribution in the main components of the EM at a certain oil temperature and voltage. It is important to note that the losses presented in the figure correspond with the EM working as motor mode. Furthermore, due to confidentiality reasons, torque, speed and power loss have been normalized. The EM maximum values of torque, speed and power were used for normalization. It can be observed that for the friction losses in the bearings as well as the friction with the air/oil mainly depend on the EM speed. However, the copper losses depend on both the speed and torque. Finally, it is important to highlight that the copper losses are the most significant source of EM inefficiency while the losses in the magnets were the less significant. When comparing Figure 4.48 and Figure 4.49 it can be seen that the impact of temperature in the EM efficiency. For instance, at low speed and high torque (operating conditions with high losses in the stator windings), the losses at high temperature were twice as much as those of low temperature. This is because the temperature on the windings directly impacts their electric resistance. Hence, the more temperature on the windings, the more electric resistance producing more power losses in the windings.

4.5.2 Electric machine thermal model

The model was based in a lumped thermal model of 18 nodes. For the structural parts of the machine, 12 nodes were selected according to tem-

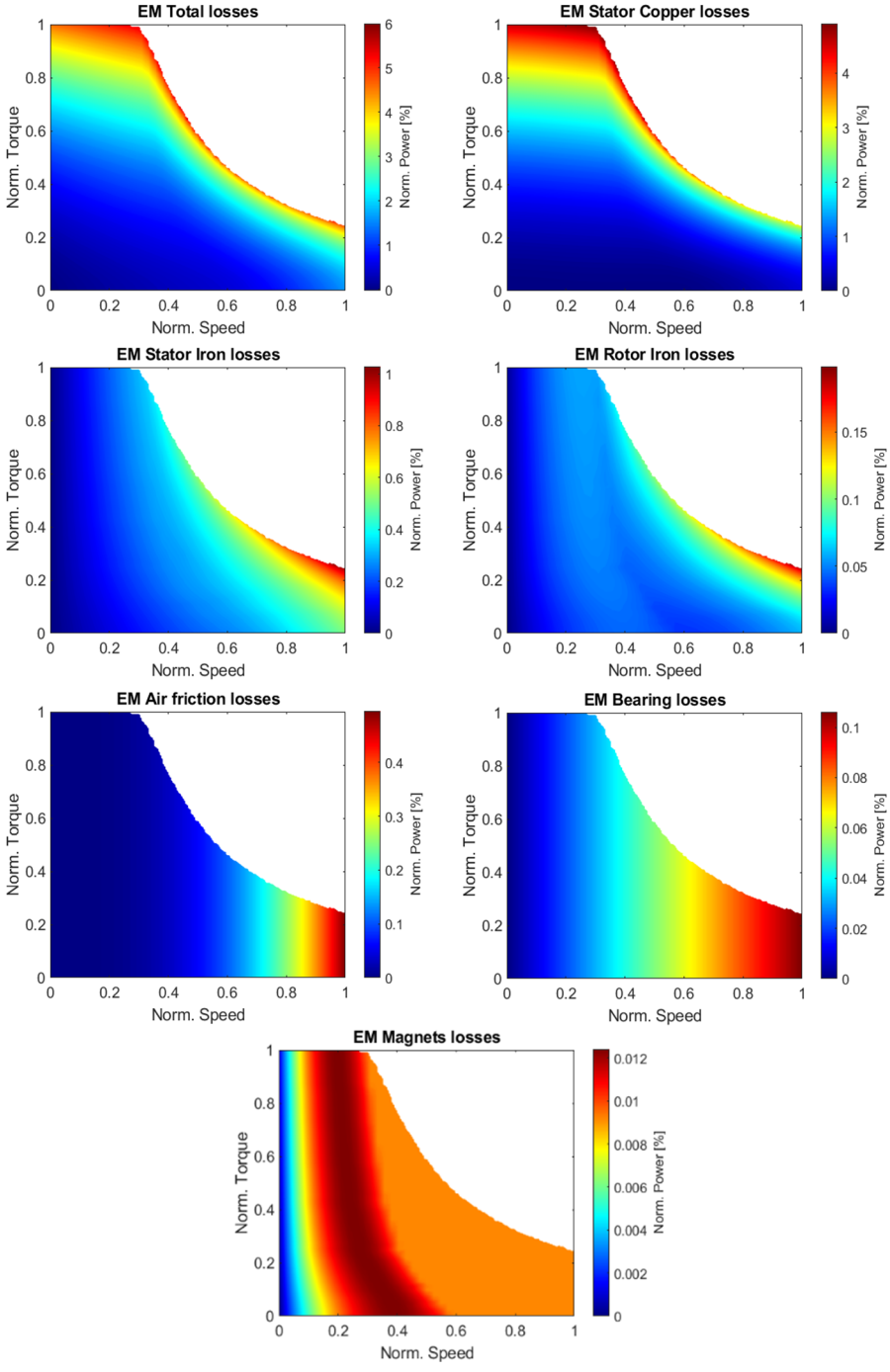

Figure 4.48: EM efficiency losses distribution at high temperature

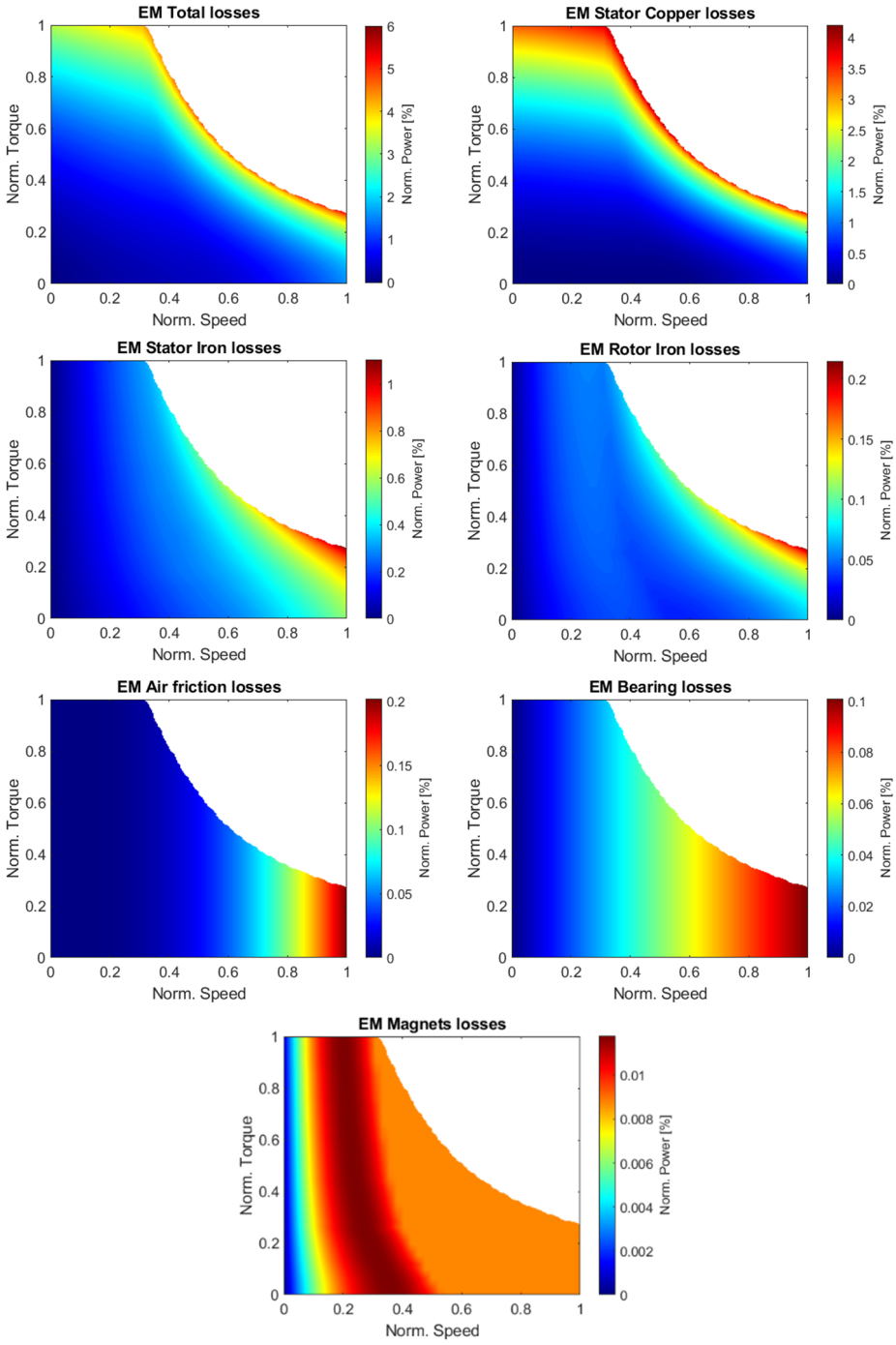

Figure 4.49: EM efficiency losses distribution at low temperature

perature sensor's location and the implementation requirements. Five additional nodes were implemented for the oil contained inside the machine. The final node modeled the coolant fluid present in the stator. Figure 4.50 presents the nodes identification in a axial cross-section view of the machine. For this work, the most relevant nodes were those representing the stator winding, stator iron and the rotor iron. Nodes 13, 17 were both in contact with the inlet oil while the node 18 was in contact with the coolant inlet. These are the nodes exchanging enthalpy with both fluids oil and coolant. The nodes with heat generation were those representing the stator windings (nodes 4, 5 and 8), stator iron (node 3), rotor iron (node 6), magnets (node 7), connection wires (node 12) and bearings (node 10). Air friction losses were evenly distributed between rotor and stator (node 6 and 3). Furthermore, the model also accounted for the heat losses to the ambient through the housing (node 1) to the ambient.

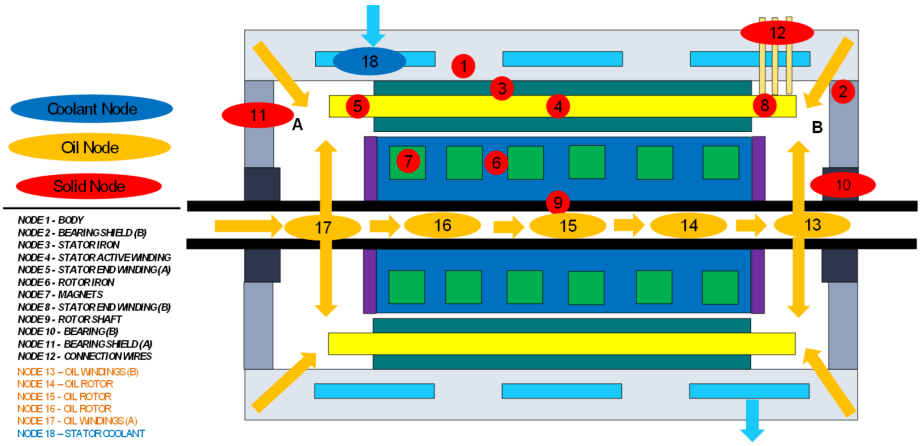

Figure 4.50: Lumped thermal model and nodes identification

Regarding the interface of the implicit thermal model, the main required inputs for the model consisted in; the required torque, required speed, voltage, fluid (coolant and oil) inlet temperatures and flows, time step, ambient temperature and initial temperature value. The model limits the required torque according to the machine specifications. Furthermore, in case the fluid inlet conditions (coolant and oil) are not given, and internal simplified thermohydraulic model provides the lumped thermal model with those variables. Figure 4.51 presents the interface of the EM thermal model and its sub-models interaction.

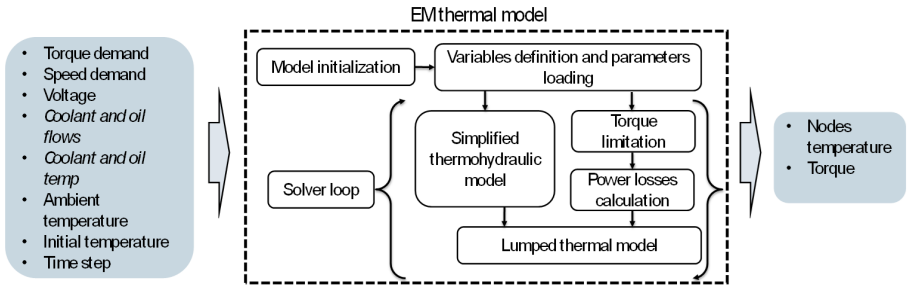

Figure 4.51: Lumped thermal model and nodes identification

Validation of EM thermal model

Four different experimental tests were used for the EM thermal model calibration and validation. Figure 4.52 shows the torque and speed evolution for each one of them. Test 1 was used for the calibration of the model and the rest for validation. Test 1 provided suitable conditions for the calibration process. The first half of the cycle consisted in a controlled swept increasing speed and decreasing torque. For the second one, constant speed was set while varying the torque between cero and a certain value at different frequencies. The time periods in which the operating conditions did not vary served for calibrating the model thermal conductance. The thermal capacitances were calibrated with the steps between operating conditions. Tests 2 and 3 were selected because of their aggressive dynamic behavior. Finally, Test 4 consisted in the standard WLTP cycle.

The results of the temperature validation presented in this section were obtained using the EM efficiency maps at a constant temperature and voltage. A selection of the most relevant nodes is presented to demonstrate the capability of the model for predicting the temperatures evolution in different test cycles. It is important to note, that the magnets temperature was not validated because the temperature sensor was placed at the extreme of the rotor and not in the middle (local hotspot according to CFD calculations). Consequently, the model significantly overestimated the magnets temperature. The simulations were carried in a machine with the following characteristics: Intel(R) Core (TM) i7-8665U CPU @ 1.90GHz and 16 Gb of memory RAM. The ratio between real time and simulation time was approximately 500/1 at a 1 Hz time step. Figure 4.53

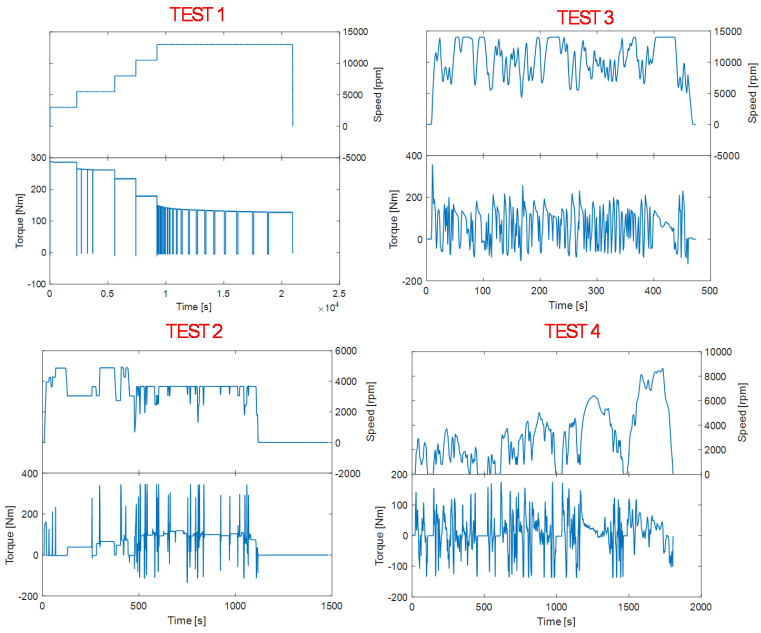

Figure 4.52: Tests speed and torque profiles for experimental calibration and validation

shows the validation of the housing temperature evolution for the cycles previously described. It can be seen that the model was capable of precisely predict the temperature trend along the cycles. Although the model slightly overestimates the temperatures for Test 2 and 4, the maximum relative error was below 0.3 % for all four cycles.

When it comes to the stator iron, the model was also capable to show great accuracy as it can be observed in the Figure 4.54. Overall, the mean average error was les than 1 % and the trends well also captured by the model. The maximum error (2 %) in this node was obtained at the beginning of Test 1 in conditions of low speed and high torque. This could be explained because of the overestimation of the heat losses in the stator windings which are in direct contact with the stator iron through the insulation phase material. For instance, Figure 4.55 also shows a significant error in that first period of Test 1. This also contributes to sustain the idea that, by not implementing a temperature dependence in the heat losses efficiency maps, the model overestimates the temperature in some regions, specially at low speed and high torque. In general, the

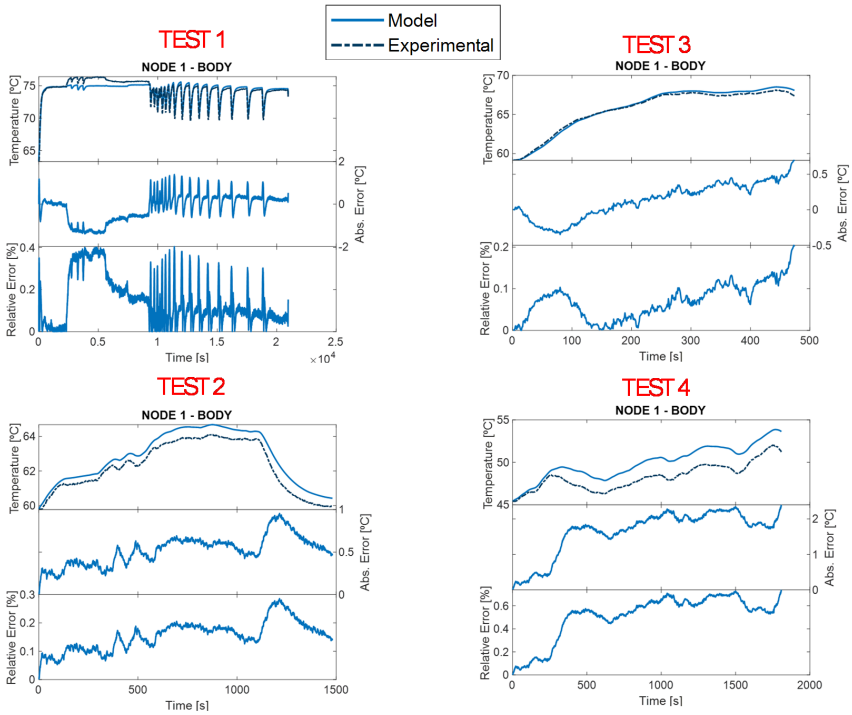

Figure 4.53: Housing (Node 1) temperature validation

model was also capable of capturing the temperature trends in the active windings. However, the model underestimates the temperature in the second half of Test 1. Similar behavior was observed in Test 3 and 4. Observing the tests 1, 3 and 4 (Figure 4.52) it can be concluded that this effect appears at high speed conditions. Taking into account that the active windings exchange heat with the end windings and the stator iron. This error could be explained if some the end windings temperature is overestimated.

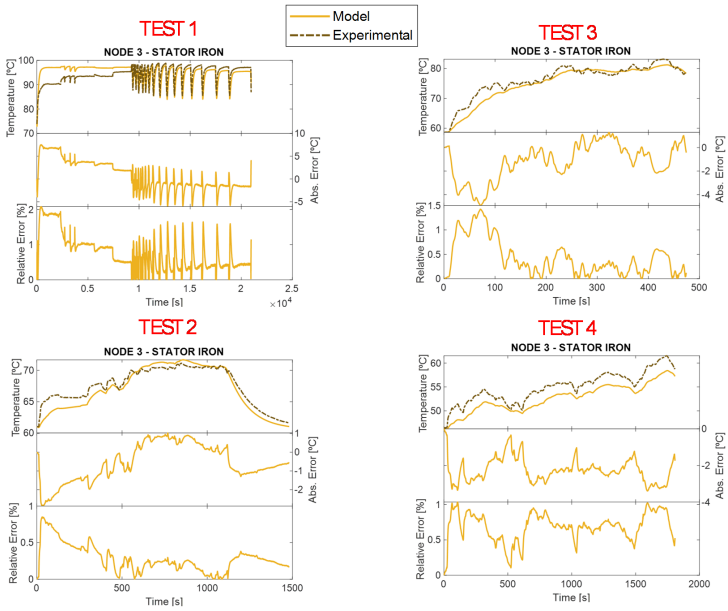

Figure 4.54: Stator iron (Node 3) temperature validation

Figure 4.56 presents the temperature evolution of the end windings in the A (gearbox) side of the machine while the Figure 4.57 shows the end windings at the B side. It can be seen that the plots in these figures have more than on experimental measurement. This is because, four sensors were implemented around the windings machine. Four at the A side and 4 at the B side. The same number were installed for the active windings, although no significant variations were observed among them. This is explained by the presence of the oil cooling through the stator which is ejected to the end windings. A complex exchange of mass and heat flux taking place at the A and B volumes (See Figure 4.21) added to the rotational speed of the rotor. This explains the temperature difference

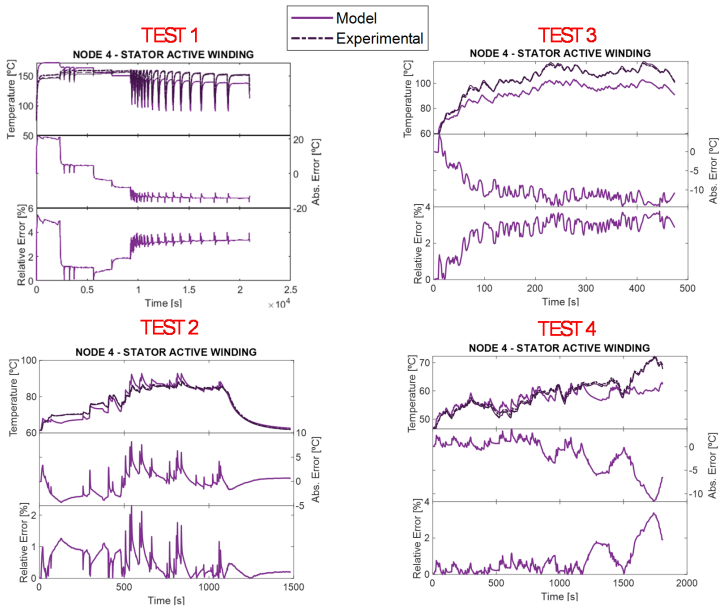

Figure 4.55: Active windings (Node 4) temperature validation

among sensors around the end windings of the machine. The sensor selected for calibrating the model was the one that presented a higher value in more experimental tests. Depending on the test profile, the maximum temperature could be measured by different sensors of the end windings. Other important aspect to note is that the temperatures measured at the B side are lower than the A side. This is explained with the oil flow distribution entering the A and B volumes. The model was also capable of reproducing this effect. Overall, the model precisely captured the trend of the temperature evolution at the end windings which is a critical node for the machine. For instance, the mean average relative error was less than 1 % which was considered acceptable taking into account the difficult to correctly model the heat transfer occurring in the A and B volumes.

In regard to the rotor temperatures, the model also capable to predict its temperatures with significant accuracy. Figure 4.58 shows the temperature evolution of the rotor iron. The average relative error was less than 1 % for four tests. Additionally, the model accurately captures de trend, specially in Test 1, 3 and 4. The iron of rotor is physically connected to the magnets and the shaft. Figure 4.59 shows the temperature evolution of the external part of the rotor iron which is in contact with the shaft. It

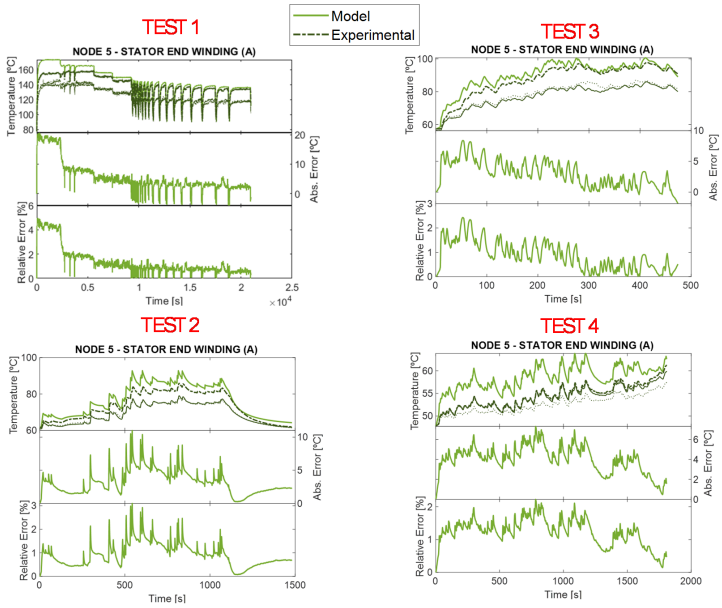

Figure 4.56: (A) side end windings (Node 5) temperature validation

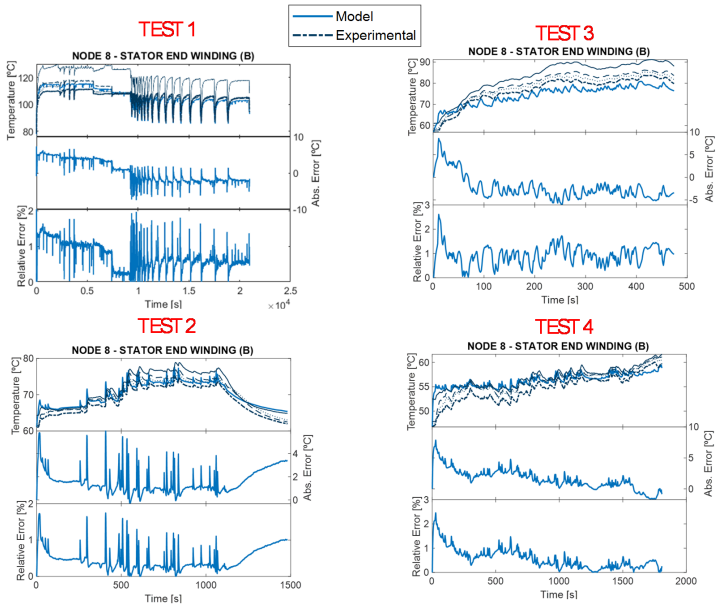

Figure 4.57: (B) side end winding (Node 8) temperature validation

can be observed that the model is able to predict the trend of the temperature with the exception of the period between 250 s and 10000 s of the Test 1. In this period, the machine speed is increasing which directly will increase the losses in the iron of the rotor and the bearing. This would increase the temperature of the shaft. However, the heat convection between the rotor shaft and the oil passing through the rotor also increases which would cool the rotor shaft. It seems that in the model, this effect is balanced, and the temperature is kept without significant variation. On the contrary, the experimental measurements show that the heat transfer to the oil has more impact than the oil absorbed from the magnets, iron and bearings. The model behavior could be improved by improving the correlation between heat convection coefficient and speed. Finally, Figure 4.60 and Figure 4.61 present the temperature evolution in the bearing at the B side and the connection wires, respectively. In case of the bearing, it can be perfectly observed that the losses increase with the speed in the Test 1. The model accurately captures those changes. However, in the Test 3 and 4, the model underestimates the temperature, presenting more thermal inertia than the experimental case. A decrease in the bearing's inertia and an improvement with the heat transfer with the oil at the B volume would improve the prediction of the model. Overall, the mean relative error was less than 2 %. For the connection wires, the model perfectly captures the trend of the temperatures evolution while keeping a low relative error. It is also observed that the maximum error is produced at the beginning of Test 1. This is for the same reason as it was for the winding nodes. The heat generated in the wires was overestimated at low speeds and high torque. Overall, the relative errors were less than 1 %.

4.5.3 Electric Drive Thermo-hydraulic Model

The electric machine of the EDS had a maximum torque of 200 Nm and a power of 50 kW. For calculating the heat rejected by the EDS (acting as a Motor or Generator) to the coolant, two efficiency maps were implemented, one for each of the two mentioned actuations. The maps are shown in Figure 4.62. Given the fact that the efficiency shows a small dependence with the voltage, the nominal voltage of the battery pack (V) was considered as input for the efficiency maps ((N, V)). Similarly to the battery case, the required mechanical power and the generated electrical power by the EDS are determined by the control of the vehicle model. With the EDS power (P_{req}) and its speed (N), the heat rejected ($\dot{Q}_{EDS}$)

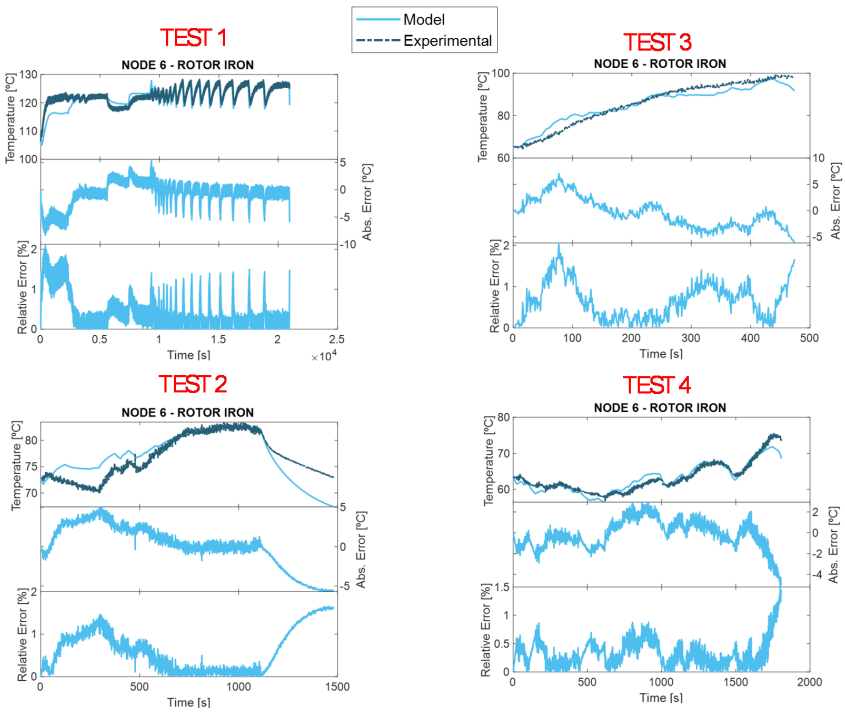

Figure 4.58: Rotor iron (Node 6) temperature validation

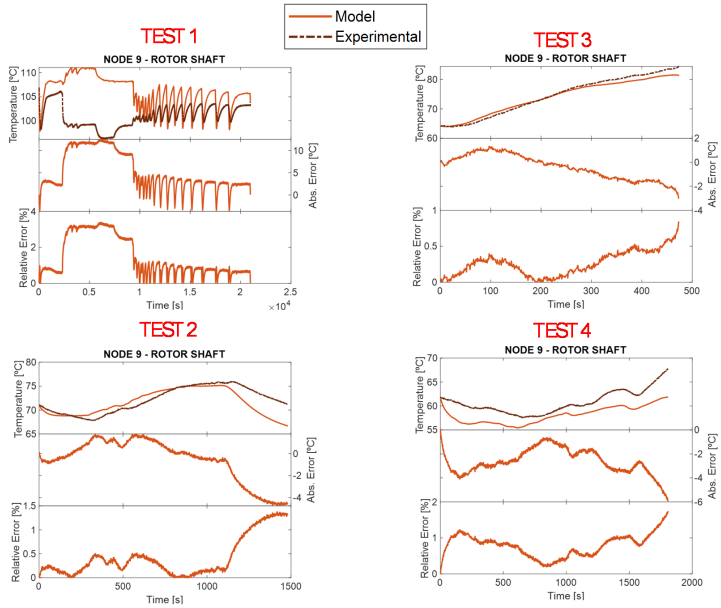

Figure 4.59: Rotor shaft (Node 9) temperature validation

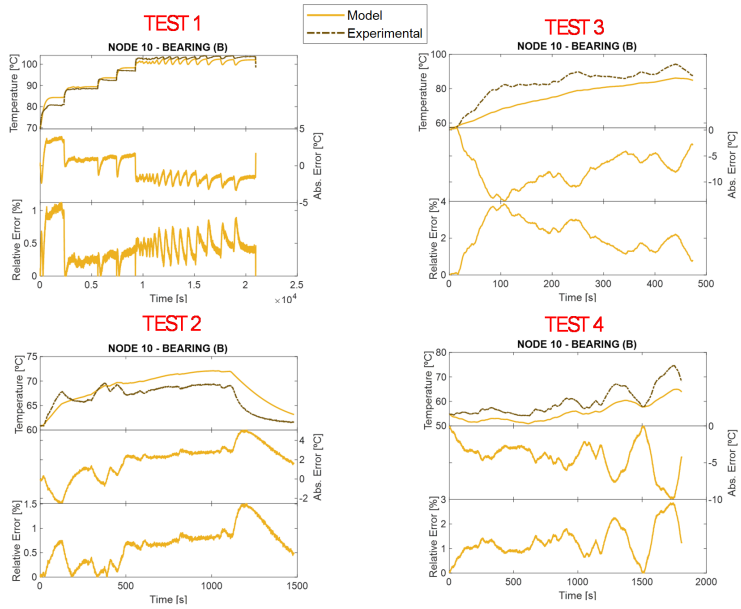

Figure 4.60: Bearing (Node 10) temperature validation

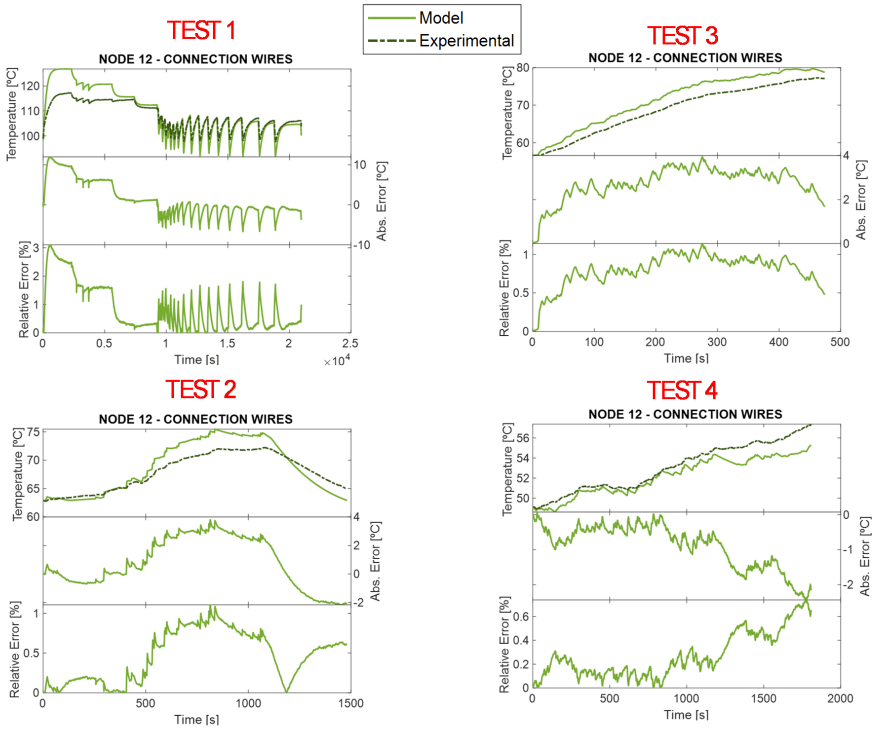

Figure 4.61: Connection wires (Node 12) temperature validation

to the coolant is calculated by using the maps of Figure 4.62, according to Equation 4.22.

$$\dot{Q}_{EDS} = P_{req}\frac{\eta(1-\eta(N,V))}{\eta(N,V)} \tag{4.22}$$

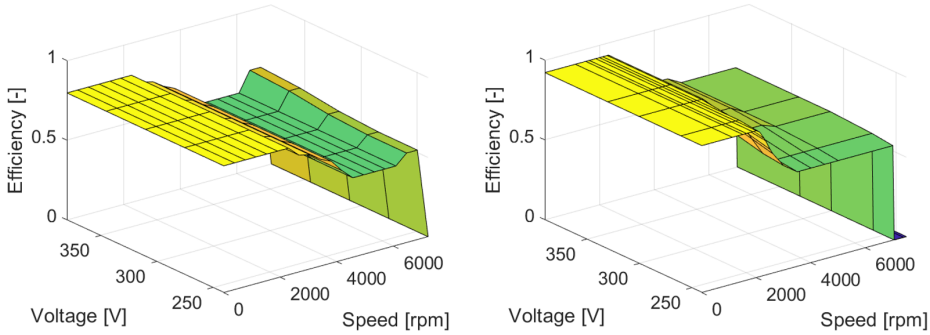

Figure 4.62: EDS efficiency maps, working as generator (left) and motor (right)

The electric drive thermal management system (EDTMS) is very similar to the BTMS. The layout is presented in the right-hand side of Figure 4.63. In this system a pump that supply a constant coolant flow equal to the 17% of the ICE maximum coolant flow is considered. This performance was decided following the same criterion as for the battery cooling system, taking the maximum heat rejected during the cycle and setting the temperature drop to 2°C. This element was implemented in the thermohydraulic model by means of a heat exchanger. Finally, this TMS also includes a thermostat that starts opening when the temperature of the coolant at the outlet of the electric drive reaches 60°C and is completely open at 70°C.

4.5.4 Inverter

The inverter model of the present work consisted in two submodels. First, the electric submodel formed by a module of ideal insulated gate bipolar transistors (IGBT) and diodes. Additionally, this submodel consisted three blocks; a 3-phase electric circuit module with 12 chips (6 IGBTs and 6 Diodes) forming a full bridge, a modulation block controlling the IGBTs gate signal following a pulsewidth modulation (PWM) method and a block for heat losses calculation. This model calculated the voltage and current

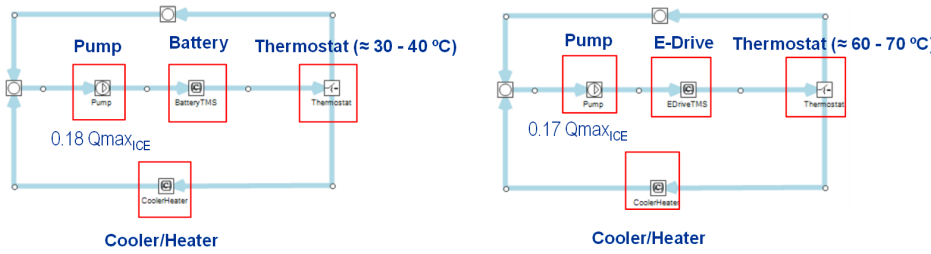

Figure 4.63: Battery TMS (left) and Electric drive system TMS (right)

through each chip and their power losses due to switchng and conduction phenomena.

Figure 4.64 presents the inverter model workflow. The DC voltage coming from the high voltage battery, the fundamental frequency needed to drive the electric machine at the desired speed and torque, the switching frequency (normally a maximum of 20 kHz for IGBTs) and the load impedance of the electric machine are the main inputs for the inverter electric model.

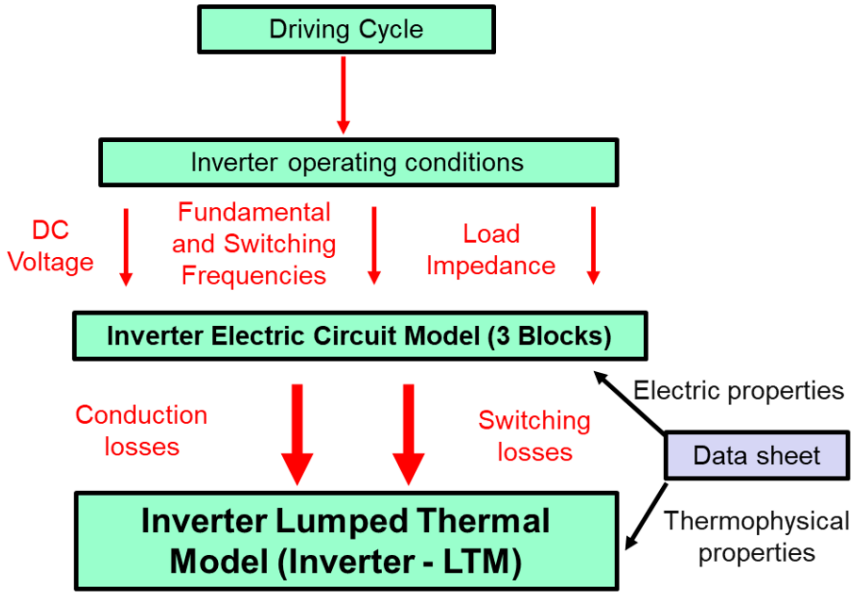

Figure 4.64: Inverter submodels algorithm

The instantaneous conductive loss of the chips is obtained by multipliying the voltage and current through the chip (i.e., IGBT or diode). Assuming that the conductive current is constant during a switching cycle, the average conductive losses can be calculated according to Equation 4.23.

$$P_{c-chip} = \frac{V_c I_c t_c}{T_s} \tag{4.23}$$

Where P_{c-chip} is the averaged conduction power loss in the chip, V_c represents the voltage drop of the chip, I_c current through the chip, t_c is the conduction time and T_s represents the switching period.

For calculating the switching losses, the energy dissipation maps during the IGBT turning on and off (i.e., E_{on} and E_{off}) provided by the data sheet were considered. Equation 4.24 and Equation 4.25 were implemented for the calculation of the switching losses of IGBT (P_{s-T}) and diode (P_{s-D}) for each switching period (T_s). However, the turn-off energy dissipation for the diode was neglected and only the forward energy (E_{for}) was considered.

$$P_{s-T} = \frac{E_{on} + E_{off}}{T_s} \tag{4.24}$$

$$P_{s-D} = \frac{E_{for}}{T_s} \tag{4.25}$$

The activation/deactivation energies, electric parameters and the geometry for the lumped thermal model were obtained from the inverter module data sheet. The thermophysical properties of the layers' materials are presented in Table 4.3. Starting from the upper side, the inverter module was composed by; the silicon IGBT/Diode, chip solder, copper, ceramic, copper, solder, base plate made of copper, thermal interface material (TIM) and the cold plate.

Second, the thermal model consisted in a lumped thermal network dividing the inverter module into 14 isothermal nodes. The conduction and switching losses in the inverter module chips were implemented as heat sources in the chips nodes of the lumped thermal model presented in Figure 4.65. This model served to calculate both the heat rejected to the coolant and the junction temperature (i.e., chip node in Figure 4.65) which is the critical hotspot in the inverter.

Table 4.3: Thermophysical properties of inverter layers

Layer	Material	Thickness (μ)	Thermal conductivity ($W/m \cdot K$)	Volumetric heat capacity ($J/m^3 \cdot K$)
1	Si	100	120	1.60E+06
2	Ag-Sn	80	100	1.65E+06
3	Cu	380	380	3.60E+06
4	Zr-Al	300	300	3.00E+06
5	Cu	370	380	3.60E+06
6	Ag-Sn	230	100	1.65E+06
7	Cu	2900	380	3.60E+06
8	TIM	100	0.5	1.50E+06
9	Cu	5000	380	3.60E+06

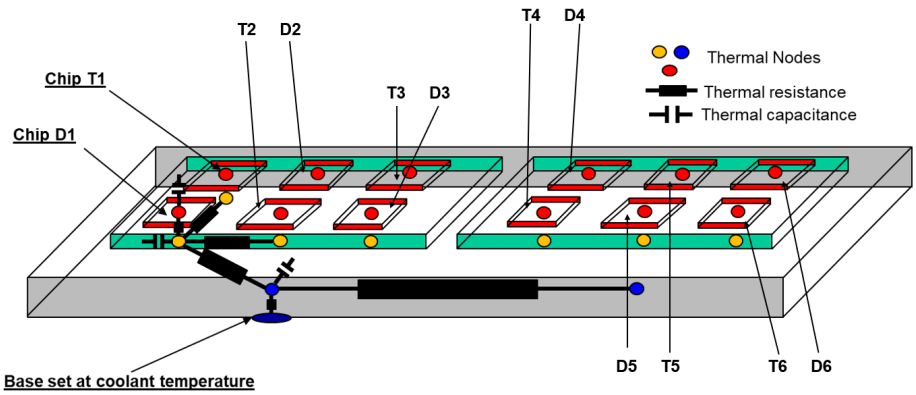

Figure 4.65: Inverter lumped thermal model

Validation of the inverter model

In order to validate the inverter model, the data presented by Batard et al. in [159] was taken as reference for the transient validation of the model. Only a single phase was experimentally measured using one leg of the inverter. In first place, a constant power step of 55W and setting the cold plate temperature constant at 20°C. Only one transistor (T1 in Figure 4.65) was active in this case, generating a constant heat power of 55W. This served to calibrate the heat capacity and main conductance of the inverter thermal model. Figure 4.66 shows the chips temperature evolution. It can be appreciated that the maximum junction temperature stabilized at 41°C for the T1. Additionally, the model accurately follows the trend of the reference during the warming process.

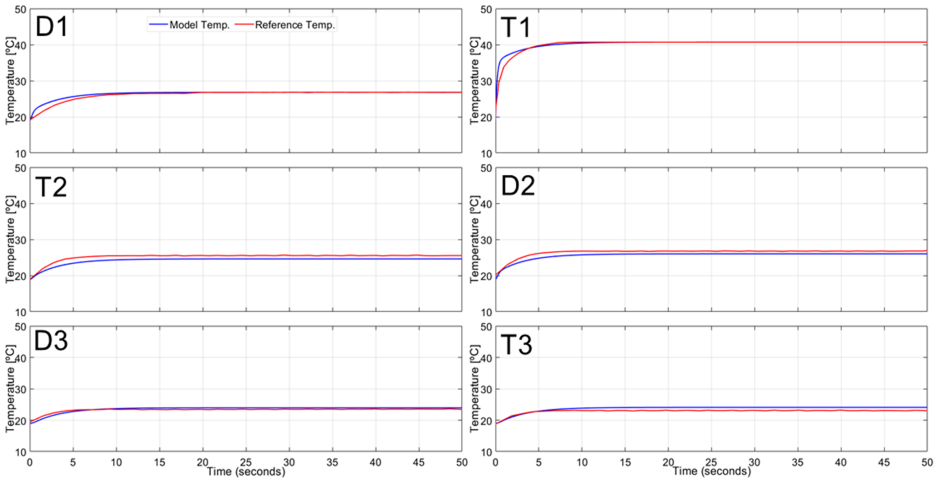

Figure 4.66: Temperature validation of inverter model for constant heat power generation

In second place, aiming to perform a validation in dynamic conditions, a load frequency of 0.1 Hz with a load current peak value of 100 A were implemented to capture the chip's temperature oscillation amplitude. Additionally, a DC voltage of 500 V and a switching frequency of 10 kHz were imposed to the model. The power evolution in the different chips follows a half sinusoidal wave with the load frequency as it can be observed in Figure 4.67. The plots show that the switches ST1 (chips T1, T2 and T3) and the SD2 (chips D4,D5 and D6) are turned on when the switches ST2 (chips T4, T5 and T6) and SD1 (chips D1, D2 and D3) are not active.

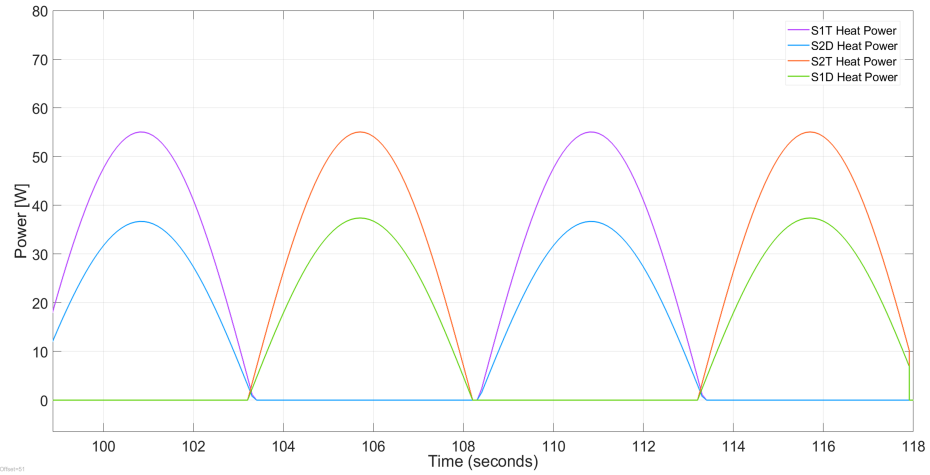

Figure 4.67: Total power loss of the switching chips for a load frequency of 0.1 Hz.

Figure 4.68 shows the temperature evolution of the different transistors and diodes. The temperature evolution during the presented period show that the model correctly captures the trend of the experimental measurement for all 6 chips. However, the model slightly underestimates the temperatures for the chips D3 and T3. Since it was assumed a constant temperature in the cold plate of 20°C for the model, an over cooling is produced in the model when compared to the experimental case in which an increase of the cold plate temperature is expected, especially at the outlet.

4.6 Vehicle cabin

The cabin model of the vehicle was also validated with data from literature [160]. Specially, for obtaining the irradiance evolution over time, the vehicle speed and vehicle's characteristics. The model is formed by two submodels according to Figure 4.69. On one hand, a lumped thermal model to calculate the heat exchange and temperatures of the air and the cabin parts; windshield (WS), side windows (LSW and RSW), roof (Rf), rear window (RW), seats and dashboard (B). On the other hand, the air conditioning (AC) simple model was based on a p-H diagram implementing the python library CoolProp [161].

The cabin was discretizied into 14 isothermal and isotropic nodes as

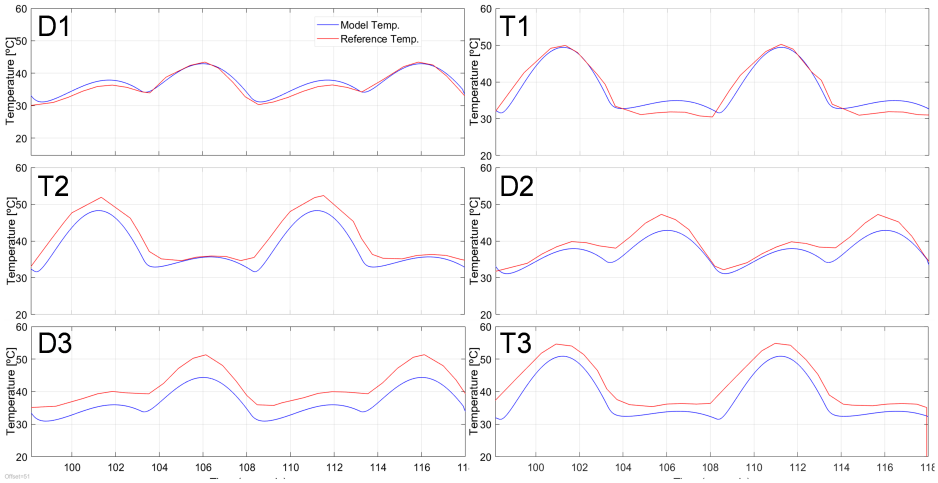

Figure 4.68: Temperature validation of inverter model for a load frequency of 0.1 Hz.

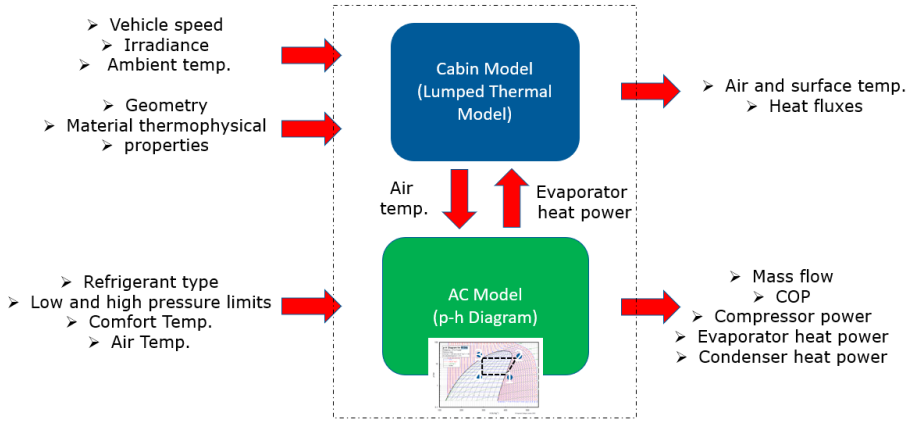

Figure 4.69: Cabin model interface

it can be seen in Figure 4.70. Each node of the figure was divided into interior and exterior. Conduction heat transfer was considered between the internal and exterior nodes. The air inside the vehicle exchanged heat with the internal surfaces of the windows, roof panel and the base (i.e., dashboard and seats) through convection phenomena. Similarly, the external surfaces were in contact with the ambient air and exchanged heat through convection and radiation processes. Each occupant of the vehicle was considered a power source of 120 W. Similarly to previous lumped thermal models, the thermal model was based in Equation 4.11. The incident solar irradiance is decomposed into: reflected, absorbed and reflected for the windows nodes. Furthermore, for the convective heat transfer coefficient between the air and the cabin surfaces, different equations were implemented depending on the location (exterior or interior). On the outside, if the vehicle was in motion, forced convection was modelled while natural convection was considered on the inside of the vehicle. These coefficients were calculated according to the Equations 4.26 (for laminar flow conditions) and 4.27 (for turbulent flow conditions) presented in [160].

$$Nu = 0.664 Re^{0.5} Pr^{1.5} \tag{4.26}$$

$$Nu = (0.037 Re^{4/5} - 871) Pr^{1/3} \tag{4.27}$$

A simple approach was taken for developing a first AC system model which assumes steady state conditions. Kinetic energy and potential energy variance of the system were assumed to be negligible and the compression process was assumed to be adiabatic. The enthalpies for each part of the circuit were calculate using the p-H diagram of the refrigerant. The refrigerant type (i.e., R134a), exterior air temperature, interior air temperature (calculated by the thermal model of the cabin) and required comfort temperature were the main inputs for the variable. The main components were the: compressor, condenser, expansion valve and evaporator (See Figure 4.71). Safety components (i.e., the receiver Dryer) were not considered.

The pressure in the evaporator was calculated according to a pre-established temperature drop (ΔT) between the evaporator (T_e) and cabin air (T_i) according to Equation 4.28. Similarly, the condenser's pressure (and temperature T_c) was calculated adding a temperature gradient to the ambient temperature (T_a) following the Equation 4.29. Saturated conditions of the refrigerant were considered at the compressor inlet and

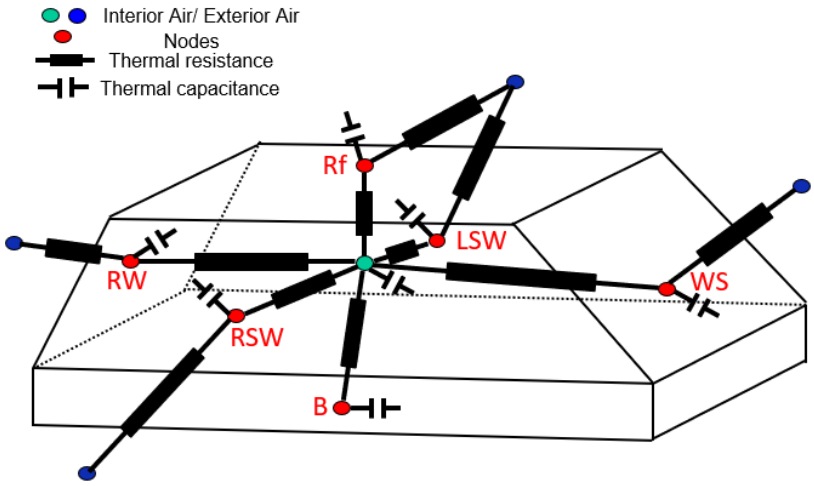

Figure 4.70: Cabin lumped thermal model.

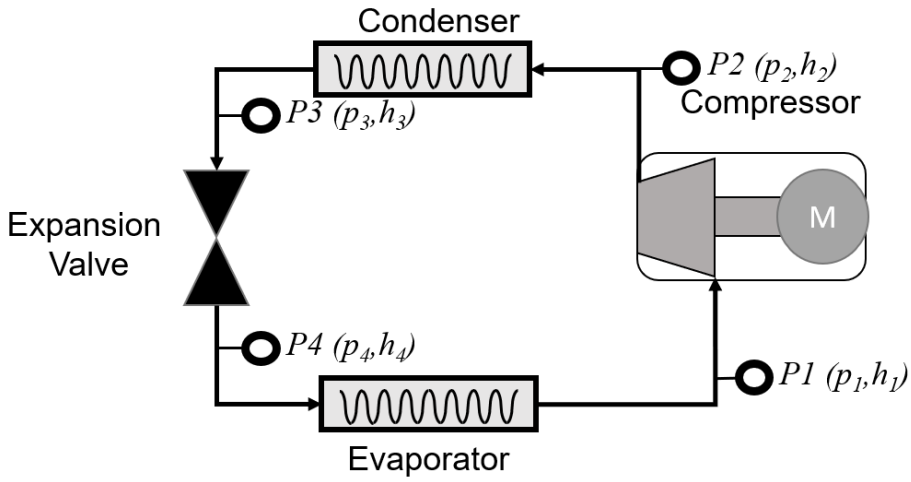

Figure 4.71: Simplified AC model scheme.

condenser outlet. With this, the conditions (pressure and enthalpy) in locations P1 and P3 (See Figure 4.71) were determined. A compressor efficiency (η) of 0.8 was assumed to calculate the real temperature of the refrigerant at the compressor outlet following the Equation 4.30.

$$T_e = T_i - \Delta T \tag{4.28}$$

$$T_c = T_a + \Delta T \tag{4.29}$$

$$\eta = \frac{h_{2s} - h_1}{h_2 - h_1} \tag{4.30}$$

Where h_{2s}, h_2, h_1 are the isentropic enthalpy in location P2 (condenser inlet), the real enthalpy in P2 (for an $\eta = 0.8$) and the enthalpy in P1 (compressor inlet).

Additionally, it was assumed that, ideally, the evaporator power was exactly the heat required to set the cabin air at the comfort temperature. This power was calculated taken into account, the air mass inside the cabin and the temperature difference between comfort an instantaneous. Finally the mass flow ($\dot{m}_r$) was calculated taking the evaporator power and its enthalpy drop between P1 (h_1) and P4 (h_4) according to Equation 4.31.

$$\dot{m}_r = \frac{\dot{q}}{\Delta he} = \frac{\dot{q}}{h_1 - h_4} \tag{4.31}$$

4.6.1 Validation of cabin model

The experimental data of two different cycles was processed to validate the cabin model. The variable measured was the air cabin temperature located in the middle of the vehicle. Cycle 1 consisted had a duration of 3.5 hours while the Cycle 2 lasted for 40 minutes. Cycle 1 considered a vehicle parked without occupants while in the Cycle 2 the vehicle has a variable speed and one human (i.e., the driver). Figure 4.72 presents the irradiance and ambient temperature evolution for both cycles while Figure 4.73 shows and the vehicle speed during Cycle 2.

Figure 4.74 present the air temperature evolution predicted by the cabin model and the reference model validated with experimental data in [160]. For the Cycle 1, it can be observed that the temperature of the air continuously increases over time since the AC is deactivated and the

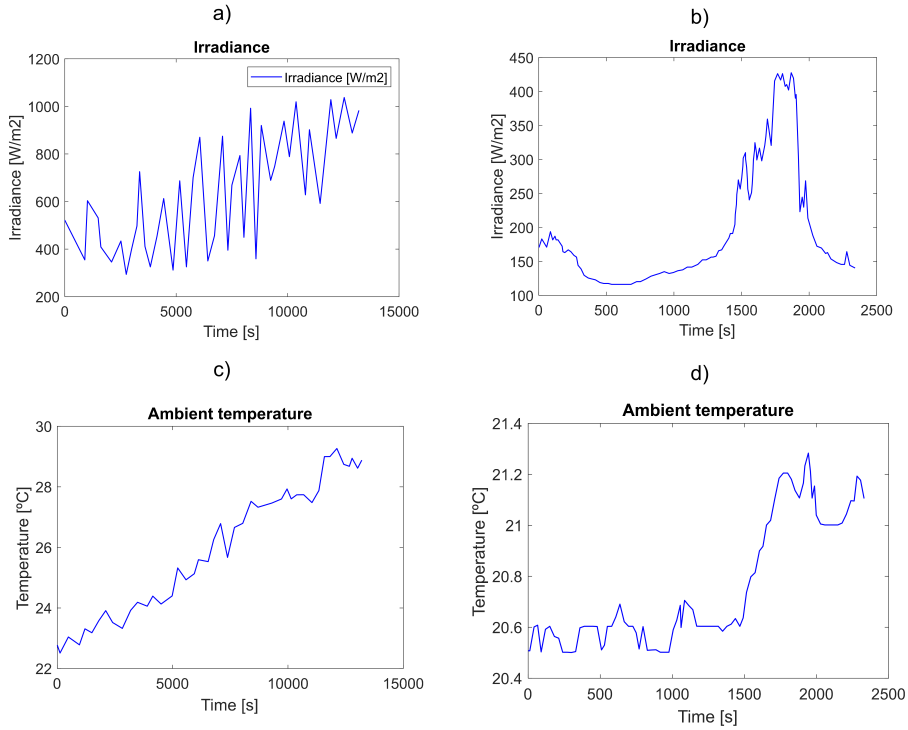

Figure 4.72: Irradiance and ambient temperature evolution in Cycle 1 (a and c) and Cycle 2 (b and d).

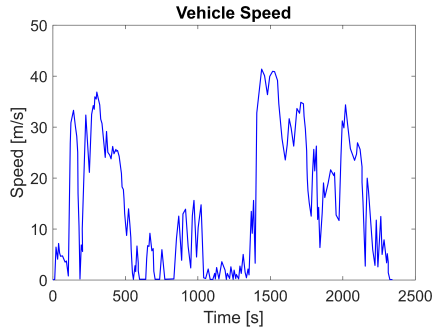

Figure 4.73: Vehicle speed evolution for Cycle 2.

external temperature also increases during the cycle. The model accurately captures the trend and the averaged error is less than 1 °C. For the Cycle 2, it can be observed that the model slightly overestimates the temperature during the first 300 s. Afterwards, the contrary is observed and the model slightly underestimates the air cabin temperature till the period if higher irradiance (See plot b of Figure 4.72). Overall, the error was considered acceptable and the model capable of predicting the air temperature during dynamic operation. Further validation needs to be performed with the AC system turned on.

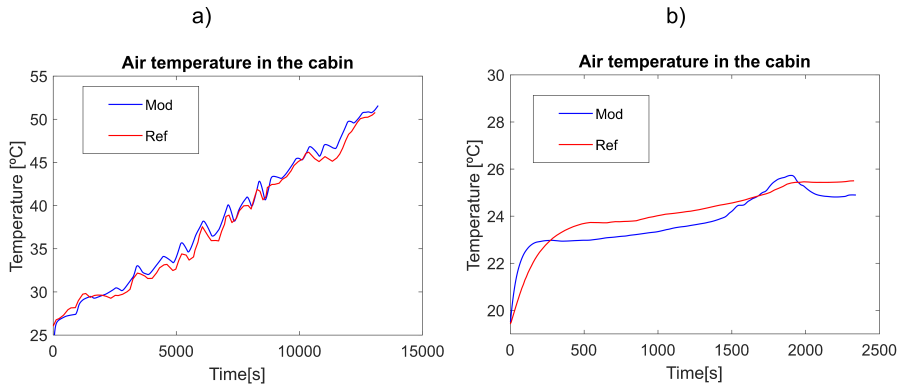

Figure 4.74: Air cabin temperature validation for Cycle 1 (a) and Cycle 2 (b).

4.7 Control oriented modeling

Additional to the models described in previous sections, it is also necessary for the control model to have fast and simplified control oriented models for the correct optimization of the energy management of the vehicle. An integrated virtual model in MATLAB-Simulink was developed including all subsystems of the hybrid propulsive system (i.e., battery, electric drive, ICE, transmission, vehicle, driver...). Figure 4.75 shows a schematic view of the hybrid vehicle submodels.

4.7.1 Internal combustion engine

Two modelling approaches can be used in the model depending on the purpose: the model implemented in the control strategy, i.e. the one

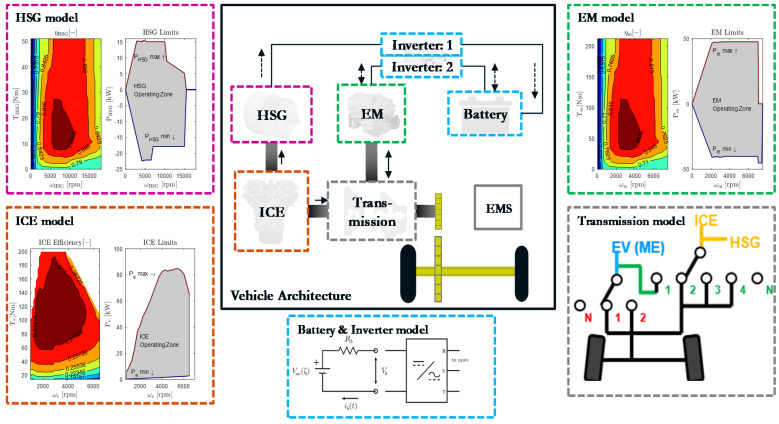

Figure 4.75: Virtual components of the hybrid vehicle.

used to take decisions on the power-split to minimize fuel consumption is a simple model based on a quasi-steady approach with an engine map, and corrections to include (to some extent) the engine dynamics and the impact of factors such as its thermal state. Note that model simplicity is required in the model-based control since several control decisions must be evaluated every time-step to choose the optimal. The model in the plant, which is used to check the impact of the control strategy may be based on the previous steady-state approach or a detailed model (1D-Model) which can be embedded by means of an S-function or FMU (Functional Mock Up Unit). The present section is focused on the control-oriented model.

The ICE model follows the classic approach for Energy Management consisting on reducing the engine model to a map of any interesting variable depending on the engine speed and throttle. Amongst the most interesting variables to map one can find the torque, the fuel consumption, the efficiency, or emissions. While the accuracy of this method to model complex and dynamic variables such as emissions is limited, this approach can provide fair enough results in terms of fuel consumption, at least to take control decisions. Figure 4.76 shows an example of this map for BSFC at warm conditions in the engine. The data is obtained by sweeping the range of operating conditions in the testbench.

Since maps such as that of Figure 4.76 are obtained in steady state conditions, they cannot capture transient phenomena. One can think on two main transient phenomena affecting ICE. The first one may be a variation in the operating conditions (engine speed and throttle) that will

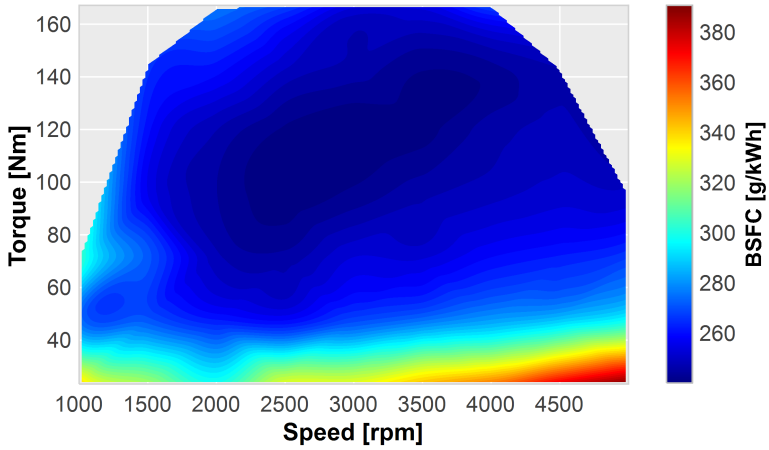

Figure 4.76: ICE fuel consumption 2D Map depending on engine speed and torque.

lead to a delayed and filtered response of the torque. The second transient phenomena strongly affecting the engine performance is the warm up, since variations in the thermal state of the engine will lead to changes in heat transfer and friction phenomena that will finally affect performance. In this sense, the model employed for control purposes is based on Equation 4.32 and 4.33:

$$M_e^0 = f(n_e, \alpha) \tag{4.32}$$

$$m_e^0 = g(n_e, \alpha) \tag{4.33}$$

where f and g map the engine speed n_e and throttle α the corresponding variable (reference effective torque M_e^0, reference fuel consumption m_e^0) by means of interpolation in a database. In the case at hand, f and g are 2D-lookup tables. The term reference in previous variables highlights that those variables have been obtained in steady state (and warm conditions).

Regarding the impact of variations in the engine operations, a filter on the reference torque is applied. The filter has the following Equation 4.34

$$M_e^k = aM_e^{k-1} + bM_e^{0,\ k} \tag{4.34}$$

where superscript k stands for the time-step, parameter a represents the influence of the torque value in the previous time-step in the current one (state matrix) and b is the weight of the current reference torque in the actual torque (input matrix). Choosing $0 \leq\ a \leq 1$ and $b = 1-a$, leads to a on-gain filter whose time constant increases with a and on the steady state $M_e^k = M_e^{0,\ k}$. The values of a and b can be obtained by calibration using engine transient test, minimizing the error between measured and model torque. Note that the values of a and b will depend on the time-step of the simulation. Regarding the impact of the engine thermal state on fuel consumption, a reduced lumped heat transfer model was used. In this sense, the thermal state of the engine is approximated by a global temperature (assumed to be that of the coolant θ_c) as the Equation 4.35 shows.

$$\begin{aligned} \dot{\theta}_c^k = &\ \frac{1}{C_c}\left(hA(\theta_c^k - \theta_{env}) + k(1-\eta_e)\right) \dot{m}_f{}^k H_c) \\ = &\ k_{0c} + \ k_{1c}(\theta_c^k - \theta_{env}) + k_{2c}(P_f^k - P_e^k) \end{aligned} \tag{4.35}$$

where k_{0c} and k_{1c} model the heat transfer between the engine and the environment (so their values depend on the cooling circuit conditions) and k_{2c} represent the contribution of the energy released in the fuel combustion which is not transformed in mechanical power. Constants k_{0c} , k_{1c} and k_{2c} will, in general, depend on the operating conditions. In the case at hand, they have different values if the engine is on or off, and the temperature is saturated to 100°C assuming that the coolant circuit is able to avoid any coolant temperature excursion above that value ($\theta_c^k < 100°C$).

Once the thermal state is determined by Equation 4.35, the reference fuel consumption can be corrected with Equation 4.36.

$$m_f = m_f^0 h(n, \alpha, \theta_c) \tag{4.36}$$

where $h(n, \alpha, \theta_c)$ is the experimentally calculated ratio (rearranging Equation 4.36) between experimental measurements at different coolant temperatures for each engine operating point. Furthermore, several steady state operating conditions were measured at different coolant temperatures (35 °C, 50 °C, 63 °C, 76 °C and 88 °C). Using these data, the $\frac{\partial h(n,\alpha,\theta_c)}{\partial \theta_c}$ 3D Map was generated and implemented in the control model. As it can be observed in Figure 4.77, measurements show that operating the engine at higher temperature has a great impact on fuel savings. For example, operating the ICE at 35 °C could mean an increase of fuel consumption of

20%. Two main reasons explain this fuel consumption increase. On one hand, lower coolant temperatures of the engine, directly mean lower oil temperatures (both coolant and oil hydraulic circuits are connected by the oil cooler) which increase friction losses due to higher oil viscosity. On the other hand, lower temperatures in the cylinder block and head, increase the temperature drop between the material and the gas. Hence, increasing heat transfer and decreasing combustion efficiency (engine less adiabatic).

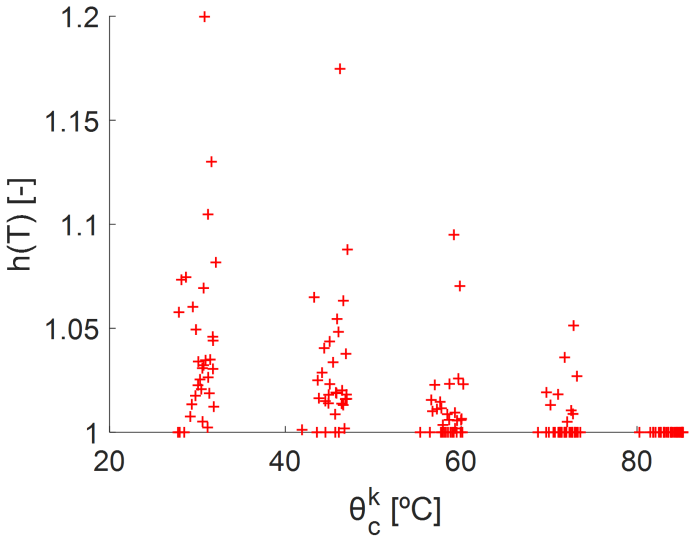

Figure 4.77: $h(n, \alpha, \theta_c)$ 3D Map of fuel consumption ratio with engine coolant temperature.

Figure 4.78 shows the evolution of the coolant temperature in a RDE with the ICE. Results show how despite a simple model, it is able to capture to some extent the evolution of the coolant temperature in a dynamic cycle such as a RDE.

4.7.2 Electric machine and power electronics

The control-oriented model employed in this work considers quasi-steady behavior, i.e. the dynamics of the processes inside the electric motor are much faster than the characteristic times of the driving cycles and consequent evolution of the main vehicle variables. This hypothesis becomes valid since, in general, the motor response is much faster than ICE dynamics and strongly simplifies the model since the typical motor map as

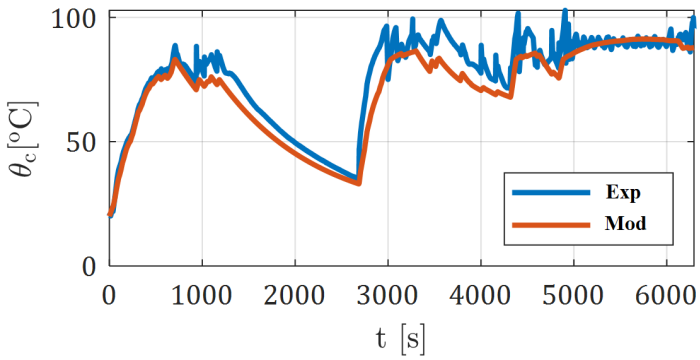

Figure 4.78: Evolution of the coolant temperature in a RDE with the ICE. Comparison between experimental results and control-oriented model.

supplied by a manufacturer representing the efficiency as a function of motor speed and torque can be directly applied. The model assumes that the motor can instantaneously supply the demanded torque if it does not exceed the maximum allowed value that may depend on the motor speed. In this sense, the torque in the motor shaft is calculated according to the Equation 4.37.

$$T_m = \min\left(T_m^{max}(\omega_m), \max(-T_m^{max}(\omega_m),\ T_m^{dem})\right) \tag{4.37}$$

Where T_m^{dem} is the torque demand and $T_m^{max}(\omega_m)$ is the maximum torque that the motor is able to produce or absorb at a certain speed ω_m. Taking into account the efficiency map of the electric machine (η_m), the Equation 4.38, 4.39 and 4.40 were used to calculate the electric power consumption of the motor P_m^{elec}.

$$\eta_m = f\left(\omega_m,\ u_{Tm}\right) \tag{4.38}$$

$$u_{Tm} = \frac{T_m}{T_m^{max}(\omega_m)} \tag{4.39}$$

$$P_m^{elec} = \begin{cases} T_m\omega_m\eta_m & \text{if } \omega_m T_m \leq 0 \\ \dfrac{T_m\omega_m}{\eta_m} & \text{if } \omega_m T_m > 0 \end{cases} \tag{4.40}$$

where cases with the motor braking or propelling are distinguished. Note the non-causality of the model, since in the actual system, the torque

at the motor shaft is a consequence of the supplied electrical power at a particular rotational speed, and the model follows the inverse path (computes the electrical power consumption from the torque and speed). In this sense, the model assumes that all the torque demanded to the motor is instantaneously supplied (excepting when maximum or minimum torque are exceeded). All the electric machines (motors and generators) are modelled in the same way and power electronics are modelled as an efficiency, which is included in the map of Equation 4.38.

4.7.3 Battery

The control-oriented model of the battery used in this work is a Thevenin equivalent circuit consisting of an ideal voltage source and a resistor in series as displayed in Figure 4.79

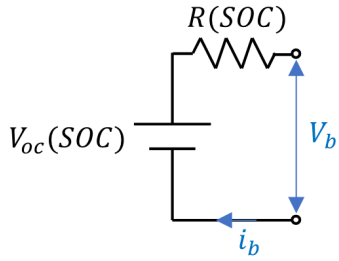

Figure 4.79: Scheme of the battery model using its Thevenin equivalent circuit temperature.

According to the previous circuit, the battery voltage at the terminals follows Equation 4.41.

$$V_b = V_{oc} - Ri_b \tag{4.41}$$

where i_b represents the current drawn from the battery and the open circuit voltage (V_{oc}) and the internal resistance (R) are model parameters to identify experimentally that may depend on the state of charge of the battery (SOC). The rate of change in the battery charge (Q_b) is the current (Equation 4.42).

$$\dot{Q}_b = -\eta_b i_b \tag{4.42}$$

where the term $\eta_b i$ represents a coulombic efficiency, minoring the variation of the battery charge during recharging. From the previous expres-

sion, one can compute the battery charge in each time (t) can be computed by current integration according to Equation 4.43:

$$Q_b(t) = Q_b(t_0) - \int_{t_0}^{t} \eta_b i_b(\tau)\, d\tau \tag{4.43}$$

The state of charge of the battery is the variable governing the Thevenin equivalent circuit parameters, and represents the ratio between the battery charge and its maximum value as it seen in Equation 4.44.

$$SOC(t) = \frac{Q_b(t)}{\overline{Q}_b} \tag{4.44}$$

Provided that the model input is the power demanded by the motor and the output is the SOC, the circuit in 4.79 is solved for the current variable following the Equation 4.45.

$$i_b = \frac{V_{oc} - \sqrt{V_{oc}^2 - 4RP_{motor}^{elec}}}{2R} \tag{4.45}$$

where the power demand of the motor should be replaced by the total power demand of the electric machines if more than one is used (e.g. series HEV).

4.7.4 Transmission

The energy transmission from the engine and motor output to the wheels is done by several clutches and gearing systems whose type and arrangement strongly depends on the powertrain type. In this sense, providing a general model is challenging. The powertrain has some degree of generality since can operate in series and parallel, so the control-oriented model developed in this activity contains both operation modes. Figure 4.80 shows such an architecture, where the vehicle can operate in pure electric mode by selecting gears 1 or 2 in the motor (M) side and neutral in the engine (ICE) side. It can operate in parallel mode by choosing independently the gears of the motor and engine branches. The system can also operate as an only ICE-propelled powertrain by selecting neutral for the motor and any of the 4 available gears for the engine. Finally, the system can operate as a series powertrain where the motor is connected to the wheels through gears 1 or 2 and the engine is connected to the generator (G) through gear S to produce electricity.

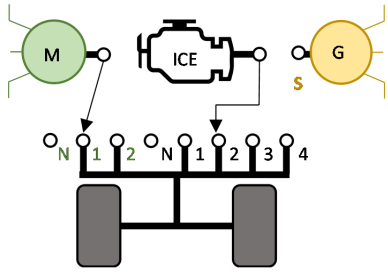

Figure 4.80: Powertrain architecture of vehicle including parallel and series operation.

The transmission is modelled as a discrete set of gear ratios with a fixed efficiency, so the kinematics and energy balance allow to compute the speed of the element upstream the transmission and the torque transferred to the transmission output axis from the speed downstream the transmission and the torque applied to the input axis according to the Equations 4.46 and 4.47.

$$\omega_{us} = \omega_{ds} R_g \tag{4.46}$$

$$M_{ds} = M_{us} R_g \eta_g \tag{4.47}$$

where R_g and η_g are the transmission ratio and efficiency which depends on the selected gear.

4.7.5 Vehicle dynamics

The model is based in longitudinal vehicle dynamics and solves the Newton equation at every time step to obtain the vehicle acceleration from the balance between traction and resistive forces (or torques). In this sense, the main terms participating in the energy balance are:

- A source term representing the net torque coming from the powertrain, including the power split, efficiency, and gear transmission ratio. Additionally, braking torque may be applied if the driver acts on the brake pedal to reduce vehicle speed and the motor is not able to absorb the braking power.
- An inertial term including vehicle mass and powertrain inertia.

- A set of sink terms considering non-conservative forces, mainly friction loses due to aerodynamic drag and rolling resistance.
- An additional term may be included to consider potential energy, allowing the assessment of the road slope effects (despite tests carried out in the present project have been done considering an horizontal road).

The previous terms can be combined in the Newton law (in torque formulation) according to Equation 4.48.

$$M_{wheel} = m_{Veh}\dot{v}r_{wheel} + J_{pwt}\dot{\omega}_{wheel} + m_{Veh}gsin\left(\beta\right)r_{wheel} + \mu\ m_{Veh}gcos\left(\beta\right)r_{wheel} + \frac{1}{2}\rho\ SC_x v^2 r_{wheel} \tag{4.48}$$

Where the variables are defined in Table 4.4:

Table 4.4: Variables definition of Equation 4.48 .

Variable	Definition
M_{wheel}	Net torque applied at the wheels
m_{Veh}	vehicle mass
J_{pwt}	global powertrain inertia
r_{wheel}	wheel effective radius
v	vehicle linear speed
$\dot{v}$	vehicle linear acceleration
$\dot{\omega}_{wheel}$	wheel angular acceleration
g	gravity acceleration
β	track slope
μ	dynamic coefficient of rolling friction
ρ	environment air density
S	vehicle front area
C_x	longitudinal aero drag coefficient

Hence, if the total torque applied to the wheels is known (from the application of the engine, motor and transmission models) Equation 4.48 can be solved for acceleration and the vehicle speed can be calculated by integration. Therefore, the presented vehicle model allows to work as a

closed loop system, in which the torque is progressively transmitted from engine and motor to the wheels and then is used to obtain the vehicle speed. And this vehicle speed is necessary to know the engine and motor operating points in the next step. There is a bidirectional information flow: Torque (M) goes from the engine and motor blocks to the vehicle dynamics block, while speed (n) goes from the vehicle dynamics block to the engine and motor blocks.

Despite the simplicity of Equation 4.48, some of the coefficients (e.g. the J_{pwt} in the case of a complex powertrain such as a HEV) are difficult to find, for this reason, the following expression (Equation 4.49) is used instead:

$$\dot{v} = \frac{M_{wheel} r_{wheel} - \left(A + Bv + Cv^2\right)}{m_{eq}} \tag{4.49}$$

where parameters A, B, C and m_{eq} are experimentally characterized in a coastdown test.

4.7.6 Driver

The objective of the driver model is to follow a given vehicle speed profile as accurately as possible. In this sense, the driver model takes a predefined sequence of vehicle speeds and modifies vehicle actuators (throttle and brake, the gear is automatically selected according to the efficiency criteria by the control strategy) to follow the desired set points. In this sense, the driver model implemented is a Proportional-Integral (PI) controller acting on a torque demand to cancel the error between the current vehicle speed and a reference.

4.7.7 Control strategy

The Energy Management technique used in the present work was the Equivalent Consumption Minimization Strategy (ECMS), which consists of a greedy algorithm based on Pontryagin's Minimum Principle (PMP). Provided a power demand, a set of candidates are defined (combinations between the different energy sources) to provide this target, and then choose the option that minimizes a defined cost function in this time-step. The cost function is a weighted average of the power delivered by the different energy sources (e.g. fuel from a tank and electricity from a battery), while other criteria or constraints can be added to the cost function with the corresponding weighting factor. In this sense, the weighting

factors play a key role in the optimization and were properly calibrated. The next sections provide a description of the basics of the ECMS and its application in the present work.

The Pontryagin's Minimum Principle states the necessary conditions for the minimization of a dynamic problem as Equation 4.50 shows:

$$\arg\min_{u} J\left(x,\ u,\ w,\ t\right) \tag{4.50}$$

subject to: $\dot{x} = f\left(x, u, w,\ t\right)$ and $J = \int_{t_0}^{t_f} L\left(x,\ u,\ w, t\right) dt + \psi\left(x\left(t_f\right)\right)$.

where J is a cost function and f is a generic state function describing the evolution of the system states (x) respect to time (t) when a series of control actions (u) and disturbances (w) are applied. The cost function consists of an integral term defined in L and a terminal cost $(\psi(x(t_f)))$, which may penalize deviations from a final desired state. One can see that the Energy Management problem perfectly fits in the framework described by Equation 4.50, a transcription can be found in Table 4.5.

Considering the Hamiltonian function (H) whose definition is presented in Equation 4.51.

$$H(x,\ u,\ w,\ t) = L(x,\ u,\ w,\ t) + \lambda^T(t) f(x,\ u,\ w,\ t) \tag{4.51}$$

where the co-state vector λ (with as many elements as states in the problem) is a time varying Lagrangian multiplier aimed to adjoint the system dynamics f to the cost function. As previously stated, PMP provides the conditions that an optimal solution (u^*) to the problem in Equation 4.49 should fulfill:

1. The optimal solution of the problem described in Equation 4.50 should minimize the Hamiltonian (Equation 4.51) in every time-step according to Equation 4.52:

$$u^*(t) = \arg\min_{u} H(x,\ u,\ \lambda,\ w,\ t) \tag{4.52}$$

2. The optimal solution of the problem described in Equation 4.50 should lead to Equation 4.53:

$$H\left(t_f\right) = -\ \psi(x(t_f)) \tag{4.53}$$

Table 4.5: Transcription of the Energy Management problem to the mathematical framework of Optimal Control.

Symbol	**Description**	**Variable in the Energy Management Strategy**
u	Control action vector	Power split
x	State vector	State of Charge of the Battery (SOC), engine thermal state (coolant temperature),...
w	Disturbance vector	Vehicle speed profile, route height profile, wind velocity and direction...
L	Lagrangian cost	Fuel consumption, energy consumption, weighted average between energy consumption and pollutants...
ψ	Terminal cost	Deviation of a target SOC, emissions exceeding certain limit,...

3. The evolution of co-state for the optimal solution should fulfill Equation 4.54:

$$\dot{\lambda}\,(t) = -\,\frac{\partial H}{\partial x} = \,-\,\frac{\partial L}{\partial x} - \lambda\frac{\partial f}{\partial x} \tag{4.54}$$

4. The terminal co-state should Equation 4.55:

$$\lambda(t_f) = \frac{\partial \psi(t_f)}{\partial x} \tag{4.55}$$

For the case of the Energy Management, Equation 4.52 and Equation 4.54 allow to calculate the solution to the problem if a solution exists and is unique. In particular, the algorithm used in this project is based on a shooting method with the following steps:

1. Assigning the initial values of the states to the optimal state trajectory ($x^*\,(t_0) = x_0$).

2. Estimate an initial value for the co-state vector ($\lambda^*\,(t_0) = \lambda_0$)

3. Compute the optimal control action (u^*) at the current time-step by applying Equation 4.52 by trying a set of candidates.

4. Compute the state derivative $f(x,\ u^*,\ \lambda,\ w,\ t)$ and integrate to obtain the state x in the next time-step.

5. Compute the co-state derivative by Equation 4.54 and integrate to obtain the co-state vector λ in the next time-step.

6. Repeat steps 3-5 until the end of the problem.

7. If the target state at the end of the problem is achieved ($x(t_f) = x_{t_f}$), λ_0 was a good guess, otherwise modify λ_0 and repeat steps 3-6.

Figure 4.81 shows a scheme of the solution algorithm explained in points 1-7.

An important issue for numerically solving the PMP is that the ordinary differential equations for co-state integration are generally ill conditioned and lead λ to blow even with tight tolerances. In the case of HEVs, the following simplification is usually considered to avoid co-state integration: consider that the Lagrangian cost is the fuel consumption ($L = m_f$)

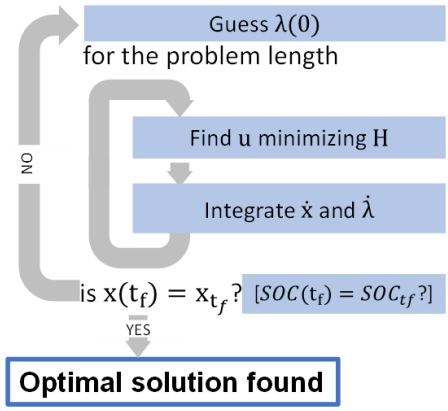

Figure 4.81: PMP solution algorithm.

and the state of the problem is the battery state of charge ($x = SOC$). Then, from Equation 4.54, Equation 4.56 is obtained.

$$\dot{\lambda}(t) = -\frac{\partial H}{\partial x} = -\frac{\partial m_f}{\partial SOC} - \lambda \frac{\partial f}{\partial SOC} \tag{4.56}$$

where the first term on the right-side is clearly 0, since the fuel consumption depends on the engine speed and throttle (that also depend on the power-split) but does not depend explicitly on the SOC. The second term represents how the battery behavior depends on the SOC, so if the battery parameters (R, V_{oc}) do not depend on the SOC, the second term will be also 0, λ will be constant and the co-state integration can be avoided. This simplification is usually considered since strongly simplifies the online implementation. Note that provided a constant λ the Hamiltonian can be interpreted as an equivalent fuel consumption that includes both the fuel and a weighted battery power. This is the basis of ECMS, which, provided an equivalence factor (s) chooses the control candidate that minimizes at every time-step a weighted average of fuel consumption and battery power ($m_f + sPb$) according to Equation 4.57:

$$u^*(t) = \arg\min_u m_f + sPb \tag{4.57}$$

Note the similarity between Equations 4.52 and 4.57. In the same way than with PMP, a shooting method is required to find the proper value of s. As s approaches 0, the use of the battery becomes cheaper, which leads to lower fuel consumption but also battery depletion, on the contrary, an

excessively high value of s will lead to battery overloading and high fuel consumption. A target SOC at the end of the cycle (usually equal to the initial value in HEVs and to the minimum allowed SOC in the case of PHEVS) provides the closing condition for the shooting method. As the proper value of s depends on the driving cycle, the shooting method requires several runs of the driving cycle to find the proper value, which is only possible for offline optimization. For online implementation, since the optimal value of s is unknown a priori, its value would be online adapted according to the difference between the measured and the target SOC, usually with a PID.

Modifications to deal with oscillating behavior

In order to make the proposed control strategy more robust, general and be able to deal with xEVs having different possible modes (e.g., series, parallel) and considering other system states (i.e., the engine coolant temperature) some modifications were introduced.

Under certain circumstances, the direct application of Equation 4.57 can produce policies resulting in poor drivability or even undesired behavior due to the potentially abrupt transitions between torque requests. As the ECMS is a greedy algorithm, i.e. minimizes the cost function at each stage without considering future consequences of the current choice, two consecutive ECMS functions can have completely different local minima, then leading to completely different control actions, e.g. engine torque demands. Note that abrupt changes in the control actions will lead to transient processes in the actual plant that are not considered by the model, so the real behavior can deviate from the expected one. This situation usually happens when Equation 4.57 is non-convex and two local minima can be near in terms of engine speed but far in terms of torque. A conceptual example is provided in Figure 4.82 where Equation 4.57 is plotted for different engine torque demands (i.e. control decisions) and engine speed (problem disturbance). It may be observed that the surface has two local minima and that for close values of engine speed around 2000 rpm the minimum jumps abruptly from 40 to 80 Nm. So eventually if the vehicle speed varies in a way that engine speed is around 2000 rpm, the demanded torque will continuously oscillate between 40 and 80 Nm, which despite is optimal for the model, is probably far from minimum fuel consumption and acceptable drivability in the actual powertrain.

To cope with this undesired behavior the following modification of Equation 4.57 was implemented as observed in Equation 4.58:

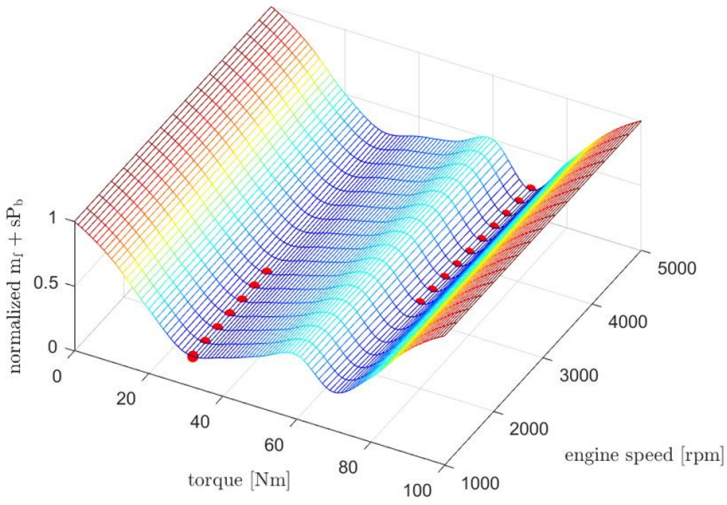

Figure 4.82: Example of non-convexity in Equation 4.57 leading to strongly different torques minimizing the cost function at two similar engine speeds.

$$\begin{aligned} u_k^* = \arg\min_u \big\{ & P_f(u_k) + sP_b(u_k) + C_{ON} u_{on,k} + C_{du}(u_k - u_{k-1}) \\ & + C_\infty((u_k - u_{k-1}) > \overline{du}) + C_\infty((n_k^e ng - n_{k-1}^e ng) > \overline{dn^{eng}}) \big\} \end{aligned} \tag{4.58}$$

where the optimal control at time-step k (u_k^*) is calculated by adjoining a cost for different terms:

- $P_f(u_k) + sP_b(u_k)$ is the direct application of the ECMS, with the particularity that fuel power ($P_f = \dot{m}_f H_c$, where H_c is the fuel heating power) instead of the fuel mass flow is used to allow the s parameter to be non-dimensional.
- C_{ON} represents the marginal cost of switching on the engine.
- C_{du} is the marginal cost associated to the engine throttle variation.
- C_∞ is an arbitrarily large cost to avoid throttle variations above certain threshold ($\overline{du}$) or, in the case of series mode where the engine is decoupled from the wheels, engine speed variations above a given limit ($\overline{dn^{eng}}$).

Note that C_{ON}, C_{du}, C_{∞}, $\overline{du}$ and $\overline{dn^{eng}}$ are calibration parameters that will depend on the problem addressed.

ECMS modifications to deal with the engine thermal state

It has been proven that engine thermal state plays a major role on its performance [137]. In this sense, provided that the engine efficiency (and potentially emissions) are strongly affected by the engine thermal state, the impact of including this variable in the energy management strategy was evaluated.

Considering that the actual engine behaves as the complete model presented in section 4.7.1, including the lumped-heat transfer model of Equation 4.35 and its impact on fuel consumption represented by Figure 4.77. Then, the coolant temperature becomes an additional state of the problem since maps past decisions (engine torque demand, so fuel injection) on future revenues and costs (fuel saving because the engine is warmed up or fuel penalties if the engine is cold due to lack of operation in previous time-steps). In this sense, the Hamiltonian presented in Equation 4.51 (or alternatively the ECMS cost function in Equation 4.57) should be upgraded with an additional state. Accordingly, for this case, Equation 4.51 was modified into Equation 4.59.

$$H' = \dot{m}_f + \lambda'_b \dot{E}_b + \lambda'_c \dot{\theta}_c \tag{4.59}$$

where $\dot{E}_b$ is the variation of the Energy stored in the battery, $\dot{\theta}_c$ is the variation of the coolant temperature, $\dot{m}_f$ is the fuel consumption and λ'_b and λ'_c are the co-states associated to battery and coolant. Note that multiplying the fuel consumption by the fuel heating power and the engine temperature by an equivalent thermal capacity of the cooling circuit allows to use non-dimensional co-states and power units for H as presented in Equation 4.60.

$$H = \dot{E}_f + \lambda_b \dot{E}_b + \lambda_c \dot{E}_c \tag{4.60}$$

where $\dot{E}_f$ is the rate of reduction in the energy in the fuel tank, $\dot{E}_b$ is the rate of reduction in the energy stored in the battery, and $\dot{E}_c$ is the reduction in the energy stored in the engine thermal state ($\dot{E}_c = -C_c \dot{\theta}_c$). It can be observed that there is some intuition beyond the application of PMP in Equation 4.60, since H represents the rate of reduction in the energy stored (in any form) in the powertrain, and the co-states λ represent the marginal cost of the battery and thermal state. In this sense,

minimising Equation 4.60 implies that the energy stored in the powertrain is maximized.

Recalling Equation 4.54 for the co-state associated to the engine thermal state the Equation 4.61 is obtained .

$$\dot{\lambda}_c(t) = -\frac{\partial H}{\partial E_c} = -\frac{\partial H}{\partial(-C_c\theta_c)} = \frac{H_p \partial m_f}{C_c \partial \theta_c} + \lambda_c \frac{C_c \partial \dot{\theta}_c}{C_c \partial \theta_c} \tag{4.61}$$

where the fuel heating power and the coolant circuit thermal capacity are assumed constants and the battery efficiency is considered independent on the engine coolant temperature. A simple look on Equation 4.61 shows that λ_c will evolve during the driving cycle since the first term is different than 0 (at least during the warm up) due to the coolant temperature effect on engine efficiency and fuel consumption, and the second term will be also different than 0 since the heat transfer in the cooling circuit depends on the coolant temperature (see Equation 4.35). In this sense, the ECMS approach considered for the battery (constant λ_b) cannot be considered for the coolant temperature and λ_c is not constant. Further analysis of Equation 4.61 shows that the first term on the right side will be non-negative ($\frac{H_p \partial m_f}{C_c \partial \theta_c} \geq 0$) since reducing the coolant temperature involves an increase in fuel consumption (reduction in efficiency), and the term multiplying the co-state is non-positive ($\frac{\partial \dot{\theta}_c}{\partial \theta_c}$) since increasing the coolant temperature will lead to lower heat coming from the combustion process (higher efficiency) and higher heat transfer with the environment. Provided that, in principle there is not any constraint on the terminal state of the coolant temperature, the application of Equation 4.55 leads to $\lambda_c(t_f) = 0$. Hence, $\lambda_c(t_0)$ should be a value leading to $\lambda_c(t_f) = 0$ after integration of Equation 4.61 during the driving cycle. For the control-oriented model considered in the present project, combining Equation 4.61 with Equation 4.33 and Equation 4.35 with the 3D map presented in Figure 4.77, leads to Equation 4.62.

$$\dot{\lambda}_c(t) = \left(-\lambda_c k_{1c} - H_p \frac{\partial h(n, \alpha, \theta_c)}{\partial \theta_c}\left(\frac{1}{C_c} - k_{2c}\lambda_c\right)\right) \tag{4.62}$$

That can be integrated to compute the evolution of λ_c. Therefore, considering the engine thermal state, leads to a Initial Value Problem, with two initial values to determine: s (provided constantλ_b) and λ_c. Both values can be obtained by a shooting method until the desired final SOC

and $\lambda_c(t_f) = 0$ are reached. In practical cases, due to the complexity of numerically integrating Equation 4.61, it is difficult to reach $\lambda_c(t_f) = 0$ and the value of $\lambda_c(t_0)$ is chosen in a way that minimizes fuel consumption. A similar approach to that followed in this model can be found in [135].

ECMS modifications to account for different powertrain modes

The ECMS is prepared to work with series and parallel architectures with different gear ratios. To this aim, there are several optimizations running at the same time which provide the optimal control outputs (demanded torques for the ICE and electric machines) and the associated cost of every mode. Then in a second optimization stage, the best option amongst the available modes is selected. Figure 4.83 shows the general scheme followed:

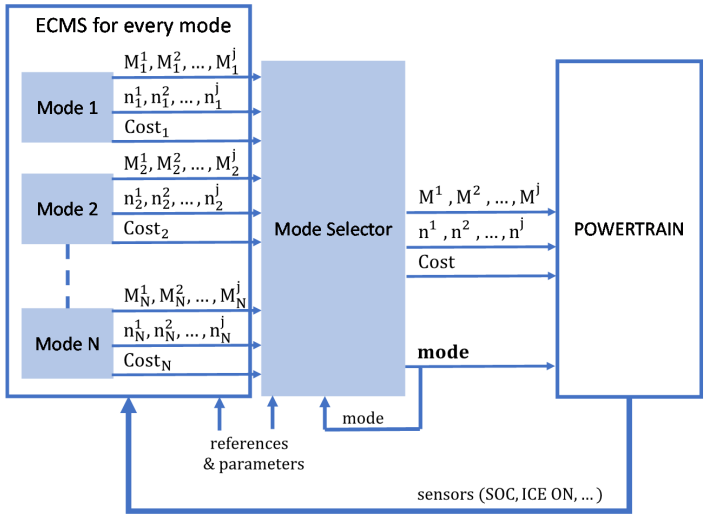

Figure 4.83: Scheme of the extension of the ECMS to integrate several (N) modes and the corresponding torque and speed demands of the j engines and electric machines.

1. The ECMS is applied independently for the N modes available in the powertrain. In this sense, for every powertrain mode i, the optimal speed and torque for any of the j engines and motors (n_i^j , M_i^j) with its corresponding minimum cost ($Cost_i$) is calculated.

2. The previous information arrives to the mode selector, where the option with minimum cost is chosen. Directly comparing the cost of

the different modes might result in a highly oscillating control policy, especially since the model barely addresses the system dynamics, that will not produce desirable results when applying the control to the actual powertrain. It should be recalled that, every time a switch between modes is carried out, the powertrain experiences a transient that the model is not able to consider. To cope with this issue, the following optimization is proposed (Equation 4.63):

$$u^*_{mode,k} = \arg \min_{i \epsilon [1,N]} \sum_{k-\Delta k}^{k} \left\{ Cost_{i,k} + C_{dmode}(i - u^*_{mode,k-1}) + C_{mode,i} \right\} \tag{4.63}$$

where $u^*_{mode,k}$ is the optimal mode to be applied at time-step k, $Cost_{i,k}$ represents the cost of mode i at time-step k, C_{dmode} is the cost of modifying the mode (so is 0 if the same mode than in previous time-step is employed) and $C_{mode,i}$ is an artificial cost to avoid the use of a particular mode (e.g. to ban the use of series mode in a vehicle which has parallel architecture exclusively). Finally, Δk is a parameter to consider the mode minimizing the cost during a given time window instead of the instantaneous one. Note that C_{dmode}, $C_{mode,i}$ and Δk are parameters to calibrate.

5

Thermal management strategies

5.1 Introduction

In this chapter, different thermal management strategies implemented in the components of the hybrid powertrain are presented. In first place, independent thermal strategies were implemented for the ICE, battery and EDS. Then, integrated thermal strategies were developed and evaluated in order to study the synergies among the thermal flows of the hybrid powertrain. Finally, a novel energy management control strategy which considers the thermal state of the engine for the power split control is detailed.

5.2 ICE thermal management strategies

5.2.1 Hydraulic circuits mass variation of the ICE

Introduction

In this section, the impact on ICE engine performance and efficiency produced by hydraulic circuits mass variation is evaluated. For this, the original layout of both cooling and oil circuits was modified reducing the volume of the circuits. For the cooling circuit, only the ducts external to the engine structure were modified (ie, their length was reduced). The galleries of the engine together with the radiator were not modified maintaining the cooling performance of the system. For the oil circuit, the volume of the oil sump was exclusively modified. The feasibility of this modification was considered possible according to the literature presented. For this, the Diesel ICE model detailed in Chapter 4 was used as fundamental tool for performing the simulation studies. All submodels of the engine were modelled with VEMOD software and validated with experimental measurements. Then, simulations in both steady state and transient conditions were launched according to a design of experiments. Finally, the most relevant results are discussed.

Simulations and results

After the model validation (detailed in Chapter 4), a parametric study based on reducing the volumes of coolant and oil circuits was performed.

As it was stated before, only the volumes outside the engine block were modified for the simulation considering that modifying the main structure of the engine (i.e. engine block galleries, piston gallery...) was not practical. For the coolant, the pipe lengths was diminished till 10 % as an extreme case. Consequently, the results obtained will show the impact of the circuit layout design and the maximum achievable gain. Additionally, this modification will not impact the maximum cooling capacity of the system. For the oil circuit, only the oil sump volume was reduced. This could be implemented in production engines by means of valves.

In order to reduce the number of simulations, a design of experiments (DoE) consisting of five cases was simulated. For the DoE (Table 5.1), the original volumes of the hydraulic circuits were taken as the base case. Then, in order to distinguish between the impact produced by coolant and oil, one circuit volume was reduced while the other was not modified as it can be seen in Table 5.1. Finally, a case modifying both volumes was also simulated. With these five cases, all possible modifications could be interpolated and maximum gains could be studied. The extreme cases, were considered as a limit and would implicate a strong decrease of pipes length. The real implementation of these modifications would imply a new coolant and oil pumps because the hydraulic resistance curve of the circuits would be altered. Thus, coolant and oil with different efficiency maps would be needed.

Given the nature of the experiment, the results did not show any significant impact on engine performance as it was expected in stationary conditions. Since the main effect of changing volume will be related to thermal inertia, this has no impact on steady state conditions. Additionally, this modification will not impact the maximum cooling capacity of the system since the original volume of the radiator has not been reduced because during the warm up period the coolant does not flow through the radiator branch. Although the total volume of the coolant circuit has been varied and its hydraulic losses have also been modified, engine coolant flow has not been significantly affected. Consequently, coolant temperature drop through the engine has not varied. Thus, any effect related to the cylinder wall temperatures has been soothed. For the same control configuration, reducing the circuits mass, leads to an increase on the temperature at which the whole system is stabilized. Thus, an improvement of the combustion processes is observed but it was not considered a consequence of the present strategy, only a matter of thermostat control settings. Thus, although the simulations were launched both in steady

state and transient conditions, only the latter ones are presented.

Table 5.1: Features of the used engine in the validation of the lumped model

Case	Coolant volume	Oil volume
Base	100%	100%
Case 1	10%	100%
Case 2	100%	10%
Case 3	55%	55%
Case 4	10%	10%

Transient simulation

In transient conditions, a significant impact was observed in engine warm up due to the fact that the thermal inertia of the system was reduced. In addition, the increment of the oil temperature reduced its viscosity and, consequently, the friction losses decreased, reducing the fuel consumption.

Ambient conditions (20°C)

In Figure 5.1, the evolution of the coolant temperature and the oil temperature for ambient conditions at 20°C can be seen in its two plots. In each plot, five curves show the temperature evolution of coolant and oil during the WLTC cycle. Each curve belongs to a particular case of the DoE in which the masses of both circuits were reduced. The base case represents the original mass of the hydraulic circuits, this case is compared with the case of maintaining the coolant mass while decreasing in 90% the mass of the oil circuit and the other way around. In the central point of the DoE a reduction of 45 % of both masses was also simulated. Overall, it is observed that the higher the thermal inertia (more fluid mass) the lower is the increase of both coolant and oil temperatures. In the plot of coolant temperature evolution, it is clear that the fastest increase is produced when both masses are reduced in 90 % reaching 80 °C in approximately 730 s. However, due to the nature of the thermostat opening control (wax thermostat), the coolant temperature stabilizes around 93°C. This is confirmed when analyzing oil temperature evolution plot, in which there is no thermostat in the circuit, thus, the oil temperature tends to stabilize around 100°C for the five cases. Furthermore, it is also visible that modifying the coolant mass has more impact than reducing the oil

mass when it comes to fasten coolant temperature increase. The same behavior is also observed in the plot of the oil temperature evolution. This is explained because there is more heat rejected to the coolant circuit than to the oil. Thus, reducing the thermal inertia of the coolant has more impact on increasing the temperature evolution. Taking into account that coolant and oil circuit are interconnected by the oil cooler. This is the reason why decreasing the thermal inertia of the oil circuit while maintaining the coolant mass hardly contributes to increasing oil temperature because the impact is limited by the oil cooler.

Figure 5.2 shows the accumulated of the heat rejected to the coolant and oil fluids until thermostat opening in ambient conditions. These plots justify the temperature evolution seen in Figure 5.1. As it can be seen in the upper plot of the Figure 5.2, the accumulated heat rejected is maximum for the base case and it decreases with the reduction of both coolant and oil volumes. The heat rejected to both coolant and oil circuits is strongly dependent on the temperature drop between the structural parts of the engine and the fluid. When the thermal inertia of the fluids is reduced, an increase of the fluid temperature is produced and, consequently, the temperature drop is diminished. For the case of heat rejected to the coolant, this is mostly influenced by the reduction of coolant volume while the oil reduction shows less impact. This is demonstrated in the b) plot of the Figure 5.2. However, it is not clear for the heat rejected to the oil as the bottom c) plot shows. Both, reduction of the coolant and oil volume seem to have similar significance on the heat rejected to the oil. This is better seen in Figure 5.3 where the reduction of the accumulated heat in the whole cycle is shown according to the reduction of both coolant and oil volumes. In the case of heat rejected to the coolant, it is observed that the isolines are practically vertical, which indicates the almost only dependence on the reduction of the volume of coolant. In the case of heat rejected to oil, the isolines form an angle of approximately 45 % indicating the same dependence with both the reduction in the volume of the coolant and that of the oil. In the case of total rejected heat, it is observed that the isolines have a slight inclination, which indicates that their dependence is greater with the reduction of the volume of coolant than with that of the oil.

Figure 5.4 shows a map of the estimated results by the model on accumulated fuel consumption and friction power in ambient conditions during the WLTC cycle. It is observed that the by reducing a 90 % both volumes during warm up time, the fuel saving obtained were around 1.2 %. Since

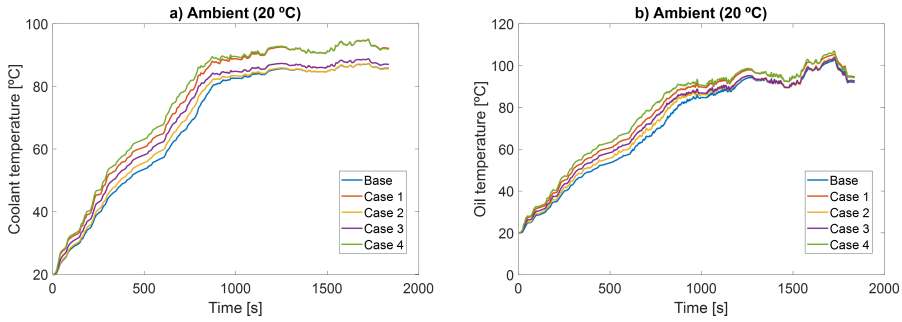

Figure 5.1: Coolant (a) and oil (b) temperature evolution for each case during a WLTC cycle in ambient conditions.

the oil viscosity decreases with temperature, a reduction on friction losses of about a 4.5 % was obtained when reducing both volumes by a 90%. This is explained taking into account the benefits produced by having higher coolant and oil temperatures during the engine warm up time. From one side, higher coolant temperature is directly translated in higher in-cylinder wall temperatures which increase the combustion efficiency. Furthermore, the reduction in oil viscosity and friction losses also contributes to reduce fuel consumption. Additionally, decreasing the coolant volume by 45 % produces a reduction in warm up time and fuel consumption of 7 % and 0.4 % respectively.

Finally, the warm up time reduction obtained for coolant (a) and oil (b) is presented in Figure 5.5. In the left plot, it is observed that reducing the oil volume to 10 % leads to a reduction of 4 % in the warm up time. If the same volume modification is applied to the coolant volume, approximately a 11 % of warm up time reduction is obtained. The right plot, shows that oil warming process has more dependency on oil volume modification as it was stated previously. For instance, reducing the oil volume to 10 % while maintaining the base coolant, reduced 7 % the oil warming process.

Cold conditions

In cold conditions, the results obtained in the simulations showed a similar trend as in the ambient ones. Both coolant and oil temperatures evolution starting from -7 °C are shown in the plots of the Figure 5.6. Although the temperatures evolution for the different cases showed a similar behaviour as the one observed in ambient conditions, warm up time increased since

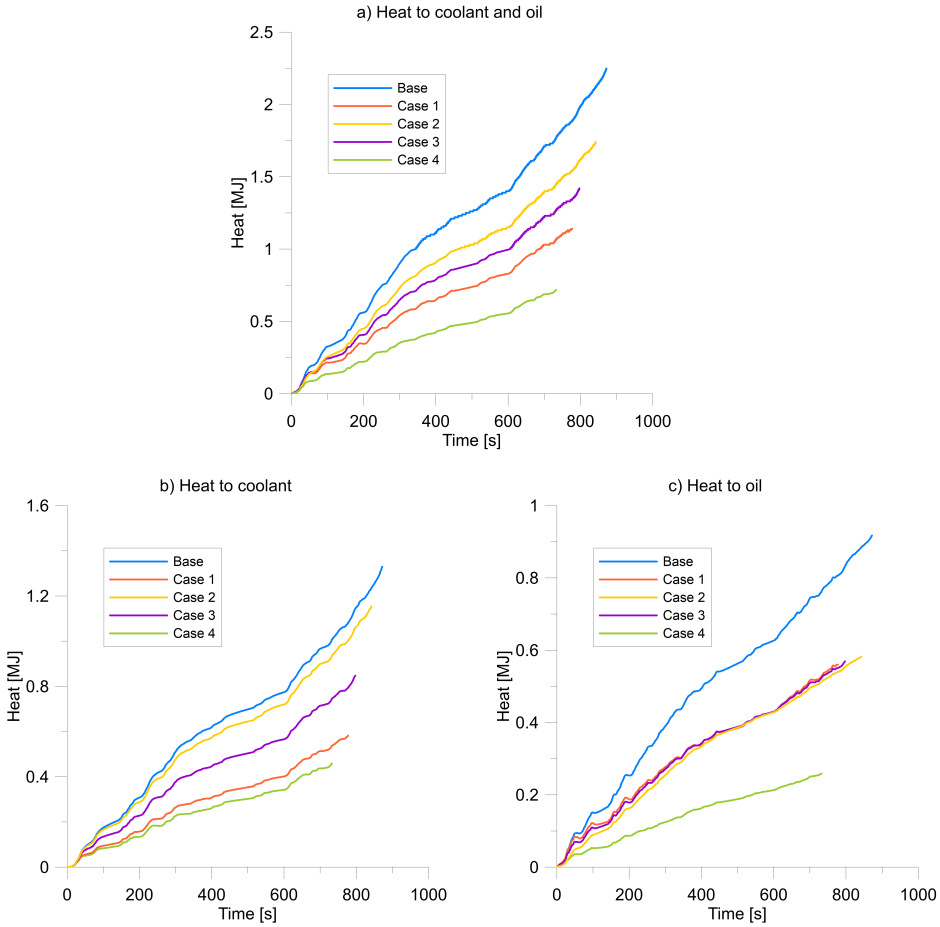

Figure 5.2: Evolution of heat rejected to coolant and oil until thermostat opening in ambient conditions

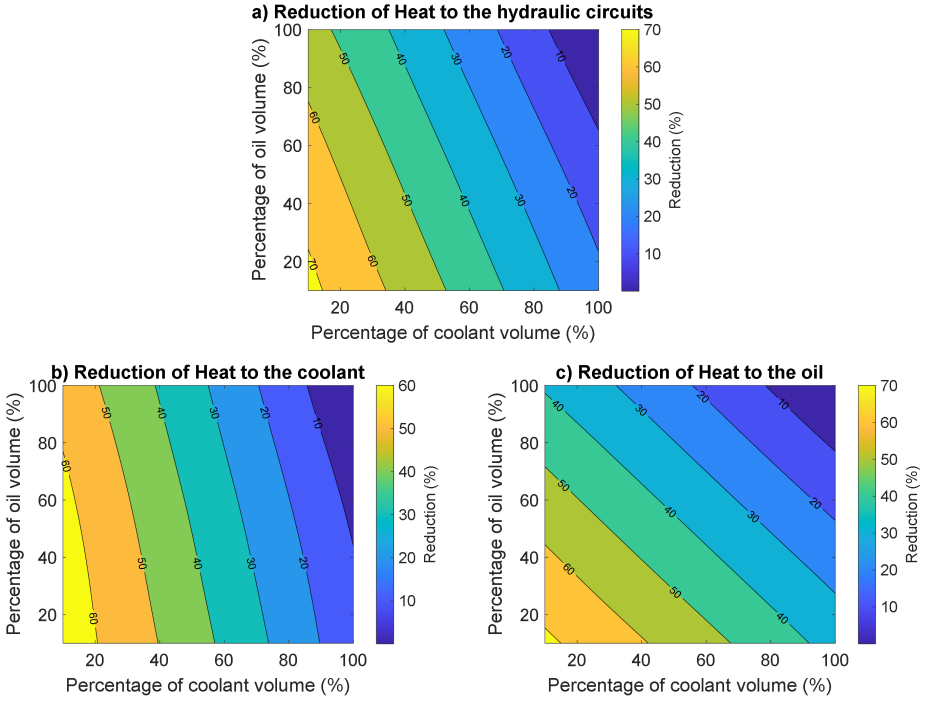

Figure 5.3: Map of heat to coolant and oil in ambient conditions

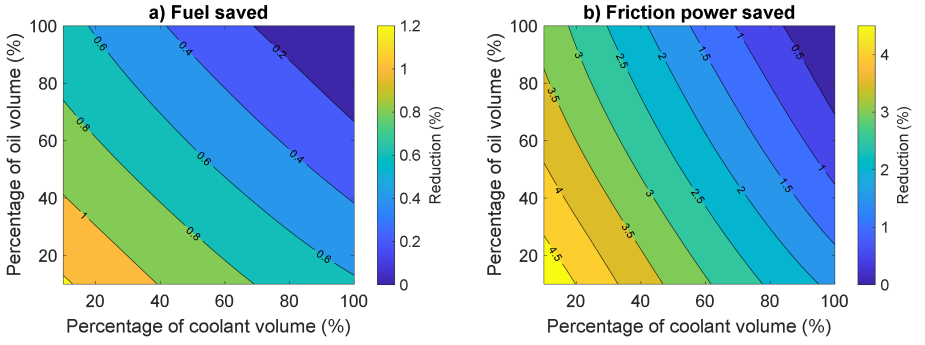

Figure 5.4: Fuel consumption (a) and friction reduction (b) in ambient conditions

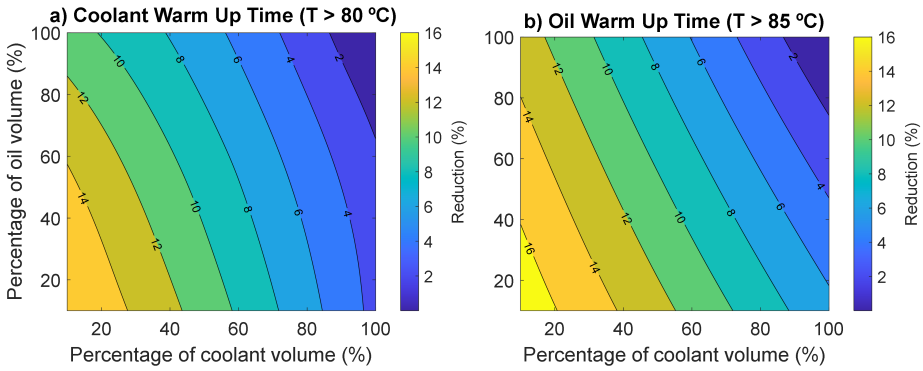

Figure 5.5: Warm up time reduction in ambient conditions

the engine initial thermal state was colder. Regarding the heat rejected to the hydraulic circuits, Figure 5.7 shows that reducing the coolant circuit volume had more impact in the heat rejected to the coolant than reducing the oil volume. For the heat rejected to the oil, variation of both circuits volume had similar impact on reducing the heat evacuated to the oil. For instance, decreasing the volume a 50 % of any circuit, would reduce the heat rejected to the oil in 24 %. Although the tendency was similar for ambient and cold conditions, the accumulated heat rejected to the hydraulic circuits during the warm up time was significantly higher for the cold simulations as it can be seen in Figure 5.8. Furthermore, for the base case, the accumulated heat rejected to both circuits was almost 30 % higher (2.25 MJ and 3.25 MJ for ambient and cold conditions respectively). This is because both coolant and oil circuits started at much lower temperature. Consequently, more energy was required during the engine warm up time.

As it was expected, the fuel consumption savings in cold conditions were higher than the ambient case. Figure 5.9 shows that a reduction of 1.8 % of fuel consumption could be achieved if the volumes of both circuits are reduced to the 10 % during warming up time period. Additionally, the friction losses decreased more than 9 %. Similarly, decreasing the coolant volume a 45 %, showed a reduction of warm up time and fuel consumption of 13 % and 0.5 % respectively. Similarly to the ambient situation, reducing the thermal inertia of the coolant directly increases the coolant temperature. This contributes to improve combustion efficiency. Additionally, given the low oil temperature at the begging of the cycle, the reduction in friction losses strongly contributes to reduce fuel consump-

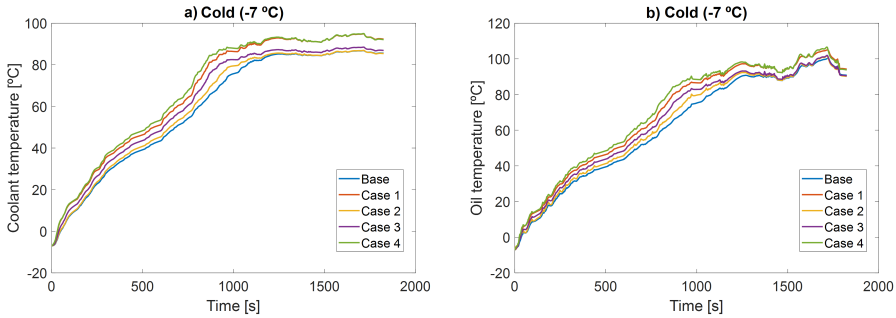

Figure 5.6: Coolant (a) and oil (b) temperature evolution for each case during a WLTC cycle in cold conditions

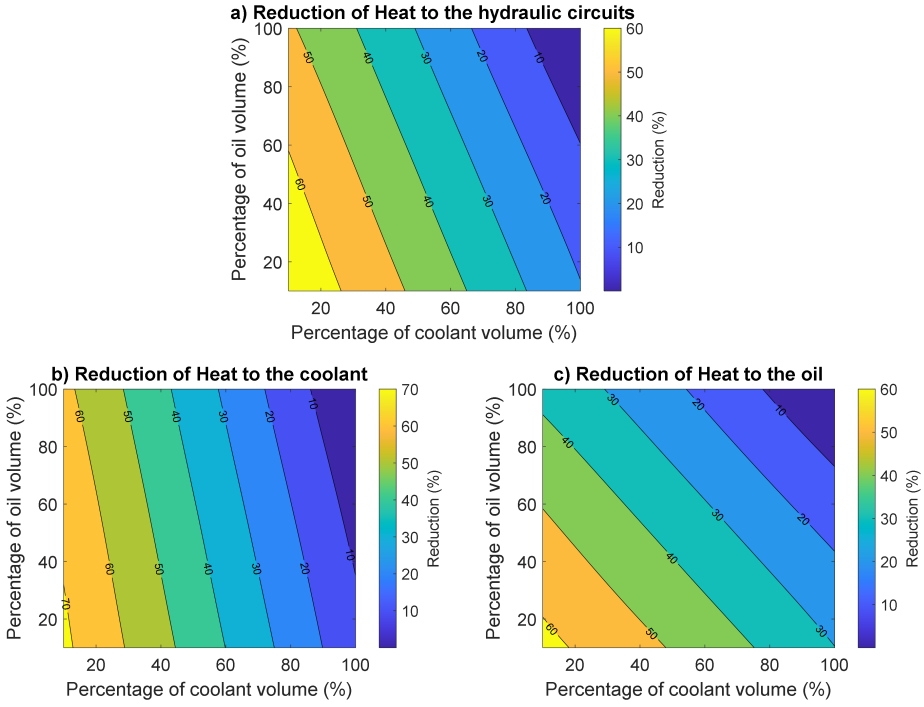

Figure 5.7: Evolution of heat to coolant and oil in cold conditions

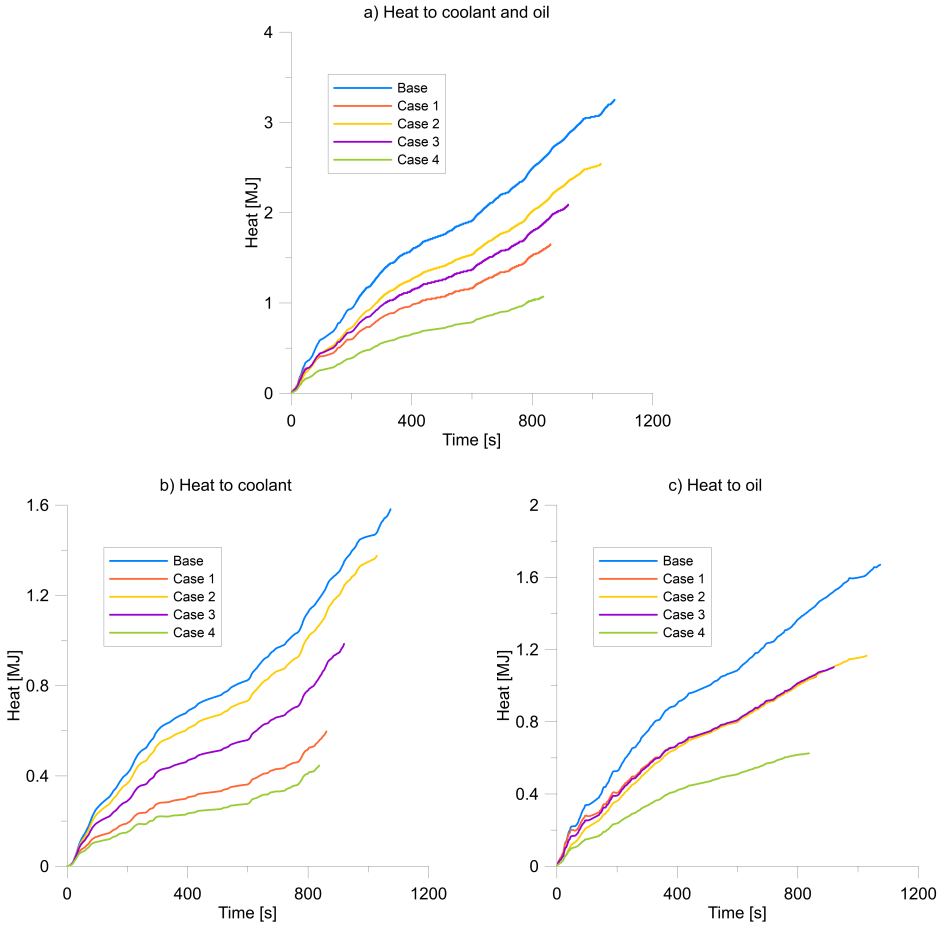

Figure 5.8: Map of heat to coolant and oil in cold conditions

tion. It is important to note that both volumes reduction contribute to combustion efficiency and friction losses improvement.

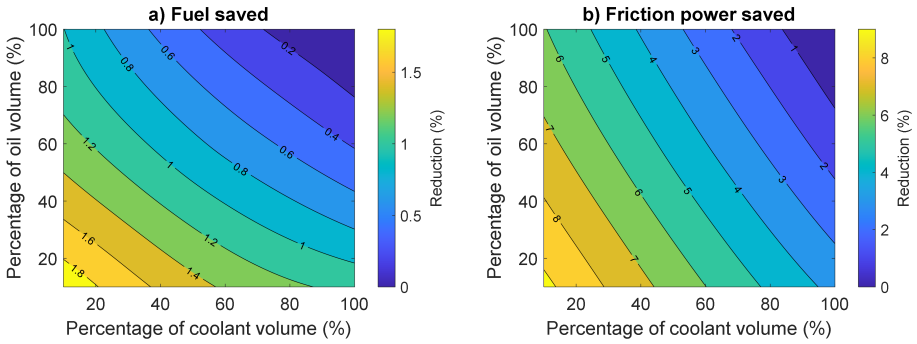

Figure 5.9: Fuel consumption (a) and friction reduction (b) in cold conditions

Finally, the warm up time reduction is presented in Figure 5.10. Similarly to the ambient case, the warm up time reduction is more sensible to the coolant volume decrease. In this case, by reducing the oil volume a 90 %, the obtained gain in warm up is around 6 %. However, by reducing the coolant mass flow the same amount, the improvement is higher than 18 %. Additionally, nearly a 10 % of oil warm up reduction is achieved when the coolant volume is reduced a 50 %. It can also be seen that warm up time is more dependent on coolant volume for cold conditions than in ambient ones (See Figure 5.5 and Figure 5.10). This is because there is more heat rejected to the coolant than to the oil circuit. Thus, when reducing the coolant volume, its temperature increases much faster. Then, the coolant temperature heats the oil by means of the oil cooler during the engine warming process.

5.2.2 Insulation of the ICE exhaust manifold and ports

Introduction

In this section, the study on engine overall efficiency and outlet turbine temperature (T4) when thermal insulation of exhaust ports, exhaust manifold and turbine intake pipes of a Diesel ICE was implemented. A experimentally based methodology was followed for the model development and validation as it was detailed in Chapters 3 and 4. Additional to the baseline engine, the extreme case of adiabatic boundary conditions was

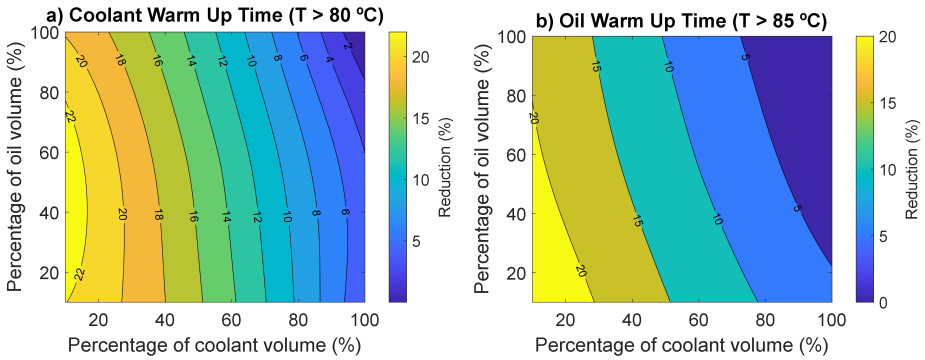

Figure 5.10: Warm up time reduction in cold conditions

simulated to evaluate the maximum possible impact. In other words, the walls of the eight (two for each cylinder of the engine) exhaust ports, the exhaust manifold and pipes before turbine were completely thermally insulted (made them adiabatic). In this way, the maximum possible gain can be studied. For that, the entire engine model was constructed and validated using VEMOD. Once the model was validated, the exhaust gas path until the inlet turbine were made adiabatic. In the following sections the results are analysed for steady state and transient conditions.

Steady-state results

The impact of making adiabatic the exhaust gas path on fuel consumption for low load (independently of engine speed) is practically negligible as Figure 5.11 shows. Additionally, the same results were observed for high engine speeds, indistinctively of the load. However, for low speed and high load the fuel consumption decreased around a 1 %.

As it was expected, by eliminating the heat transfer form exhaust line to the ambient, the gas turbine inlet temperature increased in all the considered cases since gas temperature is always higher than ambient temperature. For the case of low engine speed and load, T3 increased 30°C compared to the base case (see Figure 5.12). For high load and low engine speed the temperature gain reached 11 %. Finally, at high speeds, the temperature increased 39°C and a 85°C for low and high load respectively.

In Figure 5.13, the obtained results for turbine outlet temperature (T4) are shown. The behavior is very similar to the results commented for T3. The temperature increased a 6 % (for 1250 rpm and 25 % load), 11 % (for 1250 rpm and 100 % load) and 8 % (3500 rpm and 25-100 % load).

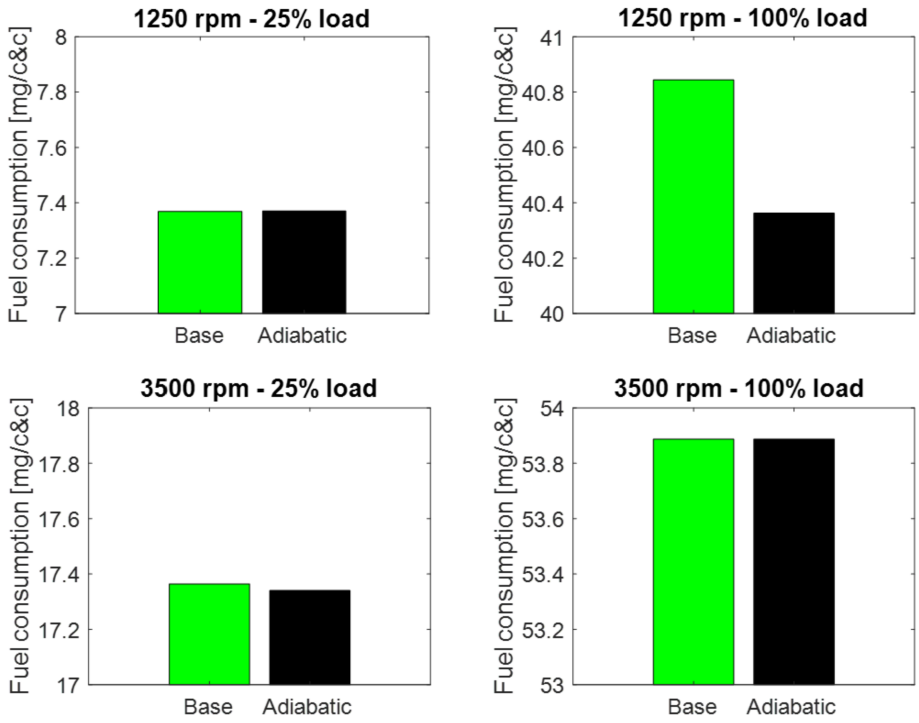

Figure 5.11: Results of the fuel consumption comparison between base and adiabatic cases for steady state conditions.

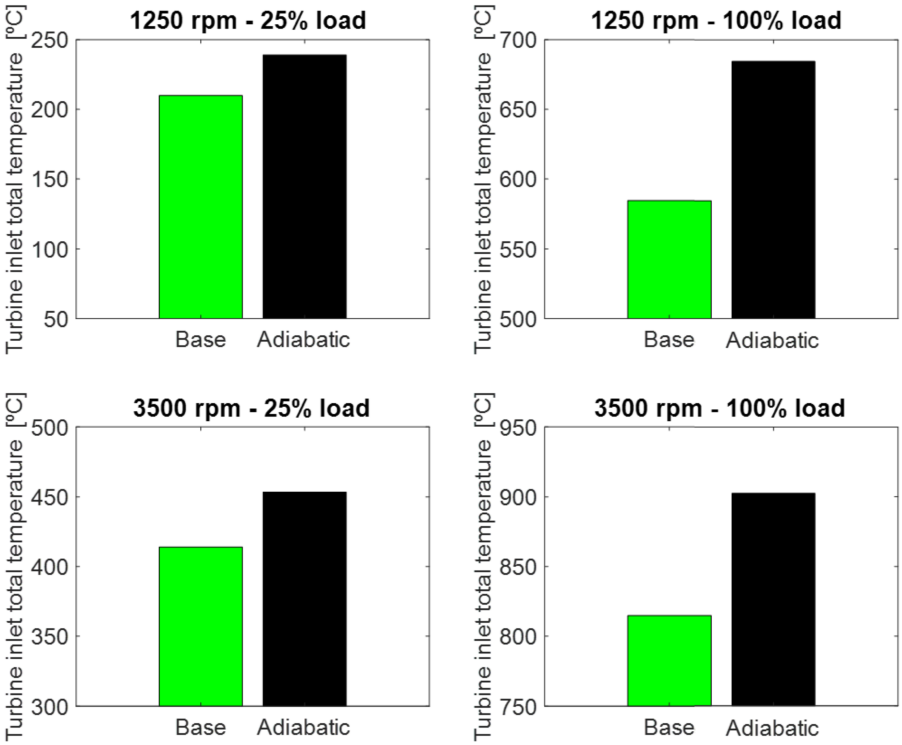

Figure 5.12: Results of T3 comparison between base and adiabatic cases for steady state conditions.

For both T3 and T4, the temperatures of the engine outlet are higher with the load increment, consequently the gains are higher when the load is increased. For low speed, the impact is more remarkable because the lower the gas speed in the pipes, the higher its residence time and therefore the higher time to exchange heat to the ambient (in the base case).

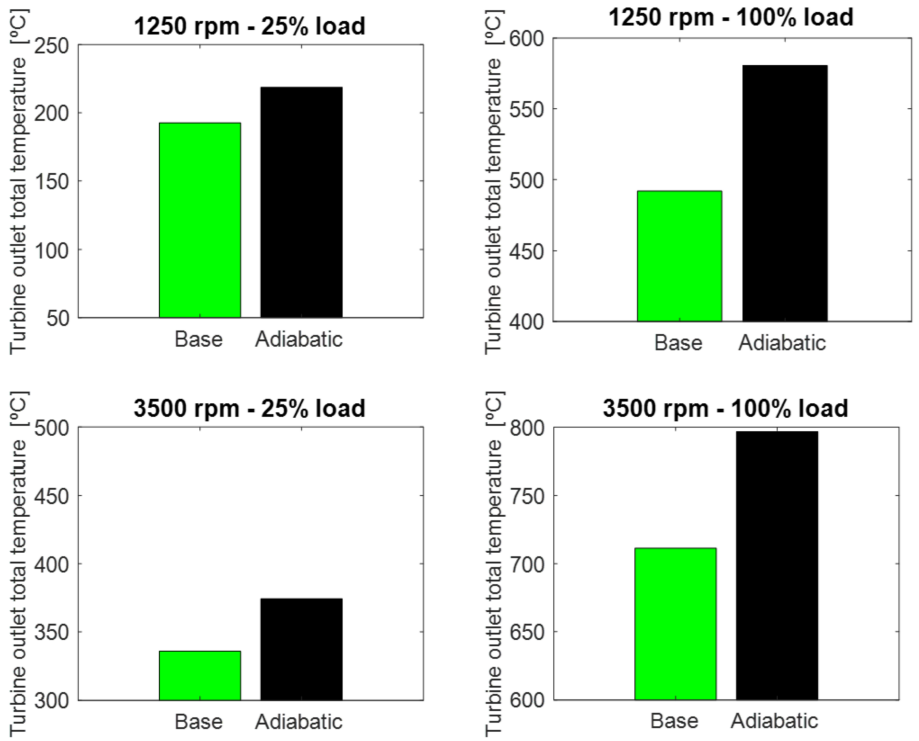

Figure 5.13: Results of T4 comparison between base and adiabatic cases for steady state conditions.

WLTC results

After the simulations in steady state, the WLTC transient cycle was simulated in ambient and cold conditions. In the following sections the most relevant results are plotted and analyzed.

Test starting from ambient temperature at 20°C

In Figure 5.14 the difference between the base and the adiabatic cases for accumulated fuel consumption, turbine energy, friction energy and heat to the coolant are plotted. For the case of fuel consumption, the adiabatic case shows more consumption during the engine warm up time. Around 800 s this trend changes and the fuel consumption decreases until the end of the cycle. This is because when the engine is cold, the friction losses are higher for the adiabatic case taking into account that the heat in the ports, instead of being rejected to the coolant (as it happens in the base line), is rejected to the exhaust gas increasing its enthalpy. So, coolant and oil temperatures are lower in the insulated case and therefore viscosity and hence friction losses are higher. In other words, during the first 800 s, the trade-off between fuel consumption reduction because of increased turbine power and fuel consumption increment due to higher friction losses (lower coolant and oil temperatures) is favourable, in this case, for the friction. Since the oil viscosity decreases with temperature, the friction losses increase is lower as the time increases as it can be seen in the plot. Notice that the accumulated values are plotted since it is difficult to appreciate the difference in instantaneous values. When the engine is already warm, the difference in accumulated fuel consumption starts decreasing. Now, the effect of turbine power gain is higher than the effect of the higher friction losses. Finally, the total heat rejected to the coolant showed a decreasing trend since the exhaust ports were isolated. The slope is higher towards the high and extra high regions due to the higher engine power demand. Although the overall fuel consumption decreases for the adiabatic case, the gain could be considered negligible in percentage. In the end of the WLTC cycle in ambient conditions, the accumulated fuel consumption reduction was 0.5 %.

In Figure 5.15, the T3 and T4 instantaneous evolution during the cycle are presented. Additionally, given the high variability of the gas temperature, the plots at the bottom of the Figure 5.15 show the quantity of time the T3 and T4 are higher to a certain value. For the adiabatic case, T3 is basically higher most of the cycle. However, for temperatures under 200°C, the base case has higher T3 when the engine is running in idle regime. This is because in those periods of time, in the base case the internal wall temperature of the pipes is higher than T3 and, then, the heat is transferred from the wall to the gas. Similar behavior was observed for T4, the adiabatic case showed a higher T4 for all the cycle. In this case, the singularity of the walls did not affect because the turbine was

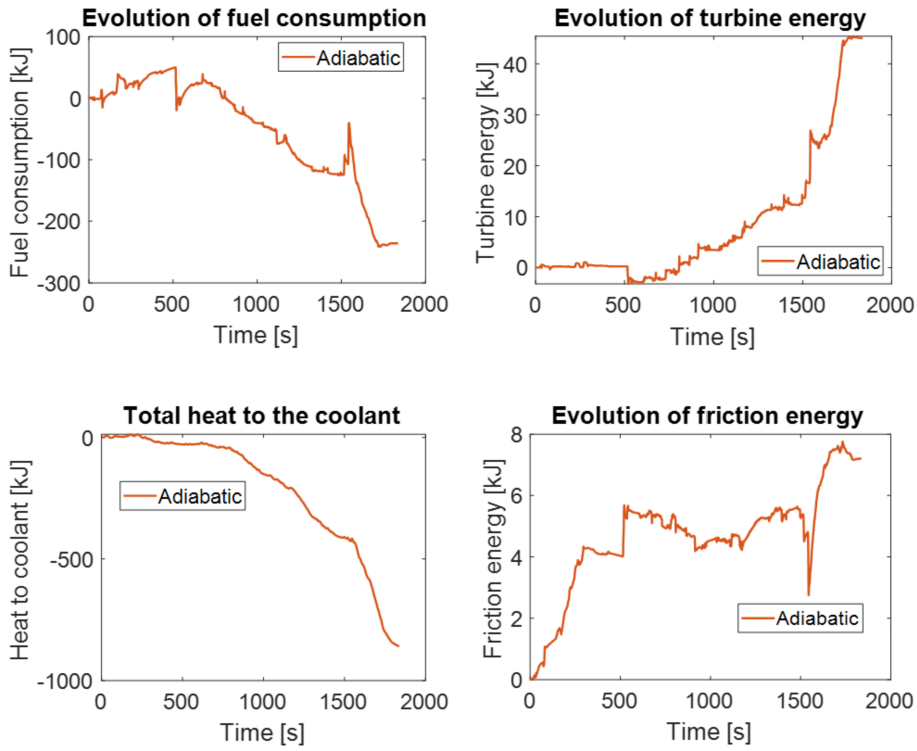

Figure 5.14: Results of accumulated comparison of fuel consumption, turbine energy, friction energy and heat rejected to the coolant between base and adiabatic cases for WLTC cycle in ambient conditions.

not thermally insulated.

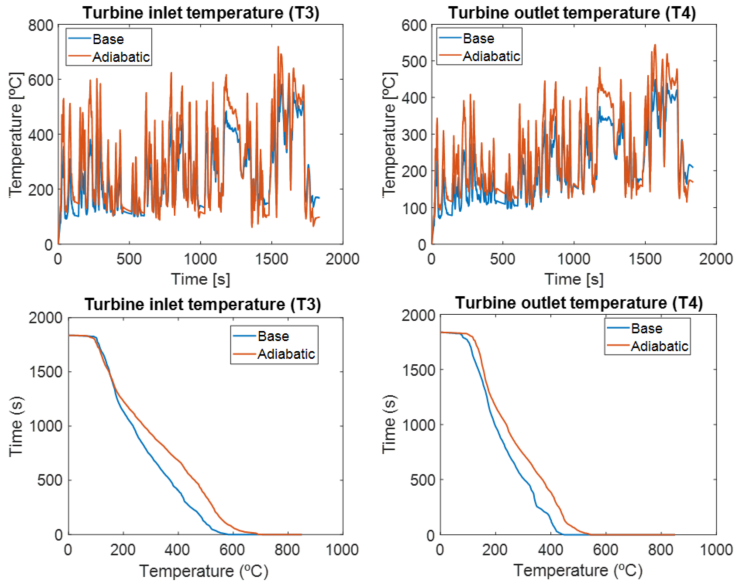

Figure 5.15: Results of T3 and T4 comparison between base and adiabatic cases for WLTC cycle in ambient conditions.

Finally, in Figure 5.16, the coolant temperature evolution is presented. The obtained warm up time (coolant temperature higher than 85°C) increase was 2 % (20 s).

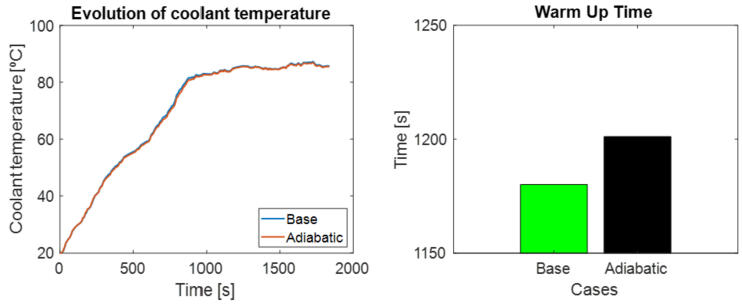

Figure 5.16: Results of coolant temperature evolution and warm up time comparison between base and adiabatic cases for WLTC cycle in ambient conditions.

Test starting from cold temperature at -7°C

In cold conditions, the fuel consumption, turbine power, friction power and the total heat to the coolant showed a similar behavior to the ambient conditions as it can be seen in Figure 5.17. However, the friction losses are higher during the warm up time and the gain obtained from the turbine is not enough to compensate these losses. Thus, the final accumulated fuel consumption is higher for the adiabatic case. It is important to note that the increment in fuel consumption is 50 kJ, which means less than 0.2 % of the total injected energy.

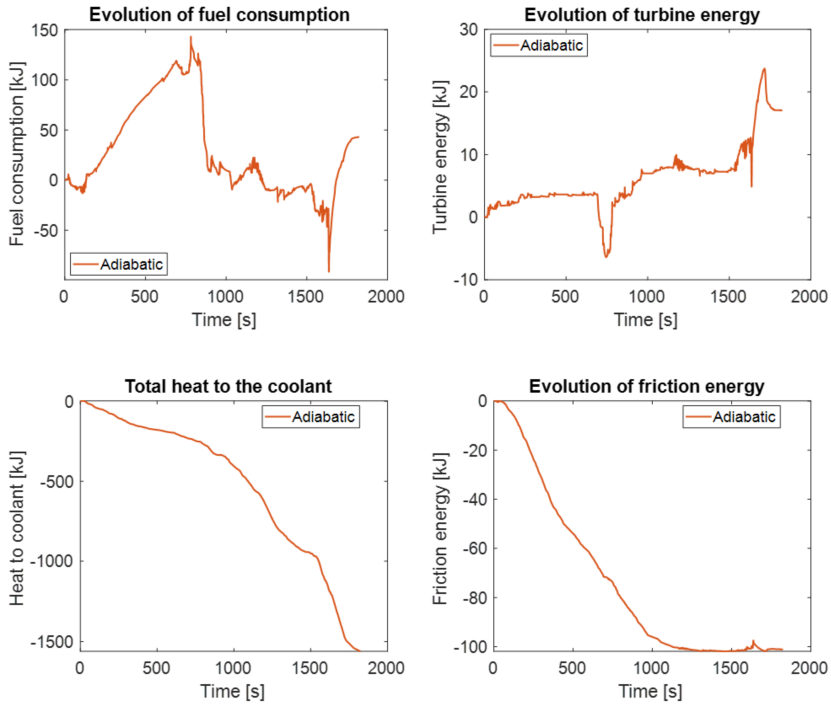

Figure 5.17: Results of accumulated comparison of fuel consumption, turbine energy, friction energy and heat rejected to the coolant between base and adiabatic cases for WLTC cycle in cold conditions.

In Figure 5.18, the T3 and T4 evolution in cold conditions are presented. For both, the adiabatic case, showed higher temperatures. T3 in the base case never reaches 600°C while, for the adiabatic, it reaches 760°C. For the T4, the maximum temperature is 500°C and 600°C for base

and adiabatic cases respectively. In the base case, during some parts of the cycle, the internal wall temperature is higher than the gas temperature (T3). This effect was also observed in ambient conditions.

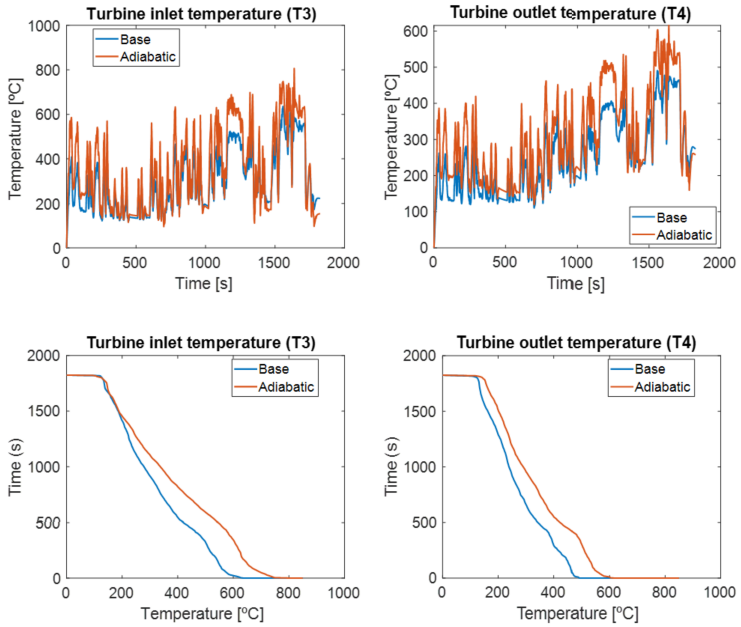

Figure 5.18: Results of T3 and T4 comparison between base and adiabatic cases for WLTC cycle in cold conditions.

Finally, Figure 5.19 shows the coolant temperature evolution in cold conditions for both cases: base and adiabatic. It can be seen that the temperature rises faster for the base case due to the heat rejected to the ports. Thus, the warm up time (coolant temperature higher than 85°C) is 10 % higher for the adiabatic case.

5.2.3 Nanofluids implementation in the thermal management system

Introduction

The assessment of the improvement of the engine thermal management system (ETMS) using nanofluids and nanoencapsulated phase change materials (NePCM) was performed using theoretical analysis and numerical simulation. A theoretical NePCM material with similar thermophysical

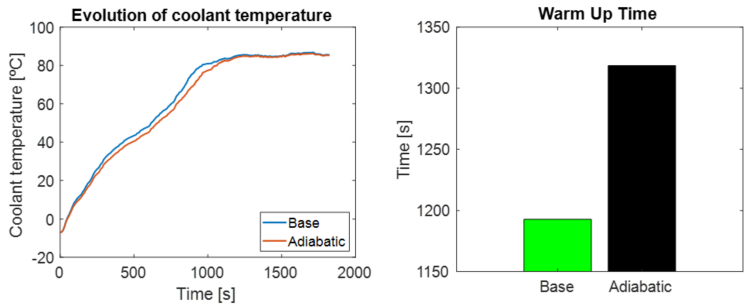

Figure 5.19: Results of coolant temperature evolution and warm up time comparison between base and adiabatic cases for WLTC cycle in cold conditions.

properties to the nanoparticle TiO2 was implemented. It was considered a nanofluid based on a composite of TiO2 and PCM with the desired melting point. An assessment of the applicability of nanofluids as coolants of a car engine by means of the use of ICE thermal model detailed in Chapter 4. This model simulates the temperature distribution in the block, piston and head-cylinder of the engine in function of the operating conditions. Simulations were performed for different nanoparticle concentration and their impact on engine heat transfer was evaluated.

Thermophysical properties of nanofluids

In order to compute the thermophysical properties of mixtures between coolants and nanoparticles the following formulas were used:

- Density: The studies about nanofluid density are quite limited and, in general, it is used the mixture theory [162]:

$$\rho_{nf} = (1 - \phi)\ \rho_b + \phi\, \rho_p \tag{5.1}$$

- Specific heat: As in the case of density, studies about nanofluid specific heat are limited and they generally use the thermal equilibrium [162]. The specific heat capacity of a nanofluid with NePCMs should take into account the contribution of the latent heat of the core of the NePCM. In this way, the specific heat capacity of the nanofluid,

c_{nf}, is obtained by:

$$c_{nf} = \frac{(1-\phi)\ \rho_b\, c_b + \phi\, \rho_p\, c_p}{(1-\phi)\ \rho_b + \phi\, \rho_p} + \frac{H_{NePCM}\phi}{\Delta T/3} sin\left(\frac{T - T_{onset}}{\Delta T/3}\right) \quad (5.2)$$

where the first term takes into account the contribution of the specific heat of the NePCM using the mixing rule and the second term takes into account the latent heat contribution of the NePCM cores. In the second term, H_{NePCM}, T_{onset} and ΔT are the phase change enthalpy, onset temperature and characteristic temperature width of the NePCM. The second term only contributes from T_{onset} to $(T_{onset} + \Delta T)$.

- Thermal conductivity: The thermal conductivity is one of the most important features of nanofluids since the most positive effects of the nanoparticle addition are presented. This fact has led to a widely researches in the open bibliography, where several models have been proposed in order to explain and predict its behaviour. However, a general agreement has not been reached due to the high variety of results found in the literature. Nevertheless, there seems to be agreement on the general trend which indicates an important increase in the thermal conductivity with the nanoparticle addition. One of the main theory is based on the formation of liquid nanolayers around the nanoparticles which explains the increase in thermal conductivity. In this work, the Yu and Choi correlation [163], Equation 5.3, has been chosen to predict the thermal conductivity of the mixture. It must be remarked that the mentioned correlation is based on the one proposed by Maxwell [164] by taking into account the existence of the mentioned nanolayers, i.e. using a conductivity for the equivalent nanoparticles that is shown in Equation 5.4.

$$k_{nf} = \frac{k_{pe} + 2\,k_b + 2\,(k_{pe} - k_b)\,(1+\beta)^3\,\phi}{k_{pe} + 2\,k_b - (k_{pe} - k_b)\,(1+\beta)^3\,\phi} k_b \quad (5.3)$$

$$k_{pe} = \frac{\left[2\ (1-\gamma) + (1+\beta)^3\,(1+2\,\gamma)\right]\gamma}{-\,(1-\gamma) + (1+\beta)^3\,(1+2\,\gamma)} k_p \quad (5.4)$$

The main problem of Equations 5.3 and 5.4 lays on the fact that no experimental data is allowable to predict nor nanolayer thickness δ neither nanolayor thermal conductivity k_l. In order to fulfil

this problem, a simplified case where the thermal conductivity of the equivalent nanoparticles and single nanoparticles are equal has been considered as it has been proposed in Mansour [165], where the ratio of nanolayer thickness and nanoparticle radio was considered constant and equal to 0.1. With these hypotheses, the predicted thermal conductivities will be slightly bigger than those predicted by the exact model. However, the deviations observed in low concentrations of nanoparticles (as the ones used in this work) are negligible.

- Viscosity: As in the previous cases, the diversity of results and models concerning nanofluids viscosity is fairly high. For this reason it was decided to use one of the benchmark model, established as reference in the majority of work on this subject. This is the one presented by Einstein in 1906 [166]. This model is applicable to very dilute suspensions of hard spherical particles, and neglects the interaction between the particles. Its expression is given in Equation 5.5.

$$\mu_{ef} = \mu_f \ (1 + 2.5\,\phi) \tag{5.5}$$

The thermophysical properties of both the water-ethylene mixture and the nanofluid are presented on Table 5.2.

Table 5.2: Thermophysical properties of the nanofluids components

Component	ρ [kg m^{-3}]	c [kJ kg K^{-}1]	k [W m^{-}1 K^{-}1]	μ 10^{-}6 [Pa s]
Water - Ethylene glycol 40 %	1011	3840	0.53	680.5
Nanoparticles (TiO_2)	4200	520	21.9	-

Overall, this model underestimates the experimental results obtained for nanofluids so it must be expected a too optimistic analysis by using it [167, 168, 169]. This will be taken into account when defining the conclusions. In Figure 5.20 it can be observed that density, thermal conductivity and viscosity are higher as the nanoparticule concentration increase due to the intrinsic properties of the nanoparticule. On the other hand, the specific heat increases with the concentration because of the latent heat absorbed by the PCM core as long as the PCM is activated (i.e., operating around its melting point).

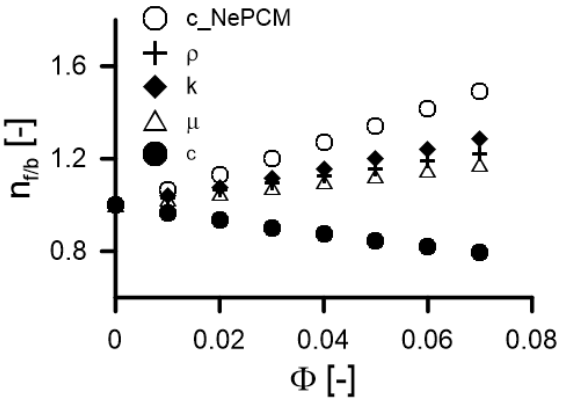

Figure 5.20: Ratio between nanofluid and base fluid properties and its dependence of the nanoparticle concentration

Effects of the nanofluids on pressure drop and convective heat transfer coefficient

The effect on pressure drop and convective heat transfer coefficient due to the change on the thermophysical properties of the mixtures of a base fluid with nanoparticles, presented in section 5.2.3, will be outlined. The comparison between the behaviour of the refrigeration with nanofluids versus with regular coolants, will be performed assuming:

- As.1. The same correlations are applicable for heat transfer and friction coefficients in both cases: standard coolant and nanofluids.
- As. 2. The geometry of the engine is not changed.

Effects on heat transfer coefficient

The variation of the convective heat transfer coefficient in an engine will be analyzed assuming that forced convection can be estimated with Equation 5.7 which is the same as Equation 5.6. This equation can be used since no specific correlation for nanofluids has been found to be valid [170] and therefore classic correlations must be used [171]:

$$Nu = 0.023\, Re^{0.8}\, Pr^{0.4} \tag{5.6}$$

$$Nu = b_4\, Re^{b_5} \cdot Pr^{b_6} \tag{5.7}$$

Choosing correctly the fitting coefficients of Equation 5.7, the Dittus-Boelter correlation [145] is obtained, which its accuracy in predicting the heat transfer coefficient in nanofluids has been demonstrated by [162]. The fitting cooefficients are shown in Equation 5.6. The expressions of the dimensionless numbers of Equation 5.7 are presented in Equations 5.8, 5.9 and 5.10.

$$Re = \frac{\rho u D}{\mu} = \frac{4\,\dot{m}}{\pi\,\mu\,D} \tag{5.8}$$

$$Pr = \frac{\mu\,c}{k} \tag{5.9}$$

$$Nu = \frac{h\,D}{k} \tag{5.10}$$

Using assumptions 1 and 2, the ratios between Reynolds numbers (Equation 5.8) and Prandtl numbers (Equation 5.9) are presented in Equations 5.11 and 5.12 respectively.

$$\frac{Re_{nf}}{Re_b} = \left(\frac{\rho_{nf}}{\rho_b}\right)\left(\frac{u_{nf}}{u_b}\right)\left(\frac{\mu_{nf}}{\mu_b}\right)^{-1} \tag{5.11}$$

$$\frac{Pr_{nf}}{Pr_b} = \left(\frac{\mu_{nf}}{\mu_b}\right)\left(\frac{c_{nf}}{c_b}\right)\left(\frac{k_{nf}}{k_b}\right)^{-1} \tag{5.12}$$

The relationship between the film coefficients with and without nanofluids, which is the appropiate simple figure of merit for comparing the forced single-phase convective heat transfer performance of a nanofluid relative to its base fluid [162], is presented in Equation 5.13 that has been obtained combining equations 5.7 5.10, 5.11 and 5.12.

$$\frac{h_{nf}}{h_b} = \left(\frac{Re_{nf}}{Re_b}\right)^{b_5}\left(\frac{Pr_{nf}}{Pr_b}\right)^{b_6}\left(\frac{k_{nf}}{k_b}\right) \tag{5.13}$$

Effects on pressure drop

The effect of nanofluids on pressure can represent a change on the power consumed by the coolant pump that can be calculated using Equation 5.14, where the pressure drop ΔP can be computed with the expression 5.15.

$$\dot{W}_b = \Delta P\,\dot{V} \tag{5.14}$$

$$\Delta P = f \frac{\rho\, u^2}{2\, D} L \tag{5.15}$$

The friction factor in Equation 5.15 is calculated using 5.16.

$$f = \begin{cases} 0.316\, Re^{-1/4} & \text{if } Re \leq 2 \cdot 10^4 \\ 0.184\, Re^{-1/4} & \text{if } Re > 2 \cdot 10^4 \end{cases} \tag{5.16}$$

Then, using Equations 5.14 and 5.15, the relationship between powers consumed by the coolant pump are obtained as Equation 5.17.

$$\frac{\dot{W}_{nf}}{\dot{W}_b} = \frac{\Delta P_{nf}}{\Delta P_b} \frac{\dot{V}_{nf}}{\dot{V}_b} = \left(\frac{f_{nf}}{f_b}\right) \left(\frac{\rho_{nf}}{\rho_b}\right) \left(\frac{u_{nf}}{u_b}\right)^3 \tag{5.17}$$

Equation 5.17 can be simplified assuming that the change of the coolant will not affect the flow regime as Equation 5.18 shows. This will not always be true and it could lead to changes in the results but, only in particular conditions the assumption will be false. Equation 5.19 show the result of applying this last assumption, where the fitting constants depend on Reynolds number according to Equation 5.16.

$$\begin{aligned} Re_{nf} &\leq Re_b \leq 2 \cdot 10^4 \\ Re_b &> Re_{nf} > 2 \cdot 10^4 \end{aligned} \tag{5.18}$$

$$\frac{\dot{W}_{nf}}{\dot{W}_b} = \left(\frac{Re_{nf}}{Re_b}\right)^{-b_7} \left(\frac{\rho_{nf}}{\rho_b}\right) \left(\frac{u_{nf}}{u_b}\right)^3 \tag{5.19}$$

Methodology

For the present study, two different cases (constant volumetric flow and constant wall temperature) are considered for comparison among three different coolants; base fluid, nanofluid and nanofluid with NePCM. These cases have been chosen in order to estimate the possible gains on heat transfer keeping the same flow and to estimate the possible gains on coolant flow (power) by keeping the same heat transfer conditions.

Case 1

The first case considered is assuming that the volumetric flow remains constant in both systems (regular coolant and with nanofluids) as Equation 5.20 shows. In this case, the ratios between the Reynolds numbers (Equation 5.11) and ratio between coolant pump power (Equation 5.19)

can be simplified. These simplifications lead to Equation 5.21 and 5.22 respectively.

$$\dot{V}_{nf} = \dot{V}_b \longrightarrow u_{nf}\, A_{nf} = u_b\, A_b \xrightarrow{As.2} u_{nf} = u_b \tag{5.20}$$

$$\frac{Re_{nf}}{Re_b} = \left(\frac{\rho_{nf}}{\rho_b}\right)\left(\frac{\mu_{nf}}{\mu_b}\right)^{-1} \tag{5.21}$$

$$\frac{\dot{W}_{nf}}{\dot{W}_b} = \left(\frac{Re_{nf}}{Re_b}\right)^{-b_7}\left(\frac{\rho_{nf}}{\rho_b}\right) \tag{5.22}$$

Figure 5.21 and Figure 5.22 show the variation of several parameters with the nanoparticle concentration for this specific case, where the following trends were observed:

- The effect of nanofluids concentration on Reynolds number is small, but in any case the higher the concentrarion, the higher the Reynolds number. This is explained since the increase of density with nanofluids concentration is higher than the increase of the dynamic viscosity (as Figure 5.20 show).

- The ratio of Prandtl numbers is highly dependent on the nanofluids concentration and decreases with nanofluid concentration. This is because of the fact that the increase in the ratio of conductivities is higher than the one observed for the dynamic viscosity. Additionally, the ratio of specific heat capacities decreases with nanofluids concentration as it is shown in Figure 5.20. On the other hand, the ratio of specific heat capacities increases with nanofluids concentration as it is shown in Figure 5.20 due to the strong effect of the second term of the Equation 5.2 as long as the nanofluid operates within the designed temperature range. Thus, this effect will be available just for a certain temperature range in which the melting point of the PCM is achieved.

- On one hand, the ratio of Nusselt number decreases with concentration when using nanofluids. This is a consequence of the two previous statements: ratio of Reynolds number is almost constant and the ratio of Prandtl numbers decreases. This result could lead to the wrong idea (as it will be shown later) that the heat transfer using nanofluids would be lower than the one obtained with the base fluids. On the other hand, the results with NePCM showed

that Nusselt number increased as a consequence of Prandtl number increase.

- The effect in convective heat transfer coefficient is very important: increases with nanofluid concentration. This effect is explained since the increase of thermal conductivity is much important than the decrease of the Nusselt number. This result confirms that the appropiate simple figure of merit for comparing the heat transfer performance of a nanofluid relative to its base fluid is the convective heat transfer coefficient and not the Nusselt number as stated by [162]. For the case of nanofluid with NePCM the same trend was observed but the film coefficient increase was much higher.
- The trend observed in the friction factor is opposite and lower than the one observed for the Reynolds number as expected since this factor depends only on Reynolds number as Equation 5.16 shows.
- The high increase observed in the coolant pump power is due to the low effect of nanoparticles in Reynolds number and the high effect that they have on density (see Figure 5.20).

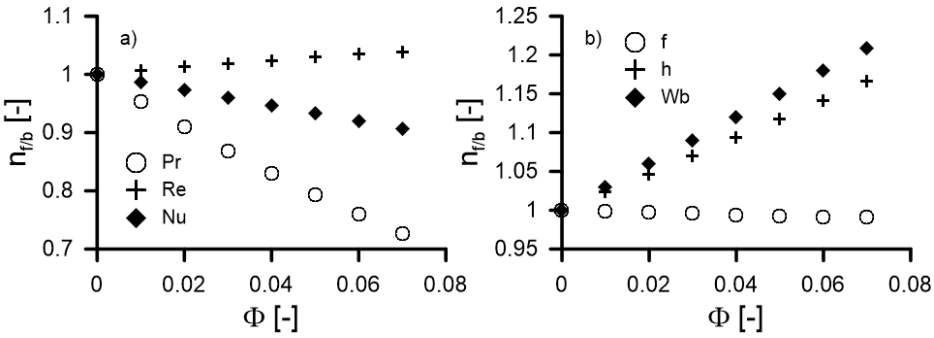

Figure 5.21: Ratio between nanofluid and base fluid properties and its dependence on the nanoparticle concentration for case 1: a) Ratio of Prandtl, Reynolds and Nusselt numbers, b) film coefficient, friction factor and pumping power ratios

Case 2

In this second case, the wall temperatures are kept constant. This fact implies that the heat transferred to coolant is kept constant, so the rela-

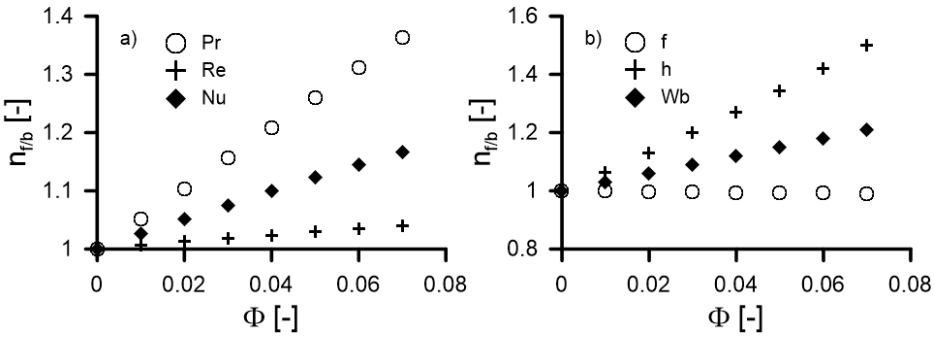

Figure 5.22: Ratio between NePCM nanofluid and base fluid properties and its dependence on the nanoparticle concentration for case 1: a) Ratio of Prandtl, Reynolds and Nusselt numbers, b) film coefficient, friction factor and pumping power ratios

tionship presented in Equation 5.23 holds.

$$\dot{Q}_{nf} = \dot{Q}_b \longrightarrow h_{nf} = h_b \tag{5.23}$$

Applying a similar methodology as in subsection 5.2.3 different ratios will be obtained. First, the ratio between the Reynolds number can be obtained by combining Equations 5.13 and 5.23. The result is presented in Equation 5.24.

$$\left(\frac{Re_{nf}}{Re_b}\right)^{b_5} = \left(\frac{Pr_{nf}}{Pr_b}\right)^{-b_6} \left(\frac{k_{nf}}{k_b}\right)^{-1} \tag{5.24}$$

In order to obtain the ratio between the coolant pump powers for this specific case, the ratio between velocities is needed. This velocities ratio (Equation 5.25) can be obtained by using the definition of Reynolds number (Equation 5.8) and the ratio between Reynolds numbers for this specific case (Equation 5.24). Now, the ratio between coolant pump powers is easily obtained, whose expression can be found in Equation 5.26

$$\frac{u_{nf}}{u_b} = \left(\frac{Re_{nf}}{Re_b}\right) \left(\frac{\rho_{nf}}{\rho_b}\right)^{-1} \left(\frac{\mu_{nf}}{\mu_b}\right) \tag{5.25}$$

$$\frac{\dot{W}_{nf}}{\dot{W}_b} = \left(\frac{Re_{nf}}{Re_b}\right)^{3-b_7} \left(\frac{\rho_{nf}}{\rho_b}\right)^{-2} \left(\frac{\mu_{nf}}{\mu_b}\right)^{3} \tag{5.26}$$

Figure 5.23 and Figure 5.24 show the variation of several parameters with the nanoparticle concentration for this specific case, where the following trends are observed:

- The effect of nanofluids concentration on Reynolds number is more important than for case 1 and following the opposite trend, i.e. the higher the concentrarion, the lower the Reynolds number. This is explained since the increase of density with nanofluids concentration is higher than the increase of the dynamic viscosity (as Figure 5.20 shows)

- The effect on Prandtl number is the same observed in section 5.2.3 since Prandtl number depend only on thermophysical propertes.

- The decrease of Nusselt number is higher than the observed in case 1 due to, on one hand, the same bahaviour in Prandtl number and, on the other, the observed behaviour on Reynolds number. However, when using NePCM nanoparticles the trend compared with the case 1 changes due to the decrease of both Prandtl and Reynolds numbers with nanoparticle concentration.

- There is no effect in convective heat transfer coefficient due to the constant wall temperature approach.

- The trend observed in the friction factor is opposite and lower than the one observed for the Reynolds number as explaneid in the previous case.

- The decrease (opposite to the observed behaviour of case 1) observed in the coolant pump power is due to the fact that the decrease in Reynolds number and the increase of densities (the power is inversely proportional to this densities ratio as Equation 5.26 show (see Figure 5.20) are more important than the increase on dynamic viscosity. The same behaviour is observed when using NePCM nanoparticle is similar but with higher decrease in pumping power. This is because the Reynolds number is even lower with this nanoparticle.

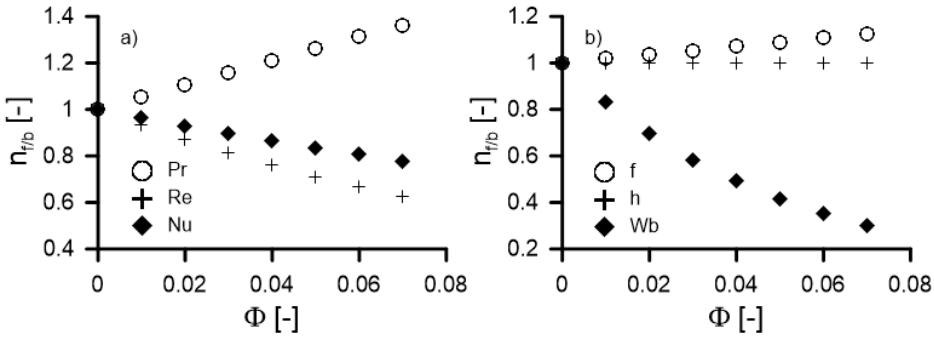

Figure 5.23: Ratio between nanofluid and base fluid properties and its dependence of the nanoparticle concentration for case 2: a) Dimensionless numbers, b) film coefficient, friction factor and pumping power

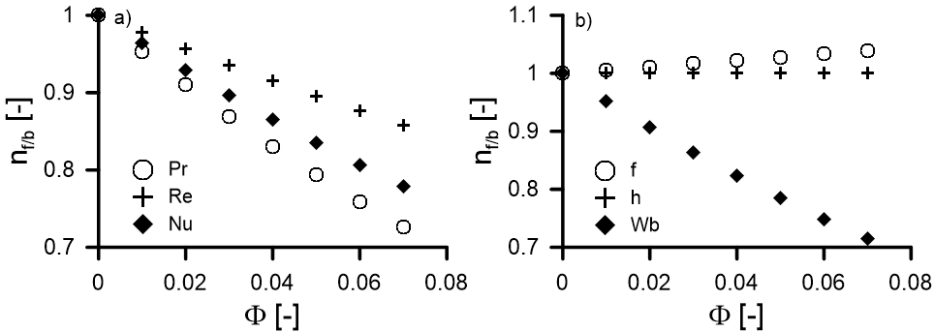

Figure 5.24: Ratio between NePCM nanofluid and base fluid properties and its dependence of the nanoparticle concentration for case 2: a) Dimensionless numbers, b) film coefficient, friction factor and pumping power

Summarizing, Table 5.3 and Table 5.4 show, in approximate form, the effect of the nanofluid concentration on the different parameters in each of the considered case. The numerical values indicates the approximate expected variation of the parameter respect a variation of 1 % increase on nanofluid concentration (i.e., linear approximation).

Results

Case 1 (Constant $\dot{V}$). Steady state

As mentioned, in this case, the coolant volumetric flow remains constant and, as a consequence, higher heat transfer coefficients are obtained with

Table 5.3: Approximate variation of the different parameters respect to nanofluid concentration

Parameter	Case 1 Constant volumetric flow rate	Case 2 Constant heat transfer
u	0	-2.4
Re	0.55	-2.0
Pr	-3.8	-3.8
Nu	-1.3	-3.1
h	2.4	0
f	-0.12	0.50
$\dot{W}_b$	3.0	-4.0

nanofluids respect to base fluid leading to an increase of the heat transferred to the coolant. The results obtained with the lumped model with different nanofluid concentrations for all the steady state engine working conditions are presented in Figure 5.25, where an increase around 18% of the convective heat transfer coefficient (which correspond of a 7% of nanoparticle concentration) leads to an increment of only 1.3% in the heat transferred to the coolant. On the other hand, when using NePCM

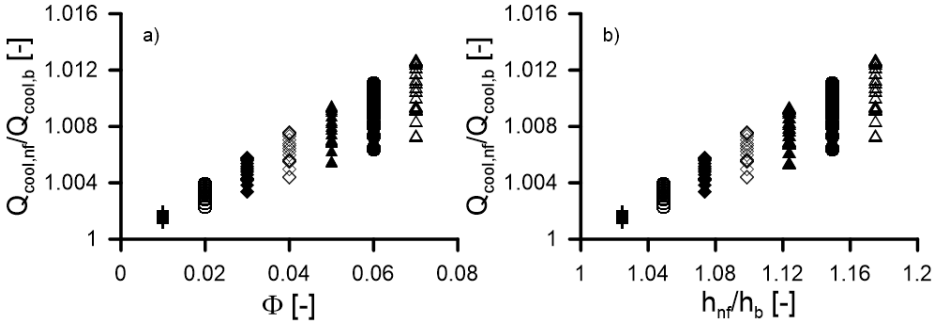

Figure 5.25: Relationship between heat transferred to the coolant depending on a) nanoparticle concentration and b) film coefficients

a similar behaviour was observed. In Figure 5.26 it is seen that the heat rejected to the coolant in this case was slightly higher (2.3% compared to base coolant) while the convective heat coefficient achieved an increment of 35% for the case of high load and speed with 7% of NePCM nanoparti-

Table 5.4: Approximate % variation of the different parameters respect to NePCM nanofluid concentration

Parameter	Case 1 Constant volumetric flow rate	Case 2 Constant heat transfer
u	0	-6.9
Re	0.55	-5.2
Pr	5.2	5.2
Nu	2.2	-3.1
h	7.1	0
f	-0.12	1.3
$\dot{W}_b$	3	-9.2

cle concentration. In addition, Figure 5.26 shows that when NePCM are used the results obtained for each test differ more than the previous case because of the second term of Equation 5.2 which depends on the coolant temperature. Thus, the higher the coolant temperature rise when passing through the engine the higher the convective heat coefficient because of the fact that the heat rejected is absorbed for the coolant as latent heat. This effect could be beneficial in engine downsizing strategy because less coolant volume would be required and detrimental for warm up of the engine as it will be seen in the following section.

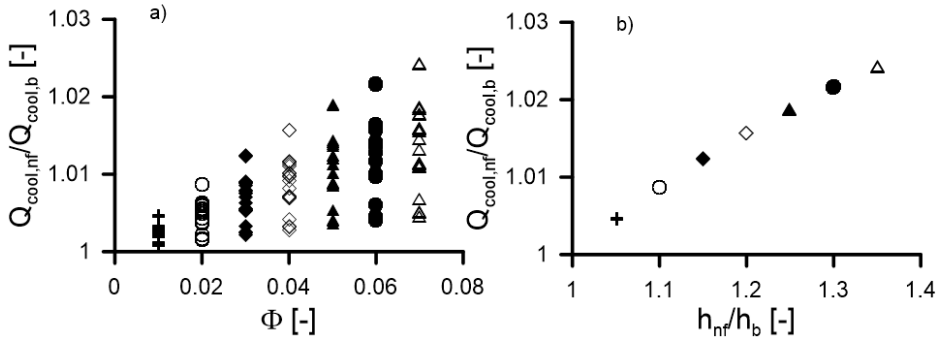

Figure 5.26: Relationship between heat transferred to the coolant depending on a) NePCM nanoparticle concentration and b) film coefficients

The explanation of this results come from the fact that the main ther-

mal resistance in the heat transfer between in-cylinder gases and coolant is the convective coefficient between gas and combustion chamber wall. This small gain will not be enough to compensate the higher power consumed by the coolant pump.

Case 1 (Constant $\dot{V}$). Constant flow - Transient

In order to study the suitability of the use of nanofluids through transient processes, a simulation with the lumped model is performed. This simulation has been performed between the same states mentioned on section 4.2.2. The obtained results are presented in Figure 5.27, which shows that the higher nanoparticle concentration has the coolant, the lower the temperatures at which the structure nodes are stabilized. This is because the increment in the nanoparticle concentration leads to a higher convective heat transfer coefficient, as it can be seen in Figure 5.21.

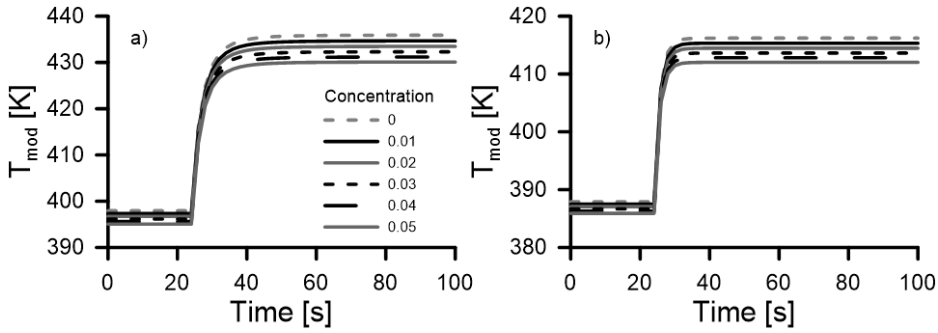

Figure 5.27: Temperature evolution during a transient process with different particle concentrations in cylinder 1: a) Exhaust side at 8 mm, b) Intake valve seat at 3.5 mm

The results obtained with NePCM are shown in Figure 5.28. The warm up time is quite similar to the case without NePCM but the final temperature is lower (around 4 K for the case of 5% nanoparticle concentration) compared to the previous case for both studied points, exhaust side and intake valve seat. This was expected due to the fact that the heat capacity is higher in this case. Additionally, there is a difference in warm up time between them due to their thermal inertia which is lower for the intake valve seat. Overall, the warming time (that could lead to a reduction on fuel consumption [21]) is not significantly affected by the use of nanofluids in these given conditions.

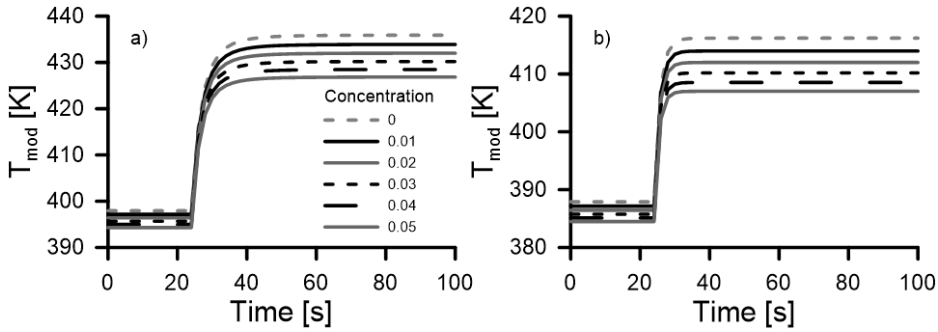

Figure 5.28: Temperature evolution during a transient process with different NePCM particle concentrations in cylinder 1: a) Exhaust side at 8 mm, b) Intake valve seat at 3.5 mm

Case 2 (Constant $\dot{Q}$). Steady state

As indicated previously, in this case, the heat transferred to the coolant was kept constant, so the advantage of using nanofluids could come from the reduction of the coolant flow allowed by the improved film coefficient of the nanofluids. This flow reduction leads to power consumption savings in the coolant pump (as Equation 5.27 shows).

$$\dot{W}_{nf} = \frac{\Delta P \dot{V}}{\eta} \tag{5.27}$$

The pressure drop is directly proportional to the square of the volumetric flow rate. The constant of proportionality was determined from experimental data measured as Equations 5.28 and 5.29 show.

$$\Delta P = b_8 \cdot \dot{V}^2 \tag{5.28}$$

$$b_8 = 5.14 \cdot 10^{-5}\, bar\, l^{-2}\, min^2 \tag{5.29}$$

Besides, the coolant pump is usually fitted to the engine crankshaft as, a consequence, the coolant volumetric flow rate is almost proportional to the engine speed, so Equation 5.30 can be used it. As above, the constant of proportionality was determined from experimental data measured (Equation 5.31).

$$Q = b_9 \cdot n \tag{5.30}$$

$$b_9 = 3.631 \cdot 10^{-2}\, l\, min^{-1}\, rpm^{-1} \tag{5.31}$$

Finally, for the usual coolant pumps used in internal combustion engines, the coolant pump performance is bounded between 0.85 and 0.9 so, conservatively, a value of 0.85 was taken in the simulations.

By combining Equations 5.27 to 5.31, the pumping power is calculated as a function of engine speed as shown in Equation 5.32.

$$\dot{W}_b = 2.89 \cdot 10^{-9} \cdot n^3 \tag{5.32}$$

Finally, to have an idea of the relative importance of this power (and the possible savings obtained) with the use of nanofluids, a comparison with the engine effective power will be performed. The obtained results are shown in Figure 5.29.

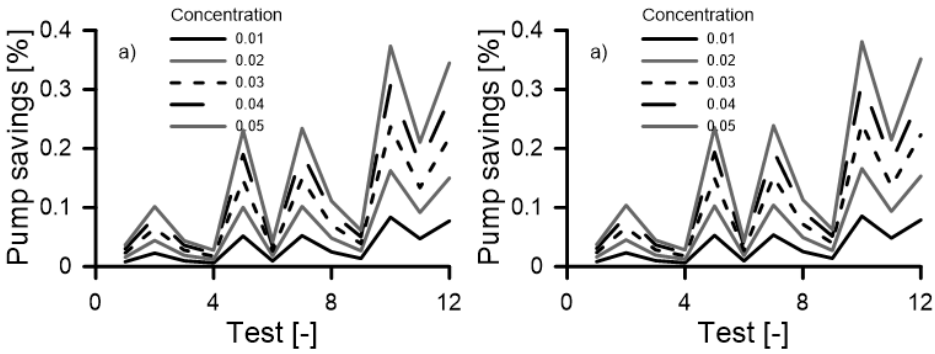

Figure 5.29: Power saved at the pump related to engine effective power: a) Re $\leq 2 \cdot 10^{-4}$, b) Re $> 2 \cdot 10^{-4}$

As it can be seen, using nanofluids leads to a limited savings in the power consumed by the coolant pump if the engine effective power is taken into account. The maximum percentage values are around 0.4 % for the highest nanoparticles concentrations evaluated. These small savings cannot possibly justify the use of these new coolants since they possibly have adverse effects (for instance, instability and bigger environmental impacts) and higher costs (maintenance).

Case 2 (Constant $\dot{Q}$). Transient

In this specific case, the study of the transient process does not give any additional information since the refrigeration is kept constant. The only parameter that would vary is the volumetric flow rate.

WLTC cycle simulation

In order to evaluate the effect in engine performance under more demanding conditions a WLTC cycle was simulated when nanofluid is used as coolant. Furthermore, it is a very dynamic cycle with diverse operating conditions which serve as a realistic scenario for assessing the real potential of nanofluid cooling strategy.

In the simulation, the NePCM nanofluid was not used due to the wide range of coolant temperature during the cycle. This would require a specific study for each particular NePCM with its own fusion temperature.

Contrary to the previous cases, for the WLTC simulation, the coolant volumetric flow and heat flux were not restrained. Figure 5.30 shows the results obtained simulating the cycle starting from ambient conditions (20 °C).

On one hand, the plot at the top represents the coolant temperature difference in the engine outlet between the case of 5 % nanoparticle concentration and base fluid. A positive value means that the temperature of the coolant is higher with the concentration. It can be seen that the maximum temperature difference is around 0.6°C. Regarding the warm up reduction time (temperature of the coolant above 80°C), it is practically negligible as it can be deduced by the plot.

On the other hand, the bottom plot shows the temperature difference in the cylinder head for the same nanoparticle concentration. It can be seen that the nanoparticle concetration in the coolant decreases the material temperature during all the cycle reaching a minimum value of -2.7°C. After 600 s there is a short period of time in which the behavior seems to be different from the rest of the cycle (temperature of the material rises with the concentration). This is due to the switching from HPEGR to LPEGR by the control system when a certain coolant temperature is reached. For the case of 5 % nanoparticle concetration this temperature is reached sooner increasing the intake air mass of the engine in those few instants.

5.3 Battery thermal management strategies

5.3.1 Introduction

This section will show the most relevant results extracted from the various studies that have been carried out using the battery model. The battery pack used for these studies was constructed by the prismatic cells as it

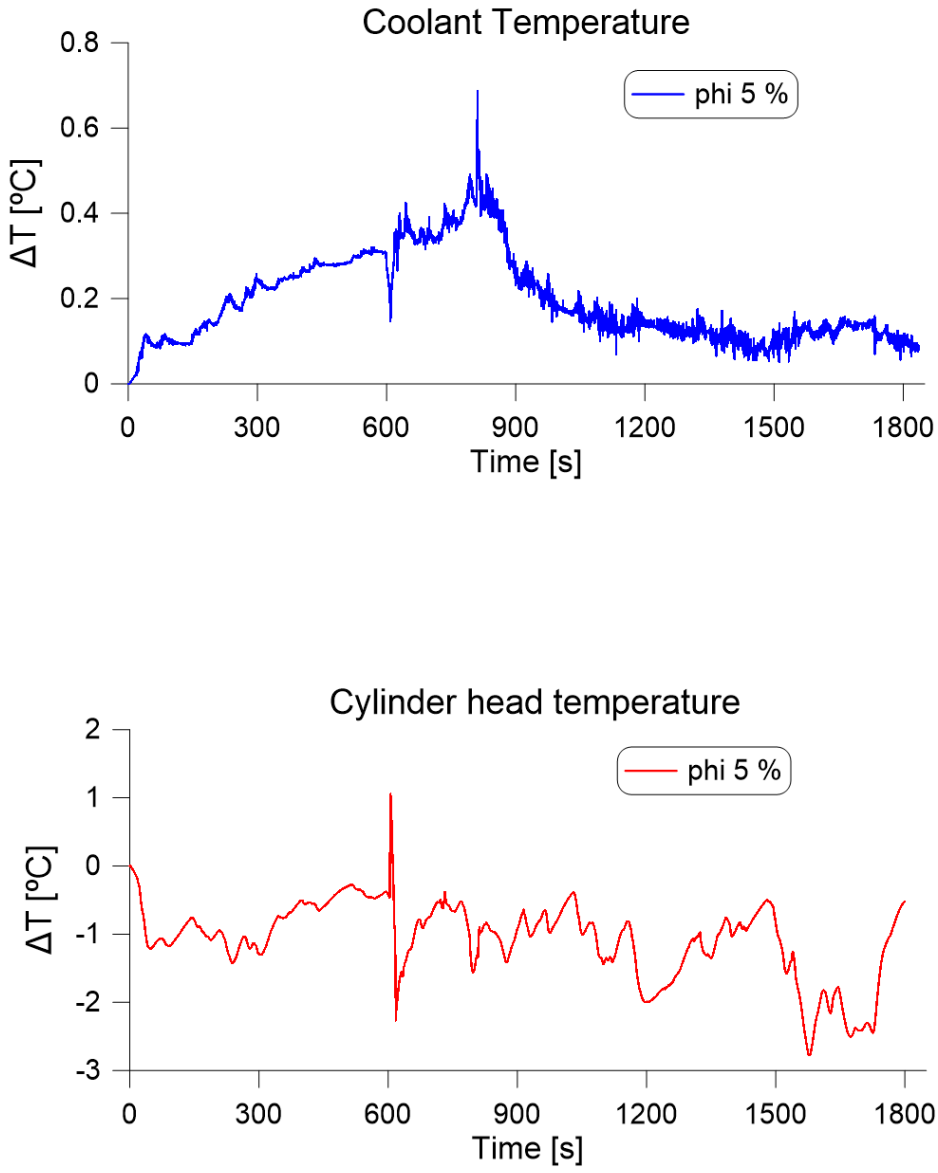

Figure 5.30: Coolant and cylinder head temperature (Intake valve seat at 3.5 mm) difference during a WLTC cycle starting from ambient conditions.

was detailed in Chapter 4. The battery pack consisted in 144 prismatic cells and 12 modules. Each module with 12 cells distributed into two rows with 6 cells each. Figure 5.31 shows the BTMS and the cooling channels of each module path. The inlet coolant flow distributes into 6 cooling paths which cooled 2 modules each as it can be seen in plot a). The thermal management strategy consisted in indirect liquid cooling with channels as it can be seen in plot b).

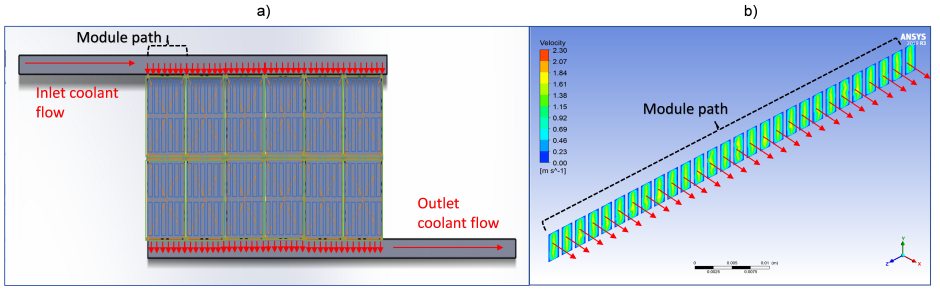

Figure 5.31: a) Battery thermal management system. b) Cooling channels in a module path.

The studies consisted in modifying different parameters of the battery thermal management system. A description of the studies is found in the following:

- In regard to the faces of the cell that interact with the coolant, the case of cooling by the base has been compared with the case of cooling by the lateral faces.
- Regarding the flow, three different possibilities have been taken into account: 0.5 l/s, 1 l/s and 2.5 l/s. The base coolant fluid was water/glycol.
- For the coolant temperature, the impact of two different temperatures, 10 °C and 20 °C, have been studied.
- Regarding the use of nanofluids, particle concentrations in the coolant fluid of 2 % and 5 % have been considered, and simulations have been carried out for a zero concentration of nanoparticles to serve as a reference.

These studies have been carried out at 3 different constant discharge

ratios: 1C, 3C and 6C, corresponding to demanding currents of 23 A, 69 A and 138 A, respectively.

Only the most relevant results obtained from the simulations will be presented and described since some strategies had shown limited impact on the thermal performance of the battery.

5.3.2 Cooling surfaces impact

For evaluating the impact of cooling different faces of the cells, a comparison between the cases of base and side cooling was performed (See Figure 5.32). Note that the channels were assumed to have the same width for both cases. Hence, for the same coolant flow, the passage area is higher for the side cooling while the coolant velocity is higher for the base cooling.

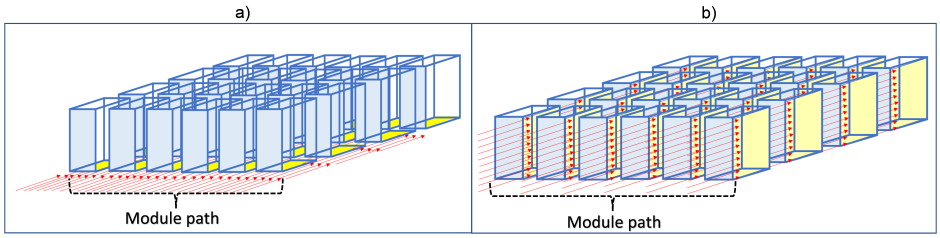

Figure 5.32: Coolant flow path for the battery module. a) Base cooling. b) Side cooling.

The boundary conditions and discharge rate for this study were; discharge rate of 1C, ambient temperature of 20 °C, coolant temperature at 20 °C and coolant flow of 0.5 l/s.

The following results show the impact on the temperatures of the battery cell: the core of the cell or active zone node (plot a) of Figure 5.33), the base of the cell (plot c of Figure 5.33) and cell side or lateral (plot b) of Figure 5.33).

As it can be seen, the temperature variation of the base cell is very limited (less than 1 %) independently of the surface in contact with the coolant. However, the active zone experienced a significant variation of 15.2 % for the same conditions. Nonetheless, laterals cooling proved to decrease the active zone temperature 3°C when compared to base cooling. Even the temperature of the base slightly decreased. Likewise, the side faces, otherwise air-cooled, drop their temperature around 2.5 °C when in contact with the coolant (plot b) of Figure 5.33).

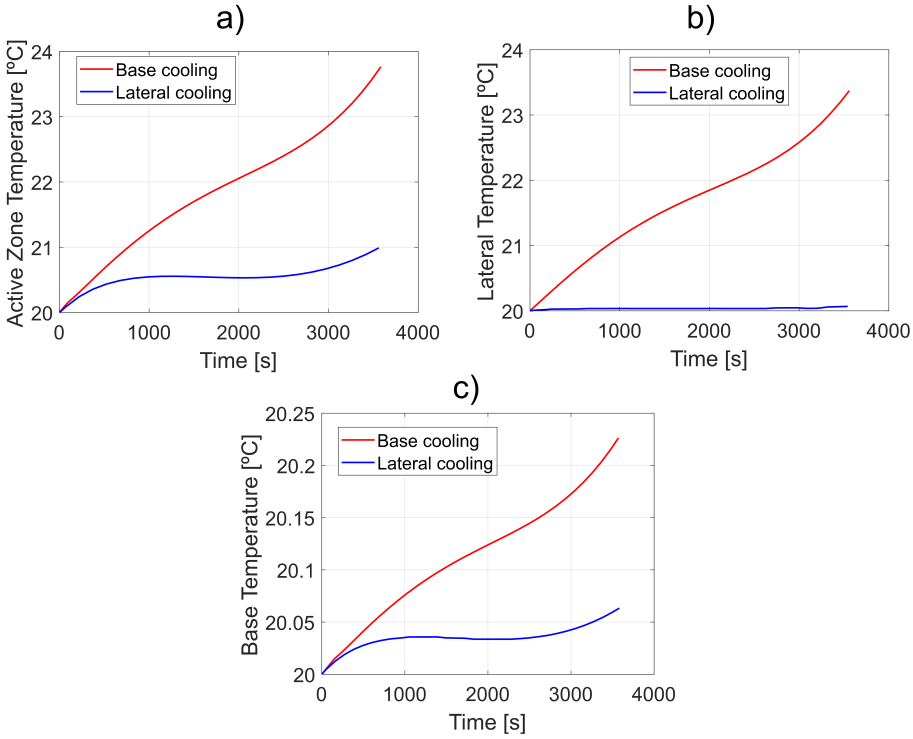

Figure 5.33: Base cooling vs side cooling. a) Active zone temperature, b) Base temperature and c) Lateral temperature.

The heat evacuated to the coolant increased considerably in the case of cooling through lateral faces. Figure 5.34 shows how its value practically tripled when compared to the base cooling case. This is due to various reasons. The main reason is the increase of cell surface in contact with the coolant since both sides of the cell are in contact with the coolant and the side area is much higher than the base one.

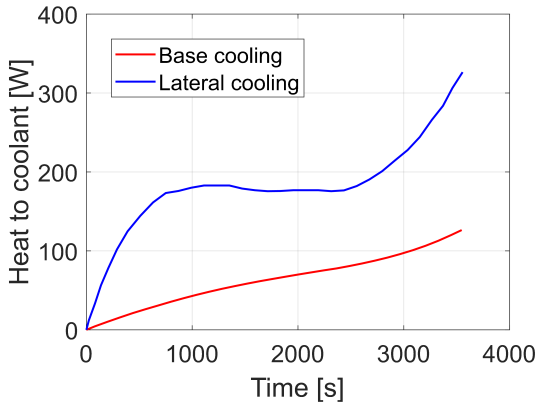

Figure 5.34: Base cooling vs side cooling. Heat transferred to the coolant fluid.

However, the thermal conductance not only depends on the area but also on the heat transfer convection coefficient between the surface and the coolant. This coefficient is higher for the base cooling case since higher velocities are achieved given the lesser passage area. Results show that the area impact is highter than the decrease in the convection coefficient as it can be seen in Figure 5.35.

5.3.3 Coolant flows impact

Figure 5.36 shows an overall comparison of the active zone temperature obtained for base and side cooling, for different coolant flows. It can be concluded that, increasing the coolant flow has limited impact in both base and side cooling.

Figure 5.37 shows that the Reynolds number, Nusselt, heat transfer convection coefficient and thermal conductance, viscosity and Prandtl number were significantly affected by coolant flow variation. In the calculation of the Reynolds number, the velocity of the fluid intervenes is

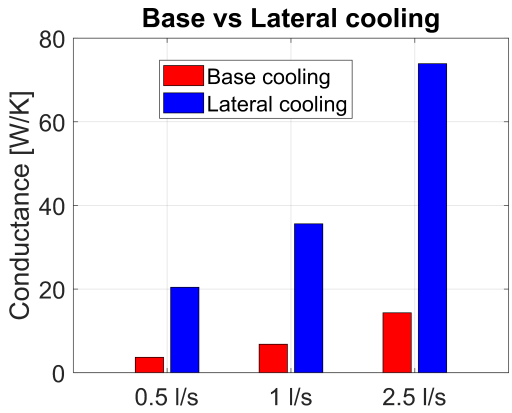

Figure 5.35: Thermal conductance. Left: Base cooling. Right: Lateral cooling

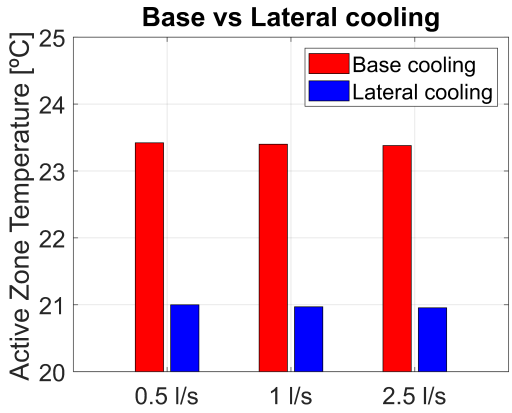

Figure 5.36: Final temperature of the Active Zone for the flows 0.5 l/s, 1 l/s and 2.5 l/s with base and lateral cooling.

directly proportional to the flow. The increase in this parameter is reflected in the Nusselt number, and this, in return, in the film coefficient and the thermal conductance.

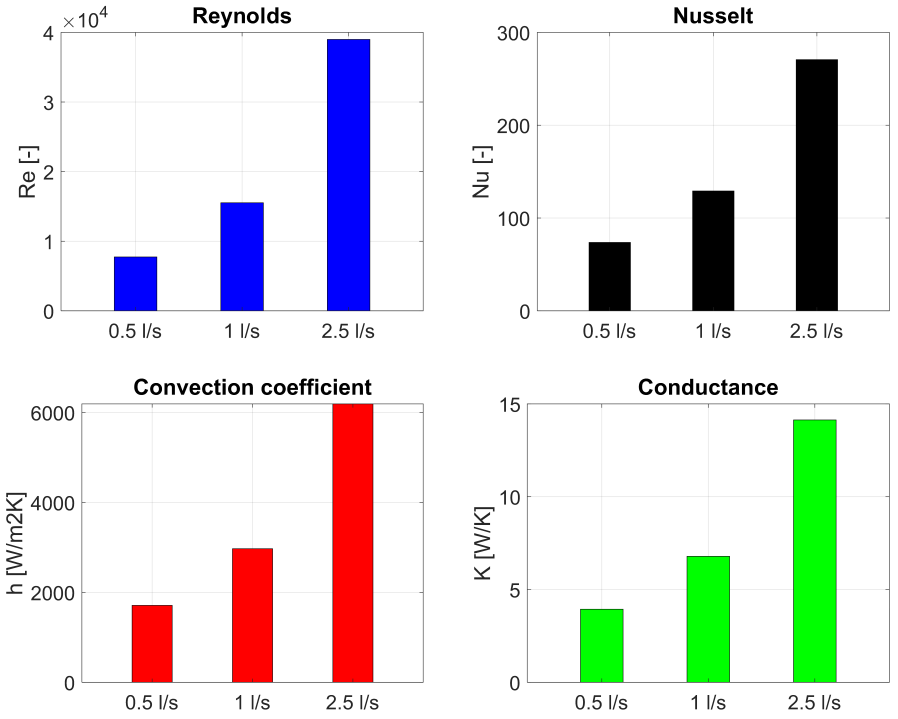

Figure 5.37: Impact of coolant flow rate on various parameters: Reynolds number, Nusselt number, film coefficient and thermal conductance.

However, the impact of flow rate variation on node temperatures and the heat generated in the cell is less than 0.1 % independently of the cooled surface (base or side cooling). Figure 5.38 shows the temperature evolution results of the assumption of cooling by the base of the cell. Overall, multiplying the coolant flow rate by 5 barely manages to reduce the cell core temperature.

5.3.4 Nanofluids impact

In order to assess the impact of using nanofluids, the same methodology and equations presented in Section 5.2.3 were implemented for calculating the heat transfer and the thermophysical properties of the nanofluid.

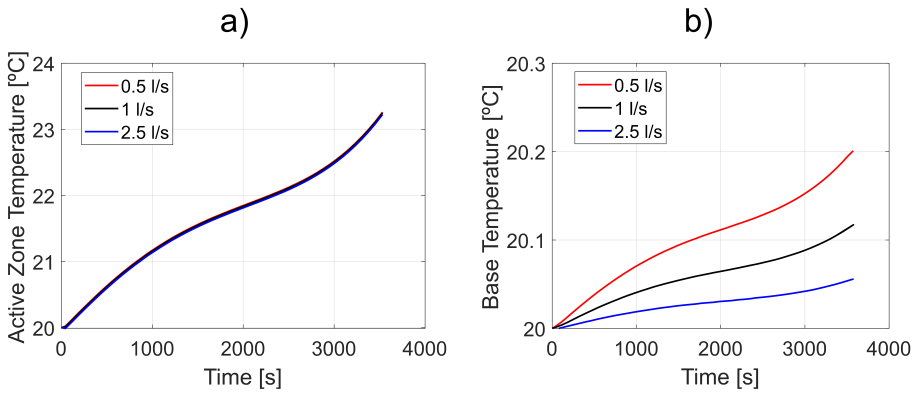

Figure 5.38: Temperature of the Active Zone (a) and Base (b) nodes for different flows in the case of base cooling.

The study was performed under the discharge conditions of 1C, ambient temperature of 20 °C temperature, coolant temperature set to 20 °C and constant flow rate of 0.5 l/s. The assumptions of cooling by the base of the cell or by the lateral faces were considered. In addition, three possible concentrations of nanoparticles are taken into account: 0 %, 2 % and 5%. The addition of nanoparticles to the base coolant had the following impact on the heat transfer parameters (See Figure 5.39):

- The Reynolds number slightly increased because density increment with concentration outweighs the increase in fluid viscosity.
- The Prandtl number decreases because the capacity of the nanofluids is less than that of the base fluid.
- As a consequence, the Nusselt number decreased. However, the considerable increase in conductivity caused a positive impact on the film coefficient and on the conductance. The thermal conductance increased a 7.5 % for 5 % of nanoparticle concentration.

Similarly, to the variation of coolant flow rate, the use of nanofluids had limited impact on the temperature of the battery cell. This is because the decrease of the thermal resistance between the surface and the coolant of the cell with nanofluids is limited when compared to the the thermal resistance between the active zone and the surface.

Simulations at higher discharge ratios were also performed with nanofluids. However, there was no improvement in its use with respect to the

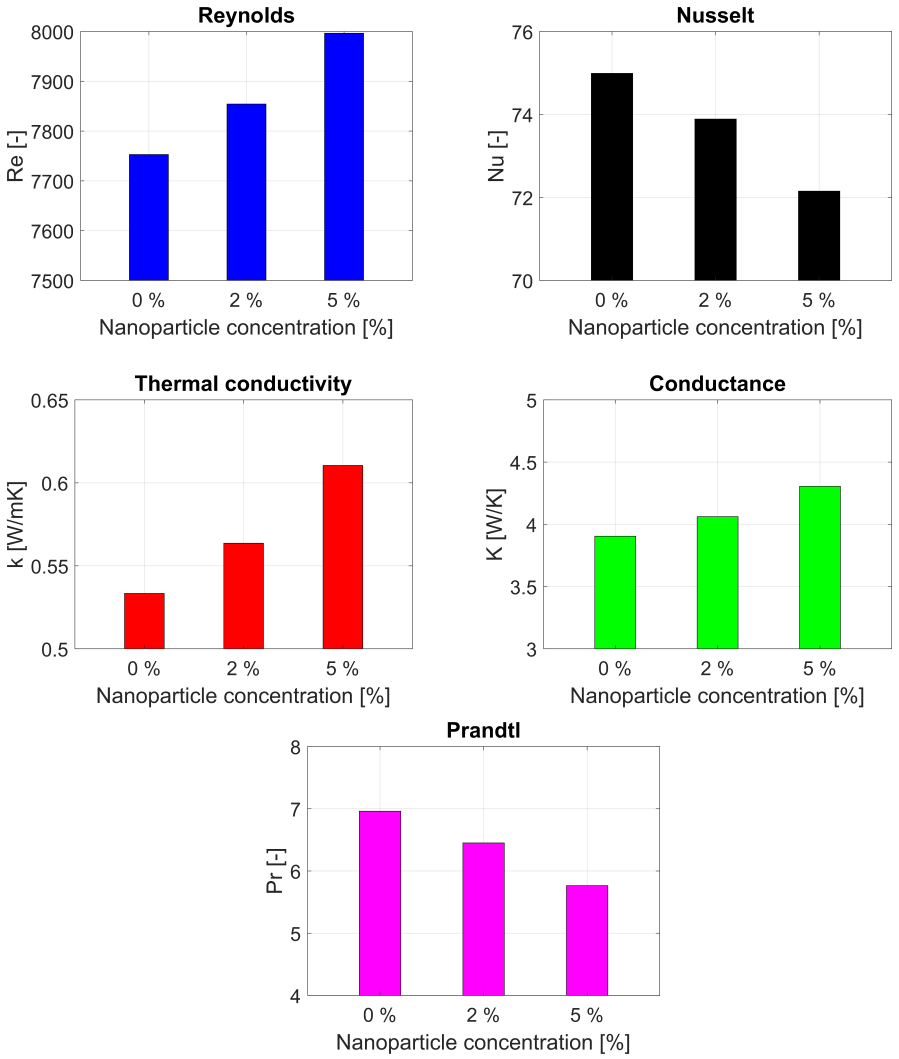

Figure 5.39: Impact of nanoparticle concentration on various parameters: Reynolds number, Prandtl number, thermal conductivity, Nusselt number, and conductance. Coolant flow rate of 0.5 l/s.

results seen for the 1C discharge ratio nor is there an improvement in the results obtained for the 6C discharge.

5.3.5 Coolant temperature impact

In order to evaluate the effect of the coolant temperature on the battery cell temperatures, a series of simulations changing the coolant temperature (i.e., a decrease of 10°C) while maintaining the rest of the parameters were carried out. The study has been carried out for a discharge rate at 1C assuming a coolant flow rate of 0.5 l/s and base cooling. Although side cooling was also studied, it was not presented since similar behaviour was observed.

Figure 5.40 presents the temperature evolution of both the active zone and the base for adiabatic conditions (i.e., without heat transfer to the ambient) for both coolant temperatures. It can be seen that the base temperature of the cell is very close to the coolant one while the there is almost 5 °C of temperature drop between the active zone and the coolant at the end of the discharge process. Comparing maximum temperatures, it can be observed that, the active zone maximum temperature decrease with the coolant temperature. The cell temperatures evolution for both coolant temperatures are very similar.

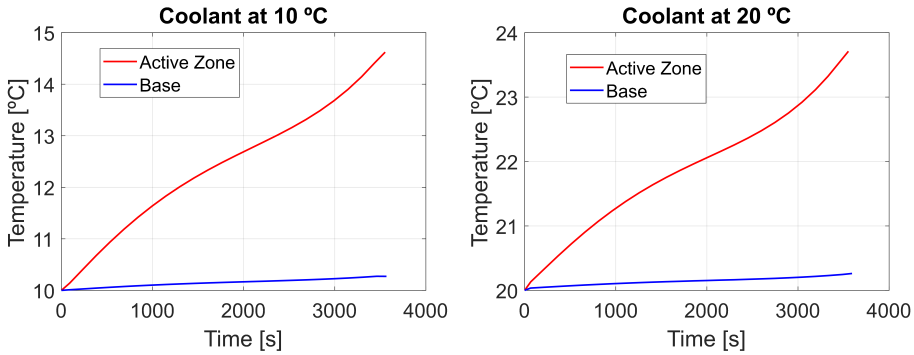

Figure 5.40: Temperatures of the Active Zone and Base nodes. Adiabatic system. Base cooling. Left: Coolant temperature 10 °C. Right: Coolant temperature 20 °C.

The temperature drops observed between the active core, the base surface and the coolant demonstrate that the cell has low internal thermal conductance which is directly related to its materials and manufactur-

ing process. Increasing the power of the TMS will scarcely improve the temperature management of the cells for this conditions.

5.3.6 High C-rate operation impact

In this section, the battery cell temperatures were studied under high power demand (i.e., high discharge ratio). Both base and side cooling were evaluated. Ambient temperature was set constant to 20 °C.

Figure 5.41 shows the heat generated by the battery pack for the different discharge rates. A significant increase in heat is appreciated as the discharge rate increases. Tripling the discharge ratio, the heat generated is multiplied by 7; with a discharge rate of 6C, this multiplication factor increases to more than 24 units. This was expected since the heat evolves with the square of the cell current. Additionally, it can also be observed that the discharge time is reduced accordingly since the battery is discharged (i.e., SOC is almost 0) in less than 600 s for the 6C case. The heat generated depend on the electric parameters of the battery electric circuit (i.e., internal resistance of the cell) which, at the same time, are affected by SOC and temperature. The temperature of the active zone of the cell is continuously increasing as it was seen in the previous sections while the SOC is decreasing. The internal resistance of the cell, increases with the SOC and decreases with the temperature as it was observed in 4. This explained the evolution of the heat generated in the cell.

Figure 5.42 shows the temperatures of the active zone for both base and side cooling under a discharge rate of 3C (plot a) and 6C (plot b). For base cooling, the maximum temperatures were achieved. For instance, the active zone temperature reached almost 45 °C (i.e., 45°C) at 6C which is already above the optimum operating temperature of the battery. The temperature of the active zone reached values of 33 °C towards the end of the discharge process for 3C. Additionally, it can also be observed that the temperature reduction achieved by side cooling was more significant with higher discharge ratio. Specifically, a decrease in the temperature of the central node of up to 7 degrees was observed in the case of discharge at 3C and of 9 degrees in the discharge at 6C, compared to the 2.7 degrees that were achieved in the discharge at 1C.

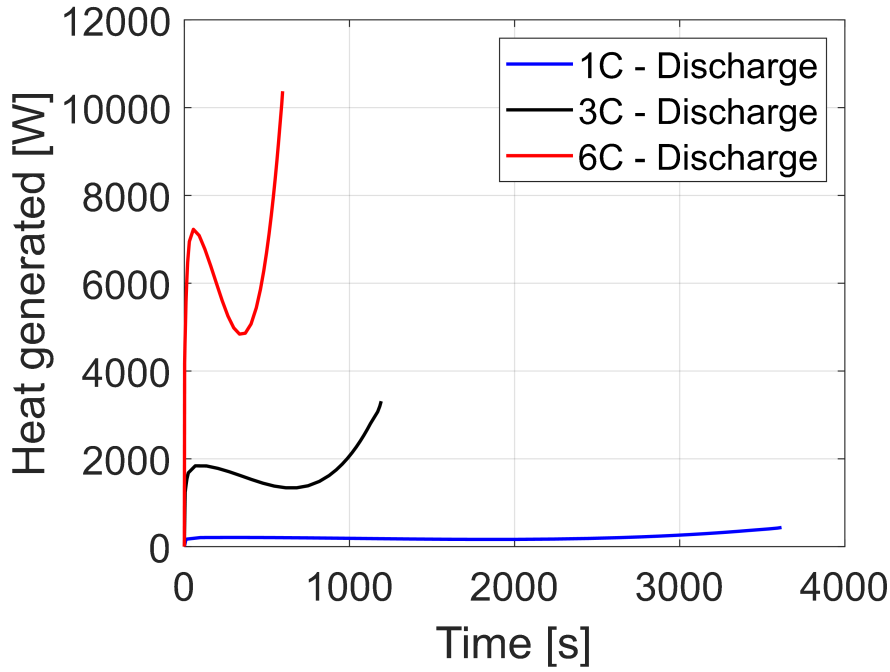

Figure 5.41: Heat generated by the battery at discharge rates 1C, 3C and 6C.

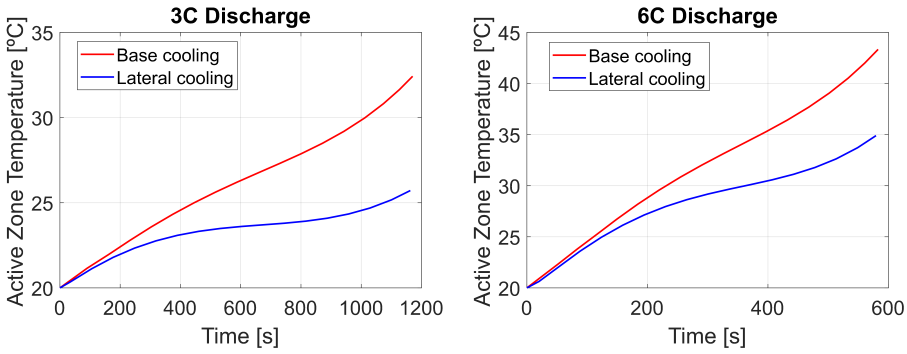

Figure 5.42: Temperature of the Active Zone for discharge at 3C and 6C.

5.4 Thermal impact on electric machines durability

5.4.1 Introduction

The thermal state of each of the components of the electric drive is critical for their correct operation in terms of efficiency, safety and durability as it was justified in the literature presented in Chapter 2. For instance, thermal durability studies are critical during the development of electric drive systems. Furthermore, running the electric machine at low temperatures directly impacts the lifetime of the device. For instance, its temperature is critical for the electric drive system control unit (EDSCU) in order to limit the torque of the machine. Hence, measurement of the EM temperature needs to be performed. Additionally, it is a difficult process that would increase both the production and maintenance cost of the ED. Furthermore, the hotspot with maximum temperature could vary depending on the operating condition of the ED and the implemented sensors would not be measuring the highest temperature of the machine.

An important phase in the developing of ED drive is to ensure that the system will run without any issues during a determinate distance. For this task numerical simulation is also critical. Using damage models which account for the ED degradation serve to strongly decrease the experimental time and costs. For instance, the cycles taken as reference are real driving data profiles. These cycles are very long and diverse. Hence, numerical simulation as well as statistical methods were used for designing practical experimental tests which could be run in the laboratory. Testing of individual components as the EM is also performed according to standards. For obtaining the efficiency maps and IP-class the tests are conducted according to the norm IEC 60034. For ensuring EM durability, safety and performance, a quasi-standards tests have established by the automotive industry. The High Temperature Operating Endurance (HTOE) and the Powered Thermal Cycle Endurance (PTCE) are well known examples.

In this section the electric machine thermal model described and validated in Chapter 4 was used to study the thermal damaging produced in the EM during real operating conditions.

5.4.2 Methodology

The thermal model was linked with damage functions for calculating both the thermal aging and the thermal cycling for the durability test design.

Finally, running both the EM thermal model and the damage models, testbench durability tests capable of reproducing the thermal derating of real driving conditions were developed.

High temperatures produce degradation in the materials of the EM. In order to account for the derating produced by the temperature in different parts of the EM, damage models based in the Arrhenius and the Coffin-Manson laws were implemented. While the first served to evaluate the thermal aging, the second studied the impact of thermal cycling. These damage models were fed by the temperature calculated by the EM thermal model.

The damage number (calculated for each node and test cycle) was the aim for designing equivalent durability experimental tests (or accelerating tests to reach thermal stresses much faster than in real operation conditions). Figure 5.43 shows a schema of the method followed for designing the experimental test.

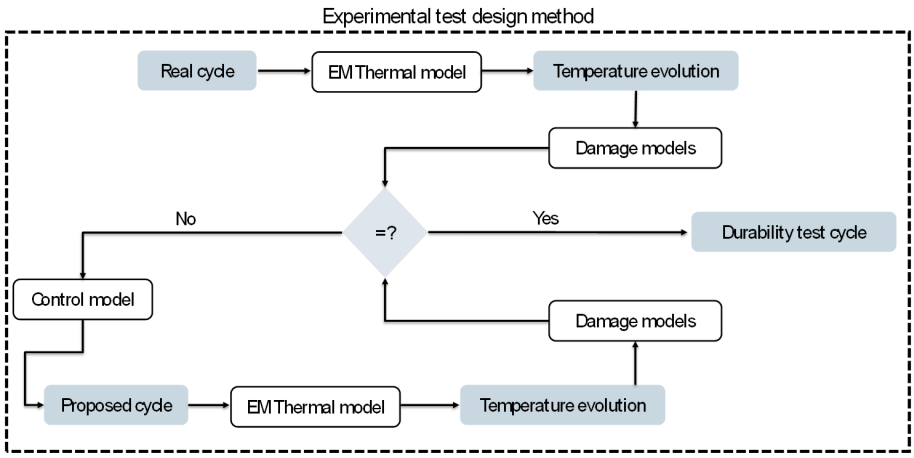

Figure 5.43: Experimental test design method

5.4.3 Damage study

The cycles used for damage calibration were obtained from real a driving database. It is important to state that these cycles are not those used in the Chapter 4, which were performed for validation of the model. A preselection of the most thermally damaging cycles was performed. These cycles had a duration of a month. Four different cycles were simulated

for calculating the damage in the critical points of the EM. One on hand, Real cycles 1 and 2 were characterized for being more aggressive in terms of thermal ageing. In other words, the machine runes more time at higher temperatures during these cycles. This would represent the real situation of driving uphill at high load and speed for a relative long time. On the other hand, real cycles 3 and 4 represented a much more aggressive driving during a short period of time. These cycles present higher torque and speed variations. Figure 5.44 shows the profile for the real driving cycles.

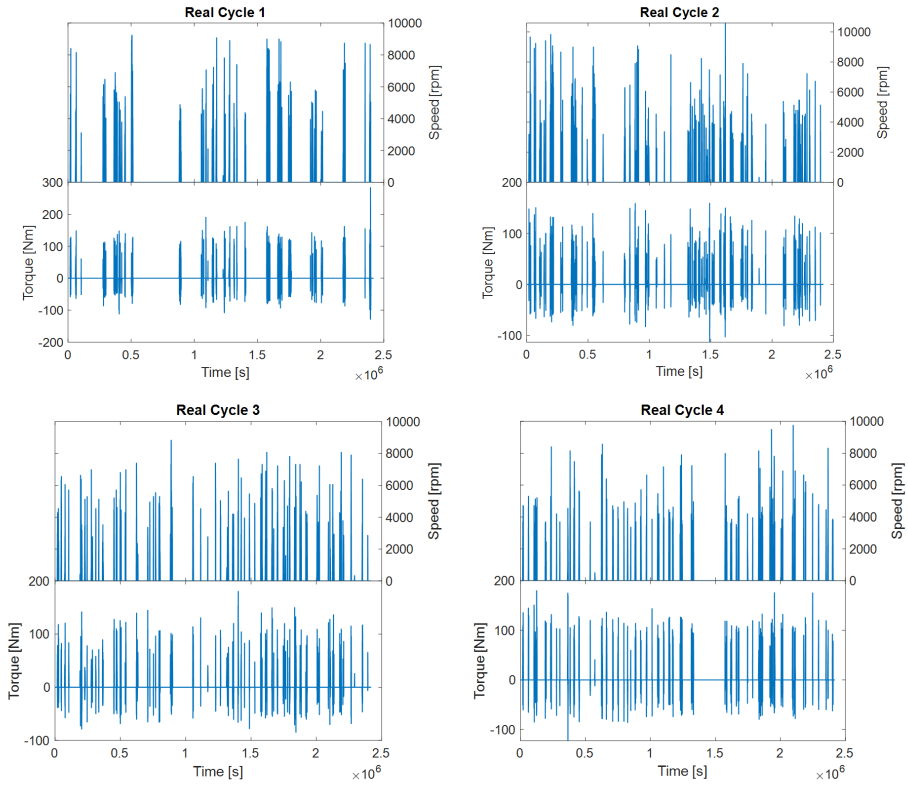

Figure 5.44: Speed and torque for real driving cycles

These cycles served as input for the EM thermal model, which was coupled with the damage models. The temperature evolution predicted by the model served as an input for the damage models alongside the energy activation and the Coffin-Manson-Model coefficient. Furthermore,

the simulations were launched for three different ambient temperature (-10 °C, 20 °C and 50 °C) in order to assess the thermal damage impact. Figure 5.45 presents the damage results for the four different cycles at different ambient temperatures. It can be observed that the higher the ambient temperature the more thermal aging damage is produced in the electric machine. This is because increasing the ambient temperature directly increases the average temperature of the machine during the cycle. On the contrary, the cycling damage increases with lower ambient temperatures since there is higher temperature drop between the ambient and the machine. Although all four cycles presented similar results, real cycle 1 and 2 presented the higher thermal aging and cycling damage, respectively. According to the results, the rotor iron (N6), the end windings (N5) and bearings (N10) presented high values of damage for both the thermal aging and cycling. The magnets (N7) and rotor shaft (N9) also presented significant damage. However, according to experience, the nodes N5, N6 and N10 are more critical nodes for the durability analysis. Furthermore, the magnets temperature was no validated accordingly and the rotor shaft is less critical and very close to the rotor iron.

Figure 5.46 presents temperature evolution of stator end windings, rotor iron and bearings for all four real cycles. It can be seen that the thermal model is capable to capture the cooling down during machine stops. Furthermore, the temperature drops are also higher with the ambient temperature as it was previously stated.

5.4.4 Durability test design

In order to design the thermal aging durability test, a series of prerequisites must be considered:

- Temperature limits must not be overcome. Temperatures must be under 170 °C for the stator windings and 160 °C for the rotor iron and magnets.
- Test duration must be as small as possible and not exceed 3 hours.
- Maximum peak toque must not be exceeded.
- Cycles can be repeated to match the target damage.

For designing the durability test with accelerated thermal damage an iterative process was followed according to the schema presented in Figure

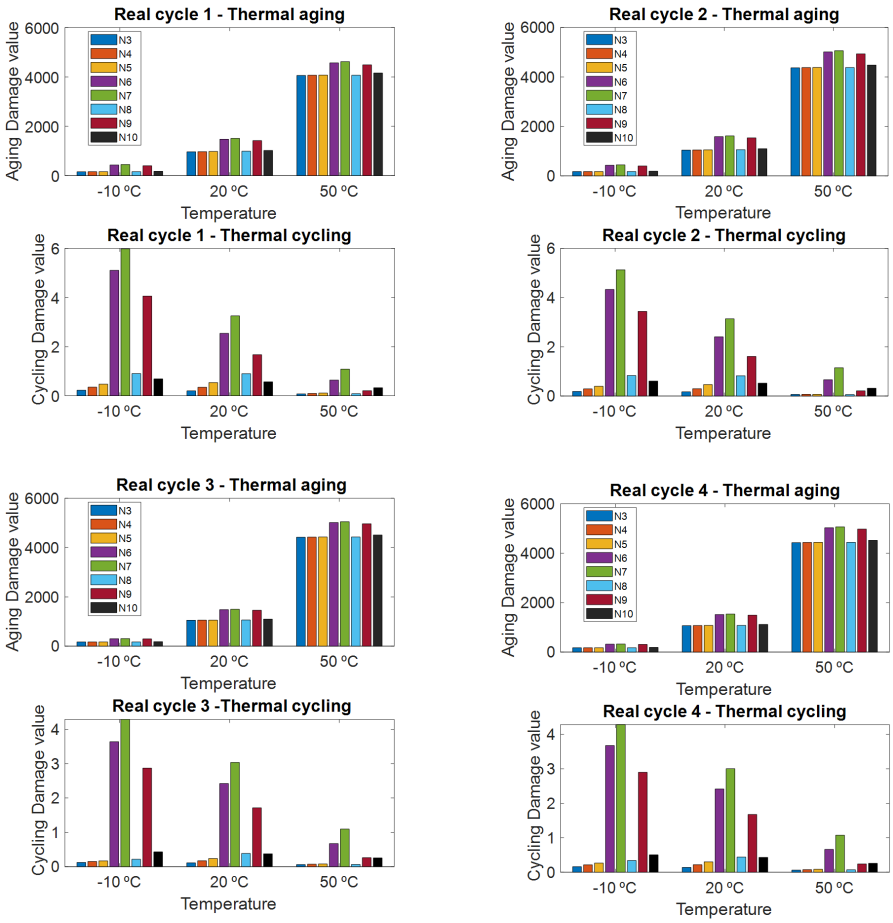

Figure 5.45: Thermal damage analysis at different ambient temperatures for real driving cycles

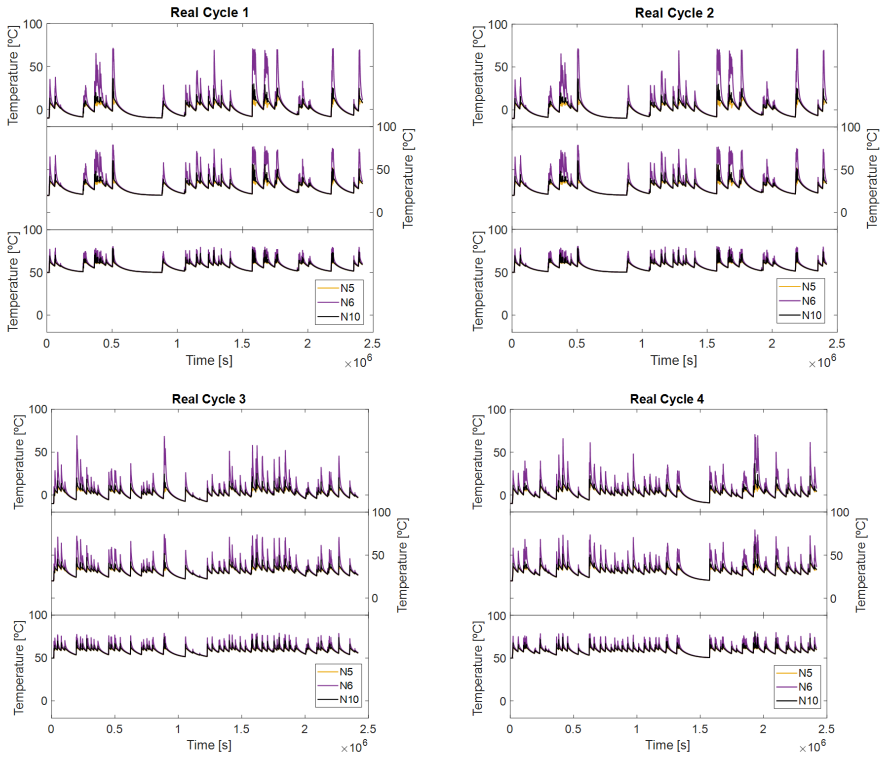

Figure 5.46: Temperature evolution of end windings, rotor iron and bearings at different ambient temperatures for real driving cycles

5.43. Depending on the cycle profile, more thermal damage was produced in the windings or the iron. In general, cycles with higher speed and less torque were more harmful for the iron parts while those cycles with high torque and less regime significatively increased the damage in the windings. Hence, two different durability cycles for aging and cycling were designed for matching the damage produced by the real cycles. Figure 5.47 shows the torque and speed profile, temperature evolution of relevant nodes and damage values for the prototype durability test 1. It can be seen that this test starts at high torque till the temperature limit is reached and then the torque is decreased at till 40 % of the maximum to maintain the highest temperature during the cycle the maximum time. Speed is mainly set constant during the cycle. Aging damage value for stator end windings (N5) was around 600 while for the real cycle 1 (Figure 5.45) it was around 1000. Hence, this cycle would need to be launched in the laboratory at 50°C two times to produce the same damage as the real cycle 2 in regard to thermal aging. In other words, a total of 4 hours of experimental testing in controlled ambient temperature conditions would be required to produce the damage similar to the real cycle 2.

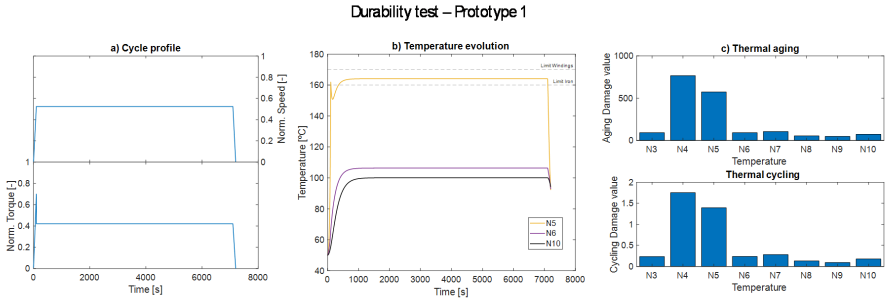

Figure 5.47: Durability test - Prototype 1. a) Cycle profile, b) Temperature evolution and c) Thermal damage at 50°C Ambient Temperature

In order to replicate the thermal aging damage produced in real cycle 2 for the rotor. Another durability test was designed (See Figure 5.48). In this case, the machine worked at very high speeds while the torque was reduced in comparison to the previous cycle. The temperature of the rotor iron (N6) was kept close to the limit during the cycle to reduce its time. Furthermore, the ageing damage value obtained for this durability test was close to 750. Observing the same damage and node in Figure 5.45 for the real cycle 2, the target ageing damage is 1800. Hence, the

durability cycle of Figure 5.48 would need to me launched three time to overcome the damage of the real cycle 2.

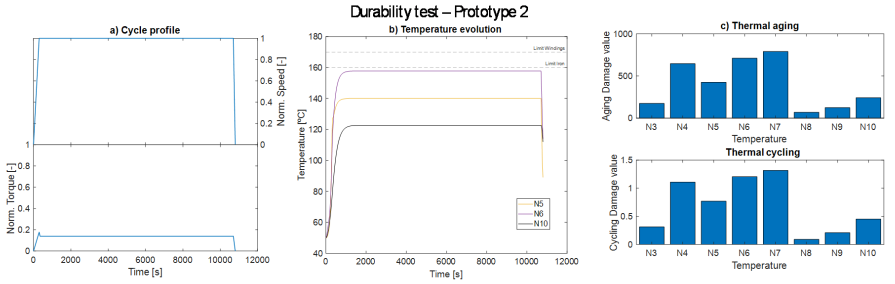

Figure 5.48: Durability test - Prototype 2. a) Cycle profile, b) Temperature evolution and c) Thermal damage at 50°C Ambient Temperature

The same approach was followed in order to design the durability test with accelerated thermal cycling damage. For these, a more dynamic profile of high speed and low torque was taken. Figure 5.49 and Figure 5.50 show the durability test prototypes for different ambient temperatures and duration. Focusing on the N6 damage aging damage, the durability cycle 3 would need to be launched in the testbench one time to achieve the cycling damage reached in real cycle 1 at 20°C. However, if the aging damage at -10°C is aimed to, the durability test 4 would be required.

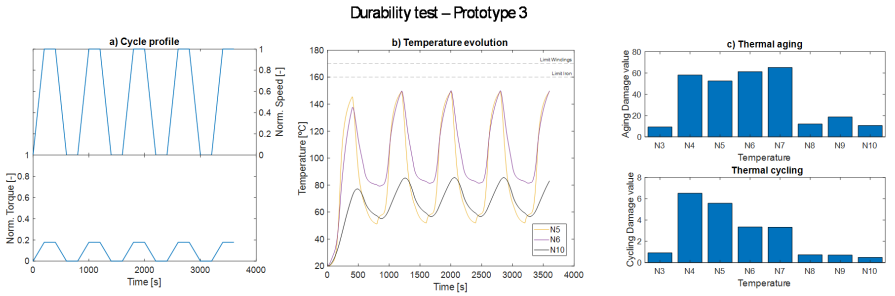

Figure 5.49: Durability test - Prototype 3. a) Cycle profile, b) Temperature evolution and c) Thermal damage at 20 °C Ambient Temperature

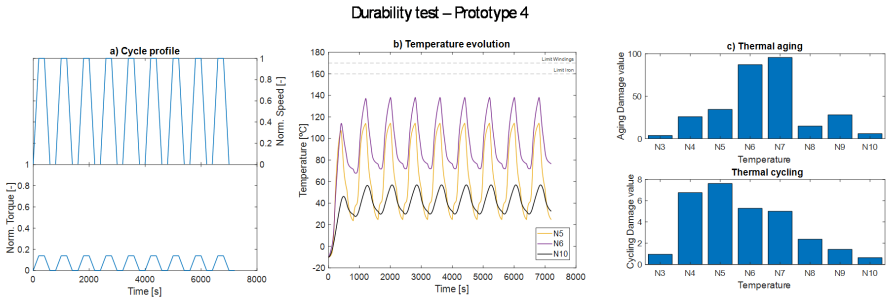

Figure 5.50: Durability test - Prototype 4. a) Cycle profile, b) Temperature evolution and c) Thermal damage at 10°C Ambient Temperature

5.5 Integrated thermal management system in electrified powertrain

5.5.1 Introduction

In this section the thermal management system of a hybrid propulsive system was constructed using the models detailed in Chapter 4. The Gasoline ICE, the battery and the EDS and their TMS were integrated to evaluate the fuel efficiency gain by benefiting from thermal synergies among powertrain subsystems.

The powertrain elements of a hybrid vehicle operate at three different levels of temperature. The ICE has the highest working temperatures ($\approx 80-90°C$), the EDS is the system with the medium temperatures ($\approx 50-60°C$) while the battery pack requires the lowest operation temperature ($\approx 15-35°C$). This situation, forces to consider a dedicated thermal management system (TMS) for each element to maintain the temperature in the required operable ranges. Two concepts of thermal management systems were considered.

The features of the TMS that have been considered in this analysis for each element are the following:

- ICE: To reduce warm up time (time the coolant needs to reach 85°C) and to avoid temperature drop at engine stops.
- EDS: Maintaining the coolant temperature below 60°C.
- Battery: Keeping the coolant temperature between 20°C and 35°C the maximum time.

The "independent" TMS system is based on designing a particular coolant circuit for each element of the powertrain of the hybrid vehicle. This case was taken as the baseline from which different layouts were explored. Although it is the less complex one, it does not allow the interaction of heat flows between the different systems.

The "integrated" two new heat exchangers (HX) were implemented in order to study the interaction among the available thermal flows and explore the synergies between the three-level temperature systems of the hybrid powertrain. These elements allow the interaction between the high (ICE) and medium (EDS) temperature circuits and between the medium (EDS) and low (Battery) temperature circuit of the TMS. Figure 5.51 shows the layout of the integrated thermal management system. The

low temperature HX connects the coolant circuit of the battery with the coolant circuit of the EDS while the high temperature HX connects the thermal flows between ICE coolant circuit and EDS coolant circuit. One of the main criteria for designing such thermal management systems was the use of the minimum elements as possible and trying to eliminate redundant components. For instance, the cooler of the independent TMS was eliminated since the preliminary results showed that keeping the battery cooler was suitable. Additionally, an actuated valve was implemented in the EDTMS to avoid cooling the ICE when it could be detrimental for fuel economy and emissions. For this purpose, this valve is completely closed when the ICE coolant temperature reaches 60°C disconnecting the low temperature fluid (EDS coolant) side of the high temperature HX.

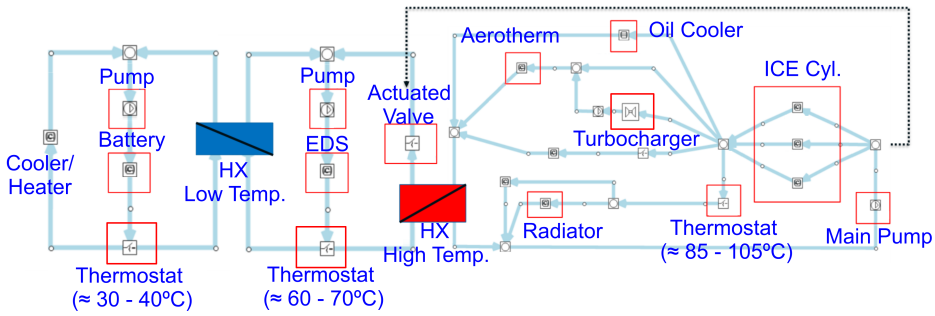

Figure 5.51: Integrated thermal management system.

Overall, the number of elements for each layout is summarized in Table 5.5. By adding two additional components it is possible to get benefits from the thermal flow interaction depending on the requirements of the different subsystem.

Table 5.5: Number of components of the TMS layouts

Components	Independent TMS	Integrated TMS
Pumps	3	3
Cooler/Heater	3	2
Thermostat	3	3
Heat Exchanger	0	2
Actuated valve	0	1
Total	9	11

5.5.2 RDE simulation results

In this section the main results obtained from the simulations of both the independent and integrated thermal management systems are presented. These thermal management systems were studied by means of a co-simulation of the ICE, Battery and EDS submodels as it can be observed in the scheme presented in Figure 5.52. Three RDE cycles were selected to evaluate the impact on operating temperature and fuel consumption of the integrated thermal management strategies.

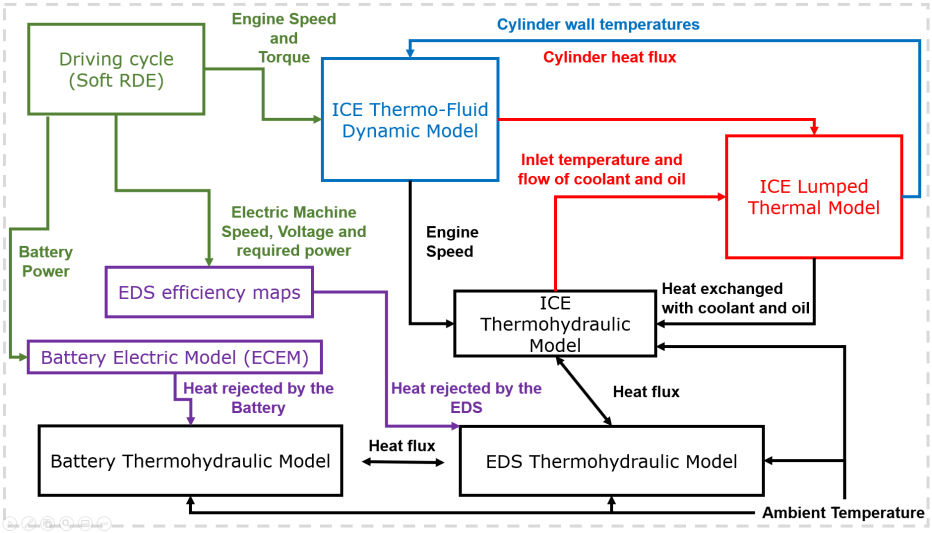

Figure 5.52: Thermal integrated co-simulation of an hybrid propulsive system.

Figure 5.53 shows the power required from each powertrain component during the RDE cycles. On one hand, when the battery power is positive, the battery pack is supplying energy (that is, in discharging mode) and when this power is negative, the battery pack is in charging mode. On the other hand, the EDS power is positive when it works as a motor and negative when it works as a generator. As explained before, the powertrain control strategy of the vehicle was defined to keep the state of charge of the battery along the cycle and to save the fuel consumed by the ICE. The simulations were launched for both warm (20°C) and cold (-20°C) conditions.

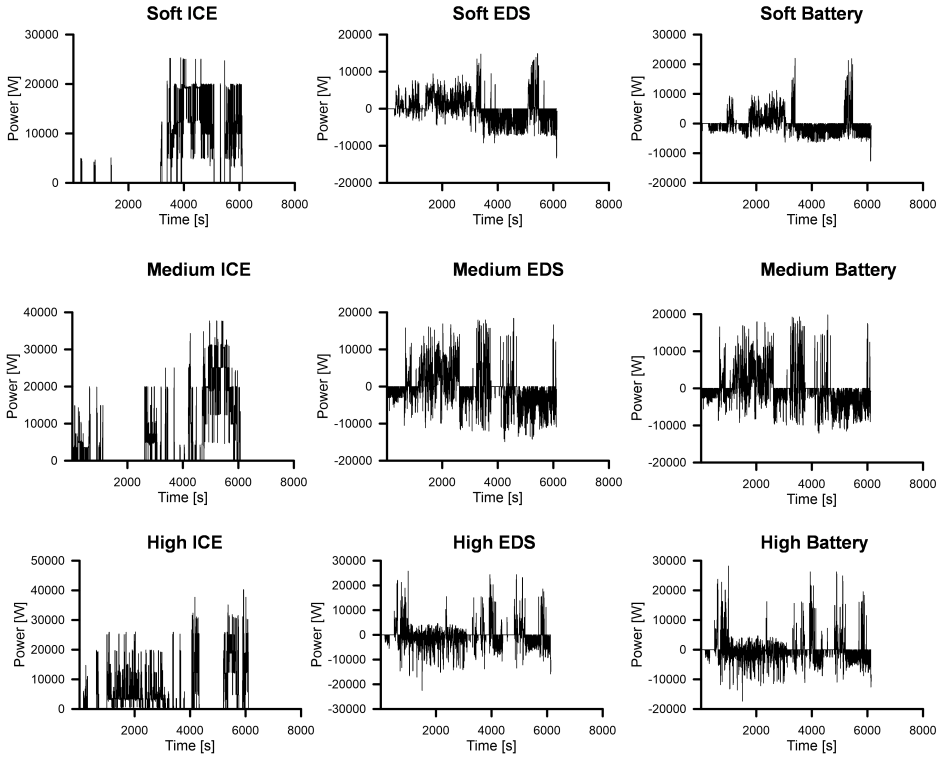

Figure 5.53: Power demanded from ICE (left), Battery (right) and EDS (middle) subsystems for each of the considered cycles.

5.5.3 Warm conditions (20°C)

In Figure 5.54 the evolution of the calculated coolant temperatures of each powertrain component with the two TMS considered during the RDE cycles at warm conditions (ambient temperature at 20°C) are shown.

With the integrated TMS configuration the temperature drops of the ICE coolant when the powertrain switches to electric mode (ICE stops) are avoided during the RDE soft cycle. During the first phase of the cycle (up to almost 4000 s) the ICE coolant temperature rises even when the engine stops due to the heat rejected by the EDS. Additionally, the integrated TMS maintains the coolant temperature above 40°C around 77.3 % of the total cycle time while in the independent TMS it is less than 46 % of the total. It is important to take into account that, the higher the coolant temperature the higher the oil temperature because of the ICE oil cooler. For the case of the EDS in the soft cycle, the integrated TMS keeps the coolant temperature above 50°C during 3035 s (a 48.0 % of the total RDE cycle) while the independent TMS maintains the coolant temperature above 50°C during 4770 s (a 75.8 % of the total RDE cycle). In other words, a slower warm-up of the EDS is produced because of the heat exchanged between the ICE and EDS system in the first phase of the cycle. Although this could slightly increase the friction losses in the EDS, the lower temperature would directly increase the machine life time by reducing its thermal ageing [172].

A similar behaviour is observed in the high cycle during the first 1500s. The integrated TMS reduced the ICE cooling during the second turn off of the engine. Additionally, the EDS warm up is reduced thanks to the heat evacuated from the ICE TMS. In this case, the battery temperature is slightly higher because of the head rejected from the EDS TMS.

Contrary to the previous cycles, the integrated TMS during the medium cycle presented limited benefit due to the nature of the cycle. From the beginning, the ICE is turned on till it reaches optimum temperature (thermostat opening). Benefits were observed during the long period (between 1000 s and 2600 s) in which the ICE is turned off. Once the temperature was close to 60°C, it was possible to use the energy available at the EDS system. Therefore, an exchange of gains is observed for this cycle. ICE warming is slightly delayed at the cost of a significant reduction in EDS warming. In other words, the control strategy was already optimum from the ICE thermal state.

In Figure 5.55 both the ICE accumulated fuel consumption for the integrated and individual TMS and their relative difference are presented. A

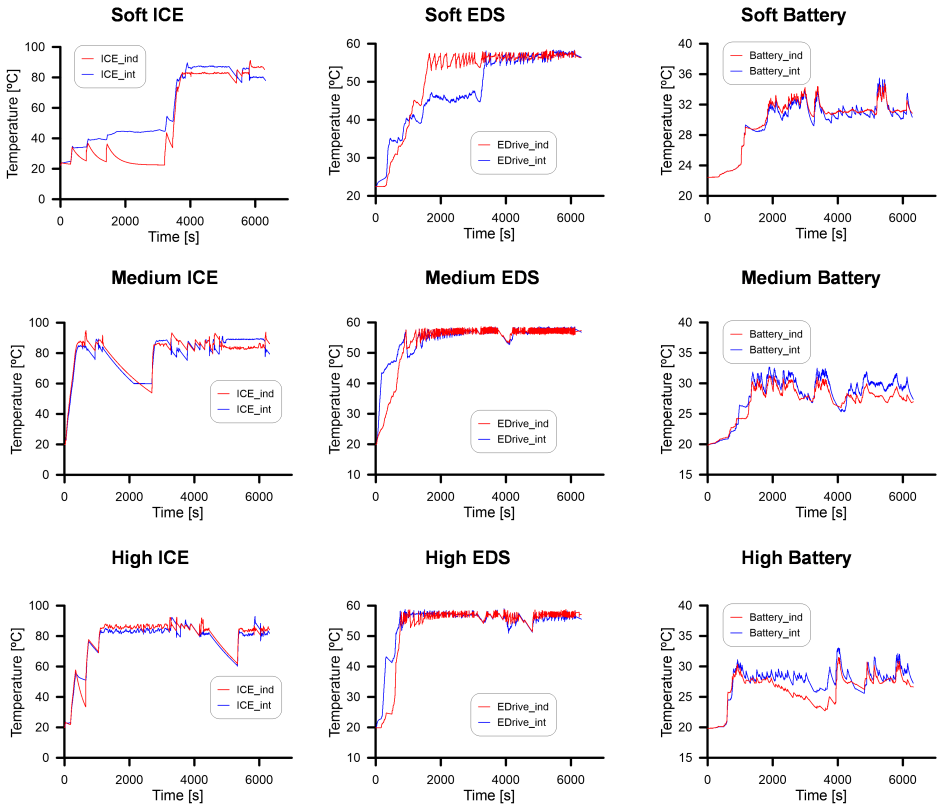

Figure 5.54: ICE, Battery and EDS coolant temperature evolution for warm conditions in RDE cycles for individual TMS and Integrated TMS where, in the legend, the *ind* indicates independent and *int* refers to integrated

negative value means that the integrated TMS decreases fuel consumption compared to the base case. Note that the more fuel is consumed during the cycle, the less relative gain is obtained because it gets diluted during the period time in which the ICE reached thermal stability (thermostat opened). For the soft cycle, the results show fuel savings around 0.62 % with the integrated TMS. However, the gain is much more significant if it is only analysed till the ICE reached thermal stability. A 1.74 % of fuel savings were obtained during this period of the soft cycle. As it was predicted in the temperatures evolution (Figure 5.54), there were also fuel gains during the ICE warming up in the high cycle. When the ICE turns on (around 180 s) there is 0.5 % of fuel saving due to the overheat absorbed from the EDS. However, the gain slightly decreased during the following 250 s in which the ICE TMS is rejecting heat to the EDS. The fuel saving immediately increase again till 0.2 % when the ICE cooling is avoided when ICE turns off (between 600 s and 1100 s). Finally, the gain is diluted with time one the engine works in optimal temperature. In the case of the medium cycle, the ICE turns on from the beginning and it does not stop till it has reached optimal temperature. This explains why in the central plots of Figure 5.55, the integrated TMS actually increases the fuel consumption till 1.6 % because it slows down the warming up of the engine while the temperature of the ICE is below 60 °C. Nevertheless, this contributes to fasten the warming up of the EDS as it was observed in Figure 5.54. However, when ICE turns off between 1000 s and 2700 s the integrated system avoid the ICE temperature drop which produces an improvement in the fuel consumption (0.2 %).

From the energy management point of view, the medium cycle has the most optimal control strategy to avoid using the ICE out of its optimum operating temperature as it happened in first half of the soft cycle.

The integrated TMS could perfectly reduce the fuel consumption if a more sophisticated TM control is applied to the system. Setting a heating priority among the different subsystems could be a good solution. For the medium and high cycle, the actuated valve could be controlled in a way that only lets heat exchange when ICE coolant temperature is below the thermal flow of the EDS. However, this would add a level of complexity to the system. As it was stated before, the nature of the proposed ITMS was to develop a simple and robust system.

This was because increasing the coolant temperature directly rises the cylinder wall temperatures improving the combustion process. Furthermore, it also contributes to increase the oil temperature, which reduces

the oil viscosity and, hence, a reduction of friction losses is produced when the temperature drops at the beginning of the cycle are avoided. The more time the ICE is operated at higher temperatures, the better its overall efficiency.

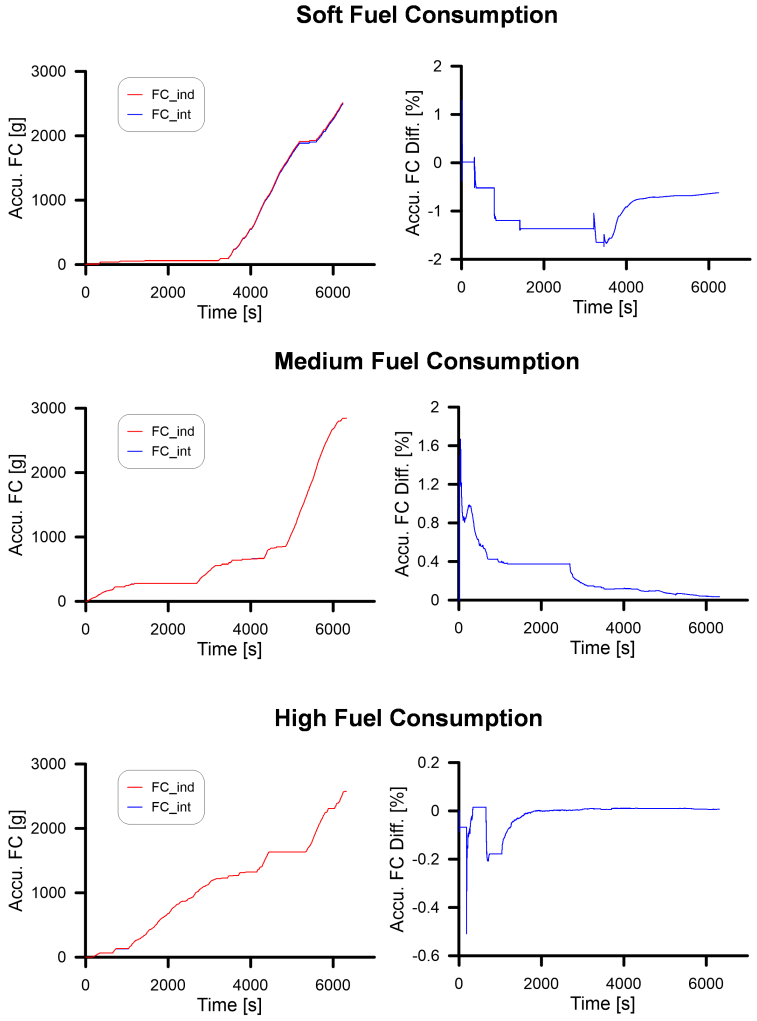

Figure 5.55: Accumulated fuel consumption for warm conditions in RDE cycles where, in the legend, the *ind* indicates independent and *int* refers to integrated

Although a potential temperature increment was expected in the exhaust gas, no significant impact was observed in the inlet (T3) and outlet

(T4) temperatures of the turbocharger with the integrated thermal management system.

5.5.4 Cold conditions (-20°C)

In Figure 5.56 the coolant temperature evolution of ICE, EDS and Battery during the RDE cycles at cold conditions are shown. For all three cycles, the trends observed are very similar to the warm case, the ICE coolant temperature drops are avoided, and the EDS warming up slows down with the integrated TMS concept of the soft cycle and increases for the medium cycle. The temperature of the battery coolant does not change because the threshold temperature for cooling start in the EDS is not achieved till the very end of the cycle.

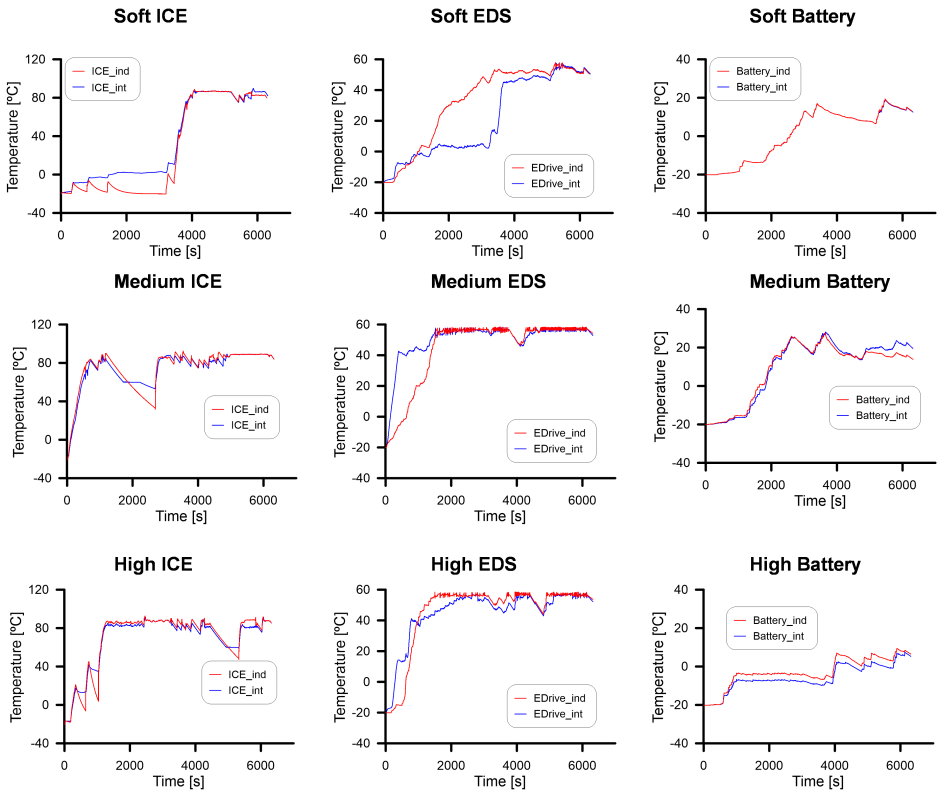

Figure 5.56: ICE, Battery and EDS temperature evolution for cold conditions in RDE cycles where, in the legend, the *ind* indicates independent and *int* refers to integrated

Finally, Figure 5.57 shows that the accumulated fuel consumption decreases almost a 3 % for the integrated TMS layout in the soft cycle. Almost double when compared with the warm case. This is because the friction losses reduction is even more significant at lower temperatures. For the medium cycle, as it happened in the warm case, the integrated TMS presented increased fuel consumption during the ICE warming time. However, this is much lower than the ambient case. Furthermore, the fuel saving during the ICE turning on after the long stop (between 1000 s and 2700 s) is much higher, reaching a 0.45 %. Finally, for the high cycle, the maximum fuel savings with the ITMS were 0.55 % during the ICE warming up. As it was stated before, the ITMS could improve the fuel saving by introducing new control algorithms.

5.6 Novel energy management control strategy in hybrid vehicles

5.6.1 Introduction

In order to assess the impact of taking into account the engine thermal state (TS) in the control strategy, the Worldwide Harmonised Light Vehicle Test Cycle (WLTC) and RDE cycles were selected for simulation and experiment. The velocity profiles of both cycles were used as inputs (i.e., vehicle speed demand) for the integrated model. For this study, the control oriented submodels detailed in Chapter 4 were implemented. Simulation results showed the optimum power split computed by the EMS of the integrated model. Afterwards, the speed and torque profiles of the internal combustion engine were launched in the testbench. For all the cases, energy management strategy consisted in battery charge sustain (i.e., both initial and end battery capacity at 50 %). Hence, the lower engine fuel consumption at the end of the cycle, the higher was the operation efficiency of the system. It is important to state that additional requirements were added to the control strategy in the model due to the testbench requirements. The ICE switching period was set to 16 seconds since higher ICE switching frequency was not possible to follow in the test-bench.

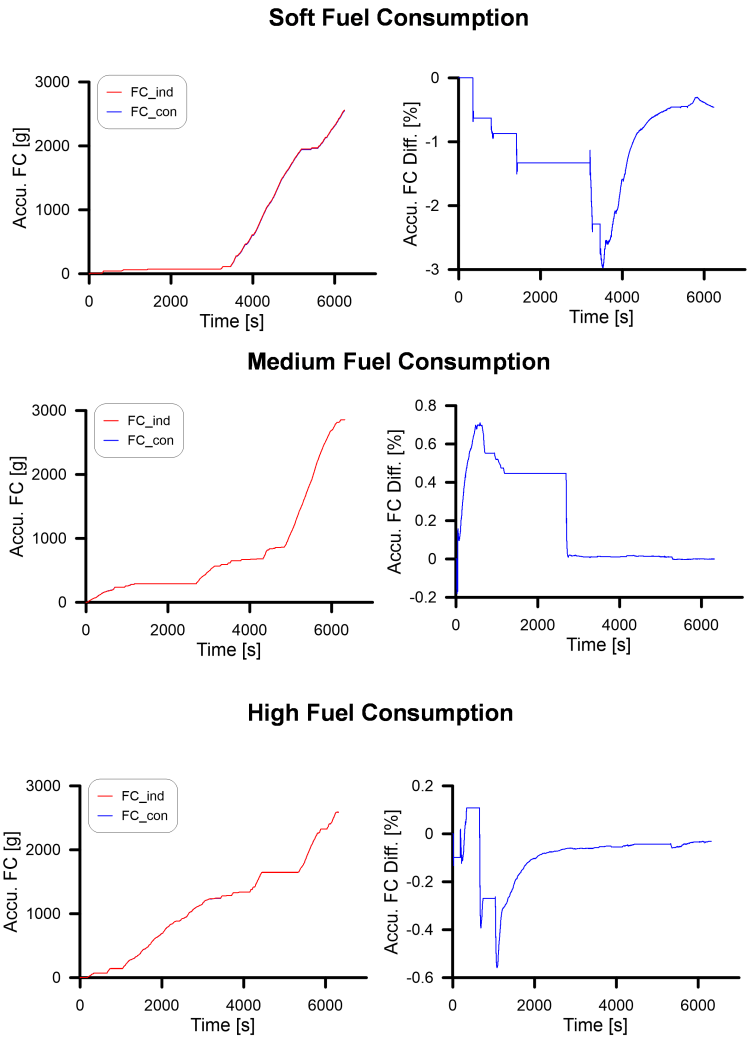

Figure 5.57: Accumulated fuel consumption for cold conditions in RDE cycles where, in the legend, the *ind* indicates independent and *int* refers to integrated

5.6.2 WTLC cycle

In Figure 5.58 it can be appreciated that in both control strategies, taking into account the engine thermal state (TS on) and without considering it (TS off) the vehicle speed demand is fulfilled. Although, the selection of the power split distribution in both control strategies was very different, the final battery SOC was practically the same complying with the simulation requirements. On one hand, when the engine thermal state control strategy is activated, almost half of the WLTC cycle is run in electric mode and the battery is discharged till 45 % at 800 s. In this moment the engine is turned on for the rest of the cycle. The EMS decided that using the engine in the most power demanding part of the cycle would reduce energy consumption. On the other hand, in the case of TS off, the engine is used since the beginning and turned off when using it has more cost than using the energy stored in the battery. It can be seen, that the battery started discharging during the last half part of the cycle when more overall power is demanded.

In Figure 5.59 the comparison between experimental and simulation results is presented for the WLTC cycle. The evolution of the engine torque, accumulated fuel consumption and coolant temperature are showed for both control strategies. It can be seen that there is a good agreement between both experimental and simulation torque. Some braking discrepancy was observed for the TS off case, however, the experiment accurately replicated the torque profile provided by the simulation. The trend of the accumulated fuel consumption was completely captured in the experimental measurements. Additionally, in both simulation and experiments, the TS on presents much lower fuel consumption as it can be appreciated in the c) and d) plots of the Figure 5.59. The fuel savings with TS on strategy were around 3.6 % and 4.1 % for the simulation and experiment, respectively. This difference could be explained by the fact that the model is underestimating the fuel consumption during the turning on of the engine given the fact that for both control strategies the model is slightly underestimating the experimental fuel consumption since the model is not capturing the surplus fuel injected during the engine start. The discrepancy in the torque profile could also contribute to the this discrepancy. Overall, taking into account the engine thermal state (TS on) has showed great fuel savings gain since operating the ICE at higher temperatures significantly reduced power friction and increased combustion efficiency. Plots e) and f) of Figure 5.59 show that with TS off, the engine is running significantly much time out of its optimum temperature range (between

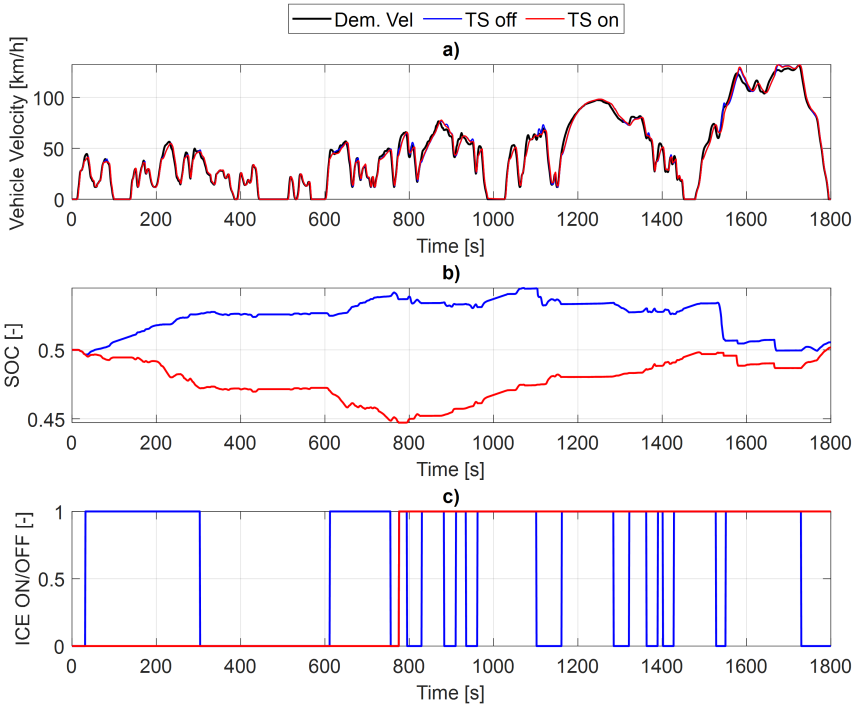

Figure 5.58: Simulation results for both control strategies during the WLTC cycle. a) Vehicle velocity. b) State of Charge of the Battery (SOC). c) ICE switch

0 and 1000 s). Furthermore, the warm up (engine coolant temperature higher than 85 °) time is higher. However, TS on only turns on the engine when it really needs it and the warming up process is much faster since its running in higher demanding conditions. Note that the slope of the coolant temperature evolution is higher than the two ICE warming phases present in the TS off case.

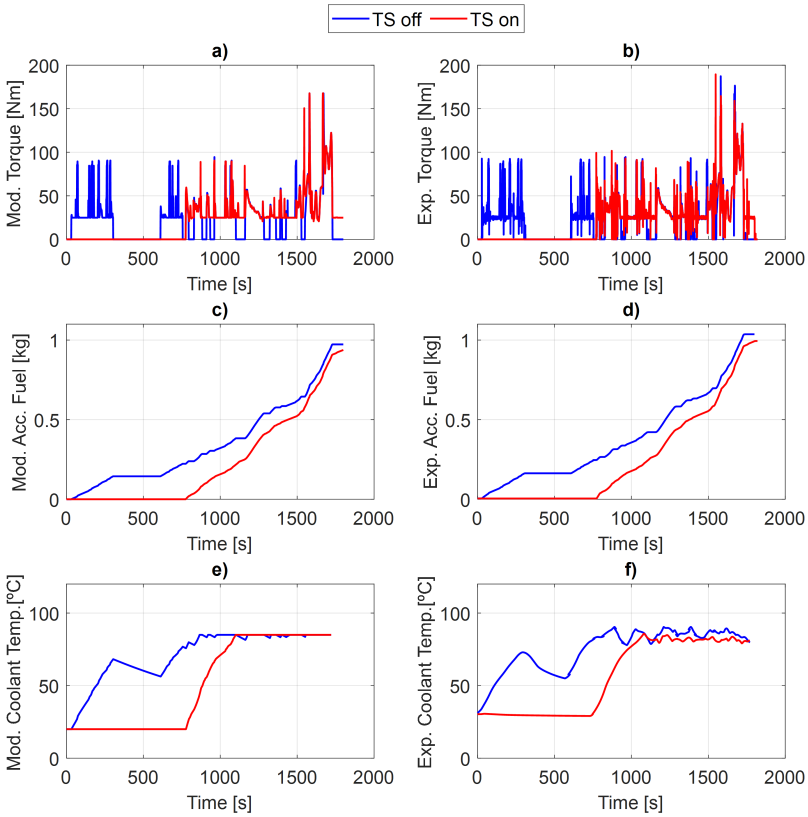

Figure 5.59: Comparison between ICE simulation results and experimental measurements for both control strategies during the WLTC cycle. a) Model Torque. b) Experimental Torque. c) Model Fuel Consumption. d) Experimental Fuel Consumption. e) Model Coolant Temperature. f) Experimental Coolant Temperature.

5.6.3 RDE cycle

In Figure 5.60 the results of both control strategies for the simulation of the RDE cycle are presented. Similarly to the previous cycle, the vehicle velocity demand was fulfilled by the energy management system in both control strategies. The SOC evolution shows that till almost 1000 s both power split distribution were the same. Then, the control strategy TS off, turns on the engine and starts charging the battery while the TS on still delays the ICE starting for more demanding conditions. Furthermore, the number of ICE switching is higher in the TS off than in the TS on case as it happened in the previous cycle. It seems that taking into account the thermal state of the engine, reduces the switching frequency of the engine. It is reasonable, that the control strategy searches for the optimum time for turning the engine while reducing the number of stops. And, hence, avoiding ICE cooling and further operation at low temperatures.

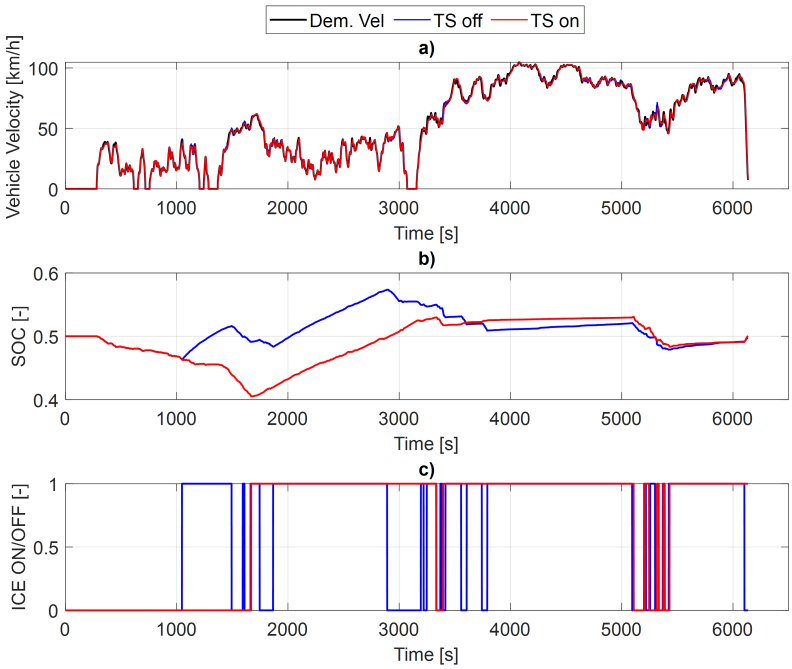

Figure 5.60: Simulation results for both control strategies during the RDE cycle. a) Vehicle velocity. b) State of Charge of the Battery (SOC). c) ICE switch

A significant agreement between the simulation results and experimental measurements can be observed in Figure 5.61. The coolant temperature error after the thermostat opens (warming up of the engine) is higher than during the rest of of the cycle because of the lumped thermal model of the engine does not include the real behaviour of the thermostat. However, this is not relevant for the study since the most impact of the strategy is obtained during the engine warming up. Additionally, the trends are captured. The evolution of the accumulated fuel consumption shows that the TS on control strategy is more efficient. Fuel savings were around 4 % and 3 % for the simulation and experiments, respectively. These gains are very similar to the ones obtained for the WLTC cycle.

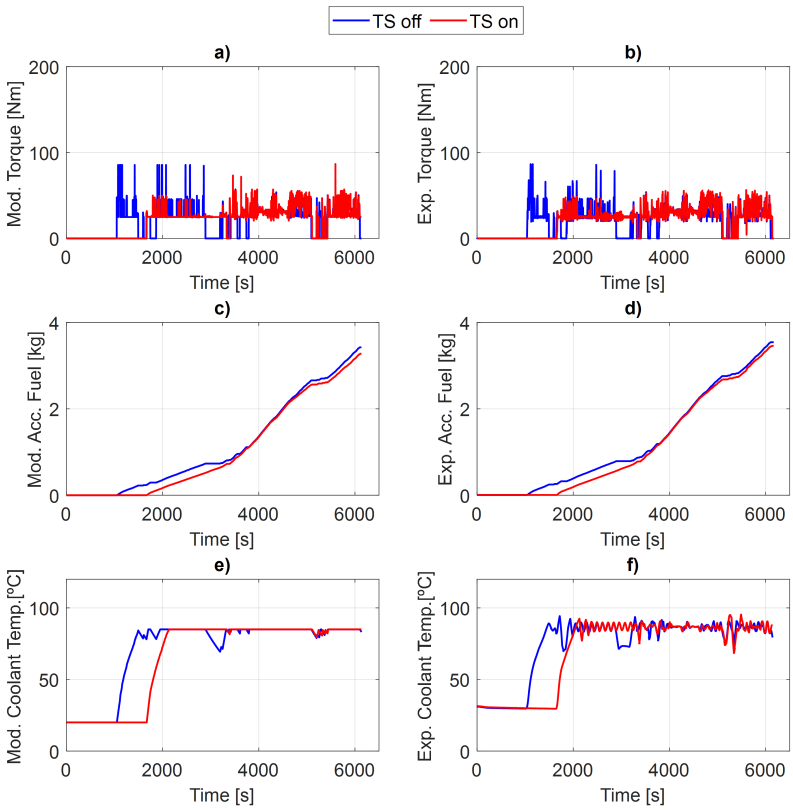

Figure 5.61: Comparison between ICE simulation results and experimental measurements for both control strategies during the RDE cycle. a) Model Torque. b) Experimental Torque. c) Model Fuel Consumption. d) Experimental Fuel Consumption. e) Model Coolant Temperature. f) Experimental Coolant Temperature.

6 Concluding remarks

6.1 Introduction

The work developed during this thesis aimed to develop a virtual platform for studying, designing and optimizing the thermal management systems of an electrified vehicle. This was motivated by the continuous regulations limiting CO2 emissions and promoting automotive electrification. Both the background knowledge of the CMT research institute and a thorough literature survey served to developing a methodology which was based on both numeral simulation and experimental measurements. Throughout the document, works concerning the implementation and improvement of submodels for different components of the electrified vehicles (i.e., Diesel and Gasoline ICEs, battery, electric machine, inverter...), development of new models and their integration into an integrated simulation tool have been described. The main submodels were experimentally validated while for the case of the inverter and the cabin submodels, the data from literature was taken as reference. Finally, studies at a component level and from a holistic perspective were carried out.

In the present chapter, the most relevant contributions and findings obtained in the development of this PhD will be highlighted. They are organized according to the same structure as the dissertation document. Afterwards, some recommendations for future work are given, with the aim of continuing the development and improvement of the integrated virtual platform for electrified vehicle simulation.

6.2 Main contributions and findings

6.2.1 ICE thermal strategies

The main conclusions of the ICE thermal management strategies ICEs can be summarized as follows:

- In this work the study of reducing the volume of the hydraulic circuits of an 1.6 L engine was carried out. A numerical model of the engine was developed and validated by means of a testing campaign in both steady and transient conditions.

  On one hand, the impact of the present thermal management strategy was practically negligible in steady state conditions. On the other hand, a significant improvement on engine efficiency was observed for transient conditions. It was also concluded that the warm up time reduction was better for the cases with lower volume of coolant and oil due to the decrease of thermal inertia. Furthermore, modifying the coolant volume had more impact in both temperatures (coolant and oil ones) than modifying the oil volume. Additionally, the heat rejected to the coolant circuit depended more on its own volume modification than the volume variation in the oil circuit. However, the heat rejected to the oil showed similar sensitivity for both circuits' variation.

  In ambient boundary conditions (at 20°C), the results showed that by reducing a 90 % both volumes during warm up time, the fuel saving obtained were around 1.2 %. Moreover, decreasing the coolant volume by 45 % produces a reduction in warm up time and fuel consumption of 7 % and 0.4 % respectively. Additionally, for cold conditions (at -7 °C), the impact was even higher, obtaining a reduction of warm up time and fuel consumption of 13 % and 0.5 % respectively. The main advantage of this new thermal strategy is

the faster decrease of oil viscosity during warm up time and, consequently, the reduction of friction losses. For the maximum volume reduction, the friction savings were higher than 4.5 % and 9 %.

The results of this work will serve as an important resource in designing and developing new thermal management systems. Either, when designing the hydraulic circuits of an engine or when engine thermal management is capable of modifying the quantity of fluid flowing thorough the engine during the warm up time.

- In regard to insulating the engine exhaust line till the turbocharger inlet, the results obtained by the Diesel ICE model concluded that in steady state conditions, the impact is practically negligible in fuel consumption. Only for low engine speed and high load a 1 % of increased efficiency was predicted. However, the impact was significant for the temperatures. T3 and T4 increased between 9 % and 18 % for the different steady state conditions. The great increments were observed for low engine speed and high load because the gas had more time to exchange heat with the surroundings in the base case (i.e., without insulation). For transient conditions, T3 and T4 behaved similar to the steady state conditions. The adiabatic case showed that the maximum achievable temperatures were higher than the base case for both ambient and cold conditions. Regarding the engine efficiency, the reduction in fuel consumption was less than 0.6 % for the ambient conditions. For cold conditions, consumption increased less than 0.2 %. For both WLTC simulations, the trade-off between friction losses and the turbine power kept the final accumulated consumption practically even for adiabatic and base case. Finally, the warm up time was increased because the heat rejected from to exhaust ports to the coolant through the walls was redirected to the exhaust gas enthalpy. This caused a warm up time increase of 20 s (2 %) and 150s (10 %) for ambient and cold conditions respectively. Especially for cold conditions, even though the consumption was not significantly impacted, this warm up time increase would mean an increment of some pollutant emissions due to cooler combustion chamber walls. Although, the quantification of the emissions was not in the scope of this work further investigations will be carried out in the future regarding this matter. Summarizing, the thermal insulation proved to have a great potential in regard to T4 increase since this would reduce the warm up time of the

aftertreatment systems. However, its impact on engine efficiency was limited in both steady and transient conditions.

- A theoretical study about the potential suitability of using nanofluids as engine coolants has been performed followed by numerical simulation for calculating the impact in a experimentally validated Diesel ICE model.

  - The evaluation of the thermal effects were carried out by using a lumped thermal model to predict the heat flux distribution over an engine in many different operation conditions in steady state and transient conditions.
  - The main features of the model have been explained as well as the validation procedure. The results obtained confirmed the reliability of the model.
  - It was quantified the variation in the nanofluid thermophysical properties with nanoparticle concentration. In order to assess the increase in the heat transfer and pump loses two cases were studied. On one hand, the volumetric flow was set constant and, on the other hand, the heat transfer coefficient was kept constant. In the study, the effect of including NePCM in the nanoparticle was evaluated. This NePCM nanofluid increased the film heat transfer coefficient compared to the normal nanofluid. In this case, it was assumed that equations for the thermophysical properties were the same as with normal nanoparticle. Additionally, it should be taken into account that the thermal conductivity and viscosity models used to predict nanofluids properties are too optimistic. The largest errors are expected in the calculation of viscosity, as experimental studies show that this model predicts much lower viscosities than those measured. Although, the Einstein model was chosen for the sake of simplicity and for the lack of a reliable general model. Furthermore, it should be noted that several hypotheses were made. For instance, it was assumed that the same correlations are applicable to nanofluids and that the flow regime remains constant having changed the coolant.
  - The results obtained showed very little improvements in engine operation through all the cases studied. In steady state conditions, although the heat transfer coefficient increased around 25

% for the case of maximum nanoparticle concentration, the heat flux only increased in approximately 1.3 %. The calculations for the case with NePCM showed the same behavior with an increment of 50 % in the heat transfer coefficient and 2.3 % in the heat flux. Regarding the pump savings, the results showed less than 0.5 % for 5 % of nanoparticle concentration. In transient conditions, the concentration of nanoparticle decreased the temperature at which the material is thermally steadied. Finally, a WLTC cycle was performed and demonstrated the limited effects in the engine thermal performance.

In addition to the limited benefits of using nanofluids in ICEs, there is the fact that applying this type of coolants in real engines would mean more investment in maintenance and manufacturing costs because of the presence of metal nanoparticles in the coolant circuit which could accumulate in some parts and plug the circuit as well as reduce the life of the coolant pump.

6.2.2 Battery thermal strategies

In this work, the study of thermal management systems in batteries have been performed using the validated electrothermal model of a prismatic cell. The thermal strategies mainly consisted in varying the boundary conditions of the battery cells: different coolant flow rates and temperatures, use of nanofluids with different nanoparticle concentration and cooling of different cell surfaces (i.e., base or lateral cooling).

Regarding the results, it has been observed that the use of nanofluids and the variation of the coolant flow rate presented a limited impact on the battery cell temperatures. However, modifying the cell surface in contact with the coolant showed significant impact. An important temperature drop of the cell active zone was observed when using side cooling compared to base cooling. Thus, it was concluded that the cell under study had low internal thermal conductivity, especially between the active zone or core and the base of the cell.

6.2.3 EDS thermal strategies

A thermal model of both the electric machine and the inverter of the electric drive systems (EDS) was developed, calibrated and experimentally validated. This model was used for developing integrated thermal

management systems and develop thermal durability tests to emulate real thermal damaging with much shorter experimental test suitable for testbench. The main conclusions for the thermal durability test design were:

- A new methodology for designing durability test for EDS prototypes has been developed and implemented.
- An electric machine implicit thermal model has been calibrated and validated with experimental data. This model was physically based and sensible to ambient temperature, coolant and oil flows conditions.
- Damage analysis at different ambient temperatures have been performed for real customer driving cycles.
- Finally, the design of the first durability tests for assessing both thermal ageing and cycling of an electric machine was performed.

6.2.4 Integrated thermal strategies

The main conclusions of the work performed for the integrated thermal management system developed for an hybrid powertrain can be summarized as follows:

A novel methodology for studying integrated thermal management systems in hybrid vehicles have been developed and validated with the support of an extensive experimental campaign performed in a 1L GDI engine designed for hybrid vehicle powertrain. Both stationary and transient RDE cycles were launched in the testbench for validating the ICE implemented submodels. The coupling of models, which have been developed and calibrated in established modeling tools, has been successfully performed benefiting from their intrinsic capabilities using the standard FMU for co-simulation. The reliability of the model implemented for predicting the thermal management of the engine has been evaluated and the obtained discrepancies were within the order of magnitude of the measurement uncertainties. Different TMSs have been designed and simulated to evaluate the thermal flows in the hybrid vehicle. The approach for designing the ITMS considered the minimization of number of components and fulfilled thermal requirements of the different components of the hybrid powertrain.

The simulation results showed that an integrated TMS allows to avoid the temperature drop of the ICE coolant when the powertrain switches to

electric mode. Additionally, the accumulated fuel consumption decreased a 1.74 % and 3 % with the integrated TMS during the ICE warming up for the RDE soft cycle at 20°C and -20°C, respectively.

Additionally, the maximum fuel saving were around 0.55 % for the aggressive cycle for both warm and cold conditions. Finally, for the case of the medium cycle, the integrated TMS proved to increase the fuel consumption during the ICE warming up time while reducing the warm up time of the EDS. Only when the ICE temperature was below the EDS optimum operating temperature, the integrated proved to be beneficial regarding fuel savings.

Additionally, a novel control strategy for the energy management system of an electrified vehicle was carried out. The main conclusions can be summarized as follows:

- A simulation platform for the energy management of xEVs has been developed and the study of an hybrid electric vehicle has been carried out with this tool. The programmed control strategy is based on the ECMS, while additional terms to compensate for dynamic issues, to consider other potential powertrain architectures and states such as the engine thermal state has been added. The Energy Management Strategy is able to consider the engine thermal state in the control algorithm, which is a novelty respect to the state of the art ECMS. In order to implement this, an extensive experimental campaign was performed at different engine coolant temperatures in order to implement a temperature dependent 3D map.

- Simulation results showed that taking into account the thermal state (TS on) of the engine reduced fuel consumption when compared to the base case. Experimental measurements confirmed those gains in both cycles. A 4.1% and 3% accumulated fuel reductions were obtained for the WLTC and RDE cycles, respectively. This is because, when the control strategy considered the thermal state of the engine, the engine was turned on only when its warming up time was going to be the fastest and the engine was operated the maximum time at higher temperatures. This contributed to decrease power losses and increase ICE fuel consumption.

6.3 Future work

The extensive scope of the present PhD thesis encompassed the study of several components of the hybrid powertrain, specially, from their ther-

mal behaviour and efficiency. Although, a great effort was invested in modelling and experimentation of these components, some subsystems still need further development and research. Furthermore, there is great potential with the developed tools for performing novel studies. Hence, contributing to design and optimize new thermal management systems for electrified vehicle.

In the following paragraphs a summary of the proposed works will be presented:

- To experimentally evaluate the most promising ICE thermal strategies implementing both the modification of the engine circuits volume and coating its exhaust line since the first improves fuel consumption and, the second, increases exhaust temperature.

- To evaluate the integration of all the ICE thermal management strategies (studied independently in this work) in a hybrid powertrain to evaluate the overall impact.

- To study the impact produced by warm up reduction engine emissions. For this, a numerical approach is recommended by implementing a validated aftertreatment system model. Afterwards, an experimental campaign should be carried out actuating on the coolant temperature of the engine.

- To develop new integrated thermal managements systems by means of the numerical models developed in Chapter 4 following the methodology proposed in this work. The studied presented in this work considered the integration of different thermal management system implementing heat exchanges between different cooling circuits. However, the suitability of specific valves (i.e., three or four way valves) could be studied with the available tools. In practice, these valves should be added to the thermohydraulic submodel. Furthermore, the integration of the cabin model with the powertrain subsystems was not evaluated.

- A more complex HVAC submodel shoud be developed. In the present work, the cabin model was capable to solve the thermal state of the vehicle's cabin as well as calculate the thermal loads. Then a simplistic approach using p-H diagrams was implemented to calculate the compressor work. However, a more complex the AC system needs to

be developed and validated with experimental measurements in order to produce high fidelity results. Additionally, further validation needs to be performed with the AC system turned on for the cabin model.

- The inverter model presented in Chapter 4 was constructed using data from literature. However, in order to improve the flexibility of the model and its application an experimental methodology should be developed for calibrating and validating the model with more extensive and accurate data.

- Although the battery model developed in the present work produced significant results, it was validated at the cell level, which inherently assumed that the battery pack operating as independent cells was ideally balanced. It is proposed to develop a flexible battery pack model using this battery cell model as source. This model should be able to take into consideration for both the electrical connections and physical locations of the cells in the pack. Additionally, experimental measurements at a pack model would also be necessary for the correct calibration and validation.

- Novel thermal management systems in battery cells should be studied such as immersion cooling with dielectric fluids. Furthermore, new cells chemistries and their application for different powertrains should be studied.

- It should be assessed if the connection between the the integrated thermal management system and the energy management system presented in this work would provide and improvement of the overall efficiency during transient cycles.

Bibliography

[1] H. Ritchie, M. Roser, P. Rosado, CO2 and Greenhouse Gas Emissions, Our World in Data. (2022).

[2] S. F. Tie, C. W. Tan, A review of energy sources and energy management system in electric vehicles, Renewable and Sustainable Energy Reviews 20 (2013) 82–102. doi:10.1016/j.rser.2012.11.077.

[3] R. Yuan, T. Fletcher, A. Ahmedov, N. Kalantzis, A. Pezouvanis, N. Dutta, A. Watson, K. Ebrahimi, Modelling and Co-simulation of hybrid vehicles: A thermal management perspective, Applied Thermal Engineering 180 (May) (2020) 115883. doi:10.1016/j.applthermaleng.2020.115883.

[4] F. Sher, S. Chen, A. Raza, T. Rasheed, O. Razmkhah, T. Rashid, P. M. Rafi-ul Shan, B. Erten, Novel strategies to reduce engine emissions and improve energy efficiency in hybrid vehicles, Cleaner Engineering and Technology 2 (November 2020) (2021) 100074. doi:10.1016/j.clet.2021.100074.

[5] G. Kalghatgi, Is it really the end of internal combustion engines and petroleum in transport?, Applied Energy 225 (May) (2018) 965–974. doi:10.1016/j.apenergy.2018.05.076.

[6] Z. Liu, J. Song, J. Kubal, N. Susarla, K. W. Knehr, E. Islam, P. Nelson, S. Ahmed, Comparing total cost of ownership of battery elec-

tric vehicles and internal combustion engine vehicles, Energy Policy 158 (2021) 112564. doi:https://doi.org/10.1016/j.enpol.2021.112564.

[7] S. Bai, C. Liu, Overview of energy harvesting and emission reduction technologies in hybrid electric vehicles, Renewable and Sustainable Energy Reviews 147 (April) (2021). doi:10.1016/j.rser.2021.111188.

[8] Y. Wang, Q. Gao, T. Zhang, G. Wang, Z. Jiang, Y. Li, Advances in integrated vehicle thermal management and numerical simulation, Energies 10 (10) (2017). doi:10.3390/en10101636.

[9] J. Bouilly, F. Lafossas, A. Mohammadi, R. Van Wissen, Evaluation of fuel economy potential of an active grille shutter by the means of model based development including vehicle heat management, SAE International Journal of Engines 8 (5) (2015) 2394–2401. doi:https://doi.org/10.4271/2015-24-2536.

[10] P. Bonkoski, A. Y. Karnik, A. Fuxman, Calibration and demonstration of vehicle powertrain thermal management using model predictive control, SAE International Journal of Engines 10 (2) (2017) 173–180. doi:https://doi.org/10.4271/2017-01-0130.

[11] S. Janarthanam, S. Paramasivam, P. Maguire, J. Gebbie, D. Hughes, HEV battery pack thermal management design and packaging solutions, SAE International Journal of Engines 10 (3) (2017) 785–789. doi:https://doi.org/10.4271/2017-01-0622.

[12] X. X. Sun, Y. C. Wang, C. M. Shao, Y. F. Wu, G. Z. Wang, Study of thermal management system for a series-parallel hybrid electric vehicle using numerical simulation, Applied Mechanics and Materials 300-301 (2013) 932–937. doi:10.4028/www.scientific.net/AMM.300-301.932.

[13] N. Hooftman, M. Messagie, J. Van Mierlo, T. Coosemans, A review of the European passenger car regulations – Real driving emissions vs local air quality (2018). doi:10.1016/j.rser.2018.01.012.

[14] T. Johnson, A. Joshi, Review of Vehicle Engine Efficiency and Emissions, SAE International Journal of Engines 11 (6) (2018) 1307–1330. doi:10.4271/2018-01-0329.

[15] J. Ko, D. Jin, W. Jang, C. L. Myung, S. Kwon, S. Park, Comparative investigation of NOx emission characteristics from a Euro 6-compliant diesel passenger car over the NEDC and WLTC at various ambient temperatures, Applied Energy (2017). doi:10.1016/j.apenergy.2016.11.105.

[16] H. Kosaka, Y. Wakisaka, Y. Nomura, Y. Hotta, M. Koike, Concept of Thermo-swing Heat Insulation on Combustion Chamber Walls and Required Thermo-physical Properties for Heat Insulation Coating, Tech. Rep. 4, Toyota Central R&D Labs (2017).

[17] R. Huber, P. Klumpp, H. Ulbrich, Dynamic analysis of the Audi valvelift system, SAE Technical Papers 3 (1) (2010) 839–849. doi:10.4271/2010-01-1195.

[18] A. Broatch, B. Tormos, P. Olmeda, R. Novella, Impact of biodiesel fuel on cold starting of automotive direct injection diesel engines, Energy 73 (2014) 653 – 660. doi:https://doi.org/10.1016/j.energy.2014.06.062.

[19] F. Payri, P. Olmeda, F. J. Arnau, A. Dombrovsky, L. Smith, External heat losses in small turbochargers: Model and experiments, Energy 71 (2014) 534–546. doi:https://doi.org/10.1016/j.energy.2014.04.096.

[20] A. Broatch, P. Olmeda, A. García, J. Salvador-Iborra, A. Warey, Impact of swirl on in-cylinder heat transfer in a light-duty diesel engine, Energy 119 (2017) 1010–1023. doi:10.1016/j.energy.2016.11.040.

[21] A. J. Torregrosa, A. Broatch, P. Olmeda, C. Romero, Assessment of the influence of different cooling system configurations on engine warm-up, emissions and fuel consumption, International Journal of Automotive Technology 9 (4) (2008) 447–458. doi:{10.1007/s12239-008-0054-1}.

[22] F. Payri, J. Martín, A. Garcia, R. Carreño, Experimental and theoretical analysis of the energy balance in a diesel engine, SAE Technical Paper 2015-01-1651 (2015). doi:https://doi.org/10.4271/2015-01-1651.

[23] C. A. Romero, Contribución al conocimiento del comportamiento térmico y la gestión térmica de los motores de combustión interna alternativos, Ph.D. thesis, Universitat Politècnica de València (2009).

[24] H. H. Pang, C. J. Brace, Review of engine cooling technologies for modern engines, Proceedings of the Institution of Mechanical Engineers, Part D: Journal of Automobile Engineering 218 (11) (2004) 1209–1215. doi:10.1243/0954407042580110.

[25] A. Osman, M. A. Hussin, S. F. Zainal Abidin, Testing and development of an enhanced and cost effective engine split cooling circuit (apr 2015). doi:https://doi.org/10.4271/2015-01-1650.

[26] A. Torregrosa, P. Olmeda, B. Degraeuwe, M. Reyes, A concise wall temperature model for di diesel engines, Applied Thermal Engineering 26 (11) (2006) 1320–1327. doi:https://doi.org/10.1016/j.applthermaleng.2005.10.021.

[27] A. J. Torregrosa, P. Olmeda, J. Martín, B. Degraeuwe, Experiments on the influence of inlet charge and coolant temperature on performance and emissions of a di diesel engine, Experimental Thermal and Fluid Science 30 (7) (2006) 633–641. doi:10.1016/j.expthermflusci.2006.01.002.

[28] H. Kang, H. Ahn, K. Min, Smart cooling system of the double loop coolant structure with engine thermal management modeling, Applied Thermal Engineering 79 (2015) 124–131. doi:10.1016/j.applthermaleng.2014.12.042.

[29] C. Soujanya, V. Sundaram, S. Sathish Kumar, Simulation of split engine cooling system, Symposium on International Automotive Technology 2015, SAE Technical Paper 2015-26-0196 (2015). doi:https://doi.org/10.4271/2015-26-0196.

[30] R. Cipollone, D. Di Battista, A. Gualtieri, Head and block split cooling in ice, IFAC Proceedings Volumes 45 (30) (2012) 400–407, 3rd IFAC Workshop on Engine and Powertrain Control, Simulation and Modeling. doi:https://doi.org/10.3182/20121023-3-FR-4025.00056.

[31] T. Sakuma, M. Yoshihara, T. Kawaguchi, T. Hamada, H. Mizuno, D. Kimura, Development of advanced non-bypass exhaust heat

recovery system using highly heat-conductive sic honeycomb, in: WCX SAE World Congress Experience, SAE International, 2019. doi:https://doi.org/10.4271/2019-01-0153.

[32] S. PI, S. Singh, A. Srivastava, M. Visaria, Numerical study of single bubble nucleate boiling heat transfer in engine cooling system, SAE Technical Paper 2019-01-0147 (2019). doi:10.4271/2019-01-0147.

[33] A. K. Haghighat, S. Roumi, N. Madani, D. Bahmanpour, M. G. Olsen, An intelligent cooling system and control model for improved engine thermal management, Applied Thermal Engineering 128 (2018) 253–263. doi:10.1016/j.applthermaleng.2017.08.102.

[34] D. Di Battista, R. Cipollone, F. Fatigati, Engine oil Thermal Management: Oil Sump Volume Modification and Heating by Exhaust Heat during ICE Warm Up, in: SAE Technical Papers, Vol. 2018-April, SAE International, 2018. doi:10.4271/2018-01-1366.

[35] D. Di Battista, R. Cipollone, Experimental and numerical assessment of methods to reduce warm up time of engine lubricant oil, Applied Energy 162 (2016) 570–580. doi:https://doi.org/10.1016/j.apenergy.2015.10.127.

[36] B. Zhou, X. D. Lan, X. H. Xu, X. G. Liang, Numerical model and control strategies for the advanced thermal management system of diesel engine, Applied Thermal Engineering 82 (2015) 368–379. doi:10.1016/j.applthermaleng.2015.03.005.

[37] M. Di Bartolomeo, F. Fatigati, D. Di Battista, R. Cipollone, A New Approach for Designing and Testing Engine Coolant Pump Electrically Actuated, in: SAE Technical Papers, Vol. 2020-April, SAE International, 2020. doi:10.4271/2020-01-1161.

[38] R. Cipollone, D. Di Battista, Sliding vane rotary pump in engine cooling system for automotive sector, Applied Thermal Engineering 76 (2015) 157–166. doi:10.1016/j.applthermaleng.2014.11.001.

[39] G. Di Giovine, L. Mariani, D. Di Battista, R. Cipollone, F. Fremondi, Modeling and experimental validation of a triple-screw pump for internal combustion engine cooling, Applied Thermal Engineering 199 (nov 2021). doi:10.1016/j.applthermaleng.2021.117550.

[40] A. J. Torregrosa, P. Olmeda, A. García-Ricós, J. Natividad, C. A. Romero, A methodology for the design of engine cooling systems in standalone applications, SAE Technical Paper 2010-01-0325 (2010). doi:10.4271/2010-01-0325.

[41] A. Kumar, V. Patil, D. Autade, T. Arthanari, J. Kamalakannan, T. Islam, Engine Warm up Optimization Using 1D Virtual Tool, in: WCX SAE World Congress Experience, SAE Technical Paper 2020-01-0319 (2020). doi:10.4271/2020-01-0319.

[42] R. D. Burke, A. J. Lewis, S. Akehurst, C. J. Brace, I. Pegg, R. Stark, Systems optimisation of an active thermal management system during engine warm-up, Proceedings of the Institution of Mechanical Engineers, Part D: Journal of Automobile Engineering 226 (D10) (2012) 1365–1379. doi:{10.1177/0954407012441883}.

[43] A. J. Torregrosa, A. Broatch, P. Olmeda, O. Cornejo, Experiments on subcooled flow boiling in IC engine-like conditions at low flow velocities, Experimental Thermal and Fluid Science 52 (2014) 347–354. doi:{10.1016/j.expthermflusci.2013.10.004}.

[44] S. U. S. Choi, J. A. Eastman, Enhancing thermal conductivity of fluids with nanoparticles, International mechanical engineering congress and exhibition, San Francisco, CA (United States), 12-17 Nov 1995.

[45] W. Daungthongsuk, S. Wongwises, A critical review of convective heat transfer of nanofluids, Renewable and Sustainable Energy Reviews 11 (5) (2007) 797 – 817. doi:http://dx.doi.org/10.1016/j.rser.2005.06.005.

[46] I. Tavman, A. Turgut, M. Chirtoc, K. Hadjov, O. Fudym, S. Tavman, Experimental study on thermal conductivity and viscosity of water-based nanofluids, Heat Transfer Research 41 (3) (2010) 339–351. doi:10.1615/HeatTransRes.v41.i3.100.

[47] S. Kakaç, A. Pramuanjaroenkij, Review of convective heat transfer enhancement with nanofluids, International Journal of Heat and Mass Transfer 52 (13–14) (2009) 3187 – 3196. doi:http://dx.doi.org/10.1016/j.ijheatmasstransfer.2009.02.006.

[48] S. Özerinç, S. Kakaç, A. G. Yazicioglu, Enhanced thermal conductivity of nanofluids: a state-of-the-art review, Microfluidics and Nanofluidics 8 (2) (2010) 145–170. doi:10.1007/s10404-009-0524-4.

[49] V. Bianco, F. Chiacchio, O. Manca, S. Nardini, Numerical investigation of nanofluids forced convection in circular tubes, Applied Thermal Engineering 29 (17–18) (2009) 3632 – 3642. doi:http://dx.doi.org/10.1016/j.applthermaleng.2009.06.019.

[50] M. Vila Millan, S. Samuel, Nanofluids and thermal management strategy for automotive application, in: SAE 2015 World Congress & Exhibition, SAE Technical Paper 2015-01-1753 (2015). . doi:https://doi.org/10.4271/2015-01-1753

[51] D. P. Kulkarni, R. S. Vajjha, D. K. Das, D. Oliva, Application of aluminum oxide nanofluids in diesel electric generator as jacket water coolant, Applied Thermal Engineering 28 (2008) 1774–1781. doi:https://doi.org/10.1016/j.applthermaleng.2007.11.017.

[52] A. Broatch, P. Olmeda, X. Margot, J. Gomez-Soriano, Numerical simulations for evaluating the impact of advanced insulation coatings on H2 additivated gasoline lean combustion in a turbocharged spark-ignited engine, Applied Thermal Engineering (2019). doi:10.1016/j.applthermaleng.2018.11.106.

[53] M. Ekström, A. Thibblin, A. Tjernberg, C. Blomqvist, S. Jonsson, Evaluation of internal thermal barrier coatings for exhaust manifolds, Surface and Coatings Technology (2015). doi:10.1016/j.surfcoat.2015.04.005.

[54] J. M. Luján, J. R. Serrano, P. Piqueras, B. Diesel, Turbine and exhaust ports thermal insulation impact on the engine efficiency and aftertreatment inlet temperature, Applied Energy (2019). doi:10.1016/j.apenergy.2019.02.043.

[55] F. J. Arnau, J. Martín, P. Piqueras, Ángel Auñon, Effect of the exhaust thermal insulation on the engine efficiency and the exhaust temperature under transient conditions, International Journal of Engine Research 22 (9) (2021) 2869–2883. doi:10.1177/1468087420961206.

[56] O. Holmer, L. Eriksson, Modeling and Analytical Solutions for Optimal Heating of Aftertreatment Systems, IFAC-PapersOnLine (2019). doi:10.1016/j.ifacol.2019.09.083.

[57] J. R. Serrano, P. Piqueras, R. Navarro, J. Gómez, M. Michel, B. Thomas, Modelling Analysis of Aftertreatment Inlet Temperature Dependence on Exhaust Valve and Ports Design Parameters, SAE Technical Papers (2016). doi:10.4271/2016-01-0670.

[58] H. Liu, Z. Wei, W. He, J. Zhao, Thermal issues about li-ion batteries and recent progress in battery thermal management systems: A review, Energy Conversion and Management 150 (2017) 304–330. doi:https://doi.org/10.1016/j.enconman.2017.08.016.

[59] A. Mahmoudzadeh Andwari, A. Pesiridis, S. Rajoo, R. Martinez-Botas, V. Esfahanian, A review of battery electric vehicle technology and readiness levels, Renewable and Sustainable Energy Reviews 78 (2017) 414–430. doi:https://doi.org/10.1016/j.rser.2017.03.138.

[60] D. C. Erb, I. M. Ehrenberg, S. E. Sarma, E. Carlson, Effects of cell geometry on thermal management in air-cooled battery packs, in: 2015 IEEE Transportation Electrification Conference and Expo (ITEC), 2015, pp. 1–6. doi:10.1109/ITEC.2015.7165807.

[61] Q. Wang, B. Jiang, B. Li, Y. Yan, A critical review of thermal management models and solutions of lithium-ion batteries for the development of pure electric vehicles, Renewable and Sustainable Energy Reviews 64 (2016) 106–128. doi:https://doi.org/10.1016/j.rser.2016.05.033.

[62] M. Zwicker, M. Moghadam, W. Zhang, C. Nielsen, Automotive battery pack manufacturing – a review of battery to tab joining, Journal of Advanced Joining Processes 1 (2020) 100017. doi:https://doi.org/10.1016/j.jajp.2020.100017.

[63] T. M. Bandhauer, S. Garimella, T. F. Fuller, A Critical Review of Thermal Issues in Lithium-Ion Batteries, Journal of The Electrochemical Society 158 (3) (2011) R1. doi:10.1149/1.3515880.

[64] R. Christen, G. Rizzo, A. Gadola, M. Stöck, Test method for thermal characterization of li-ion cells and verification of cooling concepts, Batteries 3 (1) (2017). doi:10.3390/batteries3010003.

[65] S. Arora, Selection of thermal management system for modular battery packs of electric vehicles: A review of existing and emerging technologies, Journal of Power Sources 400 (2018) 621–640. doi:https://doi.org/10.1016/j.jpowsour.2018.08.020.

[66] M. Doyle, J. Newman, A. S. Gozdz, C. N. Schmutz, J. Tarascon, Comparison of modeling predictions with experimental data from plastic lithium ion cells, Journal of The Electrochemical Society 143 (6) (1996) 1890. doi:10.1149/1.1836921.

[67] W. He, M. Pecht, D. Flynn, F. Dinmohammadi, A physics-based electrochemical model for lithium-ion battery state-of-charge estimation solved by an optimised projection-based method and moving-window filtering, Energies 11 (8) (2018). doi:10.3390/en11082120.

[68] D. Miranda, A. Almeida, S. Lanceros-Méndez, C. Costa, Effect of the active material type and battery geometry on the thermal behavior of lithium-ion batteries, Energy 185 (2019) 1250–1262. doi:https://doi.org/10.1016/j.energy.2019.07.099.

[69] H. He, R. Xiong, J. Fan, Evaluation of lithium-ion battery equivalent circuit models for state of charge estimation by an experimental approach, Energies 4 (4) (2011) 582–598. doi:10.3390/en4040582.

[70] V. Johnson, Battery performance models in advisor, Journal of Power Sources 110 (2) (2002) 321–329. doi:https://doi.org/10.1016/S0378-7753(02)00194-5.

[71] K. Huang, Y. Wang, J. Feng, Research on equivalent circuit model of lithium-ion battery for electric vehicles, in: 2020 3rd World Conference on Mechanical Engineering and Intelligent Manufacturing (WCMEIM), 2020, pp. 492–496. doi:10.1109/WCMEIM52463.2020.00109.

[72] D. Bernardi, E. Pawlikowski, J. Newman, A general energy balance for battery systems, Journal of The Electrochemical Society 132 (1) (1985) 5. doi:10.1149/1.2113792.

[73] J. Kim, J. Oh, H. Lee, Review on battery thermal management system for electric vehicles, Applied Thermal Engineering 149 (November 2018) (2019) 192–212. doi:10.1016/j.applthermaleng.2018.12.020.

[74] H. Chen, T. Zhang, Q. Gao, Z. Han, Y. Xu, K. Yang, X. Xu, X. Liu, Advance and prospect of power battery thermal management based on phase change and boiling heat transfer, Journal of Energy Storage 53 (2022) 105254. doi:https://doi.org/10.1016/j.est.2022.105254.

[75] T. Zhang, Q. Gao, G. Wang, Y. Gu, Y. Wang, W. Bao, D. Zhang, Investigation on the promotion of temperature uniformity for the designed battery pack with liquid flow in cooling process, Applied Thermal Engineering 116 (2017) 655–662. doi:https://doi.org/10.1016/j.applthermaleng.2017.01.069.

[76] T. Zhang, C. Gao, Q. Gao, G. Wang, M. Liu, Y. Guo, C. Xiao, Y. Yan, Status and development of electric vehicle integrated thermal management from btm to hvac, Applied Thermal Engineering 88 (2015) 398–409, special Issue for International Heat Transfer Symposium 2014. doi:https://doi.org/10.1016/j.applthermaleng.2015.02.001.

[77] E. Agamloh, A. von Jouanne, A. Yokochi, An overview of electric machine trends in modern electric vehicles, Machines 8 (2) (2020). doi:10.3390/MACHINES8020020.

[78] E. Gundabattini, R. Kuppan, D. G. Solomon, A. Kalam, D. P. Kothari, R. Abu Bakar, A review on methods of finding losses and cooling methods to increase efficiency of electric machines, Ain Shams Engineering Journal 12 (1) (2021) 497–505. doi:10.1016/j.asej.2020.08.014.

[79] G. D. Demetriades, H. Z. De La Parra, E. Andersson, H. Olsson, A real-time thermal model of a permanent-magnet synchronous motor, IEEE Transactions on Power Electronics 25 (2) (2010) 463–474. doi:10.1109/TPEL.2009.2027905.

[80] M. Le Guyadec, E. Vinot, L. Gerbaud, P. Lombard, A. Chaumond, T. Boussey, Building of an electrical machine thermal model in the context of a hybrid electric vehicle global optimization, in: 2017 IEEE Vehicle Power and Propulsion Conference (VPPC), 2017, pp. 1–6. doi:10.1109/VPPC.2017.8330937.

[81] G. Fang, W. Yuan, Z. Yan, Y. Sun, Y. Tang, Thermal management integrated with three-dimensional heat pipes for air-cooled

permanent magnet synchronous motor, Applied Thermal Engineering 152 (2019) 594–604. doi:https://doi.org/10.1016/j.applthermaleng.2019.02.120.

[82] P. Y. Grachev, A. A. Bazarov, A. S. Tabachinskiy, Electrical and thermal processes of HEV induction machines taking into account stator winding form, in: 2017 Dynamics of Systems, Mechanisms and Machines (Dynamics), 2017, pp. 1–6. doi:10.1109/Dynamics.2017.8239455.

[83] Z. Rehman, K. Seong, Three-d numerical thermal analysis of electric motor with cooling jacket, Energies 11 (1) (2018). doi:10.3390/en11010092.

[84] Y. Kong, D. Xu, M. Lin, Efficiency modeling and comparison of surface and interior permanent magnet machines for electric vehicle, Energy Reports 9 (2023) 419–426. doi:10.1016/j.egyr.2022.11.030.

[85] A. Zeaiter, E. Videcoq, M. Fénot, Determination of electric motor losses and critical temperatures through an inverse approach, Electrical Engineering 103 (1) (2021) 621–631. doi:10.1007/s00202-020-01098-0.

[86] A. Bousbaine, Thermal modelling of induction motors based on accurate loss density distribution, Electric Machines and Power Systems 27 (3) (1999) 311–324. doi:10.1080/073135699269325.

[87] M. Caruso, A. O. Di Tommaso, R. Miceli, C. Nevoloso, C. Spataro, F. Viola, Characterization of the parameters of interior permanent magnet synchronous motors for a loss model algorithm, Measurement 106 (2017) 196–202. doi:10.1016/j.measurement.2017.04.039.

[88] B. Sarlioglu, C. T. Morris, D. Han, S. Li, Benchmarking of electric and hybrid vehicle electric machines, power electronics, and batteries, in: 2015 Intl Aegean Conference on Electrical Machines & Power Electronics (ACEMP), 2015 Intl Conference on Optimization of Electrical & Electronic Equipment (OPTIM) & 2015 Intl Symposium on Advanced Electromechanical Motion Systems (ELECTROMOTION), 2015, pp. 519–526. doi:10.1109/OPTIM.2015.7426993.

[89] D. Han, J. Noppakunkajorn, B. Sarlioglu, Comprehensive efficiency, weight, and volume comparison of SiC-and Si-based bidirectional DC-DC converters for hybrid electric vehicles, IEEE Transactions on Vehicular Technology 63 (7) (2014) 3001–3010. doi:10.1109/TVT.2014.2323193.

[90] Z. J. Shen, I. Omura, Power semiconductor devices for hybrid, electric, and fuel cell vehicles, Proceedings of the IEEE 95 (4) (2007) 778–789. doi:10.1109/JPROC.2006.890118.

[91] E. Abramushkina, A. Zhaksylyk, T. Geury, M. El Baghdadi, O. Hegazy, A thorough review of cooling concepts and thermal management techniques for automotive WBG inverters: Topology, technology and integration level, Energies 14 (16) (2021). doi:10.3390/en14164981.

[92] P. Fan, S. Huang, H. Wang, H. Li, D. Luo, From chip to inverter: Electro-thermal modeling and design for paralleled power devices in high power application, Microelectronics Reliability 87 (2018) 271–277. doi:10.1016/j.microrel.2018.03.040.

[93] P. Ning, Z. Liang, F. Wang, L. Marlino, Power module and cooling system thermal performance evaluation for HEV application, in: 2012 Twenty-Seventh Annual IEEE Applied Power Electronics Conference and Exposition (APEC), 2012, pp. 2134–2139. doi:10.1109/APEC.2012.6166116.

[94] C. K. Liu, Y. L. Chao, J. C. Chang, W. Li, C. M. Tzeng, R. C. Fang, K. S. Kao, T.-C. Chang, C.-S. Chen, W.-C. Lo, IGBT power module packaging for EV applications, in: 2012 14th International Conference on Electronic Materials and Packaging (EMAP), 2012, pp. 1–4. doi:10.1109/EMAP.2012.6507920.

[95] G. Karoń, Safe and Effective Smart Urban Transportation—Energy Flow in Electric (EV) and Hybrid Electric Vehicles (HEV), Energies 15 (18) (2022). doi:10.3390/en15186548.

[96] D. Lanzarotto, M. Marchesoni, M. Passalacqua, A. P. Prato, M. Repetto, Overview of different hybrid vehicle architectures, IFAC-PapersOnLine 51 (9) (2018) 218–222, 15th IFAC Symposium on Control in Transportation Systems CTS 2018. doi:https://doi.org/10.1016/j.ifacol.2018.07.036.

[97] Y. C. Wang, Y. J. Yang, Z. L. Gu, Optimized design of the cooling system for a hybrid electric vehicle, Journal of Beijing Institute of Technology (1), 44–47, (2004).

[98] S. Park, A comprehensive thermal management system model for hybrid electric vehicles, Ph.D. thesis, University of Michigan, Ann Arbor, MI, USA (2011).

[99] K. Okamoto, H. Aikawa, M. Ohmikawa, K. Hayashi, Thermal management of a hybrid vehicle using a heat pump, in: WCX SAE World Congress Experience, SAE International, 2019. doi:https://doi.org/10.4271/2019-01-0502.

[100] G. Major, M. Utter, Thermal management of cabin and battery pack in HEV/PHEV/BEV vehicles. USA Patent US20120225341, 2011-03-03.

[101] X. Sun, Y. Wang, F. Wang, Thermal management technology for series-parallel hev, in: 2010 IEEE International Conference on Mechatronics and Automation, 2010, pp. 213–218. doi:10.1109/ICMA.2010.5589078.

[102] J. Liang, G. Xu, L. Jian, L. Li, Electric air conditioner system with on-board charger for phev, in: 2011 IEEE International Conference on Information and Automation, 2011, pp. 421–426. doi:10.1109/ICINFA.2011.5949029.

[103] K. Bennion, M. Thornton, Integrated vehicle thermal management for advanced vehicle propulsion technologies. SAE Technical Paper 2010-01-0836 (2010). doi:10.4271/2010-01-0836.

[104] G. Mathur, UltimateCooling™ new cooling system concept using the same coolant to cool all vehicle fluids (C599/010/2003), 2004, pp. 125–138.

[105] M. Cao, I. Kovent, J. Ku, Efficient thermal modeling and integrated control strategy of powertrain for a parallel hybrid EcoCAR2 competition vehicle, SAE Technical Papers 1 (2014). doi:10.4271/2014-01-1927.

[106] Y. Q. Dong, X. Wang, S. Xu, H. Wu, J. Zhou, Y. Ding, Designing and evaluating the integrated thermal management system of a

plug-in parallel hybrid electric vehicle, in: SAE 2020 Vehicle Electrification and Autonomous Vehicle Technology Forum, SAE International, 2020. doi:https://doi.org/10.4271/2020-01-5242.

[107] H. Fathabadi, High thermal performance lithium-ion battery pack including hybrid active-passive thermal management system for using in hybrid/electric vehicles, Energy 70 (2014) 529–538. doi:10.1016/j.energy.2014.04.046.

[108] T. Kiss, J. Lustbader, D. Leighton, Modeling of an Electric Vehicle Thermal Management System in MATLAB/Simulink, SAE Technical Papers 2015-01-1708 (2015). doi:10.4271/2015-01-1708.

[109] T. Rana, Y. Yamamoto, Universal electric vehicle thermal management system, SAE International Journal of Advances and Current Practices in Mobility, Vol. 3, No. 1 p. 604-613. doi:10.4271/2020-28-0002.

[110] C. Kaufmann, J. Frochte, A Case Study on FMU As Co-Simulation Exchange Format for FEM Models (2016).

[111] P. Lu, Q. Gao, Y. Wang, The simulation methods based on 1D/3D collaborative computing for the vehicle integrated thermal management, Applied Thermal Engineering 104 (2016) 42–53. doi:https://doi.org/10.1016/j.applthermaleng.2016.05.047.

[112] P. Casoli, A. Gambarotta, N. Pompini, L. Riccò, Development and application of co-simulation and "control- oriented" modeling in the improvement of performance and energy saving of mobile machinery, Energy Procedia 45 (2014) 849–858. doi:10.1016/j.egypro.2014.01.090.

[113] A. Picarelli, V. Avila, S. P. Robinson, Thermal management strategies for integrated hybrid vehicle subsystems, in: 6th Hybrid and Electric Vehicles Conference (HEVC 2016), 2016, pp. 1–6. doi:10.1049/cp.2016.0975.

[114] G. Lang, F. Kitanoski, C. Kussmann, Principal aspects and simulation of a hybrid demonstrator vehicle's cooling system, Asia Pacific Automotive Engineering Conference, SAE Technical Paper 2007-01-3483 (2007). doi:10.4271/2007-01-3483.

[115] T. J. Shelly, J. A. Weibel, D. Ziviani, E. A. Groll, Comparative analysis of battery electric vehicle thermal management systems under long-range drive cycles, Applied Thermal Engineering 198 (2021) 117506. doi:https://doi.org/10.1016/j.applthermaleng.2021.117506.

[116] S. Lei, S. Xin, S. Liu, Separate and integrated thermal management solutions for electric vehicles: A review, Journal of Power Sources 550 (2022) 232133. doi:https://doi.org/10.1016/j.jpowsour.2022.232133.

[117] A. Lajunen, Y. Yang, A. Emadi, Recent developments in thermal management of electrified powertrains, IEEE Transactions on Vehicular Technology 67 (12) (2018) 11486–11499. doi:10.1109/TVT.2018.2876315.

[118] J. Ma, Y. Sun, S. Zhang, J. Li, S. Li, Experimental study on the performance of vehicle integrated thermal management system for pure electric vehicles, Energy Conversion and Management 253 (2022) 115183. doi:https://doi.org/10.1016/j.enconman.2021.115183.

[119] S. Hemmati, N. Doshi, D. Hanover, C. Morgan, M. Shahbakhti, Integrated cabin heating and powertrain thermal energy management for a connected hybrid electric vehicle, Applied Energy 283 (2021) 116353. doi:https://doi.org/10.1016/j.apenergy.2020.116353.

[120] M. Shams-Zahraei, A. Z. Kouzani, S. Kutter, B. Bäker, Integrated thermal and energy management of plug-in hybrid electric vehicles, Journal of Power Sources 216 (2012) 237–248. doi:https://doi.org/10.1016/j.jpowsour.2012.05.055.

[121] IEA, Global EV Data Explorer, IEA Paris, 2021.

[122] V. S. R. Tappeta, B. Appasani, S. Patnaik, T. S. Ustun, A Review on Emerging Communication and Computational Technologies for Increased Use of Plug-In Electric Vehicles, Energies 15 (18) (2022). doi:10.3390/en15186580.

[123] I. Tsiropoulos, P. Siskos, P. Capros, The cost of recharging infrastructure for electric vehicles in the EU in a climate neutrality con-

text: Factors influencing investments in 2030 and 2050, Applied Energy 322 (June) (2022). doi:10.1016/j.apenergy.2022.119446.

[124] P. Polverino, I. Arsie, C. Pianese, Optimal Energy Management for Hybrid Electric Vehicles Based on Dynamic Programming and Receding Horizon, Energies 14 (12) (2021). doi:10.3390/en14123502.

[125] Q. Xue, X. Zhang, T. Teng, J. Zhang, Z. Feng, Q. Lv, A Comprehensive Review on Classification, Energy Management Strategy, and Control Algorithm for Hybrid Electric Vehicles, Energies 13 (20) (2020). doi:10.3390/en13205355.

[126] S. Onori, L. Serrao, G. Rizzoni, Hybrid Electric Vehicles: Energy Management Strategies, Springer, 2016.

[127] O. Sundström, D. Ambühl, L. Guzzella, On implementation of dynamic programming for optimal control problems with final state constraints, Oil Gas Sci. Technol. - Rev. IFP 65 (1) (2010) 91–102. doi:10.2516/ogst/2009020.

[128] E. Ozatay, S. Onori, J. Wollaeger, U. Ozguner, G. Rizzoni, D. Filev, J. Michelini, S. Di Cairano, Cloud-based velocity profile optimization for everyday driving: A dynamic-programming-based solution, IEEE Transactions on Intelligent Transportation Systems 15 (6) (2014) 2491–2505. doi:10.1109/TITS.2014.2319812.

[129] C. M. Martinez, X. Hu, D. Cao, E. Velenis, B. Gao, M. Wellers, Energy management in plug-in hybrid electric vehicles: Recent progress and a connected vehicles perspective, IEEE Transactions on Vehicular Technology 66 (6) (2017) 4534–4549. doi:10.1109/TVT.2016.2582721.

[130] J. Kessels, M. Koot, P. van den Bosch, D. Kok, Online energy management for hybrid electric vehicles, IEEE Transactions on Vehicular Technology 57 (6) (2008) 3428–3440. doi:10.1109/tvt.2008.919988.

[131] H.-Y. Hwang, Developing equivalent consumption minimization strategy for advanced hybrid system-II electric vehicles, Energies 13 (8) (2020) 2033. doi:10.3390/en13082033.

[132] B. Zhang, J. Zhang, F. Xu, T. Shen, Optimal control of power-split hybrid electric powertrains with minimization of energy consumption, Applied Energy 266 (2020) 114873. doi:10.1016/j.apenergy.2020.114873.

[133] K. Van Berkel, W. Klemm, T. Hofman, B. Vroemen, M. Steinbuch, Optimal Energy Management for a mechanical-hybrid vehicle with cold start conditions, 2013 European Control Conference (ECC), Zurich, Switzerland, 2013, pp. 452-457. doi:10.23919/ECC.2013.6669706..

[134] H. Chu, H. Shi, Y. Jiang, T. Shen, Modeling of engine thermal dynamics and its application in energy management of HEVs considering engine warming-up, International Journal of Engine Research (2021). doi:10.1177/14680874211044575.

[135] J. Lescot, A. Sciarretta, Y. Chamaillard, A. Charlet, On the integration of optimal energy management and thermal management of hybrid electric vehicles, IEEE, 2021.

[136] F. Payri, J. Martín, F. J. Arnau, S. Artham, Analysis of temperature and altitude effects on the global energy balance during wltc, International Journal of Engine Research 23 (11) (2022) 1831–1849. arXiv:https://doi.org/10.1177/14680874211034292, doi:10.1177/14680874211034292.

[137] A. Broatch, P. Olmeda, X. Margot, L. Agizza, A generalized methodology for lithium-ion cells characterization and lumped electro-thermal modelling, Applied Thermal Engineering 217 (2022) 119174. doi:https://doi.org/10.1016/j.applthermaleng.2022.119174.

[138] A. Pirooz, J. V. Mierlo, M. Berecibar, 3d thermal and 1d electro-thermal model coupling framework for lithium-ion battery cells in automotive industry platforms, in: 2021 IEEE Vehicle Power and Propulsion Conference (VPPC), 2021, pp. 1–6. doi:10.1109/VPPC53923.2021.9699116.

[139] A. Marinoni, M. Tamborski, T. Cerri, G. Montenegro, G. D'errico, A. Onorati, E. Piatti, E. E. Pisoni, 0D/1D Thermo-Fluid Dynamic Modeling Tools for the Simulation of Driving Cycles and the Optimization of Ic Engine Performances and Emissions, Applied Sciences (Switzerland) 11 (17) (2021) 1–21. doi:10.3390/app11178125.

[140] A. Broatch, P. Olmeda, J. Martín, J. Salvador-Iborra, Development and validation of a submodel for thermal exchanges in the hydraulic circuits of a global engine model (apr 2018). doi:https://doi.org/10.4271/2018-01-0160.

[141] J. Martín, F. Arnau, P. Piqueras, A. Auñón, Development of an Integrated Virtual Engine Model to Simulate New Standard Testing Cycles, SAE Technical Paper 2018-01-1413 (2018). doi:10.4271/2018-01-1413.

[142] Á. Auñón García, Development and validation of a virtual engine model for simulating standard testing cycles, Ph.D. thesis, Universitat Politècnica de València, Valencia (Spain) (jun 2021). doi:10.4995/Thesis/10251/168906.

[143] J. Galindo, A. Tiseira, R. Navarro, D. Tarí, H. Tartoussi, S. Guilain, Compressor Efficiency Extrapolation for 0D-1D Engine Simulations, SAE Technical Paper 2016-01-0554 (2016). doi:10.4271/2016-01-0554.

[144] F. P. Incropera, D. P. Dewitt, T. L. Bergman, A. S. Lavine, Fundamentals of Heat and Mass Transfer, 6th Edition, John Wiley & Sons, Inc., 2007.

[145] F. Dittus, L. Boelter, Heat transfer in automobile radiators of the tubular type, University of California Publications in Engineering 2 (1930) 443–461.

[146] J. Benajes, P. Olmeda, J. Martín, D. Blanco-Cavero, A. Warey, Evaluation of swirl effect on the global energy balance of a hsdi diesel engine, Energy 122 (2017) 168 – 181. doi:https://doi.org/10.1016/j.energy.2017.01.082.

[147] A. J. Torregrosa, P. Olmeda, J. Martín, C. Romero, A tool for predicting the thermal performance of a diesel engine, Heat Transfer Engineering 32 (10) (2011) 891–904. doi:10.1080/01457632.2011.548639.

[148] J. Benajes, P. Olmeda, J. Martín, R. Carreño, A new methodology for uncertainties characterization in combustion diagnosis and thermodynamic modelling, Applied Thermal Engineering 71 (1) (2014) 389–399. doi:10.1016/j.applthermaleng.2014.07.010.

[149] F. Payri, P. Olmeda, J. Martin, R. Carreño, A New Tool to Perform Global Energy Balances in DI Diesel Engines, SAE International Journal of Engines 7 (1) (2014) 43–59. doi:10.4271/2014-01-0665.

[150] J. R. Serrano, P. Olmeda, F. J. Arnau, M. A. Reyes-Belmonte, H. Tartoussi, A study on the internal convection in small turbochargers. Proposal of heat transfer convective coefficients, Applied Thermal Engineering 89 (2015) 587–599. doi:{10.1016/j.applthermaleng.2015.06.053}.

[151] F. Payri, P. Olmeda, F. J. Arnau, A. Dombrovsky, L. Smith, External heat losses in small turbochargers: Model and experiments, Energy 71 (2014) 534–546. doi:https://doi.org/10.1016/j.energy.2014.04.096.

[152] V. Tziolas, N. Zingopis,G. Montenegro, A. Onorati, G. D'Errico, T. Cerri, A. Marinoni, Prediction of driving cycles by means of a co-simulation framework for the evaluation of IC engine tailpipe emissions, SAE Technical Papers (June) (2020) 13. doi:10.4271/2020-37-0011.

[153] L. Gascón, J. M. Corberán, Construction of second-order TVD schemes for nonhomogeneous hyperbolic conservation laws, Journal of Computational Physics 172 (1) (2001) 261–297. doi:10.1006/jcph.2001.6823.

[154] R. S. Benson, J. H. Horlock, D. E. Winterbone, The Thermodynamics and Gas Dynamics of Internal-combustion Engines, no. v. 1 in Oxford science publications, Clarendon Press, 1982.

[155] J. M. Luján, C. Guardiola, B. Pla, V. Pandey, Impact of driving dynamics in RDE test on NOx emissions dispersion, Proceedings of the Institution of Mechanical Engineers, Part D: Journal of Automobile Engineering 234 (6) (2020) 1770–1778. arXiv:https://doi.org/10.1177/0954407019881581, doi:10.1177/0954407019881581.

[156] X. Lin, H. E. Perez, S. Mohan, J. B. Siegel, A. G. Stefanopoulou, Y. Ding, M. P. Castanier, A lumped-parameter electro-thermal model for cylindrical batteries, Journal of Power Sources 257 (2014) 1–11. doi:10.1016/j.jpowsour.2014.01.097.

[157] S. Panchal, I. Dincer, M. Agelin-Chaab, R. Fraser, M. Fowler, Transient electrochemical heat transfer modeling and experimental validation of a large sized LiFePo4/Graphite battery, International Journal of Heat and Mass Transfer 109 (2017) 1239–1251. doi:10.1016/j.ijheatmasstransfer.2017.03.005.

[158] A. Arcila, X. Marcelle, Study of Conjugate Heat Transfer in Battery Cooling Systems for xEV Applications, Master's thesis, Universitat Politècnica de Valencia (2021).

[159] C. Batard, N. Ginot, J. Antonios, Lumped dynamic electrothermal model of IGBT module of inverters, IEEE Transactions on Components, Packaging and Manufacturing Technology 5 (3) (2015) 355–364. doi:10.1109/TCPMT.2015.2392625.

[160] D. Marcos, F. J. Pino, C. Bordons, J. J. Guerra, The development and validation of a thermal model for the cabin of a vehicle, Applied Thermal Engineering 66 (1) (2014) 646–656. doi:10.1016/j.applthermaleng.2014.02.054.

[161] I. H. Bell, J. Wronski, S. Quoilin, V. Lemort, Pure and pseudo-pure fluid thermophysical property evaluation and the open-source thermophysical property library coolprop, Ind. Eng. Chem. Res. 53 (6) (2014) 2498–2508. doi:10.1021/ie4033999.

[162] W. Yu, D. M. France, E. V. Timofeeva, D. Singh, J. L. Routbort, Comparative review of turbulent heat transfer of nanofluids, International Journal of Heat and Mass Transfer 55 (21–22) (2012) 5380 – 5396. doi:http://dx.doi.org/10.1016/j.ijheatmasstransfer.2012.06.034.

[163] W. Yu, S. Choi, The Role of Interfacial Layers in the Enhanced Thermal Conductivity of Nanofluids: A Renovated Maxwell Model, Journal of Nanoparticle Research 5 (1-2) (2003) 167–171. doi:10.1023/A:1024438603801.

[164] J. Maxwell, A treatise on Electricity and Magnetism, Mac Millan, 1873.

[165] R. B. Mansour, N. Galanis, C. T. Nguyen, Effect of uncertainties in physical properties on forced convection heat transfer with nanofluids, Applied Thermal Engineering 27 (1) (2007) 240 – 249. doi:http://dx.doi.org/10.1016/j.applthermaleng.2006.04.011.

[166] A. Einstein, A new determination of the molecular dimensions, Ann. Phys. 324 (1906) 289–306.

[167] W. Duangthongsuk, S. Wongwises, Measurement of temperature-dependent thermal conductivity and viscosity of TiO2-water nanofluids, Experimental Thermal and Fluid Science 33 (4) (2009) 706–714. doi:10.1016/j.expthermflusci.2009.01.005.

[168] M. Kole, T. K. Dey, Viscosity of alumina nanoparticles dispersed in car engine coolant, Experimental Thermal and Fluid Science 34 (6) (2010) 677–683. doi:10.1016/j.expthermflusci.2009.12.009.

[169] M. Chandrasekar, S. Suresh, A. C. Bose, Experimental investigations and theoretical determination of thermal conductivity and viscosity of Al_2O_3/water nanofluid, Experimental Thermal and Fluid Science 34 (2) (2010) 210 – 216. doi:http://dx.doi.org/10.1016/j.expthermflusci.2009.10.022.

[170] J. Sarkar, A critical review on convective heat transfer correlations of nanofluids, Renewable and Sustainable Energy Reviews 15 (6) (2011) 3271 – 3277. doi:http://dx.doi.org/10.1016/j.rser.2011.04.025.

[171] S. M. Sohel Murshed, C. A. Nieto de Castro, M. J. V. Lourenço, M. L. M. Lopes, F. J V. Santos, A review of boiling and convective heat transfer with nanofluids, Renewable and Sustainable Energy Reviews 15 (5) (2011) 2342 – 2354. doi:http://dx.doi.org/10.1016/j.rser.2011.02.016.

[172] X. Wang, B. Li, D. Gerada, K. Huang, I. Stone, S. Worrall, Y. Yan, A critical review on thermal management technologies for motors in electric cars, Applied Thermal Engineering 201 (2022) 117758. doi:https://doi.org/10.1016/j.applthermaleng.2021.117758.